# Beyond classical Electrodynamics: Mesoscale Electron Dynamics and Nonlinear Effects in Hybrid Nanostructured Systems

FRIEDRICH-SCHILLER-
UNIVERSITÄT
JENA

Habilitationsschrift

vorgelegt am 19. Oktober 2022

der Physikalisch-Astronomischen Fakultät

der Friedrich-Schiller-Universität Jena

von

Dr. Christin DAVID

aus Königs Wusterhausen

Gutachter

1. Prof. Dr. Kathy Lüdge, Technische Universität Ilmenau
2. Prof. Dr. Ulf Peschel, Friedrich-Schiller-Universität Jena
3. Prof. Dr. Søren Peder Madsen, Aarhus Universitet, Dänemark

Erteilung der Lehrbefähigung am 14. Juni 2023

– To my parents –

For unconditional love and for creating the best place in the world: home.

– To Robert –

I cannot fathom where I would be today without you. I wouldn’t want to be anywhere else though.

# Abstract

This work investigates the optial properties of hybrid metal-dielectric and ionic-solid largely regular nanostructures in the presence of nanosized features such as gaps and thin walls in tubular structures. The fundamental optical response of plasmonic, ionic and dielectric systems is considered from a classical electromagnetic perspective, including properties of amorphous materials, rough interfaces, nonlinear and semi-classical charge interactions. We focus hereby on two aspects: (i) nonclassical effects stemming from the quantum nature of freely moving charges and (ii) nonlinear optical response. The overall aim is to realistically describe complex nanoparticle distributions and ultrathin multilayers with reliable and rapid methods of computational nanophotonics while extending its scope towards multiphysics aspects beyond classical electrodynamics. The analytical and numerical models developed over the past years are presented in this work in detail with standard, but necessary technical details available in the appendices.

We often assume a multilayered system where one layer is a nanostructure with either one- or two-dimensional symmetry, i. e., a grating or laminar structure in the first and an array of nanoparticles (disks, holes, pillars, etc.) in the latter case. Given the symmetries and overall composition of the structure, our method of choice is the Fourier Modal Method (FMM) (also referred to as Rigorous Coupled Wave Analysis (RCWA)) together with the scattering matrix approach to connect the different layers.

The standard FMM formulation is extended to include spatial dispersion effects of conduction band electrons in metals introducing not only an additional boundary condition, but an overall third longitudinal solution to the standard transversal solutions of the electromagnetic wave equation.

In simple geometries, single nanoparticles and planar homogeneous structures, such effects have an impact on their optical response for very small system parameters, e. g. gap sizes of the order of 1 nm, particle sizes below 10 nm and film thicknesses of similar order. We find, however, that anomalous diffraction in nanostructures and strong coupling of particles to semiconductor substrates can further promote the influence of short-ranged charge carrier interaction onto a larger structure. Strong electromagnetic coupling of semiconductor surfaces to spatially dispersive metal nanoparticles can lead to an Autler-Towns splitting (dynamical Stark effect) of modes that is not classically observed. Hereby, the particle sizes need to be again of the order of 10 nm and below. On the other hand, regular nanostructures offer a range of high parallel momenta contributions from diffracted waves which are not available in planar homogeneous systems. Therefore, light-induced charge dynamics can be excited in nanostructured systems even with light at normal incidence and for much larger structural parameters of the order of 100 nm. Moreover, nanostructured systems enable the coupling to nonclassical longitudinal modes via an increased number of geometrical parameters that can achieve a nonclassical limit. In holey metal films, e. g., the hole size can be considered

classical as long as a small hole-to-hole distance provides nanoscale metallic bridges where spatial dispersion effects take place locally.

Next to metal-dielectric interfaces and plasmonic optical response in such systems, we are interested in soft plasmonics, where charge interactions in ionic systems are studied in analogy to plasmons in solid metals. This can be used to describe, e. g. electrolytes in chemical or biological systems, e. g. as part of nerve cell signaling. Ions are much heavier and slower than electrons which shifts their plasmonic resonances outside of the optical window into the GHz regime. Here, positive and negative charges typically coexist and the light-induced charge dynamics needs to be expanded towards not only one, but two (or more) longitudinal excitations. This two-fluid model for ionic systems was first introduced through our work and we have studied spherical systems, chains of ionic microspheres and planar electrolyte-solid systems. Similar findings as for the electron plasma were made with respect to ionic systems with, however, overall much weaker electromagnetic response even under resonant conditions due to the material system. In general, ionic systems can be treated within a soft plasmonic approach in full analogy to the plasmonics of electron response in rigid metal solids.

As a further step, we use the standard FMM formulation to explore the impact of higher harmonic waves from the local fields around the nanostructures studied. This way, we explore surface second harmonic generation (SSHG) in one- and two-dimensional structures, as well as THG in amorphous nanoparticle composites embedded in a transparent host matrix.

Within the FMM, second order nonlinear quantities such as the material-dependent susceptibility and the macroscopic polarization can be treated fully in reciprocal space. Ultimately, an overlapp integral of the second order polarization, calculated from the local fields at the Fundamental Harmonic (FH), and the local fields at the Second Harmonic (SH) determines the nonlinear fields around the nanostructure which can be calculated from a line integral of the corresponding reconstructed quantity in reciprocal space. This makes FMM a rapid computational approach for assessing nonlinear optical response. Apart from classically expected SSHG, we consider metal gratings with spatial dispersion towards truly nanosized gaps and study the impact of nonlocal electron-electron interaction on the nonlinear response in metallic nanostructures.

We investigate amorphous composites of nanoparticles embedded in a transparent host matrix employing effective medium theories (EMTs) to homogenize the respective layers for efficient use within FMM in comparision to real-world samples as obtained from Atomic Layer Deposition (ALD). These EMTs include Bruggeman (Br), Maxwell-Garnett (MG) and modified Maxwell-Garnett-Mie (MMGM). For dispersive media, only very small volume fractions yield a good agreement with different compuational techniques such as Finite Difference Time Domain (FDTD). Within this regime, we study ALD samples deposited onto a metal grating both in the linear and nonlinear regime. Nonlinear properties of the amorphous composite can stem from either the host or the metallic nanoparticle inclusions or both media. Due to local field enhancement occurring at the inclusion surface, the effective third order

susceptibility of the effective homogeneous layer is strongly increased as compared to the intrinsic susceptibility of a single nanoparticle. This leads to an overall enhancement of nonlinear optical properties in amorphous composites which we studied in close collaboration with experimental partners.

The present work is organized as follows.

The first part and chapter is dedicated to the fundamentals of computational nanophotonics. First, we discuss the challenges in nanoscale optical modeling and critically compare the suitability of a number of available computational methods for different systems underlining again why we focus on the Fourier Modal Method for most of this work. Then we introduce the classical FMM as far as is needed to develop the extensions pointed out above. Fundamental aspects and limitations are discussed. We conclude the first chapter with our own applications of the standard method to nanostructured devices for spectroscopy and photovoltaics to demonstrate its applicability to experiments and design tasks. The highlighted works deal with two extensions to analytically Fourier transformable unit cells for FMM routines, namley hollow nanotube pillars and supercells with disk-shaped particles of different size and composition. For photovoltaic systems, an emphasis was put on the accurate inclusion of optimized doping profiles and the photocurrent gain attributed to nitride nanostructures.

Part II deals with nonclassical aspects of the optical response of charged plasma in nano- and mesoscopic systems as part of a large-scale device structure. In the second chapter, we introduce spatial dispersion in general and the hydrodynamic model to combine Maxwell's equations with the dynamics of a charged and freely oscillating plasma. We then turn explicitly to the Fourier Modal Method and introduce its extension to include the hydrodynamic response model in the third chapter. This is further applied to holey metal films and the impact of nonclassical charge interaction on Extraordinary Optical Transmission (EOT) is studied. In chapter 4, We discuss a number of effects regarding mesoscopic electron dynamics in nanoparticle arrays with applications to photovoltaic (PV) devices including the details on the aformentioned mode splitting. Lastly, we turn to a generalized two-fluid hydrodynamic model that is capable of describing nonclassical interactions in ionic systems (and electron-hole systems, which we have not pursued) in chapter 5. Here, we derive modified Mie coefficients for a system with two interacting charged ionic fluids confined in spherical membranes.

Part III introduces with chapter 6, nonlinear optical effects first in general terms before diving into the fundamentals of surface second harmonic generation in chapter 7. This is then exploited in the Fourier Modal Method (FMM) to gain insight into the surface second harmonic generation in one- and two-dimensional structures and analyze the optical response not only in specific higher orders of the fundamental frequency but also in higher orders of diffraction in close collaboration with local experimental partners. We study in particular cases under double resonant excitation, i. e. resonant coupling of a specific diffraction order into the grating structure at both the fundamental and second harmonic wavelength exploiting Rayleigh anomalies.

We further discuss amorphous composites in chapter 8 whose linear optical properties

can be obtained applying effective medium theories (EMTs) to real-world ALD samples. In section 8.1, this is extended to third order Kerr nonlinearities, i. e. the self-phase modulated (SPM) case, and discussed for thin films using the Fourier Modal Method (FMM) self-consistently. This is further applied to nonlinear polarization holography in section 8.2 for the cross-phase modulated (XPM) case, where the phase and amplitude of the nonlinear polarization reveal intrinsic dephasing times in the studied materials. For amorphous composites, these properties become dependent on the metal loading.

These ongoing efforts aim at shaping light with nonlinear diffraction gratings. Overall conclusions and an outlook to future directions is given in chapter 9.

# Zusammenfassung

Die vorliegende Habilitationschrift untersucht die optischen Eigenschaften hybrider, metall-dielektrischer und ionisch-rigider meist regulärer Nanostrukturen, welche nanoskale geometrische Merkmale aufweisen wie Spalten und ultradünne Wände in Nanoröhrchen. Dabei wird die grundlegende optische Antwort plasmonischer, ionischer und dielektrischer Systeme aus Sicht der klassischen Elektrodynamik betrachtet, wobei amorphe Materialien, rauhe Oberflächen, nichtlineare und nichtklassische Wechselwirkungen zwischen Ladungsträgern im Besonderen Beachtung finden werden. Wir konzentrieren uns auf zwei Hauptaspekte: (i) nichtklassische Effekte, die sich aus den quantenmechanischen Eigenschaften frei beweglicher Ladungsträgern ergeben, sowie (ii) nichtlineare optische Systemantwort.

Das Ziel ist die möglichst realistische Beschreibung komplexer Nanopartikelverteilungen und ultradünner Schichten mit verlässlichen und zugleich zügigen Methoden der computergestützten Nanophotonik während wir Ihre Anwendungen jenseits der klassischen Elektrodynamik erweitern hin zu multiphysikalischen und multiskalen Aspekten. Analytische und numerische Modelle, die hierbei von uns über die letzten Jahre entwickelt wurden, werden im Detail vorgestellt, wobei nötige Grundlagen in den Anhängen dargestellt werden.

Häufig gehen wir von einem Multilagensystem aus, bei dem eine Schicht nanostrukturiert ist. Dies kann eine eindimensionale Rillenstruktur oder ein zweidimensionales Gitter aus Nanopartikeln (Scheiben, Löcher, Säulen, Röhrchen) sein. Aufgrund der Symmetrie und Zusammensetzung der Struktur ist die Methode unserer Wahl die Fourier Modal Method (FMM), auch Rigorous Coupled Wave Analysis (RCWA), zusammen mit der Streumatrixmethode um die verschiedenen Lagen miteinander mittels Randwertbedingungen zu verbinden.

Die Standardformulierung der FMM wird um räumlich-dispersive Effekte der Leitungsbandelektronen in Metallen erweitert. Dies führt nicht nur zu einer zusätzlichen Grenzbedingung, sondern zu einer dritten, longitudinalen Lösung zur elektromagnetischen Wellengleichung neben den bekannten transversalen Lösungen in klassischen, homogenen Medien.

In einfachen Geometrien wie einzelnen Nanopartikeln und flachen, homogenen Lagen haben solche Effekte einen Einfluss auf die optische Antwort für sehr kleine Systemparameter, wie z. B. Abständen von ca. 1 nm, einem Durchmesser von Nanopartikeln von unter 10 nm und Schichtdicken derselben Größenordnung.

Wir haben in unseren Studien zeigen können, dass anomale Beugungseffekte in räumlich-dispersiven Nanostrukturen und starke Nanopartikel-Substrat-Kopplungseffekte den Einfluss kurzreichweitiger Leitungsträger-Leitungsträger-Wechselwirkung auf eine großskalige Struktur begünstigen kann. Starke elektromagnetische Kopplung von Halbleiteroberflächen und räumlich-dispersiven Metallnanopartikeln führt zu einer Autler-Towns-Aufspaltung (dynamischer Starkeffekt) von Moden, welches klassisch nicht beobachtet wird. Hierbei müssen die Partikelgrößen jedoch wieder im Bereich von ca. 10 nm und darunter liegen. Reguläre Nanostrukturen bieten hingegen hohe Beiträge des parallelen Impulses aus Wellen höherer

Beugungsordnung, die in ideal flachen Systemen nicht auftreten, und nichtklassische, longitudinale Ladungsträgerdichtewellen anregen können. Damit kann lichtinduzierte Ladungsträgerdynamik in nanostrukturierten Systemen auftreten, selbst wenn bei senkrechtem Lichteinfall und für relativ große Strukturparameter, z. B. Schichtdicken im Bereich von einigen 100 nm. Zusätzlich bieten Nanostrukturen weitere geometrische Systemparameter, die bei ideal flachen Strukturen nicht auftreten und ebenfalls die Kopplung an nichtklassische, longitudinale Moden erlauben. So können z. B. in löchrigen Metallfilmen die dielektrischen Perforationen klassisch groß sein, während ihr Abstand die metallischen Brücken dazwischen auf die Nanoskala reduzieren kann, so dass räumlich-dispersive Effekte lokal von Bedeutung für die gesamte Struktur werden.

Neben metallisch-dielektrischen Grenzflächen und plasmonisch-optischer Antwort in solchen Systemen haben wir in den vergangenen Jahren Plasmonik in weicher Materie untersucht, wo die Wechselwirkung zwischen ionischen Ladungsträgern in Flüssigkeiten in Analogie zu Elektronen in rigiden Metallstrukturen betrachtet wird. Dieser Ansatz kann für Elektrolyten in chemischen und biologischen Systemen verwendet werden, z. B. zur Studie der Kommunikation von Nervenzellen, sogenannten Axonen, wo einfache elektrische *Kabeltheorie* schnell auf seine Grenzen stößt. Ionen sind viel schwerer und langsamer als Elektronen in Festkörpern. Dies verschiebt die ionischen Plasmonresonanzen aus dem optischen Spektralbereich ins GHz-Regime. Positive und negative Ladungsträger koexistieren in Elektrolyten und deren lichtinduzierte Dynamik und Wechselwirkung muss erweitert werden, um zwei (oder mehr) nichtklassische, longitudinale Anregungen zu integrieren. Wir haben ein solches Zwei-Flüssigkeitenmodell für ionische Systeme entwickelt und an sphärischen, ionischen Mikropartikeln, sowie flachen Elektrolyt-Festkörper-Grenzflächen untersucht. Die Ergebnisse zu ionischen Systemen sind qualitativ vergleichbar mit denen eines reinen Elektronenplasmas in Metallen, wobei die elektromagnetische Antwort selbst unter Resonanzbedingungen geringer ist, was bei dem betrachteten Materialsystem zu erwarten ist. Insgesamt gilt, dass ionische Systeme mehrerer Ladungsträger innerhalb des Ansatzes der weichen Plasmonik in vollständiger Analogie zu plasmonischen Eigenschaften von Elektronen in metallischen Festkörpern durchgeführt werden kann.

Im zweiten großen Abschnitt untersuchen wir ausgehend von der Standardformulierung der FMM höhere Harmonische. Hier betrachten wir im Besonderen oberflächeninduzierte zweite Harmonische SSHG, die aus den Nahfeldern um Nanostrukturen entstehen, sowie dritte Harmonische THG in amorphen Kompositen aus sphärischen Nanopartikeln eingebettet in transparente Materialien.

Innerhalb der FMM können nichtlineare Größen zweiter Ordnung wie die materialabhängige Suszeptibilität und die makroskopische Polarisation komplett im reziproken Raum entwickelt und propagiert werden, analog zu den linearen Kenngrößen wie den elektrischen und magnetischen Feldern. Um ein nichtlineares Feld an der zweiten Harmonischen SH zu bestimmen, muss zu guter letzt ein Überlappintegral aus der makroskopischen Polarization zweiter Ordnung, welches aus den lokalen Feldern an der Grundschwingung FH berechnet

wird, und den lokalen Feldern an der zweiten Harmonischen SH bestimmt werden. Dazu muss ein Linienintegral um die Nanostruktur durchgeführt werden, welches sich aus der im reziproken Raum gefundenen Lösung durch Fouriertransformation ergibt. Dies zeigt, dass die FMM als computergestützte Methode in der Tat sehr geeignet ist, zügig und zuverlässig nichtlineare Eigenschaften von regulären Nanostrukturen zu bewerten. Neben klassisch zu erwartenden Oberflächennichtlinearitäten SSHG werden räumlich-dispersive Effekte in metallischen Nanostrukturen betrachtet und der Einfluss nichtlokaler Elektron-Elektron-Wechselwirkung auf die nichtlineare Antwort untersucht.

Weiterhin untersuchen wir amorphe Komposite, d. h. sphärische Nanopartikel, die in ein transparentes Material eingebettet sind. Wir verwenden effektive Materialtheorien (EMTs) um amorphe Lagen für den effizienten Einsatz in der FMM zu homogenisieren. Diese können mit Ergebnissen zu Proben aus der Atomlagenabscheidung (Atomic Layer Deposition (ALD)) verglichen werden. Die betrachteten EMTs umfassen Bruggeman (Br), Maxwell-Garnett (MG) und die modifizierte Maxwell-Garnett-Mie-Theorie (MMGM). Bei dispersiven Materialien führen nur sehr geringe Füllfaktoren zu einer guten Übereinstimmung mit anderen numerischen Methoden wie der Finite Difference Time Domain (FDTD). Innerhalb dieses Regimes untersuchen wir ALD-Proben, die auf metallische Nanostrukturen aufgesetzt werden sowohl im linearen als auch im nichtlinearen Regime. Dabei können nichtlineare Eigenschaften dritter Ordnung im amorphen Komposit sowohl vom transparenten Host als auch von den eingebetteten Nanopartikeln oder sogar von beiden Medien gleichzeitig stammen. Aufgrund lokaler Felderhöhungen an der Oberfläche eingeschlossener, metallischer Nanopartikel ist die effektive Suszeptibilität dritter Ordnung der homogenisierten Schicht deutlich verstärkt im Vergleich zur intrinsischen Suszeptibilität einzelnen Nanopartikel. Dies führt zu einer Verstärkung der nichtlinearen Eigenschaften von amorphen Kompositen, welche wir zusammen mit experimentell arbeitenden Partnern untersucht haben.

Die vorliegende Habilitationsschrift ist wie folgt aufgebaut. Das erste Kapitel beschäftigt sich mit einigen ausgewählten Grundlagen der computergestützten Nanophotonik. Zunächst diskutieren wir die Herausforderungen, die optische Simulationen von nanoskalen Systemen mit sich bringen und vergleichen kritisch die Eignung einer Anzahl numerischer Methoden auf verschiedene Probleme mit dem Ziel, unsere Wahl für die Fourier Modal Method (FMM) zu unterstreichen, aber auch ihre möglichen Grenzen aufzuzeigen. Dann führen wir die grundlegenden Gleichungen der Standardformulierung der FMM soweit ein, wie es nötig ist, die nachfolgenden Erweiterungen zu nichtklassischen und nichtlinearen Eigenschaften gut nachvollziehen zu können. Am Ende des ersten Kapitels demonstrieren wir anhand eigener Arbeiten zusammen mit experimentellen Kollaborateuren Anwendungen der klassischen FMM auf Nanostrukturen für Entwicklungsaufgaben in der Spektroskopie und Photovoltaik. Die so hervorgehobenen Arbeiten verwenden zwei Erweiterungen mit Nanostrukturen deren Fouriertransformationen der jeweiligen Einheitszelle analytisch sind, nämlich hohle Nanoröhrchen und Superzellen mit Partikelscheiben unterschiedlicher Größe und Komposition. Für photovoltaische Systeme liegt der Fokus auf der akkuraten Beschreibung optimierter Dopingprofile

und der Erhöhung des Photostroms durch Nanostrukturen aus verschiedenen Nitriden.

Teil II beschäftigt sich mit nichtklassischen Aspekten der optischen Materialantwort in Ladungsträgerplasmen in nano- und mesoskalen Systemen als Teil eines größeren Bauelements. Im zweiten Kapitel führen wir zunächst die räumliche Dispersion eines frei beweglichen, oszillierenden Ladungsträgerplasmas allgemein ein. Wir verwenden hierfür das hydrodynamische Modell für das freie Elektronengas gekoppelt an die Maxwellschen Gleichungen. Im dritten Kapitel wenden wir uns der Fourier Modal Method (FMM) zu und ihrer Erweiterung um das hydrodynamische Modell. Dies wird angewendet auf perforierte metallische Filme, wo wir den Einfluss lichtinduzierter Elektronendynamik und Ladungsträgerwechselwirkung auf außergewöhnliche Transmissionsverstärkung EOT untersuchen. In Kapitel 4 diskutieren wir die Auswirkung von mesoskopischer Elektronendynamik in Nanopartikelgittern mit Anwendungen in der plasmon-assistierten Photovoltaik PV, wie z. B. die oben genannte Modenaufspaltung. Zu guter Letzt generalisieren wir das hydrodynamische Modell zu einem Zwei-Flüssigkeitenmodell, das nichtklassische Ladungsträgerwechselwirkungen in ionischen Systemen (sowie Elektron-Loch-Plasmen, die von anderen Arbeitsgruppen untersucht wurden) in Kapitel 5 betrachtet. Hier werden modifizierte, nichtlokale Mie-Koeffizienten für ein System wechselwirkender geladener ionischer Fluide räumlich eingeschränkt in sphärischen Membranen hergeleitet.

Teil III führt in Kapitel 6 zunächst allgemeine Konzepte der nichtlinearen Optik ein. Wir verwenden die Fourier Modal Method (FMM) im Besonderen zur Untersuchung der oberflächeninduzierten zweiten Harmonischenerzeugung in Nanostrukturen in Kapitel 7, wo wir Kenngrößen der SSHG in ein- und zweidimensionalen Strukturen betrachten und die nichtlineare optische Antwort z. B. in den verschiedenen Beugungsordnungen in enger Kollaboration mit experimentellen Partnern untersuchen. Wir erforschen im Besonderen Systeme mit doppelt resonanter Anregung, d. h. Licht wird resonant unter einer ausgewählten Beugungsordnung gleichzeitig an der fundamentalen wie auch an der zweiten Harmonischen in die Struktur eingekoppelt. Hierbei werden Rayleigh-Anomalien an den unterschiedlichen Wellenlängen und Grenzschichten ausgenutzt.

Danach diskutieren wir in Kapitel 8 optischen Eigenschaften amorpher Komposite, wie sie aus ALD-Proben gewonnen werden, und ihre selbstkonsistente Integration in die FMM. Dies wird in Kapitel 8.1 erweitert um die dritte Harmonische im Fall der Selbstphasenmodulation (SPM) bzw. Kerr-Nichtlinearitäten in solchen Strukturen zu ermitteln, speziell wenn diese in dünnen Schichten verwendet werden. Weiterhin wird das so beschriebene System in Abschnitt 8.2 für nichtlineare Polarizationsholographie verwendet. In dieser Messtechnik ist die Krossphasenmodulation (XPM) von Bedeutung, Phase und Amplitude der nichtlinearen Polarization verwendet werden um intrinsische Dephasierungszeiten zu bestimmen. Diese hängen bei amorphen Kompositen von der Volumendichte der metallischen Einschlüsse ab.

Diese Vorhaben untersuchen Konzepte, Licht mittels linearer und nichtlinearer Beugungsgitter zu manipulieren. Kapitel 9 bietet eine Zusammenfassung und einen Ausblick auf zukünftige Arbeiten.

# Contents

# I On Computational Nanophotonics

# 1. Nanoscale Optical Modeling

Classical electrodynamics based on Maxwell's equations and the electromagnetic wave equation derived from them is incredibly successful in describing optical (and electric and magnetic) properties of systems over a wide range of wavelengths from radio frequencies to the infrared (IR) to the visible (VIS) down to the ultraviolet (UV). The high scalability of its fundamental equations enables their application to many problems in electromagnetism such as scattering and wave interference. Structures range from the subnanometer, atomic scale, to antennas the range of meters to interferometers of several kilometers in size. In the Laser Interferometer Gravitational-Wave Observatory (LIGO) experiment, e. g., coherent laser light travels a distance of 1200 km along 4 km long arms to detect tiny disturbances caused by interference with graviational waves [1] obeying still the fundamental laws of wave optics. In comparison, the original Michelson-Morley-interferometer fitted on a $1 \times 1$ m$^2$ sized table with only tens of meters in distance traveled [2].

Despite its validity over a wide range of wavelengths and spatial distances it remains difficult to combine fundamental effects beyond classical electrodynamics over multiple scales in a single framework. Introducing multiscalar and multiphysics aspects, e. g. for a large-scale device with nanoscale features and molecules in the proximity of its surface, is a major challenge in optical modeling [3]. Fig. 1.1 gives an example for the different scales in a photovoltaic (PV) device. On the atomic scale, material properties such as the bandstructure, absorption rates and its surface chemistry are best obtained with ab initio quantum models such as Density Functional Theory (DFT) [4–6] or within the (time dependent) local density approximation ((TD)LDA) [7–10]. However, an entire layer of such a material, including electron transport or exciton generation as well as details of the morphology, such as a rough interface or porosity, can no longer be described feasibly with first principle calculations. Typically, statistical methods, Molecular-Dynamic (MD) [11–13], Non-Equilibrium Green's Functions (NEGF) [14] and Monte-Carlo [15, 16] simulations are theoretical frameworks suitable for modeling electron transport through and absorption rates of nano-scale components. One common semiclassical approach to the description of nanosized structures is the Random Phase Approximation (RPA) [17–19]. The device scale, in the example of Fig. 1.1 a solar cell made of functionalized multilayers, is typically well described by classical nanophotonic computational methods. We discuss a few of them in more detail in the next section. Similarly, the optics of the total module is well described with electromagnetics, though other properties such as mechanical stability and realiability under realistic environmental conditions, such as rain, heat and frost, become of interest at this scale beyond the pure electro-optics.

This work concentrates on optical modeling on the nanoscale incorporating nanostructured features into a large-scale device structure. Over the past years, we developed methods to account for effects beyond classical electrodynamics in standard nanophotonic simulation

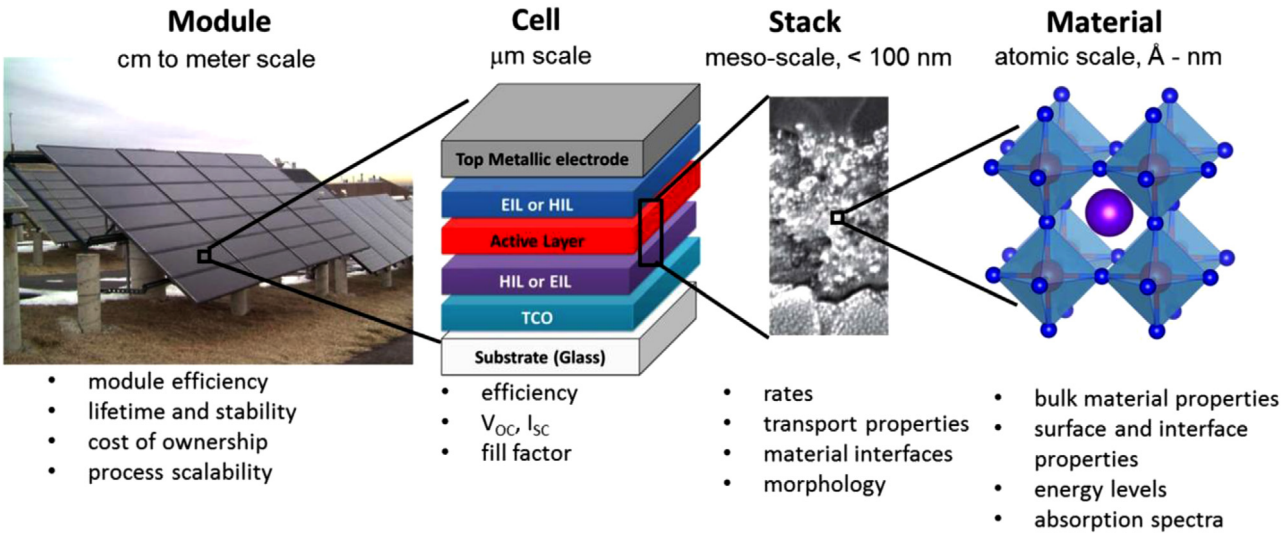


Fig. 1.1.: Illustration of multiscale and multiphysics challenges in electro-optical modeling of large-scale devices using the example of photovoltaic modules. [3]

schemes.

One reason of the continued interest in nanosized systems are the tremendous advances in fabrication techniques made in the past decades in, e. g., chemical synthesis (etching) [20–24], lithography [25–27], particle self-assembly through (laser) annealing [26, 28, 29], and nanoimprint [30–33]. Typically, self-assembly and chemical synthesis yield random nanoparticle (NP) distributions with randomized size and shape characteristics at reduced costs, while lithography techniques allow for high precision in size, shape, and placement with nanometer resolution [26, 34]. Nanoimprint in particular is a promising route to combine the best of both worlds as it allows to keep costs low using a single imprint template which in turn can be the result of a complex optimization procedure [32]. Topology optimization allows tailoring a metasurface to any specified performance task [35, 36] and is widely used in mechanical manufacturing [37]. Finally, demanding multi-objective optimization procedures can combine target performance from different fields such as specific optical and mechanical properties [38].

Nanostructures and nanoparticle arrays allow efficient forward scattering of incident light increasing the exposure of an underlying material system to photons. In addition, local field effects can create strong coupling and high local fields, in particular, in hybrid metal-dielectric systems, where surface plasmoncs can occur [39]. Research efforts exploit such effects with functionalized layers to optimize light trapping or guidance. Plasmon-assisted processes such as direct increase of the charge carrier generation or indirect enhancement of energy conversion effects from neighboring nanocrystal structures have received much interest [40–46]. Aging and oxidization effects in metals and the short-range of strong near-field effects pose practical challenges. Bio-markers and molecular rulers [47–49] allow to bring photo-active materials such as rare-earths [44], quantum dots [41, 43] and dyes close to NP surfaces. On the other hand, all-dielectric metasurfaces [50, 51] avoid the downsides of metal losses and reactivity while providing moderate field enhancement in tailored hot-spots.

The key task in modeling systems at the verge between the atomic and nanoscale is the integration of the quantum nature of atoms, electrons and molecules and their interaction with electromagnetic fields, the interplay of optically excited nanocrystals with complex energy transfer mechanisms stemming from electron transport. Mesoscale electron dynamics, surface morphology and thermal effects are not typically captured in standard electrodynamics. Though such effects are highly localized, optical coupling can lead to an impact on a larger device via retardation and lattice effects. [52] Semiclassical approaches allow maintaining the advantages of computational nanophotonics through extension of the standard theories [53–56]. This is a central challenge in multiscalar modeling and one of the main motivators behind our choice of the Fourier Modal Method (FMM) for characterizing the impact nanosized features have as part of a large-scale multilayered device. Regarding the multiphysics aspect, this work concentrates on two major phenomena, mesoscale electron dynamics and nonlinear effects in nanostructured systems as part of a large-scale device and their description within the FMM. Furthermore, we broaden the discussion to a few other topics such as rough surface morphology and ion dynamics in soft matter systems.

The next section gives an overview on modeling classical light-matter interactions on the nanoscale and presents a few approaches to some detail. Here, we want to clarify further advantages of the FMM as well as some of its limitations before diving into the details. In section 1.2, we derive the fundamental equations for the FMM and discuss the main features and limitations of the standard formulation of this compuational method. The last section in this chapter gives several examples of our work in recent years where the standard FMM was applied to photovoltaic (PV) systems and in spectroscopy. Part II discusses our contributions to microscopic electron dynamcis. Chapter 3 concentrates on regular metal nanostructures as described with the FMM while Chapter 5 presents first steps towards spatial dispersion in soft matter replacing electrons and metal structures with ions as part of an electrolyte. This concludes the first part.

## 1.1 Comparing available Computational Methods

Within computational nanophotonics, a multitude of numerical approaches are available each with their very own advantages and disadvantages [57]. The optical properties of nanoparticles with arbitrary shapes [22, 23, 58], two-dimensional particle arrays [52, 56, 58] as well as three-dimensional photonic crystal structures [59] can be described. Multiple scattering techniques [60] allow to study particle clusters on the basis of the scattering matrix of a specified particle type. This is in particular interesting for layers with random distributions [26]. The scattering matrix for nanoparticles (NPs) of arbitrary shapes can be obtained via e. g. Boundary Element Method (BEM), Discrete Dipole Approximation (DDA) or Finite Element Method (FEM) [22, 44, 58].

This section shall serve as an overview and comparison of some existing computational methods, their advantages and bottlenecks, e. g. with respect to their computational effort [22, 57]. Note that the majority of them yield rigorous solutions to Maxwell's equations in

frequency space depending on one or more quality parameters determining convergence of the results. All discussed field quantities are, thus, assumed to depend with $e^{-i\omega t}$ on time. The electromagnetic field consists of effectively two three-dimensional vectors $\mathbf{E}$ and $\mathbf{H}$ with complex amplitudes. The displacement field $\mathbf{D} = \epsilon_0\mathbf{E} + \mathbf{P}$ is obtained from the field in free space with permittivity $\epsilon_0$ and the polarization $\mathbf{P}$ of any objects considered. Within linear response, each object has a unique optical response to an external field inscribed in its polarizability $\alpha$ via $\mathbf{P} = \alpha\mathbf{E}$. Typically, retardation is neglected for nanoparticles and the quasistatic approximation is introduced through $\mathbf{E}(\mathbf{r}, t) \approx \mathbf{E}(\mathbf{r})$ and a scalar field $\phi(\mathbf{r})$ is soley used with $\mathbf{E} = -\nabla\phi$. On the other hand, oftentimes only the lowest order dipole response is taken into account. Both these approximations allow for analytic solutions to a number of nano-optical systems. However, if we want to solve these complex fields in the presence of coupled nanoparticles of arbitrary shape of any distribution as part of a large-scale device, numerical methods are needed. In principle, all the methods described here can be applied to complex nanostructured systems. However, the differences in the parametrization of such structures and how these methods deal with dielectric functions and symmetries can make one beneficial over the other.

#### Discrete Dipole Approximation (DDA)

The DDA, also known as Coupled Dipole Method (CDM), builds a nanoparticle from dipoles placed on a regular lattice [22,57]. It is, thus, a method subdividing the particle volume $V$, but not the surrounding medium. This has advantages regarding a distribution of nanoparticles as the medium between them does not play a role in, e. g. storage demand. The response of each polarizable element $i$ at its position $\mathbf{r}_i$ is self-consistently obtained from its polarizability $\alpha_i$ with respect to both the incident field $\mathbf{E}^{\mathrm{in}}$ and scattered field $\mathbf{E}^{\mathrm{s}}_j$ produced from every other element

$$\mathbf{P}_i(\mathbf{r}_i, \omega) = \alpha_i \left( \mathbf{E}^{\mathrm{in}}(\mathbf{r}_i, \omega) + \sum_{j \neq i} \mathbf{E}^{\mathrm{s}}_j(\mathbf{r}_i, \omega) \right). \tag{1.1}$$

Particles on substrates need to include the respective image dipoles. Though the parametrization is fairly straightforward, the method becomes more and more time consuming with the particle number. In addition, due to the explicit use of dipoles an upper limit for the particle size $a$ and its dielectric function value $\epsilon$ with respect to the incident wavenlength $\lambda$ is given by $|a\sqrt{\epsilon} < 5\lambda|$ to respect the dipolar approximation of the material response. For a spectrum consisting of $n_\omega$ points, the computational time scales with $n_\omega V^3$ [22].

#### Boundary Element Method (BEM)

The fields and their derivatives or a charge and current distribution, respectively, at the boundaries between homogeneous regions are the basis of BEM [22,57,61,62]. Auxilliary boundary charges and currents are used to express the fields scattered by the considered nanoparticle. These are connected to the scalar $\phi$ and vector potential $\mathbf{A}$ of the electromagnetic field

through

$$\mathbf{E}(\mathbf{r},\omega) = i\omega\mathbf{A}(\mathbf{r},\omega) - \nabla\phi(\mathbf{r},\omega). \tag{1.2}$$

Imposing the usual boundary conditions, a system of surface integrals over the electromagnetic Green's function

$$G(\mathbf{r}) = \frac{e^{i\mathbf{k}\mathbf{r}}}{4\pi|\mathbf{r}|} \tag{1.3}$$

is obtained [57, 61]. A discretization of the surfaces is needed to cast that into a set of linear equations which results in a computational effort of $n_\omega V^2$. Depending on the surface morphology, the parametrization can become complex. This method can well exploit symmetries of the considered nanoparticle. For axial symmetry, only the integral over the surface contour remains while the angular dependence can be integrated before the discretization step reducing the surface integral to a line integral [61]. With this, BEM is a formidable method to describe particles of arbitrary shape and complex symmetric systems such as tip-substrate structures.

#### Multiple Elastic Scattering of the Multipole Expansion (MESME)

MESME allows evaluating the optical properties of particle clusters with an arbitrary distribution [60]. It is based on the knowledge of the scattering matrix of each single nano-object in the system, e. g. Mie coefficients for nanospheres or core-shell structures. Such scattering matrices can be calculated numerically for more complex shapes from, e. g., BEM and enable subsequently a much faster evaluation of the scattering and near-field properties in complex nanoparticle distributions. This is by far the fastest method limited only by the number of nanoparticles in the system of any size or shape to about $\sim 10^3$. However, homogeneous regions other than in particles, such as substrates, cannot be included.

#### Finite Difference Time Domain (FDTD)

FDTD is, in contrast to the previously described methods, propagating the entire electromagnetic field in time steps on a spatial grid. It is, thus, the most direct method to solve Maxwell's equations. When time-resolved fields are used to excite a given system or the time-dependent optical response is required, this should without doubt be the method of choice. Due to its discretization of the entire inner and outer volume of a nanoparticle, it can be applied to complex, nonsymmetric setups, but it also requires to run the calculations in a large parametrized volume to account for the incident electric field. Therefore, a large storage demand is inherent to this method as well as a higher time consumption than other methods able to exploit symmetries more directly. If a spectrum is calculated with resolution $\Delta\omega$ related to the number of time steps, the computational demand is proportional to $V^{\mathrm{total}}\,\omega/\Delta\omega$.

#### Multilayers and Photonic Crystals

Several theoretical approaches exist to describe regular nanostructured layers, i. e. photonic crystals [59]. Complex layered systems are best described within a scattering or transfer matrix approach, that for homogeneous layers is equivalent to Fresnel equations for a single interface and derived expressions for multiple layers. The Fourier Modal Method (FMM), also known as Rigorous Coupled Wave Analysis (RCWA), is a fast and reliable computational approach [56, 63–65] that casts the electromagnetic wave equation into an eigenvalue problem. It is based on a plane-wave expansion (PWE) of the fields according to the one- or two-dimensional symmetry of the considered nanostructure. This enables the evaluation of large-scale, regular devices possibly with nanoscale features, such as wedges, nanogaps and thin walls [66]. No discretization of the surface or volume is needed, however, the convergence strongly depends on the number of plane waves taken into account. For all-dielectric systems, tens to hundreds are sufficient, but hybrid metal-dielectric systems need hundreds to thousands of expansion coefficients to be considered. The high contrast in the refractive indices across boundaries limits a fast convergence of the oscillating fields.

#### Remarks on mesoscopic charge carrier dynamics

Classcial material models rely on tabulated refractive indices from measurements from bulk materials formulated into Drude-Lorentz models fitted to the measured data [67–69]. Such data does not include or distinguish surface and finite size effects. When applying light to nanosized systems, the inherent quantum nature of materials plays an increasingly important role often yielding additional damping channels accounting for confinement effects [70]. Classical electrodynamics uses the local response approxmiation (LRA) and confinement and nonlocal interaction effects stemming from the spatial dispersion of charge carrier interactions are not included in the standard material models and the absorption in thin films and nanoparticle clusters is underestimated. First principle theories can address charge carrier dynamics and their mutual interaction with light in detail [4–9, 71]. However, the computational effort increases rapidly with the system size. One the other hand, effective microscopic theories such as the RPA [17–19] allow investigating fundamental damping mechanisms arising from electron scattering in the bulk material and with the particle surface. Moreover, it allows addressing electron irradiation effects stemming from the accelerated movement of the oscillating electrons forming the plasmon excitation. For simple geometries, analytic expressions for the damping phenomena can be obtained [18, 54, 55, 72].

Spatial dispersion of electron-electron coupling has been studied in semiclassical methods with the hydrodynamic approach [53,70,73,74], where the dynamics of the electron plasma are separated from polarization effects of bound electrons. This theory yields an additional wave solution, an electron pressure wave, longitudinal in character, and can be solved for different geometries leading to nonlocal extensions of, e. g., Mie and Fresnel coefficients [53, 75]. The advantage of semiclassical models lies in their mostly analytic formulation and thus compatibility with and straightforward integration into existing numerical procedures. In addition, the common assumption of a material system to consist of a series of homogeneous

regions in space with abrupt, hard-wall boundaries also fails on the nanoscale, where the wavefunctions of electrons are no longer bound within an arbitrary particle size, but can extend smoothly into the surrounding dielectric medium. This electron spill-out has also captured some attention due to its possible overlap for facing metal surfaces with subnanometer gaps [73, 76, 77]. The main observations of nonlocal theories in nanosized particles are a blueshift of the plasmon resonance with respect to the common local approximation, field quenching and plasmon broadening. However, such theories have shown a sizable effect for very small particle and layer sizes $< 10$ nm or gaps in the system $< 1$ nm.

**Conclusions**

It should be noted that the methods briefly described in this section have been developed and improved further exploiting, e. g., adaptive meshing, Fast Fourier Transform (FFT) and Galerkin schemes [57, 78–81].

The aim of this work is to consider nonclassical and nonlinear effects stemming from nanostructures and their impact on large-scale devices. Our method of choice is the FMM as it enables us to study one- and two-dimensional regular nanostructure arrays with a straightforward control over geometrical parameters. We restrict ourselves to structures simple enough to obtain the Fourier transform of their respective unit cells analytically, see appendix A. This allows concentrating on formulating additional computational modules to deal with the multiphysics aspects of interest. One of our efforts over the past years was finding a formulation of the FMM approach including semiclassical corrections [52] to study the effects surface and quantum properties of the electron plasma would have on the larger device structure and how they impact its performance. This is discussed in Part II. More recently, we incorporated procedures to assess nonlinear effects and higher harmonic generation into FMM. These are presented in Part III. A major limitation to convergence is posed by the frequent use of hybrid metal-dielectric systems. Hence, special care is taken to check and report on the computational time and convergence as a function of the plane-waves taken into account.

Where necessary and appropriate, we include calculations based on other methods in particular multiple scattering techniques [60] for clusters of nanoparticles and the Boundary Element Method for rough surface morphologies [57, 61, 62].

## 1.2 Fourier Modal Method in Classical Electrodynamics

The Fourier Modal Method (FMM) is at the heart of this work and can be used to design and optimize optical devices with broad applications from solar cells, optical sensors, spectroscopic and microscopic systems. It is a frequency space method and is best suited for layered systems of which one or more layers are nanostructured in the plane parallel to the layered structure as depicted in Fig. 1.2.

In this section, we introduce the basic equations needed for an implementation of the FMM from standard concepts describing periodic photonic crystals. These are based on a rigorous

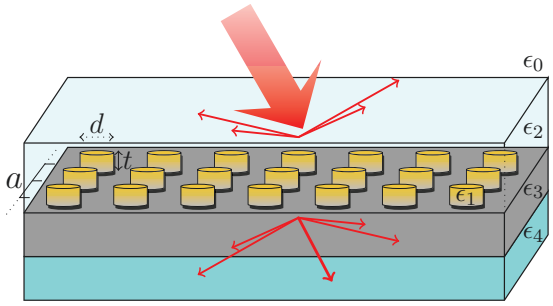


Fig. 1.2.: Example for a two-dimensional nanostructure made from circular nanodisks in a rectangular unit cell.

plane-wave expansion (PWE) method limited only by the number of plane waves that can be taken into account. To include further layers towards a device structure, this is combined with the planar scattering matrix approach [64, 65]. From this basis, further numerical modules to investigate nanostructures with spatial dispersion in its metal components and nonlinear properties in any of its constituent materials are developed in the next chapters.

We consider nanostructured multilayered devices in two steps. Firstly, we evaluate the modes of a photonic crystal infinite in $z$-direction and with a one- or two-dimensional periodicity in the $x$-$y$-plane. We formulate the electromagnetic wave equation as an eigenvalue equation in reciprocal space. Its eigenvectors represent the possible electromagnetic fields and their polarization in the nanostructure and its eigenvalues contain the propagation directions and wavenumbers of different diffraction orders. Secondly, we determine the boundary conditions of a finite slab of the photonic crystal bordering to other layers in the multilayered system. With the scattering matrix method, optical properties of the finite system are calculated such as near-field maps or transmission spectra. At all time, we maintain the capability to distinguish the contributions of different diffraction orders from each other and the fully integrated result.

### 1.2.1 Preparations

The electromagnetic eigenvalue equation can be formulated in terms of the electric or the magnetic field. Though equivalent in terms of their physical meaning, mathematically, it has advantages to use the formulation in terms of the magnetic field [59]. Starting from Maxwell's equations in structured, but homogeneous materials with spatial permittivity (permeability) function $\epsilon(\omega, \mathbf{r})$ ($\mu(\omega, \mathbf{r})$) without external charges and currents using the convention mentioned before that yields $\partial_t \bullet = -i\omega \bullet$

$$\nabla \times \mathbf{H} = -i\omega \mathbf{D} = -i\omega\epsilon_0\epsilon(\omega, \mathbf{r})\mathbf{E}, \qquad \nabla \times \mathbf{E} = i\omega \mathbf{B} = i\omega\mu_0\mu(\omega, \mathbf{r})\mathbf{H}, \tag{1.4}$$

we introduce a plane-wave expansion (PWE) to describe all diffraction orders

$$\mathbf{H}(\mathbf{R}, z) = \sum_{\mathbf{G}} \tilde{\mathbf{H}}(\mathbf{G}, z) e^{i(\mathbf{G}+\mathbf{k}_\parallel)\mathbf{R}} \tag{1.5}$$

with two-dimensional reciprocal lattice vectors $\mathbf{G} = (G_x, G_y)^T$ and $\mathbf{R} = (x, y)^T$. The parallel momentum $\mathbf{k}_\parallel = (k_x, k_y)^T$ is the part of the wave vector $\mathbf{k}$ of the external field that is in-plane with the structure. This can be defined through an angle of incidence, e. g. in spherical coordinates $k_x = k_0 \sin\theta \cos\varphi$ and $k_y = k_0 \sin\theta \sin\varphi$, with $k_0 = \sqrt{\epsilon_{\text{in}}}\, \omega/c = \sqrt{\epsilon_{\text{in}}}\, 2\pi/\lambda$ defining the frequency $\omega$ and wavelength $\lambda$, resp., of the incident light in the outer medium with permittivity $\epsilon_{\text{in}}$. The free-space permittivity $\epsilon_0$ is together with the free-space permeability $\mu_0$ connected to the speed of light $c$ via $\epsilon_0\mu_0 = 1/c^2$. On the other hand, some setups provide large parallel momenta through evanescent waves, where the definition of an incident angle is no longer feasible.

Assuming a rectangular two-dimensional lattice in real-space, the reciprocal lattice vectors are $\mathbf{G}_{nm} = 2\pi/a_x\, n\hat{\mathbf{x}} + 2\pi/a_y\, m\hat{\mathbf{y}}$ where $a_x, a_y$ are the lengths of the real-space lattice vectors defining the size of the rectangular unit cell and $n, m \in \mathbb{Z}_0$ are integers. Let $N = 2n_G + 1$ be the number of plane waves (in one dimension) taken into account with diffraction orders ranging from $-n_G \ldots n_G$. The sign is connected to the direction of the diffracted wave. Note that always $|n|, |m| \leq (N-1)/2$.

The in-plane magnetic field $\mathbf{h}_\parallel$ in reciprocal space is then described by a vector with $2N$ components in one-dimensional structures as compared to $2$ before the expansion

$$\mathbf{h}_\parallel = \begin{pmatrix} \mathbf{h}_x \\ \mathbf{h}_y \end{pmatrix} = \begin{pmatrix} \tilde{H}_x(\mathbf{G}_{-n_G}, z) \\ \vdots \\ \tilde{H}_x(\mathbf{G}_{n_G}, z) \\ \tilde{H}_y(\mathbf{G}_{-n_G}, z) \\ \vdots \\ \tilde{H}_y(\mathbf{G}_{n_G}, z) \end{pmatrix}. \tag{1.6}$$

The vectorial character of the components $\mathbf{h}_x, \mathbf{h}_y, \mathbf{h}_z$ stems from the expansion in Fourier coefficients. Matrices that emerge in the eigenvalue equation have, thus, the dimension $2N \times 2N$ in one-dimensional structures. Convergence critically depends on the number $n_G$ taken into account and at the same time poses the main limitation of this approach as the related vectors and matrices increase quickly with $n_G$.

In the same way, the permittivity $\epsilon(\omega, \mathbf{r})$ and for magnetic materials the permeability $\mu(\omega, \mathbf{r})$ are expanded into Fourier components

$$\epsilon(\omega, \mathbf{r}) = \sum_{\mathbf{G}} \epsilon(\mathbf{G}) e^{i\mathbf{G}\mathbf{R}} \tag{1.7}$$

over a unit cell. For simple structures, their Fourier coefficients are analytical which are collected in appendix A. Suffice to say, that the material properties are described by a matrix $\hat{\epsilon}, \hat{\mu}$ of dimension $N \times N$ when introducing the PWE. This is for isotropic materials with scalar material functions in real-space. For anisotropic materials that are $3 \times 3$ tensors before the expansion, the reciprocal counterpart would increase accordingly to a $N \times N$ matrix where each entry is a $3 \times 3$ tensor. Note that for a strictly two-dimensional system $N \to N^2$ as both

$G_x$ and $G_y$ run from $-n_G \dots n_G$.

Now we are equipped to derive the eigenvalue equation and with its solution obtain the optical properties of a regular photonic crystal extended indefinitely in the $z$-direction, i. e., with constant material properties in the $z$-direction.

### 1.2.2 Properties of an Infinte Photonic Crystal

We introduce the PWE for $\nabla \times \mathbf{H} = -i\omega\epsilon_0\epsilon(\omega, \mathbf{r})\mathbf{E}$ and write for each component

$$\partial_y \mathbf{h}_z - \partial_z \mathbf{h}_y = i\hat{k}_y \mathbf{h}_z - ik_z \mathbf{h}_y = -i\omega\epsilon_0 \hat{\epsilon}\mathbf{e}_x, \tag{1.8}$$

$$\partial_z \mathbf{h}_x - \partial_x \mathbf{h}_z = ik_z \mathbf{h}_x - i\hat{k}_x \mathbf{h}_z = -i\omega\epsilon_0 \hat{\epsilon}\mathbf{e}_y, \tag{1.9}$$

$$\partial_x \mathbf{h}_y - \partial_y \mathbf{h}_x = i\hat{k}_x \mathbf{h}_y - i\hat{k}_y \mathbf{h}_x = -i\omega\epsilon_0 \hat{\epsilon}\mathbf{e}_z \tag{1.10}$$

and analogous for $\nabla \times \mathbf{E} = i\omega\mu_0\mu(\omega, \mathbf{r})\mathbf{H}$

$$\partial_y \mathbf{e}_z - \partial_z \mathbf{e}_y = i\hat{k}_y \mathbf{e}_z - ik_z \mathbf{e}_y = i\omega\mu_0 \hat{\mu}\mathbf{h}_x, \tag{1.11}$$

$$\partial_z \mathbf{e}_x - \partial_x \mathbf{e}_z = ik_z \mathbf{e}_x - i\hat{k}_x \mathbf{e}_z = i\omega\mu_0 \hat{\mu}\mathbf{h}_y, \tag{1.12}$$

$$\partial_x \mathbf{e}_y - \partial_y \mathbf{e}_x = i\hat{k}_x \mathbf{e}_y - i\hat{k}_y \mathbf{e}_x = i\omega\mu_0 \hat{\mu}\mathbf{h}_z. \tag{1.13}$$

Each component of the parallel momentum $k_x, k_y$ becomes a diagonal matrix $\hat{k}_x, \hat{k}_y$ which includes the reciprocal lattice vectors $G_x, G_y$

$$\hat{k}_{x,nm} = k_x + \hat{\mathbf{x}} \cdot \mathbf{G}_{n0}\delta_{nm} \qquad \text{and} \qquad \hat{k}_{y,n'm'} = k_y + \hat{\mathbf{y}} \cdot \mathbf{G}_{0m'}\delta_{n'm'}. \tag{1.14}$$

Next, we eliminate the electric fields $\mathbf{e}_i$ from the equations for the magnetic field. In addition, making use of the orthogonality condition $\mathbf{k} \cdot \mathbf{H} = 0$, we can eliminate the $z$-component of the magnetic field

$$\mathbf{h}_z = -\frac{1}{k_z}\left(\hat{k}_x \mathbf{h}_x + \hat{k}_y \mathbf{h}_y\right). \tag{1.15}$$

Thus, the method is reduced to calculating the magnetic fields $\mathbf{h}_x, \mathbf{h}_y$ in plane with the structure. The remaining two equations can be rearranged to read

$$k_z^2 \mathbf{h}_x = \hat{\epsilon}\left(\left(\frac{\omega}{c}\right)^2 \hat{\mu}\mathbf{h}_x + \hat{k}_y \hat{\epsilon}^{-1}\hat{k}_x \mathbf{h}_y - \hat{k}_y \hat{\epsilon}^{-1}\hat{k}_y \mathbf{h}_x\right) - \hat{k}_x \hat{k}_x \mathbf{h}_x - \hat{k}_x \hat{k}_y \mathbf{h}_y, \tag{1.16}$$

$$k_z^2 \mathbf{h}_y = \hat{\epsilon}\left(\left(\frac{\omega}{c}\right)^2 \hat{\mu}\mathbf{h}_y - \hat{k}_x \hat{\epsilon}^{-1}\hat{k}_x \mathbf{h}_y + \hat{k}_x \hat{\epsilon}^{-1}\hat{k}_y \mathbf{h}_x\right) - \hat{k}_y \hat{k}_x \mathbf{h}_x - \hat{k}_y \hat{k}_y \mathbf{h}_y. \tag{1.17}$$

This defines the electromagnetic wave equation in form of an eigenvalue equation. Hereby, the eigenvalues are the $z$-components of the propagation vectors $k_z^2$ supported by the structure defining the direction of the corresponding diffraction order and the related in-plane magnetic field vectors $\mathbf{h}_{\|}$ are the eigen vectors.

We can write this in a compact way [64] as a matrix equation

$$k_z^2 \mathbf{h}_\parallel = \left( \mathcal{E} \left( \left( \frac{\omega}{c} \right)^2 \hat{\mu} - \mathcal{K} \right) - K \right) \mathbf{h}_\parallel, \tag{1.18}$$

with the matrices

$$\mathcal{E} = \begin{pmatrix} \hat{\epsilon} & 0 \\ 0 & \hat{\epsilon} \end{pmatrix}, \qquad \mathcal{K} = \begin{pmatrix} \hat{k}_y \hat{\epsilon}^{-1} \hat{k}_y & -\hat{k}_y \hat{\epsilon}^{-1} \hat{k}_x \\ -\hat{k}_x \hat{\epsilon}^{-1} \hat{k}_y & \hat{k}_x \hat{\epsilon}^{-1} \hat{k}_x \end{pmatrix}, \qquad K = \begin{pmatrix} \hat{k}_x \hat{k}_x & \hat{k}_x \hat{k}_y \\ \hat{k}_y \hat{k}_x & \hat{k}_y \hat{k}_y \end{pmatrix}. \tag{1.19}$$

Solutions to this eigenvalue equation allow solving the classical Maxwell's equations and computing the Bloch modes forming in the structure as well as the allowed propagation directions for the $\mathbf{k}$-vector for any angle of incidence $(k_x(\theta, \varphi), k_y(\theta, \varphi))^T$ or incident evanescent wave. The unit cell of the structure is described via $\hat{\epsilon}$ and $\hat{\mu}$ at a specified frequency of the incident light. Please note the remarks on the practical use of the inverse of the permittivity matrix appearing in $\mathcal{K}$ in appendix A.

One major advantage of this method is that different diffraction orders are readily available as the varying entries in the extended magnetic field vector $(\mathbf{h}_x, \mathbf{h}_y)^T$ in reciprocal space. This enables analyzing the contribution to a specified total quantity stemming from each diffraction order separately. This includes properties of computational interest such as the convergence behaviour. Analyzing the eigenvalues allows discussing the nature of the diffracted waves as, e. g., $Re(k_z) \equiv 0$ describes modes purely evanescent in $z$-direction. The $z$-component of the field is retrieved any time through the orthogonality condition $\mathbf{k} \cdot \mathbf{H} = 0$ as the electric and magnetic fields are orthogonal to each other and to their propagation direction. Real-space field distributions are obtained from inverse Fourier transform once the eigenvalue equation is solved and are a major tool to investigate near-field properties.

For optical materials of our interest $\mu = 1 \longrightarrow \hat{\mu} = \mathcal{I}$ becomes the identity matrix. In the following, we will, thus, neglect the permeability.

### 1.2.3 Finte Photonic Crystal Slab

Characterizing the modes and bandstructure of the infinite two-dimensional photonic crystal often gives a first important insight into its optical properties. In practical applications, however, nanostructures with a finite extension become part of a complex, large-scale device. We next apply the boundary conditions of electromagnetic fields at interfaces to the crystal structure to obtain a description of a finite nanostructured slab of thickness $d$.

Firstly, we specify the magnetic field further and write it as a field stemming from forward (amplitude vector $\mathbf{a}$) and backward (amplitude vector $\mathbf{b}$) propagating waves. The fields in each layer are expanded as

$$\mathbf{h}_\parallel = \mathbf{\Phi}(\hat{f}_{k_z}(z)\mathbf{a} + \hat{f}_{k_z}(d-z)\mathbf{b}). \tag{1.20}$$

The propagators $\hat{f}_{k_z,nm}$ in $z$-direction are defined as the diagonal matrices

$$\hat{f}_{k_z,nm}(z) = e^{ik_z z}\delta_{nm}. \tag{1.21}$$

Note that the parallel propagation is inherent in the PWE eq. (1.5) so that it does not appear here explicitly. The eigenvalue equation becomes

$$k_z^2\mathbf{\Phi} = \left(\mathcal{E}\left((\omega/c)\right)^2 - \mathcal{K}\right) - K\Big)\,\mathbf{\Phi}, \tag{1.22}$$

where $\mathbf{\Phi}$ can be understood as the matrix that contains in each of its $2N$ columns the normalized eigen vectors $(\mathbf{h}_x, \mathbf{h}_y)^T$ corresponding to different diffraction orders. The amplitude vectors $\mathbf{a}, \mathbf{b}$ remain unknown until the boundary conditions are solved.

The in-plane electric field $\mathbf{e}_\parallel$ is derived from the magnetic field through Maxwell's equations with the practical definition

$$\mathbf{e}_\parallel = \begin{pmatrix} -\mathbf{e}_y \\ \mathbf{e}_x \end{pmatrix} \tag{1.23}$$

and

$$\mathbf{e}_\parallel = \mathcal{E}\left(\left(\frac{\omega}{c}\right)^2 - \mathcal{K}\right)\mathbf{\Phi}(k_z\omega\epsilon_0)^{-1}. \tag{1.24}$$

Similarly to the previous case, $\mathbf{e}_z$ can be obtained from its orthogonality condition. Note that the solutions to the classical electromagnetic wave equation are strictly transversal and that we obtain two per diffraction order.

The boundary conditions are given by the continuity of in-plane field components $\mathbf{e}_\parallel$ and $\mathbf{h}_\parallel$ which can be written in a compact way for each layer $l$ as

$$\begin{pmatrix} \mathbf{e}_{\parallel,l} \\ \mathbf{h}_{\parallel,l} \end{pmatrix} = \mathcal{M}_l \begin{pmatrix} f_{kl}(z)a_l \\ f_{kl}(d-z)b_l \end{pmatrix}, \qquad \mathcal{M}_l = \begin{pmatrix} \mathcal{M}_{l,00} & -\mathcal{M}_{l,00} \\ \mathbf{\Phi}_l & \mathbf{\Phi}_l \end{pmatrix}, \tag{1.25}$$

with

$$\mathcal{M}_{l,00} \equiv ((\omega/c)^2\mathcal{I} - \mathcal{K}_l)\mathbf{\Phi}_l(k_{l,z}\omega\epsilon_0)^{-1}. \tag{1.26}$$

The layer index $l$ is a reminder that each layer is comprised of a different material leading to different input parameters and, ultimately, different solutions to the eigenvalue equation in each layer. It should be noted, however, that homogeneous, i. e. non-structured layers, have simple analytic solutions to the eigenvalue equation, namely

$$\mathbf{\Phi} = \mathcal{I} \qquad \text{and} \qquad k_z^{\mathbf{G}} = \sqrt{k_0^2\epsilon_{\text{in}} - |\mathbf{k}_\parallel - \mathbf{G}|^2}. \tag{1.27}$$

An analytical inverse [64] of the $2 \times 2$ block matrix $\mathcal{M}_l$ exists from which the interface matrix $I$

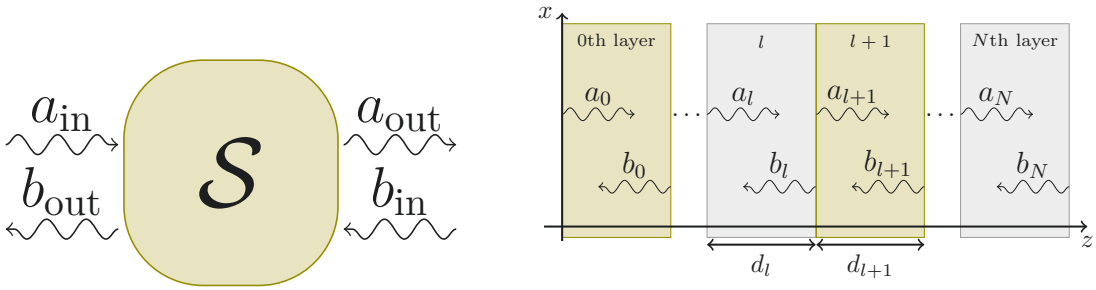


Fig. 1.3.: A scattering matrix is a mathematical object that connects incident quantities through the (optical, electronic, thermal etc.) response to corresponding outoing quantities: $\begin{pmatrix}\mathbf{a}_{\text{out}}\\ \mathbf{b}_{\text{out}}\end{pmatrix} = \mathcal{S}\begin{pmatrix}\mathbf{a}_{\text{in}}\\ \mathbf{b}_{\text{in}}\end{pmatrix}$. On the right, we illustrate the multilayered system and the relevant forward ($\mathbf{a}_l$) and backward ($\mathbf{b}_l$) scattering coefficients and thickness $d_l$.

can be calculated more efficently than through direct inversion

$$I^{l,l+1}_{\text{LRA}} = \mathcal{M}_l{}^{-1}\mathcal{M}_{l+1} = \frac{1}{2}\mathcal{M}^{-1}_{l,00}\mathcal{M}_{l+1,00}\begin{pmatrix}1 & -1\\ -1 & 1\end{pmatrix} + \frac{1}{2}\mathbf{\Phi}_l^{-1}\mathbf{\Phi}_{l+1}\begin{pmatrix}1 & 1\\ 1 & 1\end{pmatrix}. \tag{1.28}$$

This matrix contains the boundary conditions at the interface between layer $l$ and layer $l+1$ in a compact way. The scattering matrix $\mathcal{S}$, illustrated in Fig. 1.3 for the cross-layer field propagation follows an iterative scheme to propagate solutions which is given here for completeness [64].

$$\mathcal{S}^{l'l+1}_{11} = [I^{l,l+1}_{11} - f_{k_z l}\mathcal{S}^{l'l}_{12}I^{l,l+1}_{21}]^{-1}f_{k_z l}\mathcal{S}^{l'l}_{11} \tag{1.29a}$$
$$\mathcal{S}^{l'l+1}_{21} = \mathcal{S}^{l'l}_{22}\mathcal{S}^{l'l+1}_{11} + \mathcal{S}^{l'l}_{21} \tag{1.29b}$$
$$\mathcal{S}^{l'l+1}_{12} = [I^{l,l+1}_{11} - f_{k_z l}\mathcal{S}^{l'l}_{12}I^{l,l+1}_{21}]^{-1}\left(f_{k_z l}\mathcal{S}^{l'l}_{12}I^{l,l+1}_{22} - I^{l,l+1}_{21}\right)f_{k_z l+1} \tag{1.29c}$$
$$\mathcal{S}^{l'l+1}_{22} = \mathcal{S}^{l'l}_{22}\mathcal{S}^{l'l+1}_{12} + \mathcal{S}^{l'l}_{22}I^{l,l+1}_{22}f_{k_z l+1}. \tag{1.29d}$$

The first step in this iteration is given by $\mathcal{S}^{l,l} = \mathcal{I}$. If only $\mathbf{a}_0$ contributes to the incident field and no light is incident onto the last layer ($\mathbf{b}_N = 0$), the reflection coefficient is given by $\mathcal{S}^{0,N}_{21}\mathbf{a}_0$ and the transmission coefficient results from $\mathcal{S}^{0,N}_{11}\mathbf{a}_0$ and can be used further to calculate the transmitted and reflected photon flux [24]. These results on far-field quantities obtained in reciprocal space do not need to be Fourier transformed into real-space. Apart from calculating the entire scattering matrix of a complex layered system, it can also be computed partially and, thus, used to obtain the amplitude vectors within a specific layer. This can be used to study near-fields in nanostructured layers or absorption efficiencies in light harvesting devices as in some of the following examples. Only in case near-field information is sought after the fields made from $\mathbf{a}_l$ and $\mathbf{b}_l$ scattering coefficients need to be transformed back.

As a final note, due to the isomorphic relation between electrodynamics and quantum mechanics, the scattering matrix approach discussed in this section can with little adjustments be used in quantum systems describing, e. g., electron wavefunctions with propagation eigenvalues defined through their energy in relation to the work functions of the materials

the electron passes. Most notably, different boundary conditions need to be applied at the interface between materials, but the overall scheme remains the same.

## 1.3 Applications to Nanophotonic Devices

In this section, we want to briefly discuss some of the applications of the standard Fourier Modal Method (FMM) and how the basic procedure introduced in the previous section can be used to describe the optical properties of complex multilayered devices within classical electrodynamics.

Both regular and irregular (self-assembled) arrays of both dielectric and plasmonic particles have been investigated for further improving light management in 3rd generation solar cells [82–91]. Nanotechnology has opened up different routes to reduce front surface reflection [24, 28, 92], boost internal absorption through up- and down-conversion [41, 93, 94] and increase light trapping employing particle layers as back reflectors [95–98]. Light harvesting has mostly exploited collective and scattering properties, but also field enhancement effects on the nanoparticle surfaces. While regular particle arrays typically show narrow spectral resonances, randomly distributed particles yield a broader optical response at weaker coupling strengths. [75, 99]

Nanostructured layers as extra components to photovoltaic devices face another difficulty. Even commercially available baseline solar cells are already highly optimized. The *Solar cell efficiency tables* Ref. [100] record the highest photocurrent $J_{\mathrm{sc}}$ measured for n-type c-Si integrated back contact (IBC) systems at $42.65$ mA/cm$^2$ (efficiency of $26.7 \pm 0.5\%$), while thin-film modules achieve $J_{\mathrm{sc}} = 38.5$ mA/cm$^2$ (efficiency of $21.2 \pm 0.4\%$). With this in mind, nanostructured layers need to add a convincing amount to the photocurrent or overall efficiency.

The central quantitiy to evaluate the performance of solar cells with respect to their optical properties is the short circuit photocurrent $J_{\mathrm{sc}}$ which is obtained from integrating the absorption $A(\lambda)$ over the solar spectrum

$$J_{\mathrm{sc}} = \frac{q}{hc} \int_{\lambda_{min}}^{\lambda_{max}} \lambda A(\lambda) \mathrm{AM}_{1.5G}(\lambda) \mathrm{d}\lambda, \tag{1.30}$$

where $q$ is the electric charge, $h$ is the Planck constant, and $\mathrm{AM}_{1.5G}(\lambda)$ denotes the solar spectrum that reaches the surface of earth. The relative photocurrent gain is calculated from

$$\Delta\eta_{\mathrm{Jsc}} = 1 - {}^{J_{\mathrm{sc}}}\!/_{J_{\mathrm{sc}}^{\mathrm{ref}}}$$

comparing the photocurrent of a flat baseline cell $J_{\mathrm{sc}}^{\mathrm{ref}}$ with the equivalent solar cell decorated with a nanostructure.

In spectroscopy, the target wavelengths can differ from the VIS central to PV devices. Functionalized surfaces for spectroscopy, e. g., surface enhanced Raman scattering (SERS), are pursued where the measurements benefit from artificially roughened surfaces exploiting

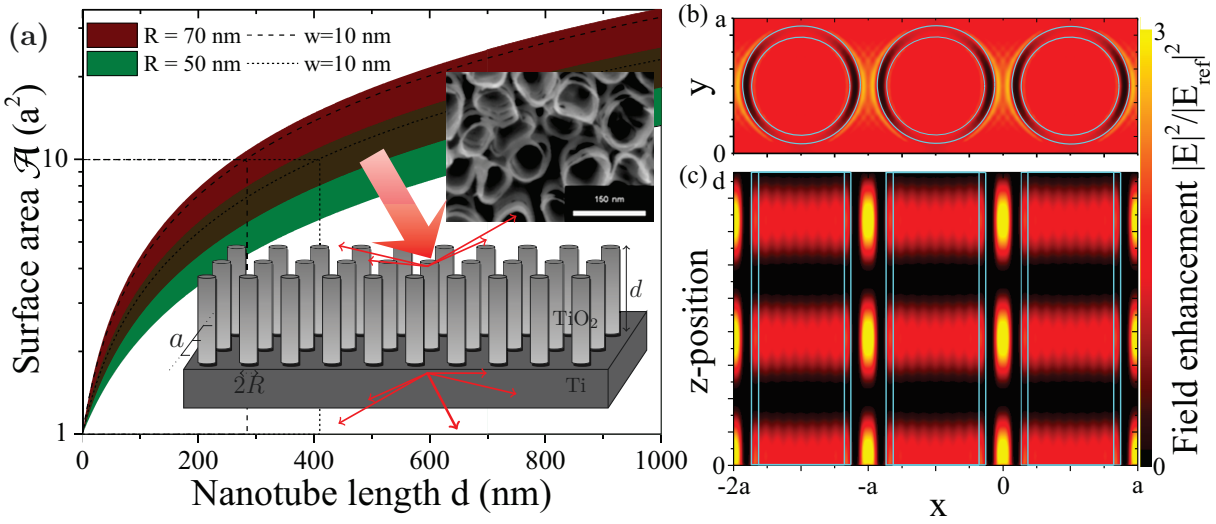


Fig. 1.4.: (**a**) Increase in surface area as a function of nanotube length $d$ for two different outer radii $R$ and lattice period $a = 160$ nm. The shaded areas span the minimum to maximum achievable surface area from solid nanopillars (wall thickness $w = R$) to ultrathin walls $w \to 0$, the dashed lines mark $w = 10$ nm. Insets: SEM image of real geometry after self-assembly of hollow $TiO_2$ nanotubes on a Ti substrate [101] and illustration of the idealized structure used in our modeling; (**b**,**c**) Field enhancement of a $d = 500$ nm NT with $R = 70$ nm for three neighboring unit cells (**b**) at the top of the NTs $z = d$ and (**c**) in the orthogonal plane in the center of the unit cell at $y = a/2$.

local field enhancement in hot-spots rather than regular nanostructures with spectrally thin resonances. However, for specific detection tasks, carefully tailored regular surface structures are pursued as well.

We take a special interest in thin-walled hollow nanotube pillars grown from Ti foil. Arrays of $TiO_2$ nanotubes (NTs) have wide applications in sensing [102], as filters and nanosized test tubes in biomedicine [103], as photonic crystal fiber lasers and demultiplexers [104–106], and as nanostructured electrodes for SERS [101, 107]. In addition, the possible enhancement of reaction or transport rates due to a large surface area, see Figure 1.4(a), strong electron confinement and short diffusion paths make them highly interesting nanostructures for (photo-)catalysis [108–111] and PV [112–116]. While typically grown on Ti substrates or alloys, $TiO_2$ NTs can be produced as membranes through a lift-off process [117]. This technique allows employing them on different substrates such as Si or GaAs for solar cells. A further advantage for use in bionanotechnology, catalysis and related fields is the biocompatiblity of the material [101, 107], which makes an additional protective coating of the obtained oxide unnecessary. Self-assembled nanostructures are favorable with view to their fabrication costs in particular in a highly competitive industry such as PV technology [3, 26]. The high refractive index (RI) of $TiO_2$ makes this an interesting material for a broad range of further photonic and hybrid applications, i.e., exploiting plasmon-assisted enhancement effects by combining with metal nanoparticles or planar waveguide structures [39, 118]. These setups are typically used to enhance intrinsically low quantum efficiencies, e. g., rare earth transition rates [116], and to

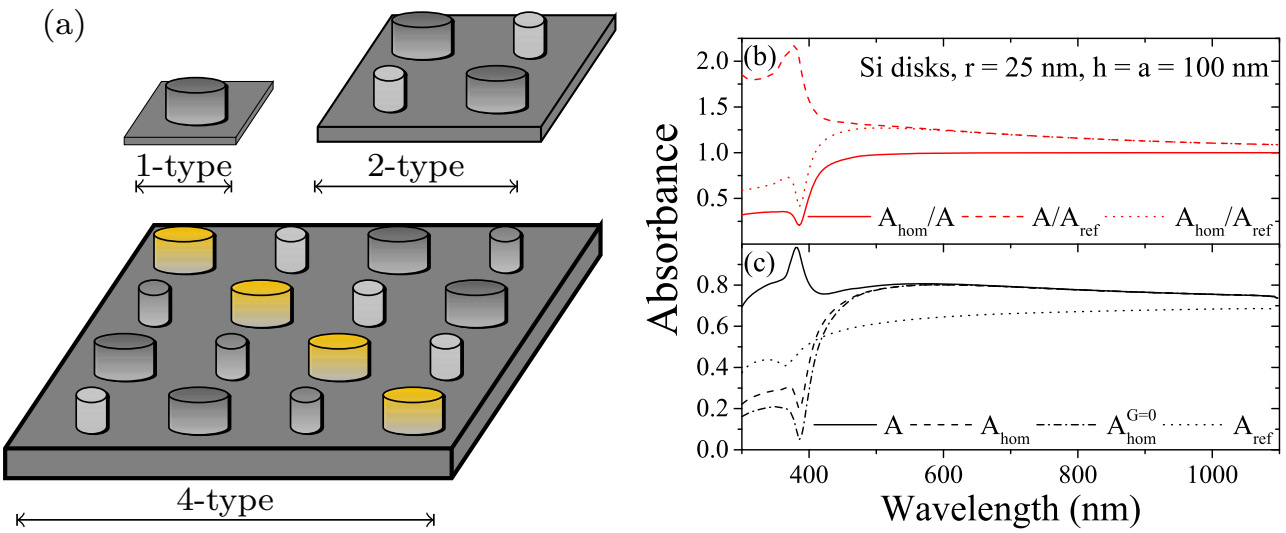


Fig. 1.5.: (a) Unit cells of multi-type particle layers from the standard 1-type unit cell to 2- and 4-type unit cells which allows to study particle layers of varying composition and configuration. (b), (c) The absorbance of the bare Si reference cell $A_{\mathrm{ref}}$, the overall device absorption $A$ and the absorption in the homogeneous, active Si wafer region $A_{\mathrm{hom}}$ are compared (b) relative to the absorbance of the reference cell and (c) in absolute values. The example spectrum shows these quantities for $r = 25$ nm Si particle layer with $a = 100$ nm, $d = 100$ nm, including the lowest order of diffraction $A_{\mathrm{hom}}^{G=0}$.

sensitize the UV-active $TiO_2$ towards visible light [109] which is important for photocatalytic reactions. The nanotubular geometry adds directionality to incoming light improving charge transfer towards an electrode or photon scattering towards a photo-active substrate [114, 115]. The sensitivity in such photonic crystal structures is high and robust with respect to fabrication defects due to collective optical modes in the regular lattice structure [33].

### 1.3.1 Multi-type Particle Layers for Solar Cells

One basic aspect of the FMM is the use of a unit cell to describe nanostructured layers. Our work Ref. [56] investigates multi-type particle layers combining nanodisks of different radii and configurations in a single unit cell. Such a layer with particles made of a single material of varying sizes can be fabricated with e. g. EBL techniques [26]. Broadband total absorption can be achieved in a regular particle array combining different particle sizes and shapes to create a spectral overlap of resonances. This has been demonstrated experimentally for metamaterials in the mid-infrared region [119, 120] and total absorption was also predicted for textured graphene surfaces [121]. We emphasize that in photovoltaic devices it is not enough to reduce the overall device reflectivity or boost its overall absorption: the absorption within the photo-active region must be enhanced and parasitic absorption avoided [28, 122]. The latter can stem from resonant absorption in the textured layer or ohmic heating in metal components, respectively.

We investigated regular Si particle arrays as textured front layers made of unit cells that include more than a single particle, shown in Fig. 1.5(a), and how they influence light trapping

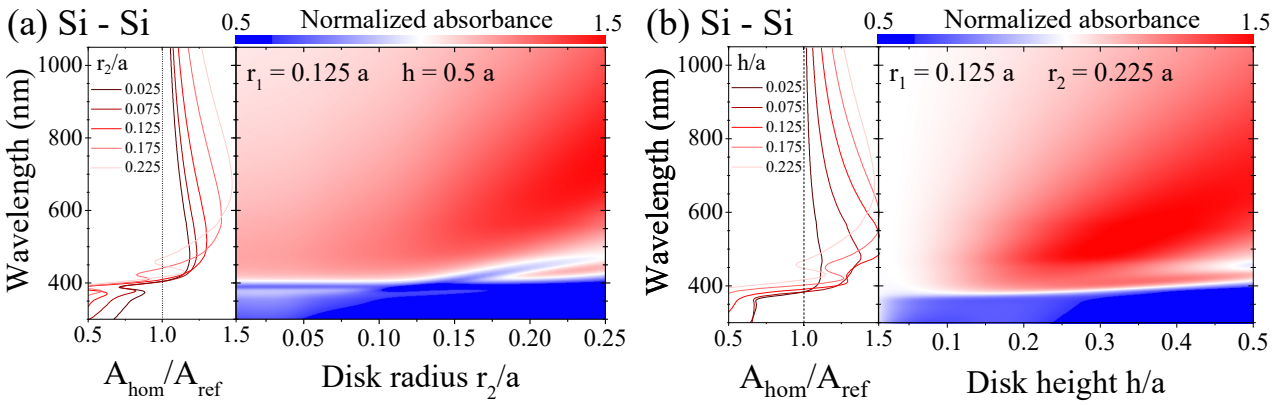


Fig. 1.6.: 2-type cells made of Si using (a) different disk radii $r_2$ while keeping constant height $h = 100$ nm and $r_1 = 25$ nm, and (b) scaling the height for these cells with constant $r_1 = 25$ nm and $r_2 = 45$ nm. Selected curves are plotted on the left hand side of each contour.

in the underlying structure [56]. These multi-type particle layers are placed on top of a thick Si wafer which is supported on a $SiO_2$ substrate. Both lower layers are considered to be homogeneous and described by a wavelength-dependent permittivity [68]. The structured layer efficiently decreases the RI of the front surface and thus reduces reflection and improves significantly the light scattered forward into the structure. This is corrected by losses in the particle array itself, which we denominate absorption of the homogeneous region $A_{\mathrm{hom}}$ as opposed to total absorption of the optical device.

The FMM allows a straightforward extension to include several particles within a single unit cell, which is detailed in appendix A.2.2. While the computational effort is increased by a finite summation over the number of particles in the unit cell, one has to keep in mind that the size of the unit cell increases and thus, in order to obtain results of equal quality, a similarly higher number of plane-waves has to be considered, which is the main drawback in this approach. This leads to a moderate increase in the computational time $(2N)^2 \rightarrow (2mN)^2$, with $m$ the multi-type number (square root of particle number in the unit cell). Si has a low refractive index contrast to air and convergence is reached rapidly. Note that averaging over orthogonal polarization directions is not necessary as long as we maintain a symmetric unit cell. However, this approach does allow for asymmetric, including random [75], particle distributions and an arbitrary assignment of material properties.

An improvement of the average absorbance for already 1-type layers, see Fig. 1.5(b), lies first of all in the effective reduction of the refractive index on the front surface reducing the reflectivity and allowing a larger fraction of the incoming light to be transmitted into the structure. Additionally, diffracted and scattered light exhibits an increased optical path length inside the structure, which enhances the absorption mainly within the long wavelength spectrum of the light coupled into the structure. However, this can be further improved by providing an even larger density of (resonant) optical modes which can be done by combining different particle sizes within a single structure.

Fig. 1.6(a) shows the normalized absorbance for an all Si 2-type layer where two diagonal

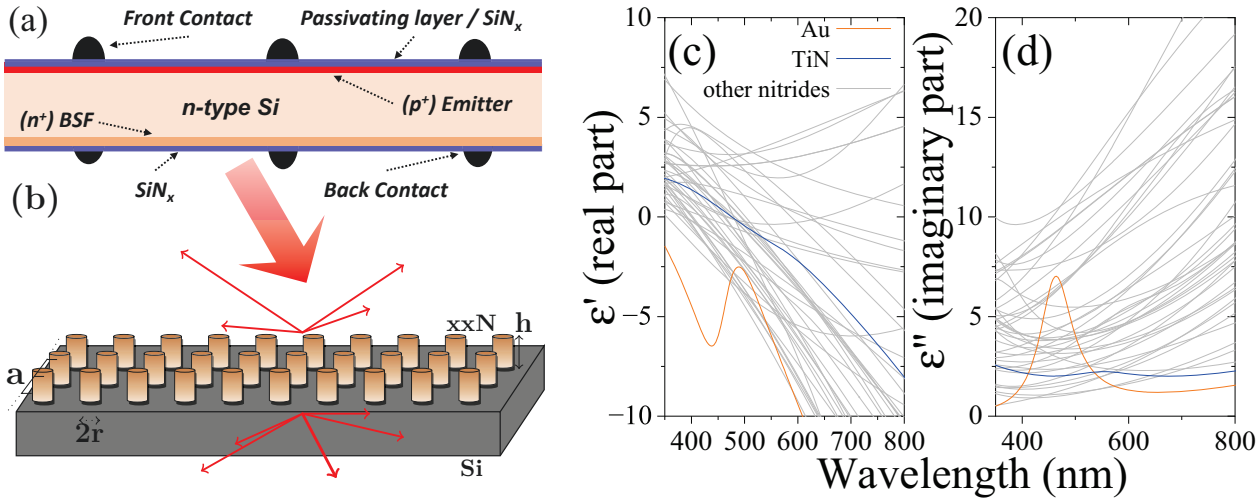


Fig. 1.7.: Illustration of the considered setup and its range. (**a**) n-PERT BiSoN cell, here with flat passivating layer as simulated. (**b**) Cylindrical pillars of height $h$ and radius $R$ made of nitrides and other materials for comparison standing on the n-PERT device with particle-particle separation $a$. The nanopillars are placed within the $SiN_x$ passivation. Range of measured (**c**) real and (**d**) imaginary part of the permittivity of gold (orange [69]), TiN (blue [123]) and further nitride materials (grey [124]).

disks have a fixed radius of 25 nm (0.125 a) and height of $h = 0.5a = 100$ nm. The size of the other two disks is changed to produce the contour plot relative to the corresponding 1-type Si result. For smaller sizes, the absorption in the blue range is suppressed through absorption in the disks which yields a smaller, but still positive, enhancement of the short circuit current. The normalized absorbance is close to 1 for small disk heights, but increases significantly for taller disks, see table 1.1.

| $h$ (nm) | 20 | 40 | 60 | 80 | 100 |
|---|---|---|---|---|---|
| $\eta_{\mathrm{Isc}}$ | 5% | 17% | 28% | 33% | 32% |

Table 1.1.: Relative photocurrent gain of the Si-Si 2-type cells with particle sizes $r_1 = 25$ nm, $r_2 = 45$ nm, varying height $h$, and lattice constant $a = 100$ nm.

Multi-type layers made of Si disks with two different radii achieved up to 33% and with four different radii, namely $r_1 = 15$ nm , $r_2 = 25$ nm , $r_3 = 35$ nm , $r_4 = 45$ nm and a periodicity of $a = 400$ nm, up to 40% improvement in the short circuit current within the photo-active region. Despite the use of several smaller disks, this constitutes an increase in the efficiency compared to the 2-type cells which underlines the effect of boosting the absorption by providing a multitude of optical modes through the particle layer.

### 1.3.2 Accurate Doping Profiles

A further aspect of photovoltaic devices is their designed doping profiles which are obtained through an imbalance of charge carriers. These are redistributed in the front and/or back surface region of the solar cell in a drift diffusion phase. Measurements of the carrier distribution as a function of the depth into the solar cell reveal the final doping profiles.

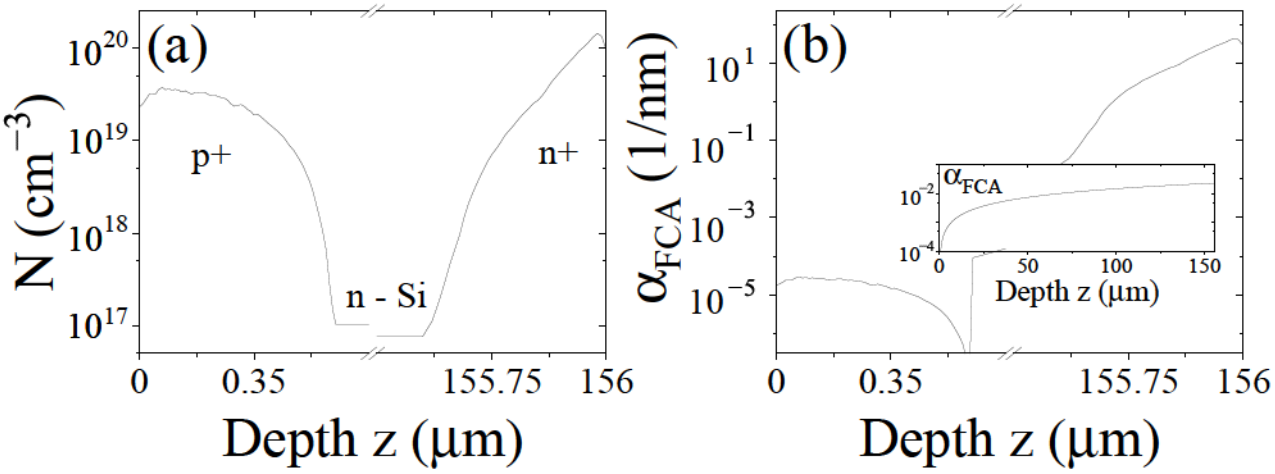


Fig. 1.8.: Si doping profiles as input for device modeling. (**a**) Electron doping as a function of the depth of the cell obtained from experimental measurements. (**b**) Calculated free carrier absorption across the cell. The inset shows the adiabatic connection in the n-doped center of width 150 $\mu$m.

In recent years, conductive transition metal nitrides have been proposed as alternative plasmonic materials, allowing for resonant field enhancement effects while at the same time being less absorptive over a broad range of the spectrum [124–126]. Fabrication processes and studies to integrate these materials for PV applications are in place [127]. We compare the potential photocurrent gain from an additional layer made of nanopillars of nitrides with other material classes obtained in an optimized c-Si baseline solar cell, considering an experimental doping profile. The solar cell parameters of the fabricated samples considered in this study have been taken from an n-PERT BiSoN process developed at ISC Konstanz [128]. The BiSoN solar cell employs a low-cost industrial fabrication process developed on n-type mono-crystalline wafers with textured front side boron as an emitter and flat rear-side phosphorous diffusion as a back surface field (BSF). The experimental short circuit current $J_{sc}$ with a standard industrial antireflection coating, has been measured between $39.0 - 39.2$ mA/cm$^2$. A schematic representation of the n-PERT BiSoN cell with a flat front side is illustrated in Figure 1.7(a). This is combined with an additional front layer of disk-shaped nanoparticles, see Figure 1.7(b). The nanostructure leads to diffraction of light in forward and backward direction, as indicated by the red arrows in this figure.

Diffused p+– and n+– doping profiles were measured and used for the electro-optical modeling of the flat base structure. With the measured doping profiles, we account for integrated electro-optical effects stemming from the free carrier absorption (FCA) in doped Si [129]. We present simulations of nanostructured PV devices achieving a realistic description of a highly efficient and low-cost industrial photovoltaic device with the aim to improve the photocurrent further through nanostructuring.

The real and imaginary part of the permittivity $\epsilon(\omega) = \epsilon' + i\epsilon''$ of a material, see for instance

Figure 1.7(c) and (d), are related to the wavenumber

$$k^2 - \kappa^2 = (\omega/c)^2\epsilon' \text{ and } 2k\kappa = (\omega/c)^2\epsilon'', \tag{1.31}$$

where the imaginary contribution $\kappa$ gives the absorption coefficient $\alpha(\omega) = 2\kappa = (\omega/c)^2\epsilon''/k = \omega\epsilon''/(cn)$. The real-valued refractive index is obtained from

$$n(\omega) = \sqrt{\frac{1}{2}\left(\epsilon'(\omega) + \sqrt{(\epsilon'(\omega))^2 + (\epsilon''(\omega))^2}\right)}. \tag{1.32}$$

This is typically approximated to $n(\omega) \approx \sqrt{\epsilon'(\omega)}$ for low absorptivity. We obtain the absorption coefficient of Si from

$$\alpha(\omega) = \frac{\omega}{c}\frac{\epsilon''}{n_{\mathrm{Si}}}. \tag{1.33}$$

This coefficient is a measure of the exponential absorption inside the considered material with intensity dropping as $I \sim e^{-\alpha z}$. Eq. (1.33) can be used to reconstruct the related permittivity $\epsilon'' = \alpha c n_{\mathrm{Si}}/\omega$. With this approach the effect of free carrier absorption in highly doped Si is added to the experimentally available permittivity of undoped Si [68]. Using measured data for the electron density $N(z)$ in c-Si wafers, we calculate the FCA and the resulting modified permittivity following the empirical relation $\alpha(z) = \mathcal{C}N(z)\lambda^\delta$ discussed in depth in Ref. [129]. Hereby, we use their results on p+–doping ($\delta = 2.18$ and $\mathcal{C} = 1.8 \times 10^{-9}$) and n+–doping ($\delta = 2.88$ and $\mathcal{C} = 1.68 \times 10^{-6}$). The range of validity is given for $\lambda \in \{1, \ldots, 1.5\mu\text{m}\}$ and $N \in \{10^{18}, \ldots, 5 \times 10^{20}\}$ due to available data in their study. The calculations presented here are within the VIS spectrum.

The total width of the c-Si region is $d_{\mathrm{Si}} = 155\ \mu$m and the additional doping profiles affect about $0.4\ \mu$m at the front and back of the structure. For each subdivision of these regions, the free carrier absorption is calculated and from this the modified permittivity $\epsilon(\omega)$ of doped Si which results in capturing the absorption effects, see Figure 1.8(b), beyond the usage of available data [68] for undoped bulk material. These multilayered systems typically converge for $\sim 10^2$ subdivisions. The photocurrent for the simulated baseline cell before introducing the front side emitter and back surface field is $J_{\mathrm{sc}}^{\mathrm{ref}} = 28.33$ mA/cm$^2$. Adding the free carrier absorption through the doping profiles increases the photocurrent for the completed baseline cell to $J_{\mathrm{sc}}^{\mathrm{ref}} = 36.29$ mA/cm$^2$. In comparison, the measured photocurrent for the n-PERT BiSoN cell including an antireflection coating is $J_{\mathrm{sc}}^{\mathrm{exp}} = 39.2$ mA/cm$^2$.

Adding nanopillars of different materials to this setup, we give a competitive overview of results for $\Delta\eta_{J_{\mathrm{sc}}}$ in Figure 1.9 for three geometries varying the $r/a$–ratio. To each material $r/a = 0.125$ , $r/a = 0.25$ , and $r/a = 0.5$ are shown side-by-side. The colors are meant as a guide to the eye: yellow for moderate, orange or red for high losses due to parasitic material absorption in the nanostructure itself. The different shades of blue indicate positive photocurrent gain from minor (light blue) to moderate (dim blue) to large (bright blue) gains. Metals show strong losses for the case of touching nanopillars ($a = 2R$). The same is true for

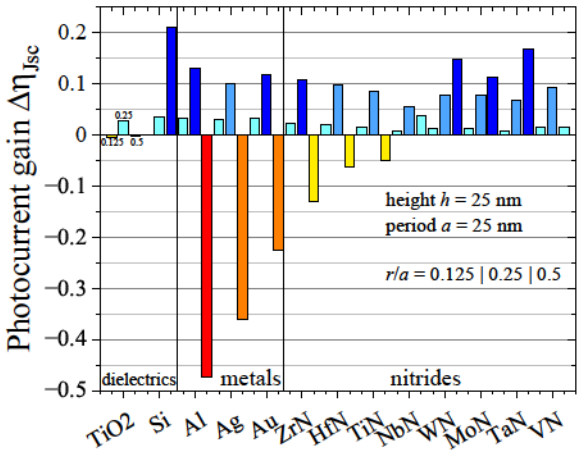


Fig. 1.9.: Relative photocurrent gain for an n-doped Si solar cell with particle layers of different materials. Comparing the different material classes for three geometrical setups with varying $r/a$-ratio showing $r/a = 0.125$ , $r/a = 0.25$ , and $r/a = 0.5$ side-by-side for each material.

those nitrides whose plasmonic resonance is most comparable to gold, i. e., ZrN and HfN and, thus, have an overlap with the optimized spectral region of the baseline solar cell. In these cases, the absorption in the nanoparticle layer strongly hinders the absorption within the baseline cell. Overall, this case is connected to the shading effect. If too much additional material is placed on top of the solar cell device, the incident light will be either reflected or absorbed in the particle layer itself, which strongly reduces the photocurrent yield.

Typically, most materials have their largest photocurrent gain for the medium sized nanopillar structure, i. e., there is not too much nor too little scattering material. In contrast, some materials show strongest photocurrent gain for the largest particle to lattice parameter ratio. This includes the dielectric Si and the nitrides WN, MoN and TaN with relative gain of over 10% in these particular cases. From all the nitrides studied, these materials look most promising combining the best of the two other worlds: their field enhancement is moderate and their associated plasmon resonance is far away from the wavelength region where the baseline cell is highly optimized [128], hence, contributing to improve the device at other wavelengths. At the same time, they exhibit strongest photocurrent gains for further increasing the nanopillar particle size. We can, thus, characterize two types of nitrides: nitrides for which the shading effect remains a problem similar to metals, and others which behave like dielectric scatterers with high photocurrent gain.

### 1.3.3 Nanotube Arrays for Raman Spectroscopy

Two-dimensional arrays of hollow nanotubes made of $TiO_2$ are a promising platform for sensing, spectroscopy and light harvesting applications [66, 101, 117, 130]. Their straightforward fabrication via electrochemical anodization, growing nanotube pillars of finite length from a Ti foil, allows precise tailoring of their geometry and, thus, optical resonances. The NT arrays obtained can show a high degree of order and regularity, see Fig. 1.4 which allows studying and optimizing their properties with FMM. Annealed crystalline $TiO_2$ NTs show an

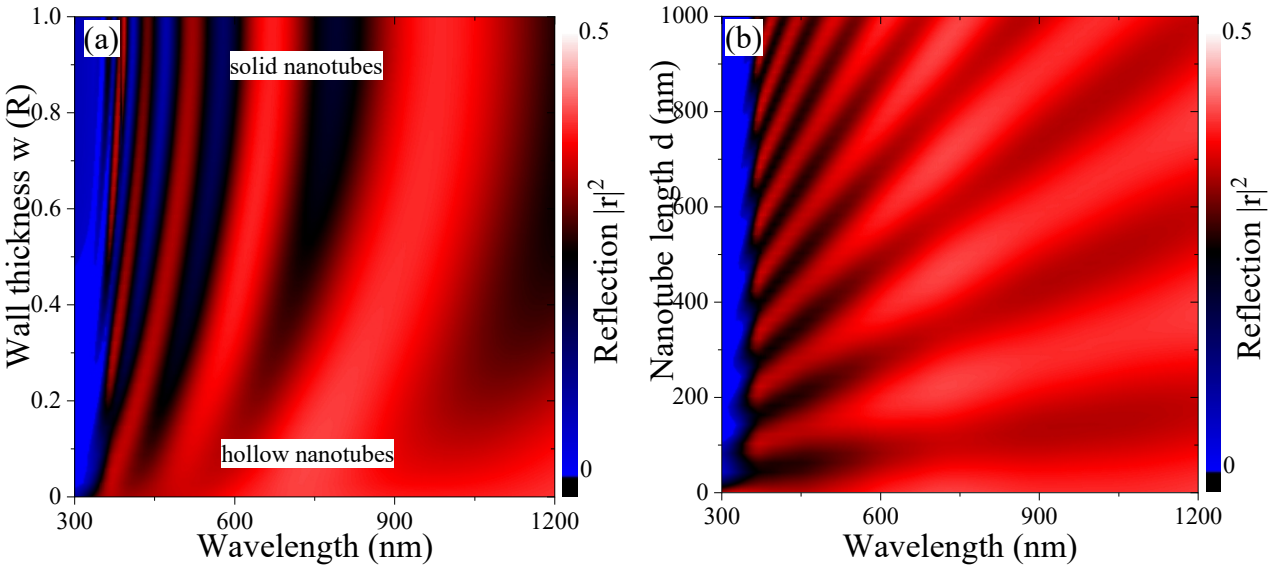


Fig. 1.10.: Studying the reduction in surface reflection for spectra of $TiO_2$ NT arrays as a function of (**a**) nanotube wall thickness $w \in \{0^+ \dots R\}$, and (**b**) nanotube length $d \in \{0 \dots 1000\}$ nm.

increased charge carrier doping level allowing to further improve electron transfer efficiency for bio-electrochemistry applications [107]. We demonstrate that FMM is highly apt to explain experimental findings in hollow nanotube arrays, in particular, that additional, free electrons can yield high optical field enhancement in densely packed, thin-walled $TiO_2$ NT arrays, independent from the chemical environment [101].

We theoretically investigate these photonic crystal structures with respect to reduction of front surface reflection, achievable field enhancement, and photonic bands [66]. Next to calculating the overall reflection, the Field Enhancement Factor (EF) is assessed as it is the central quantity for Raman spectroscopy.

It was observed experimentally that additional charge carriers are injected into the system during the growth process of $TiO_2$ nanotubes [101,111]. We account for this effect considering refractive index (RI) data modified by the presence of free electrons in a Drude model

$$\epsilon(\omega) = \epsilon_{\mathrm{TiO_2}} - \frac{n_e e^2}{\epsilon_0 m_e} \frac{1}{\omega(\omega + i\gamma)}. \tag{1.34}$$

We assume a small, intrinsic damping $\gamma = 0.01$ eV, varying the carrier density $n_e$. The calculations were performed using frequency-dependent, tabulated RI data in the visible spectrum for $TiO_2$ from Ref. [131] measured from thin films and Ti from Ref. [67] for bulk material. Besides explaining experimental findings with respect to field enhancement, this approach allows identifying the doping level and conductivity of the fabricated samples.

We normalize the electric field $\mathbf{E}$ with respect to the field obtained for a flat Ti electrode $\mathbf{E}_{\mathrm{ref}}$ ($d = 0$ case). The evaluation is done either (i) directly as $\mathrm{EF} = |\mathbf{E}(x,y,z)|^2 / |\mathbf{E}_{\mathrm{ref}}|^2$ used

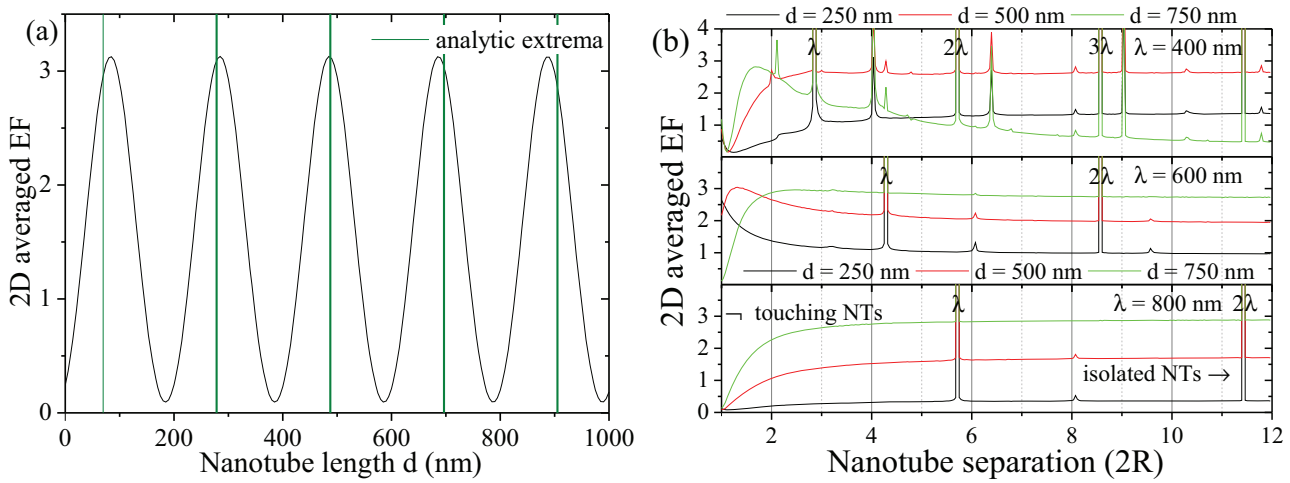


Fig. 1.11.: (**a**) Averaged field enhancement $E^{\mathrm{av,2D}}$ in the unit cell at the top of the NTs $z = d$ at $\lambda = 600$ nm as a function of nanotube length compared to analytic maxima, Eq. (1.36); (**b**) Averaged enhancement factor $|\mathbf{E}^{\mathrm{av,2D}}|^2/|\mathbf{E}_{\mathrm{ref}}|^2$ within the unit cell as a function of the nanotube lattice parameter $a \in \{2R \dots 24R\}$ with $R = 70$ nm for several nanotube lengths $d$ and excitation wavelengths $\lambda$. Divergences are observed where the ratio $a/R$ is an integer and, in particular, where the lattice parameter coincides with a multiple of the wavelength.

in field maps, or (ii) as 2D averaged EF, taking the mean over the unit cell area ($x-y$-plane)

$$\mathrm{EF}^{\mathrm{av,2D}}(z) = \frac{1}{a^2\,|\mathbf{E}_{\mathrm{ref}}|^2}\int_0^a dx \int_0^a dy\,|\mathbf{E}(x,y,z)|^2\,, \tag{1.35}$$

typically, at the top of the NTs ($z = d$). If not stated otherwise, an interparticle distance $a = 160$ nm, a particle diameter of $2R = 140$ nm and a wall thickness of $w = 10$ nm are used. This defines a dense NT array where the $TiO_2$ pillars are not yet touching.

Convergence is reached quickly in this dielectric system. 169 Plane-waves ($n, m \in \{-6 \dots 6\}$) are usually enough to produce converged far-field spectra, 529 ($n, m \in \{-11 \dots 11\}$) was used for near-field data, but convergence was checked for up to 961 plane-waves ($n, m \in \{-15 \dots 15\}$), in particular, where plasmonic properties emerge when free carrier doping was assumed.

The hollow $TiO_2$ nanotube structures discussed are shown in an SEM image [101] and the related simulated structure is likewise depicted in the inset of Figure 1.4(a). We consider the active surface $\mathcal{A}$ of a unit cell with and without nanotubes in Figure 1.4(a). For nanotubes with outer radius $R$ and wall thickness $w$, the surface area becomes $\mathcal{A} = a^2 + d2\pi(2R - w)$. Hence, the active surface increases linearly with the tube length from $a^2$ for the flat device while the slope flattens with increasing unit cell size. A ten-fold surface area is reached at nanotubes of a few hundred nanometers long which is well within experimentally achievable setups [101, 117]. Figure 1.4(b) and (c) show the electromagnetic field enhancement along the $x-y$- and $x-z$-planes, resp., revealing an oscillatory structure for field maxima in between the nanotubes and inside the hollow structures along the nanotube length. Typically, the field inside the nanotube (NT) wall is supressed and an enhancement is observed directly

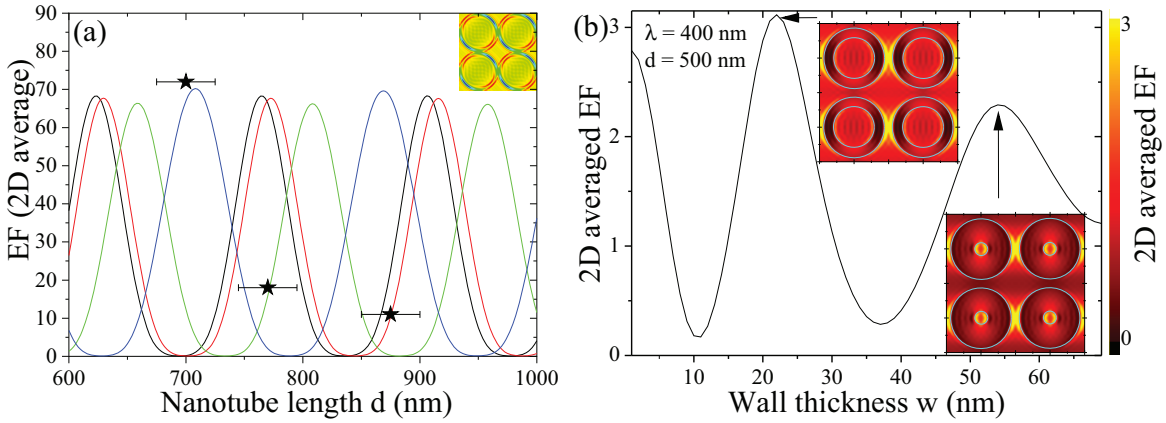


Fig. 1.12.: (**a**) Comparison of the calculated averaged field enhancement $|\mathbf{E}^{\mathrm{av,2D}}|^2/|\mathbf{E}_{\mathrm{ref}}|^2$ for different doping levels with experimental enhancement factors (stars). The black curve is the undoped result, the red curve has lowest, the blue largest doping. (**b**) Same as a function of the wall thickness $w$ for $d = 500$ nm and $\lambda = 400$ nm adding the field maps for two maxima.

at the $TiO_2$ surface. The overall enhancement is small compared to other material choices, but stable for the entire UV and VIS spectrum.

Strong optical lattice effects are observed in $TiO_2$ hollow nanotubes where the influence of the wall thickness on the front surface reflection is studied in Figure 1.10(a). Furthermore, Figure 1.10(b) shows this dependence for the NT length $d$. Reflection minima are hereby linearly shifting with the wavelength, rendering a broadband optimization impractical. Shorter NT lengths are most promising, since the shifted optimum is varying slowly across the spectrum. This oscillation with the nanotube length in the spectrum is connected to the spatial oscillations of the electromagnetic field across the nanotube length, investigated further in Figure 1.11(a). The maximum value of the intensity evaluated at the front surface $z = d$ follows a sinusoidal law related to Bragg diffraction in crystal structures

$$|\mathbf{E}|^2 \sim |\mathbf{E}_0|^2 \sin^2(kd) = |\mathbf{E}_0|^2 \sin^2\left(\sqrt{\epsilon_{\mathbf{GG}}}\frac{2\pi}{\lambda_{\mathrm{exc}}}d\right). \tag{1.36}$$

The field enhancement in the $x-y$-plane of the nanotube array shows a general dipole field distribution around the nanotubes, see Figure 1.4(b) and insets in Figure 1.12(b). Hereby, the roots are characterized by $d = n\lambda_{\mathrm{exc}}/(2\sqrt{\epsilon_{\mathbf{GG}}})$ with integer $n$. Hence, the maxima are found for $n \pm \frac{1}{2}$ values. The position of these analytic maxima as a function of the nanotube length are marked in Figure 1.11(a). Discrepancies can be expected, since taking the diagonal value $\epsilon_{\mathbf{GG}}$ of the permittivity matrix becomes less valid for longer nanotubes where higher order Fourier components become increasingly important, see the small descrepancies in Figure 1.11(a).

Further analytically comprehensive traits of this crystal structure are shown in Figure 1.11(b). The two-dimensional averaged EF is shown as a function of the NT separation for a number of wavelengths and NT lengths. Here, we observe a number of divergent resonances, which can be understood in an empty lattice picture. Resonant bands are found where $|\mathbf{k}_{\parallel} - \mathbf{G}| = k$.

However, if the parallel momentum is $\mathbf{k}_{\parallel} = 0$, then the reciprocal lattice vector $|\mathbf{G}| = {}^{2\pi n}/_{a}$ equals the wave vector $k = {}^{2\pi}/_{a}$, leading to the condition $\lambda n = a$. Hence, where the lattice parameter $a$ is a multiple of the wavelength $\lambda$, we observe strong resonant field enhancement promoted by geometrical lattice conditions. Weaker, non-divergent resonances are often observed close to the condition of $a = 2nR$ at lower wavelengths, i. e., higher photonic energies. Here, the lattice parameter is a multiple of the NT diameter. However, since we study hollow NTs and not solid nanopillars, these resonances are less pronounced and dominated by losses. Calculations including a low doping of additional free electrons is compared to experimentally available data [101] in Fig. 1.12(a). This allows to estimate the doping effect of the growth process.

Figure 1.12(b) studies the dependence of the $TiO_2$ thin-walled nanotube arrays on the wall thickness, a degree of freedom not typically available in nanoarrays fabricated with physical methods. Figure 1.12(b) shows the 2D averaged field enhancement, adding the near-field maps of the two observed maxima and indicating the wall thickness. Note that for sufficiently thin walls, optical surface modes from both sides of the ring layer can couple and lead to higher local fields.

The straightforward fabrication and geometrical tuning of $TiO_2$ nanotubes makes this an ideal material system to study photonic crystals made of hollow nanotube arrays for bio-chemical applications in spectroscopy and catalysis.

### 1.3.4 Rough Surface Morphologies

Complex nanostructed matter is of great interest for spectroscopy, biochemical sensors, microscopy, (photo-)catalysis [109] and 3rd generation photovoltaic systems [132], due to their tunability of spatial and spectral properties, boosting energy conversion efficiency with high local fields or improving absorption through directional scattering.

Surface roughness poses a major challenge to theoretical methods aiming at accurately describing realistic experimental situations. The inclusion of additional scattering effects of naturally rough surfaces as well as deliberately roughened structures such as, e. g. Raman electrodes and the systematic investigation of structures with low symmetries, such as composites and random particle distributions makes a feasible numerical description of rough surface morphologies necessary.

In this section, we briefly summarize two ways in which we have used the FMM to assess optical properties from rough surfaces.

#### Scattering from rough silver surfaces for photovoltaics

Rough silver layers were studied in an experiment by Springer et al. Ref. [133] with a focus on absorption loss spectroscopy as a function of surface roughness. The optical properties of the corresponding flat layered devices intended for photovoltaics can be obtained with the FMM. In addition, we applied diffraction theory [134, 135] to model the specular and diffuse far-field properties of the samples, see Fig. 1.13, with varying surface morphology. This is based on the Fourier analysis of an aperture function that contains the height information and

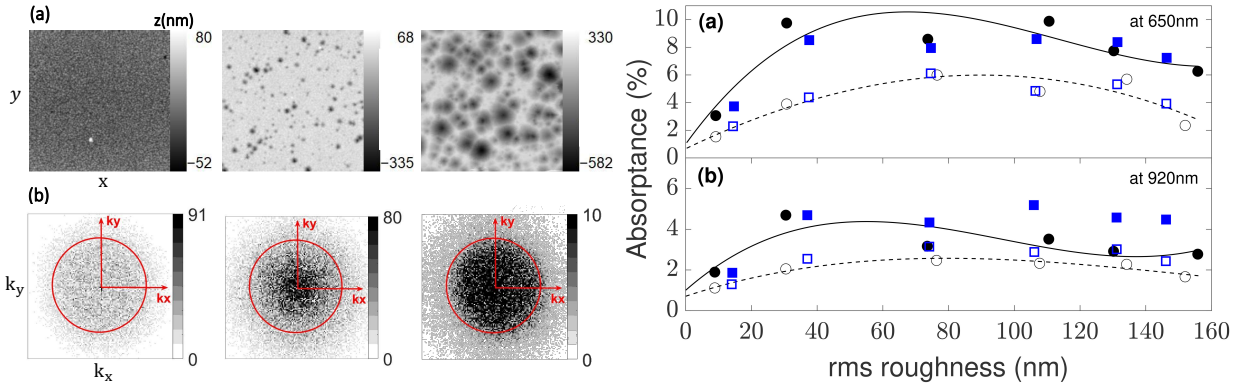


Fig. 1.13.: (Left) (a) Height function $z(x, y)$ extracted from AFM images of rough Ag surfaces (Ref. [133]) with varying root mean square (rms) roughness and (b) their Fourier components of the reflected scalar field. The red circle indicates the condition $k_x^2 + k_y^2 = k_0^2 n^2$. (Right) Absorptance of two devices compared to corresponding experimental data (blue) [133].

is thus fully compatible with the FMM although the large number of diffracted waves makes it unfeasible to use a fully numeric scattering approach. Using the original data provided by the authors [133] we obtained excellent agreement with their experimental findings [136]. This method, however, relies on a number of approximations and does not allow studying near-field effects in a rigorous way as the contribution of evanescent waves prominent in metallic structures is suppressed.

#### Raman Scattering from rough TiN nanostructures

Another focus is put on rough surface morphologies in optical sensing and catalysis. Metasurface platforms for Raman spectroscopy [137] where rough surfaces are of particular interest. In continuation of our collaboration Ref. [101], we recently studied rough TiN nanostructures. The structure was obtained from regular photonic crystals of $TiO_2$ nanotubes through nitridation. During this process the regular structure collapsed and Raman measurements were performed on the rough surface morphology, see Fig. 1.14(a) for the structure and Fig. 1.14(b) for the measured absorption spectrum.

We used the Fourier Modal Method (FMM) to assess the two observed peaks in the absorption. Comparing the optical response of the regular structures to the measured results allowed the identification of the observed optical modes. The maximum absorption at around 400 nm can be associated to the surface plasmon polariton (SPP) of the conductive nitride substrate. We found a lattice resonance of the collapsed nanopillar structure at around 700 nm. In a regular lattice, this lattice resonance is especially sensitive to changes in the nanopillar height leading to sizeable shifts in its peak position as well as in its overall predicted absorption value. Hence, we are using an averaging procedure over a range of regular two-dimensional structures employing the FMM. Our technique yields good results where the range of heights necessary for the averaging procedure was estimated by SEM imaging and lead to a natural broadening of the lattice resonance peaks.

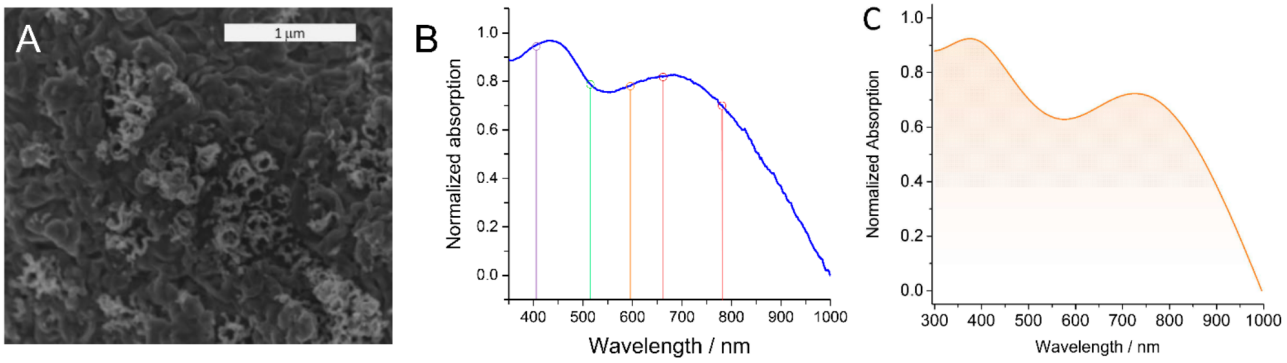


Fig. 1.14.: (A) SEM image of a TiN electrode created from TiO2 nanotubes. (B) UV-Vis spectrum of the nanostructured TiN electrode. Colored vertical lines indicate the laser excitation wavelengths in the SERS experiments. (C) Calculated relative absorbance $A = 1 - R - T$ from averaging over a range of nanotube lengths with good agreement to the measured result.

# II

# Mesoscopic Charge Dynamics

# 2. Nonlocality in Nanostructures

An accurate description of microscopic properties of metal nanoparticles (MNPs) is important to predict the optical response of, e. g., molecules in close proximity to metal surfaces, the resulting field enhancement and quenching effects. While ab initio methods can do this for isolated particles and small coupled systems, they cannot describe the performance of large-scale devices employing regular arrays or randomly distributed particles. Nanoparticles as part of functionalized layers in sensing, spectroscopy [101] and light harvesting applications, such as photovoltaics [26, 28, 34, 84, 99] and photocatalysis [109, 138–141], can improve the performance of such devices. They are efficient subwavelength scatterers improving the light trapping effect and free charge carriers in MNPs provide, in particular, large local fields enhancing charge carrier generation and absorption in a photo-active material, and light-induced effects from other nanostructures such as spectral conversion [116] or photoluminescence [41] efficiencies.

For over a hundred years, modeling of the optical properties of MNPs relies on classical electrodynamics. In highly symmetric cases (spherical and cylindrical NPs) analytic solutions are obtained within Mie scattering theory [142] using corresponding basis functions. The electric part $\mathbf{E}$ of the electromagnetic field creates a polarization field $\mathbf{P} = \alpha(\epsilon_1, \epsilon_2)\mathbf{E}$ in solid matter, expressed in terms of the permittivities $\epsilon_1(\omega)$ and $\epsilon_2(\omega)$ of the environment and the bulk material of the scatterer, respectively. The polarizability $\alpha$, depending only on the optical response at a frequency $\omega$, neglects microscopic electron interaction effects at the ultimate nanoscale arising not only from the quantum nature of the free electron gas in metals, but also from accelerated motion in the plasmon oscillation.

Light-matter interaction involves processes within the electron subsystem in solids, crystals and molecules. Inhomogeneities on the length scale of the de Broglie wavelength $\lambda_e = \frac{h}{\sqrt{2mE}}$ produce scattering and interference effects of electrons which mutually interact with incoming light, see Figure 2.1a. Hereby, $h$ is Planck's constant, $m$ is the (effective) electron mass which depends on the bulk material, and $E$ is the energy of the electron wave. Typically, this wavelength is about 7.5 nm in solids at room temperature $T = 300\,\mathrm{K}$, where $E = k_B T$ with the Boltzmann constant $k_B$. For MNPs, the main source of electron scattering is the particle surface, see Figure 2.1b, where the surface-to-volume ratio indicates the relevance of such scattering events.

Microscopic interaction effects of electrons in atomistic matter are accurately described using first-principle methods, e. g., Density Functional Theory (DFT) [4–6]. These solve Schrödinger's equation for a large, but finite number of electron wave functions from all atoms in the considered system. Unfortunately, even with strong approximations such as the Time Dependent Local Density Approximation (TDLDA), time-consuming algorithms limit their applicability to particles of a few nanometers in size [7–9] with available computers. Hence, the complex electromagnetic field distributions arising from functionalized surfaces cannot

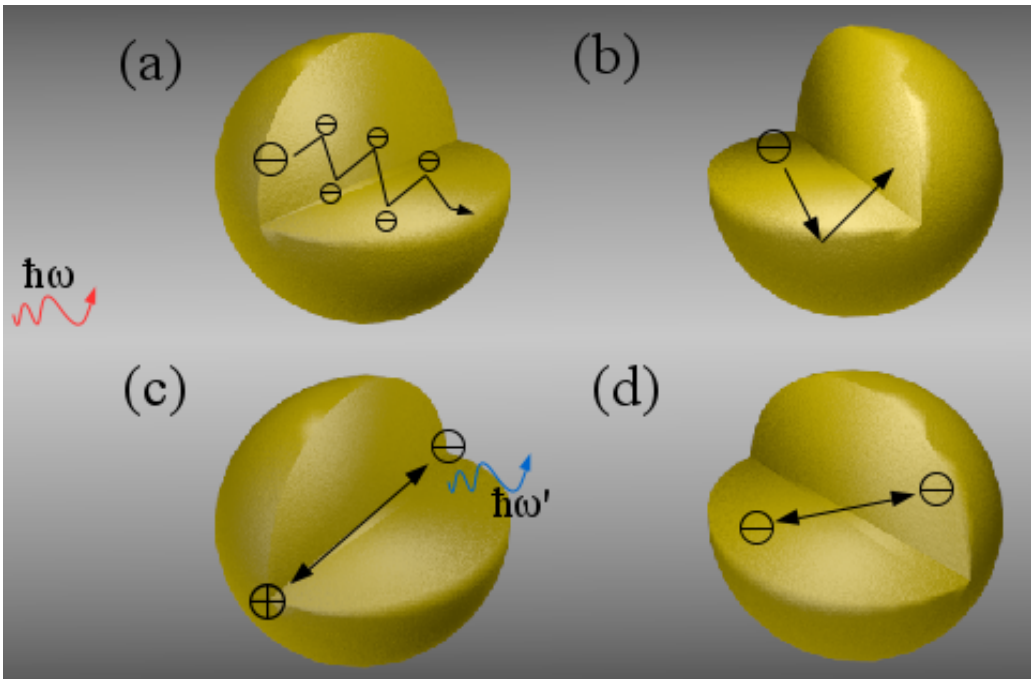


Fig. 2.1.: Illustration of sources of plasmon damping and electron interaction phenomena. (**a**) Electron-electron collisions in the bulk material; (**b**) Electron-surface collisions due to confinement; (**c**) Electron irradiation due to acceleration during plasmon oscillation; (**d**) Short-ranged electron-electron interactions, such as Coulomb force and electron diffusion.

be captured and the light-matter interaction is simplified to single particles [6–9]. Moreover, advances in fabrication of nanostructures along with experimental access to particle sizes and interparticle spacings below 10 nm led to the possibility of direct or indirect observation of such effects [21, 143, 144]. In recent years, experiments to verify nonlocality stemming from the quantum nature of free electrons in metals [76, 145–148] were made and theories pursued the extension of classical electrodynamics to scalable, semi-classical descriptions of damping and interaction effects stemming from the quantum nature of charge carriers as illustrated in Figure 2.1.

The original formulation of light scattering by a sphere by Gustav Mie in 1908 [142] excluded microscopic dynamics of the conduction band electrons in bulk and related surface effects. However, efforts to extend it have been made since the 1970s [149–158]. Advanced semi-classical material models can be derived from perturbative theories [53, 159]. A description of the Lorentz friction in metals from RPA [55, 160], i. e., the loss of energy in the collective motion of electrons due to acceleration in the plasmon oscillation [18, 54, 55, 72, 161, 162] was introduced. Short-ranged electron–electron interactions, such as the Coulomb force and diffusion, are investigated by separating the free electron dynamics from the core electron polarization via the hydrodynamic equation for an electron plasma [52, 53, 70, 71, 74, 75, 163–176]. Such spatial dispersion effects are inherently nonlinear and have been reviewed with respect to nonlinear phenomena in Ref. [177] and have most recently been summarized in Ref. [178] with respect to modeling efforts.

It should be noted that a major advantage of ab initio methods lies in their capability to

account for the electron spill-out of the electron density into the surrounding dielectric medium from the evanescent tail of the electron wave functions. It was shown within the hydrodynamic framework that the electron spill-out can be adequately incorporated [73, 174] and a potential dependent on the tunnel current can be accounted for [77].

The major challenge in modeling complex hybrid metal-dielectric systems is, thus, describing the impact of localized mesoscopic charge interactions effects at nanoscale features [70, 177]. Though such effects are highly localized and short-ranged, optical coupling can lead to mediating their influence on the overall device performance via retardation effects [162, 179] in a large-scale, patterned structure, as discussed in detail for one- and two-dimensional gratings in chapter 3. The strong optical coupling of metal nanoparticles with semiconductor substrates needs to be considered beyond the classical approach [180] which is presented in chapter 4. Classical electrodynamics does not address optically induced charge interactions effects in standard schemes such as Mie or Fresnel coefficients. Mesoscopic electron dynamics plays a major role in highly doped semiconductors and metallic nanostructures, however, charge interactions are also of wider interest in ionic systems. We introduce the concept of soft plasmonics and its nonlocal formulation in chapter 5.

Our approach relies hereby on the semiclassical hydrodynamic model as the main ingredient in the Generalized Nonlocal Optical Response (GNOR) approach [70]. The advantage of employing semi-classical theories is their mostly analytic formulation and thus compatibility and straightforward integrability with existing numerical procedures for improved electro-optical simulations.

## 2.1 Phenomenological Approach

Typically, the optical response of a metal is described with the Drude model via the frequency-dependent permittivity

$$\epsilon_D(\omega) = \epsilon_b - \frac{\omega_p^2}{\omega(\omega + i\gamma_p)}, \tag{2.1}$$

where $\epsilon_b$ is the background permittivity given by bound (valence band) electrons, $\omega_p^2 = {}^{n_0 e^2}/_{\epsilon_0 m_e}$ is the plasmon frequency, determined by the material dependent (bulk) electron density $n_0$ and mass $m_e$, and $\gamma_p$ is the inherent (bulk) damping rate. This widely used Drude model applies only to bulk material and should be modified for nanostructures to include effects due to the finite size of the system. One of the corrections considered by Kreibig and von Fragstein [181] is the inclusion of an additional damping due to the scattering on the physical particle boundaries, depicted in Figure 2.1(b). This is in particular important in particles of sizes equal or smaller than the mean free path $\lambda_b$ of electrons in bulk metal. In such a case, the electrons will classically experience additional scattering from the boundary of the system. Kreibig damping is described as $\gamma_K = {}^{v_F}/_{L_{\text{eff}}}$, where $v_F$ is the Fermi velocity of the electron gas and $L_{\text{eff}}$ is the effective mean free path of electrons resulting from collisions with the particle surface [157, 181, 182]. In spherical particles, it can be replaced by the radius of the

nanoparticle $R$, to become $\gamma_K(R) = {}^{Cv_F}/_R$, where $C$ is a constant of the order of unity which depends on the type of scattering and particle radius. Similarly, collision effects in the bulk, depicted in Figure 2.1a, can be described via the damping term $\gamma_p = {}^{v_F}/_{2\lambda_b}$. We will consider such phenomenological expressions together with further analytic damping terms from RPA calculations in chapter 4.

## 2.2 Hydrodynamic Model

In this work, we apply the hydrodynamic model [163, 183] to calculate the electric field $\mathbf{E}$ at a given frequency $\omega$. Its central idea is to treat the conduction band electrons as a plasma with the (linearized) Navier–Stokes equation, separate their dynamics from bound valence electrons and couple the electromagnetic wave equation with the hydrodynamic equation via the induced charge current. This emphasizes a real-space interaction [53, 74, 168, 184]. The semi-classical corrections include Coulomb interactions and diffusion effects [70] through the pressure term. This results in an additional excitation, longitudinal in character, which can be interpreted as a pressure-wave stemming from the electron charge. In comparison, in the case of the local response approxmiation (LRA), only transverse TE and TM modes can be excited.

The induced current $\mathbf{j}^{\mathrm{ind}}$ and charge $\rho^{\mathrm{ind}}$ densities

$$\mathbf{j}^{\mathrm{ind}} = \frac{i\epsilon_0}{\omega + i\gamma_p}\left(\omega_p^2\mathbf{E} - \beta^2\nabla\rho^{\mathrm{ind}}\right) \tag{2.2}$$

couple to the electromagnetic wave equation as

$$\nabla\times\nabla\times\mathbf{E} - k^2\varepsilon_b\mathbf{E} = i\omega\mu_0\mathbf{j}^{\mathrm{ind}}. \tag{2.3}$$

This wave equation describes a polarization field stemming from the valence electrons with dielectric background $\varepsilon_b$. In contrast to a traditional Drude model, see eq. (2.1) above, an additional pressure term $p = \beta^2\rho^{\mathrm{ind}}$ couples to the electromagnetic wave equation with interaction strength of the conduction band electrons $\beta = \sqrt{3/5}v_F$, where $v_F$ is the Fermi velocity. The pressure of the electron gas can be derived from classical gas theory and is detailed in appendix B.

Using $\nabla\mathbf{D} = \rho^{\mathrm{ind}}$, we can write the wave equation in a compact form in terms of the induced charge density

$$\nabla^2\mathbf{E} + k^2\varepsilon_D\mathbf{E} = \eta\nabla\frac{\rho^{\mathrm{ind}}}{\epsilon_0}, \qquad \text{where} \qquad \eta = \frac{1}{\varepsilon_b} - \frac{k^2\beta^2_{\mathrm{GNOR}}}{\omega(\omega+i\gamma)}. \tag{2.4}$$

On the left hand side, the Drude expression $\varepsilon_D$ is recovered. Together with the continuity equation $\nabla\mathbf{j}^{\mathrm{ind}} = i\omega\rho^{\mathrm{ind}}$, we readily obtain a separate wave equation for the induced charges,

describing the nonlocal interactions

$$-\beta_{\mathrm{GNOR}}^2 \nabla^2 \rho^{\mathrm{ind}} = \frac{\varepsilon_D}{\varepsilon_b} \omega(\omega + i\gamma_p)\rho^{\mathrm{ind}}. \tag{2.5}$$

This yields the wave vector of the longitudinal field and motion of electrons

$$q = \frac{1}{\beta_{\mathrm{GNOR}}} \sqrt{\frac{\varepsilon_D}{\varepsilon_b} \omega(\omega + i\gamma_p)}. \tag{2.6}$$

Nonlocal theories predict finite distributions of induced charges at an illuminated metal surface—in contrast to classical electrodynamics, where charges are induced in a $\delta$-sheet—with a characteristic penetration depth $|\mathrm{Im}(1/q)|$ comparable to the electron spill-out [53, 185]. The main observations of nonlocal theories are a blueshift of the plasmon resonance with respect to the common local approximation and plasmon broadening, in particular tied to the diffusion coefficient $D$ which can be set to fully capture the broadening found with Kreibig damping [70, 74]. Simple geometries, such as MNPs, nanoshells and clusters described with nonlocal Mie coefficients [53], and thin metal slabs and waveguides described with nonlocal Fresnel coefficients [75] show a remarkable nonlocal response only in the limit of small particles <10 nm and separations <1 nm. The impact of spatial dispersion is seen in terms of significant blueshifts of the surface plasmon resonance (SPR) by several tenths of nanometer as well as plasmon quenching. Furthermore, this approach was extended to go beyond the hard wall boundary condition $\varepsilon_{\mathrm{lhs}}\mathbf{E}_{\mathrm{lhs}} = \varepsilon_{\mathrm{rhs}}\mathbf{E}_{\mathrm{rhs}}$ of standard electromagnetism to consider smooth electron density distributions at realistic metal surfaces in addition to electron–electron interaction [73, 174].

A fundamental perspective on the origin of spatial dispersion in the interaction of charges is inherent to the full solution of the displacement field $\mathbf{D}$ in the Coulomb equation

$$\nabla\mathbf{D}(\omega, \mathbf{r}) = 0 \Rightarrow \mathbf{D}(\omega, \mathbf{r}) = \epsilon_0 \int d\mathbf{r}' \varepsilon(\omega, \mathbf{r}, \mathbf{r}')\mathbf{E}(\omega, \mathbf{r}'). \tag{2.7}$$

It is common to assume a local response approxmiation (LRA) in classical electrodynamics relying on permittivities that depend only on the frequency of the incident light field. However, nonlocal interaction effects dominates electron coupling over short distances as depicted in Figure 2.1(d) [159]. In homogeneous media, we can assume a dependence on the distance $|\mathbf{r} - \mathbf{r}'|$ rather than on the specific position of electrons, which allows solving Maxwell's equations in Fourier space $\mathbf{D}(\omega, \mathbf{k}) = \epsilon_0\varepsilon(\omega, \mathbf{k})\mathbf{E}(\omega, \mathbf{k})$.

The dependence on the wave vector $\mathbf{k}$ enables us to describe nonlocal electron-electron interaction such as Coulombic forces and electron diffusion effects in the Generalized Nonlocal Optical Response (GNOR) model [70, 74]. Here, the nonlocal strength paramter $\beta$ is extended by the diffusion parameter $D$ so that

$$\beta_{\mathrm{GNOR}}^2 = \beta^2 + D(\gamma_p - i\omega). \tag{2.8}$$

It is important to note that the large-$k$ response that originates in the subwavelength oscillations of plasmonic excitations is not only an inherent prerequisite for many intriguing wave phenomena, but also particularly sensitive to nonlocality. However, the common Mie result has no upper wavelength cut-off and does suppress short-range electron interactions which can strongly dampen the response beyond $\omega/v_F$. Accounting for nonlocal response leads to longitudinal pressure waves as additional solutions to the combined system of differential equations of the electromagnetic wave equation and the (linearized) Navier-Stokes equation. This is in contrast to the phenomenological damping expressions derived by Kreibig and for the RPA approach. Such additional waves offer further damping channels as well, however, they can also support resonant enhancement effects [52, 75, 141, 176].

Thus, this system of coupled equations yields an additional wave solution, longitudinal in character, and can be solved for different geometries leading to nonlocal extensions of Mie [53, 168] and Fresnel coefficients [75], including for charge carriers in electrolytes [141]. Typically, hard-wall boundary conditions are assumed for the additional boundary condition

$$\hat{\mathbf{n}} \cdot \mathbf{j}^{\mathrm{ind}} \equiv 0 \tag{2.9}$$

prohibiting electrons to trespass through the particle surface into the dielectric surrounding, using a uniform electron density $n_0 \sim \omega_p^2$ inside the material and neglecting the electron spill-out. However, it was shown that a smooth surface distribution of electrons can be taken into account accurately [73, 174] and that the hydrodynamic model is capable of dealing with the spill-out by solving the above equations with position-dependent material parameters $n(z), \omega_p(z), \varepsilon_D(z)$, e. g. within a multilayer approach.

The interest in GNOR of nanostructures extends to many scientific fields. We introduce in chapter 3 the hydrodynamic model for implementation into the Fourier Modal Method (FMM) and its application to plasmonic crystals and extraordinary optical transmission (EOT) [52,176] is subsequently discussed. Chapter 5 transfers the hydrodynamic model to coupled ion dynamics in electrolytes [55, 141] for which a two-fluid approach for interacting positive and negative charges is necessary. A two-fluid model is also necessary to describe coupled electron and hole dynamics in (highly doped) semiconductors [186, 187].

# 3. Nonlocality in Periodic Gratings

## 3.1 Nonlocality in Multilayered Systems

The increasing ability to fabricate particle arrays and holey metal films with nanoscale resolution has made the design and characterization of a wide range of nanostructured materials an attractive field to achieve new solutions towards total light control. Plasmonic crystals are intensely studied both in theory and experiment for their unique optical properties. Hybrid photon-plasmon modes are found for corrugated metal films [188, 189], nanoparticle and hole arrays [190–193], photonic crystals supported by metal substrates [194, 195] and in a range of other periodic and aperiodic realizations. Photons are strongly confined at the edge of band gaps in the crystal structure yielding strong local field enhancements. Such structures can achieve unidirectional emission radiation through plasmon induced transparency and photon tunneling effects that are interesting for optical filters and light guidance through directed transmission [69, 196–199].

Using the hydrodynamic model introduced in the previous section, we aim to include short-ranged electron-electron interactions in periodic grating systems as part of a complex multilayer. Nonlocal Fresnel coefficients [75] can be used to describe homogeneous nonlocal metallic layers in the system together with the planar scattering matrix method [64, 65]. In this section, we derive the necessary equations to include nonlocal properties of metallic components in grating structures in the framework of the Fourier Modal Method (FMM). Hereby, we focus on the limitations and challenges of the nonlocal extension of the FMM as a generalization of the standard method in the local response approxmiation (LRA).

Within the framework of the hydrodynamic model, we observe significant changes with respect to the commonly employed local response approximation, but also in comparison with homogeneous metal films where nonlocal effects have previously been considered [75]. Notably are the emergence of a contribution from nonlocality at normal incidence and the surprisingly large structural parameters at which finite blueshifts are observed, which we attribute to diffraction that offers non-vanishing in-plane wave vector components and increases the penetration depth of longitudinal nonlocal modes.

One of the main differences to the local case discussed in section 1.2 is the coupling to an additional wave equation for the free conduction band electrons. Similarly to the electromagnetic wave equation, it has to be expanded into higher diffraction orders and formulated as an eigen value equation. This will be demonstrated in detail in the next section. Hence, not only the permittivity $\varepsilon_D(\omega, \mathbf{r})$, but also further material parameters such as the strength of the nonlocal interaction $\beta$ and the plasma frequency $\omega_p$ are modulated across the two-dimensional crystal. All those parameters are typically step functions in real space when neglecting the electron spill-out and the respective Fourier transforms are analytical for many geometries, see appendix A.

We study the impact of spatial dispersion on promising building blocks for photonic circuits. Our aim is to investigate the influence of spatial dispersion in metal components of two-dimensional plasmonic crystals and to increase the understanding of the underlying physical phenomena and investigate the limiting regimes of structural parameters towards the LRA at the nanoscale. While we focus our discussion on holey metal films, the presented theoretical framework is applicable to any type of periodic gratings in one and two dimensions.

### 3.1.1 Infinite nonlocal Plasmonic Crystals

The additional wave equation for the nonlocal longitudinal modes is scalar in terms of the induced charge density $\rho^{\mathrm{ind}}$. The dimension of the related vectors in reciprocal space is, thus, reduced with respect to the local problem and the increase in computational effort is moderate. As for the local problem, eigenvalues and modes from the infinite crystal are used in the scattering matrix technique to describe the case of a plasmonic crystal slab of finite thickness between two homogeneous semi-infinite dielectric regions, see inset in Fig. 3.1(a). In this specific setup (IMI – insulator-metal-insulator), the complexity of the original local problem can be maintained and with it the iterative steps in propagating the scattering matrix. However, the field expressions and boundary conditions – extended by an additional boundary condition stemming from Navier–Stokes equation – become more involved leading to complex expressions for the interface matrices.

As the nonlocal contributions are pressure-like waves of longitudinal character, they only add to the electric field, but leave the magnetic field unchanged [53,74], i. e. $\mathbf{e}_{\parallel} = (-e_y, e_x)^T = \mathbf{e}_{\parallel 0} + \mathbf{e}_{\parallel \mathrm{nl}}$, $\mathbf{h}_{\parallel} \equiv \mathbf{h}_{\parallel 0}$. The nonlocal wave equation is, thus, independent from the local contributions and results from the divergence of the induced current density $\mathbf{j}^{\mathrm{ind}}$, eq. (2.2), where the continuity equation $i\omega\rho^{\mathrm{ind}} = \nabla\mathbf{j}^{\mathrm{ind}}$ is used. After introducing the plane-wave expansion (PWE), we obtain the eigenvalue equation

$$q_z^2\hat{\rho} = \left((\hat{\beta}^2)^{-1}\omega(\omega + i\hat{\gamma}_p)\hat{\varepsilon}_\perp\hat{\varepsilon}_b^{-1} - \hat{k}_x\hat{k}_x - \hat{k}_y\hat{k}_y\right)\hat{\rho}. \tag{3.1}$$

From Eqs. (2.3) and (2.2) we find the relevant matrix for nonlocal contributions [73,75]

$$N_{00} \equiv -i\left[\hat{\varepsilon}_\perp\omega(\omega + i\hat{\gamma}_p)\right]^{-1}\hat{\beta}^2\begin{pmatrix} -\hat{k}_y \\ \hat{k}_x \end{pmatrix}\hat{\rho}. \tag{3.2}$$

Both expressions – $M_{00}$ from the local boundary conditions and $N_{00}$ for the nonlocal contributions – are key ingredients to compute the optical properties of the finite crystal slab. The expression $N_{00}$ shows that – for vanishing parallel momentum $k_{\parallel} = 0$ – a homogeneous metal film does not support this type of pressure waves, but a nanostructured surface allowing for multiple diffraction orders still results in $\hat{k}_x \neq 0, \hat{k}_y \neq 0$ and is able to sustain such modes even for light at normal incidence. This is a striking difference to previous results for nonlocal, but homogeneous thin films [26,33].

### 3.1.2 Optical Properties of the finite Crystal

The fields are in each layer expanded as

$$\rho_l = \hat{\rho}_l(f_{ql}(z)\mathbf{a}_{l,\mathrm{nl}} + f_{ql}(d-z)\mathbf{b}_{l,\mathrm{nl}}), \tag{3.3}$$

where $\hat{\rho}_l$ are the matrices containing the (nonlocal) charge density eigenvectors obtained in the previous section. The diagonal matrices $f_{ql}(z)_{nn'} = \delta_{nn'}\exp(iq_{l,zn}z)$ are propagators composed of the respective eigenvalues $q_{l,zn}$ and $\mathbf{a}_{l,\mathrm{nl}}, \mathbf{b}_{l,\mathrm{nl}}$ are the nonlocal forward and backward scattering coefficients within each region.

Transversal and longitudinal fields are summed up

$$\begin{pmatrix}\mathbf{e}_{\parallel,l}\\ \mathbf{h}_{\parallel,l}\end{pmatrix} = \mathcal{M}_l\begin{pmatrix}f_{kl}(z)a_l\\ f_{kl}(d-z)b_l\end{pmatrix} + \mathcal{N}_l\begin{pmatrix}f_{ql}(z)a_{l,\mathrm{nl}}\\ f_{ql}(d-z)b_{l,\mathrm{nl}}\end{pmatrix}, \qquad \mathcal{N}_l = \begin{pmatrix}N_{00} & N_{00}\\ 0 & 0\end{pmatrix}. \tag{3.4}$$

A full solution without further restrictions requires $4\times 4$ block matrices and two additional boundary conditions for the induced charge and current to be continuous in order to solve for the four unknowns involved here. However, we can strongly simplify the calculation when we evoke the additional boundary condition first. This poses a few limitations to our approach, mainly that we restrict ourselves to metallic nanostructures in between dielectric layers. This procedure and the widely analytic solution to the additional boundary condition are discussed in the next section. Anticipating the results, we will be able to rewrite

$$\begin{pmatrix}\mathbf{e}_{\parallel,l}\\ \mathbf{h}_{\parallel,l}\end{pmatrix} = \mathcal{M}_l^\star\begin{pmatrix}f_{kl}(z)a_l\\ f_{kl}(d-z)b_l\end{pmatrix} \tag{3.5}$$

with an extended matrix $\mathcal{M}_l^\star$. This allows maintaining the scattering matrix scheme on extracting $f_{kl}(z)$ and $f_{kl}(d-z)$ from the parameters found, as discussed in section 3.1.4, and we can still find an analytic inverse for $\mathcal{M}_l^\star$. This together with reducing the problem to the original matrix equations of $2\times 2$ block matrices leads to a moderate increase in computational effort in contrast to a waste increase in computational demand for the full problem of $4\times 4$ block matrices. This latter case, however, would have to be solved for nonlocal metal-metal interfaces.

### 3.1.3 Additional Boundary Condition

Treating the free conduction band electrons with the linearized hydrodynamic equation makes it necessary to consider an Additional Boundary Condition (ABC) [26, 53, 168, 184, 200, 201]. The component along the surface normal of the induced current density should vanish $\hat{\mathbf{n}}\cdot\mathbf{j}^{\mathrm{ind}} \equiv 0$ at the crystal slab interfaces when both neighboring layers are dielectric, i. e. local, and a trespassing of the electron current is prohibited in the limit of an exceedingly high work function of the metal. It should be noted that this assumption neglects the impact of the electron spill-out relevant to metals with more modest work functions [33, 174, 175, 202] and does not allow for neighboring metal layers.

While this step introduces a non-iterative aspect into the layer-by-layer solution of the scattering matrix approach [64], it reduces the computational effort enormously, since we can solve the ABC inside the crystal layer independently from electronic properties of neighboring layers. We show in this section that we can maintain the dimensionality of the original problem with this limitation, instead of solving a system of four unknowns (local and nonlocal forward and backward scattering amplitudes) which would make an extension of the scattering matrix approach to $4 \times 4$ matrices of block matrices necessary in each iteration step immensely increasing computational demand.

We start from Eq. (2.2) using Eq. (3.2) with $0 = \hat{\mathbf{n}} \cdot \mathbf{j}^{\mathrm{ind}} = j_z^{\mathrm{ind}}$

$$0 = \omega_p^2 e_z - \beta^2 \partial_z \rho^{\mathrm{ind}} = \omega_p^2 e_z^0 - \frac{\varepsilon_b}{\varepsilon_\perp} \beta^2 \partial_z \rho^{\mathrm{ind}}. \tag{3.6}$$

Note that we omit the layer index $l$ for clarity, all material parameters and field amplitudes relate to the central plasmonic crystal layer in the considered IMI structure. Inserting the $e_z^0$ component and expanding into the field amplitudes Eq. (3.3), we summarize material parameters in the matrix

$$\mathcal{L} = i(\hat{\rho})^{-1} \frac{1}{q_z} (\hat{\beta}^2)^{-1} \frac{\hat{\varepsilon}_\perp}{\hat{\varepsilon}_b} \frac{\hat{\omega}_p^2}{k} \frac{1}{\hat{\varepsilon}_\perp} \begin{pmatrix} -\hat{k}_y & \hat{k}_x \end{pmatrix} \Phi, \tag{3.7}$$

and can write the ABC in a compact way

$$\mathcal{L}(f_k(z)\mathbf{a} + f_k(d-z)\mathbf{b}) = f_q(z)\mathbf{a}_{\mathrm{nl}} - f_q(d-z)\mathbf{b}_{\mathrm{nl}}.$$

We evaluate this for the two interfaces $z = 0$ and $z = d$ and abbreviate $f_\xi = f_\xi(d)$

$$\mathcal{L}(\mathbf{a} + f_k \mathbf{b}) = \mathbf{a}_{\mathrm{nl}} - f_q \mathbf{b}_{\mathrm{nl}}, \tag{3.8a}$$
$$\mathcal{L}(f_k \mathbf{a} + \mathbf{b}) = f_q \mathbf{a}_{\mathrm{nl}} - \mathbf{b}_{\mathrm{nl}}, \tag{3.8b}$$

from which we can work out

$$[I_N - f_q f_q]\mathbf{a}_{\mathrm{nl}} = (\mathcal{L} - f_q \mathcal{L} f_k)\mathbf{a} + (\mathcal{L} f_k - f_q \mathcal{L})\mathbf{b}, \tag{3.9a}$$
$$[I_N - f_q f_q]\mathbf{b}_{\mathrm{nl}} = (f_q \mathcal{L} - \mathcal{L} f_k)\mathbf{a} + (f_q \mathcal{L} f_k - \mathcal{L})\mathbf{b}. \tag{3.9b}$$

In the next step, the interface matrix needs to be adjusted to include the additional terms.

### 3.1.4 Interface Matrix in nonlocal Case

The extended interface matrix $\mathcal{M}_l^\star$ can be built by using Eqs. (3.9) in Eq. (3.4) which yields the general, z-dependent expressions

$$\begin{aligned} M_{l,00}^\star = &\quad M_{00} + N_{00}[I_N - f_q f_q]^{-1}(f_q(z)(\mathcal{L} - f_q \mathcal{L} f_k) + f_q(d-z)(f_q \mathcal{L} - \mathcal{L} f_k)) f_k(z)^{-1}, \\ M_{l,01}^\star = &-M_{00} + N_{00}[I_N - f_q f_q]^{-1}(f_q(z)(\mathcal{L} f_k - f_q \mathcal{L}) + f_q(d-z)(f_q \mathcal{L} f_k - \mathcal{L})) f_k(d-z)^{-1}. \end{aligned}$$

Two cases can occur: Is the nonlocal crystal layer the next $l+1$ layer, we simply find

$$I^{l,l+1} = \mathcal{M}_l{}^{-1}\mathcal{M}^{\star}_{l+1} = I^{l,l+1}_{\mathrm{loc}} + \frac{1}{2}M_{00}^{-1}N_{00}\begin{pmatrix}\chi & \xi\\ -\chi & -\xi\end{pmatrix} \tag{3.10}$$

with the parameters

$$\chi = [I_N - f_q f_q]^{-1}([I_N + f_q f_q]\mathcal{L} - 2f_q\mathcal{L}f_k), \tag{3.11}$$
$$\xi = [I_N - f_q f_q]^{-1}([I_N + f_q f_q]\mathcal{L} - 2f_q\mathcal{L}f_k^{-1}). \tag{3.12}$$

When the nonlocal layer is the current layer $l$, the inverse of the extended matrix is needed. Due to our simplified approach of having the metal crystal layer between dielectric layers, this inverse is analytic

$$(\mathcal{M}^{\star}_l)^{-1} = \begin{pmatrix}(\nu)^{-1} & (\nu)^{-1}\mu\Phi_l^{-1}\\ -(\nu)^{-1} & (I_N - (\nu)^{-1}\mu)\Phi_l^{-1}\end{pmatrix}, \tag{3.13}$$

where $\nu = 2(M_{00} - N_{00}(\chi+\xi)/2)$, $\mu = M_{00} - N_{00}\chi$ and the interface matrix becomes

$$(\mathcal{M}^{\star}_l)^{-1}\mathcal{M}_{l+1} = (\nu)^{-1}M'_{l+1,00}\begin{pmatrix}1 & -1\\ -1 & 1\end{pmatrix} + \Phi_l^{-1}\Phi'_{l+1}\begin{pmatrix}(\nu)^{-1}\mu & (\nu)^{-1}\mu\\ (I_N - (\nu)^{-1}\mu) & (I_N - (\nu)^{-1}\mu)\end{pmatrix}. \tag{3.14}$$

It should be noted, that in the homogeneous case $N_{00}\mathcal{L} = \frac{k_{z\perp}}{k\varepsilon_\perp}\frac{k_\parallel^2}{qk_{z\perp}}\left(1 - \frac{\varepsilon_\perp}{\varepsilon_b}\right) \equiv \frac{k_{z1}}{k\varepsilon_\perp}g$ as found previously [26] for nonlocal Fresnel coefficients.

## 3.2 Diffraction Anomalies in two-dimensional Plasmonic Crystals

We observe significant changes with respect to the local response approxmiation (LRA), but also in comparison with homogeneous metal films where nonlocal effects have been considered [26, 33, 203]. The most striking observations are the emergence of a contribution from spatial dispersion at normal incidence and the surprisingly large structural parameters at which small, but finite blueshifts of resonances in the optical response are observable when compared to the spectral position predicted in the LRA [52]. The former can be attributed to the diffraction the incoming light experiences due to the space modulated crystal structure, which provides contributions from higher parallel momenta via $\mathbf{k}_\parallel^{\mathbf{G}} = \mathbf{k}_\parallel + \mathbf{G} = (k_x + {}^{2\pi}/_a\, n)\hat{\mathbf{x}} + (k_y + {}^{2\pi}/_a\, m)\hat{\mathbf{y}}$ in the plane-wave expansion. Hereby, reciprocal lattice vectors $\mathbf{G}$ define the diffraction order through integers $n, m$. The latter effect can be seen as an interplay of a larger number of geometrical parameters relevant in a crystal that do not play any role in homogeneous films: not only film thickness, but also hole (or particle) size and lattice period become important. Moreover, when considering metal films with dielectric holes, larger holes provide narrow metal bridges or constrictions between different unit cells. From

these results, a remarkable impact on high-Q sensing applications, quantum dot emitters, molecular decay rates and absorption spectra in large area nanostructured materials is anticipated. A nonlocal methodology for 2D PICs can give a full account on the impact of nonlocal response for important concepts and applications in photonics, such as particle array enhanced spectroscopic methods [53, 69, 197, 198, 204–208] and transmission through holey metal films. We show that additional pressure waves induced by the electron oscillation lead to a change in the band structure and electromagnetic fields supported by a plasmonic crystal. This has previously been shown in 1D hyperbolic metamaterials and slit arrays [201, 209–211] and in 2D periodic particle arrays exploiting the nonlocal polarizability of single particles [212].

The inset in Fig. 3.1(a) depicts the setup of the finite plasmonic crystal – here a holey gold film. In Fig. 3.1(b) and (c) we compare the developed theory in the homogeneous limit (vanishing hole size $r \to 0$) with analytic theory [26] for two cases of parallel momentum that result in local response in (b) and nonlocal response in (c). Note that for the homogeneous film the power flux of the incoming light vanishes for excitation with an evanescent source in Fig. 3.1(c), where coupling to higher diffraction orders is not possible, so that we compare the resulting reflection and transmission coefficients directly. Comparing to previous theoretical results on plasmonic crystals, Refs. [69, 197], Fig. 3.1(a) reveals that these earlier studies are within the local-response regime as both local and nonlocal descriptions coincide. However, on decreasing the film thickness in the otherwise unchanged setup from $t = 250\,\text{nm}$ to $t = 150\,\text{nm}$ and $t = 100\,\text{nm}$, we begin to observe differences in the spectra. Those are in agreement with previous findings on nonlocal interaction, that is, we observe a blueshift in the transmission peak (and reflection dip) positions as well as a reduction of the peak magnitudes (increase in the dips, resp.). Most strikingly, we consider light at normal incidence which in the case of a homogeneous film always results in a suppression of longitudinal waves that need a finite value in the parallel momentum to emerge, cp. Fig. 3.1(b).

The crystal structure does provide modes of higher order with finite in-plane components in the wave vector through $\mathbf{G}$ which become larger for smaller $a$ and we expect an increasing influence on decreasing the distance between the air holes. This is seen in Fig. 3.2. The stable mode A is the usual surface plasmon polariton present at the front surface of a homogeneous metal film. The observed blueshift of the modes B and C with respect to the spectral position predicted in the LRA increases on decreasing the hole-hole separation, while both theories converge for larger hole distances. The geometry of the two-dimensional crystal allows switching its properties from local to nonlocal through further parameters as in the simple case of homogeneous layers. Interestingly, decreasing the hole size does yield the homogeneous film limit for vanishing hole sizes, so that indeed larger dielectric holes result in a stronger nonlocal response. For a hole radius close to the maximum of $r = 0.5a$ thin metal bridges are left between the neighboring holes and we conclude that strong nonlocal effects in holey metal films stem thus from fields scattered at the edges of the dielectric holes and longitudinal fields arising in thin metal walls confined by these holes. The film thickness plays

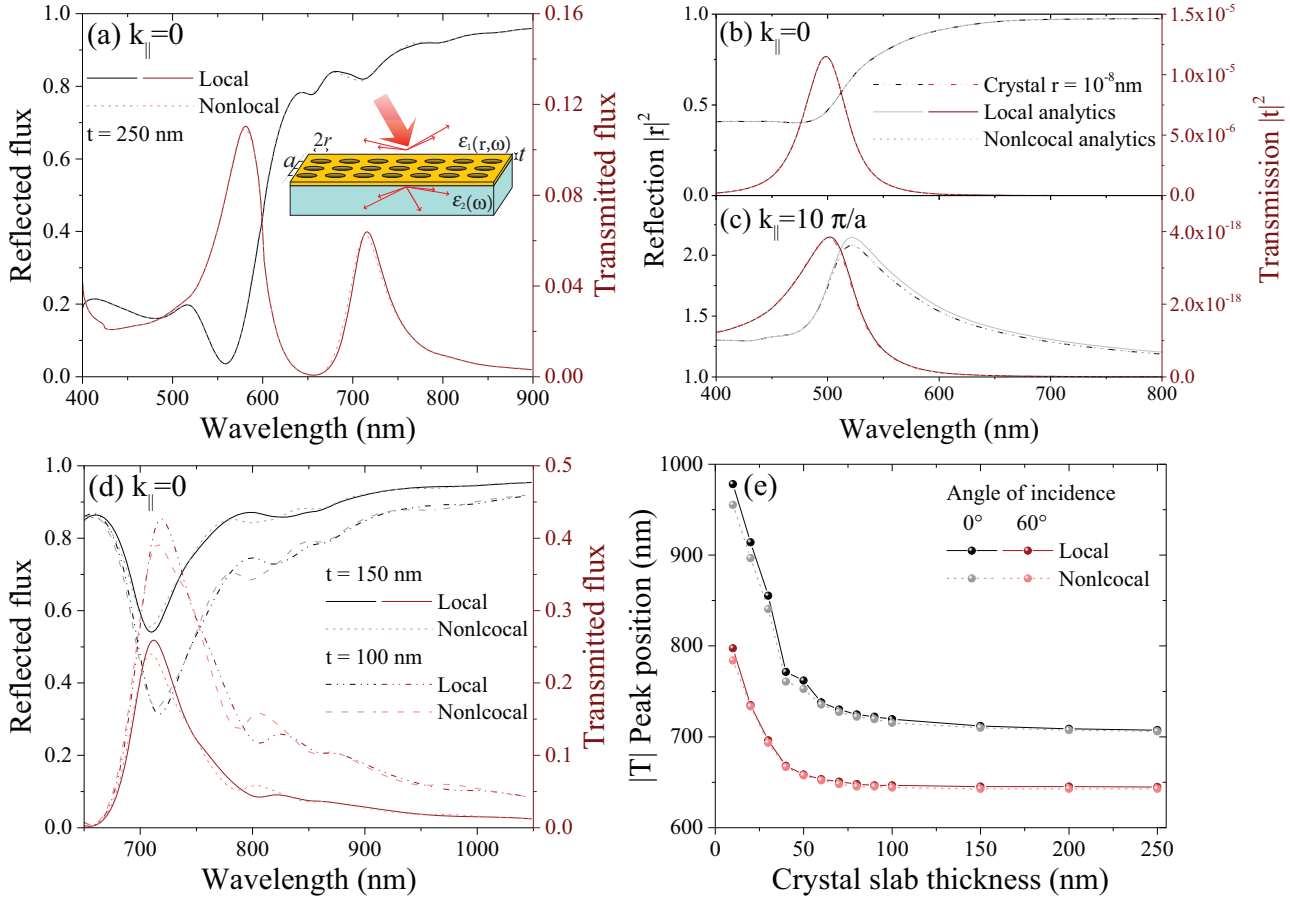


Fig. 3.1.: (a) A holey metal film with thickness $t$ of space-modulated, frequency dependent permittivity $\varepsilon_1$ (using bulk gold properties from tabulated experimental data) is investigated, see inset. The lattice constant is $a$ and separates air holes of radius $r$. A substrate with $\varepsilon_2$ supports the structure. The local crystal limit, see Refs. [69, 197], with $a = 400\,\text{nm}$, $r = 114.5\,\text{nm}$, $t = 250\,\text{nm}$ and $\varepsilon_2 = 2.25$ is shown. At this film thickness, no nonlocal response is noted. (b), (c) For a symmetric environment ($\varepsilon_1 = \varepsilon_2 = 1$) the homogeneous film limit ($r \to 0$) is demonstrated, see Ref. [26]. (b) At vanishing parallel momentum local and nonlocal theories coincide (no longitudinal waves supported in a homogeneous film at $k_\parallel = 0$). (c) For high enough parallel momentum, the homogeneous film shows nonlocal optical response. (d) Reducing the film thickness to $t = 150\,\text{nm}$ and $t = 100\,\text{nm}$ reveals resonance shifts and reduced intensities in the optical response induced by nonlocal effects in the crystal structure. (e) The film thickness is varied for two angles of incidence and the position of the lowest order transmittance peak is shown. Sizable resonance shifts are found for $t \leq 50\,\text{nm}$.

a similar role as for homogeneous nonlocal films, i. e. the thinner the nanostructured layer the stronger the observed resonance shifts as shown in Fig. 3.1(d) and (e).

Let us consider the analytic limit of a homogeneous metal film, where Eq. (1.22) reduces to $k_z = \sqrt{(\omega/c)^2\epsilon_\perp - k_\parallel^2}$, while the nonlocal wave number Eq.3.1 becomes $q_z = \sqrt{\epsilon_\perp/(\beta^2\epsilon_b)\omega(\omega+i\gamma) - k_\parallel^2}$. Assuming vanishing parallel momentum and damping, as well as for the sake of argument a Au metal film described by a Drude model with constant $\epsilon_b = 9$, the remaining values allow a direct comparison to the expected analytic value through $\sqrt{(c/\beta)^2/\epsilon_b} \approx 90$. The local and nonlocal wave numbers differ by a large factor in quantity

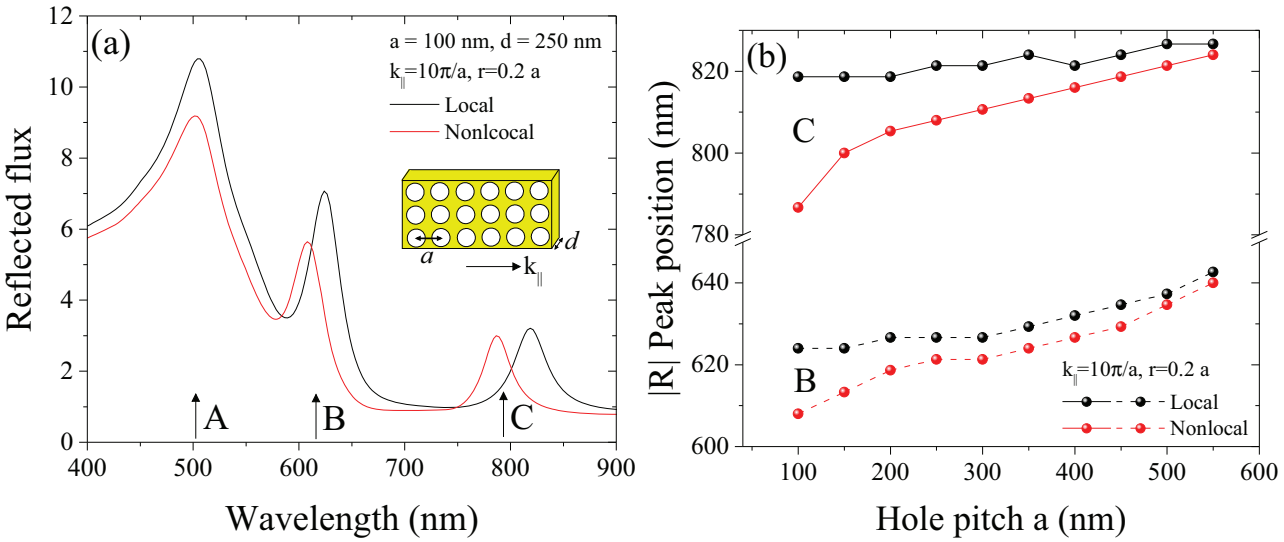


Fig. 3.2.: (a) Reflection and (b) shift in peak positions as a function of hole separation for local and nonlocal plasmonic crystals using $k_{\|} = 10\pi/a, r = 0.2a, t = 250\,\text{nm}$ and in (a) for constant $a = 100\,\text{nm}$ for experimental data of gold. The reflected modes B and C are strongly impacted in the nonlocal theory at this high parallel momentum.

which means that the wavelength of the associated induced nonlocal electric field is much smaller than the wavelength of the transversal solutions [52].

To conclude, for a plasmonic crystal placed in a dielectric environment, an extension of an existing rigorous plane-wave method accounting for nonlocal response in the metal components of the crystal wad achieved that maintains the complexity of the original problem. Hereby, the additional boundary condition stemming from the hydrodynamic equation for the free electron gas was exploited in an analytic way. An additional, but scalar eigenvalue equation has to be solved, and the interface matrices used in the layer-by-layer propagation (scattering matrix theory) become more involved. It was demonstrated that nonlocal response plays a role already at normal incidence for nanostructured metal films whereby diffraction plays a major role in offering in-plane components in the wave vector not present in the incoming wave. Furthermore, a number of geometrical parameters influences the impact of nonlocality in these systems: (i) decreasing film thickness and (ii) increasing hole size in accordance to what can be expected from homogeneous films, as well as (iii) decreasing hole separation and (iv) thin metal walls confined between dielectric holes. We expect that our findings will stimulate additional studies of plasmonic crystals when taking into consideration nonlocal effects in holey films of experimentally accessible parameters in two-dimensional hole arrays.

## 3.3 Extraordinary Optical Transmission

Light transmitted through tiny apertures can be significantly enhanced thanks to the excitation of surface plasmons at the patterend structure. [192] The ability to efficiently squeeze light through a metal film with an array of holes smaller than the wavelength of the incoming

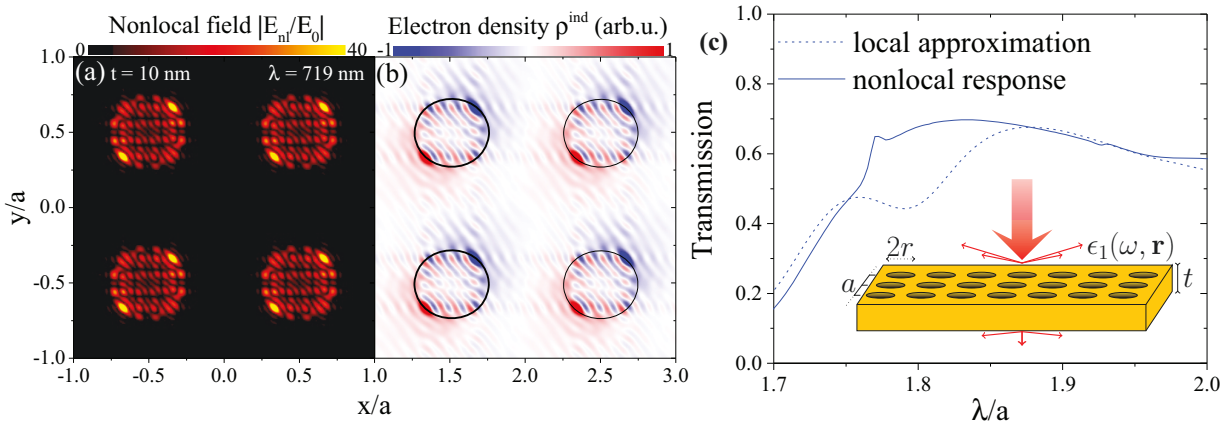


Fig. 3.3.: (a) Contribution of the nonlocal mode ($D = 0$) to the electric field $E_{\mathrm{nl}}$ at the front surface for a holey gold film with lattice constant $a = 200\,\mathrm{nm}$, radius $r = 0.25a$ and $t = 10\,\mathrm{nm}$ at resonance frequency $\lambda = 719\,\mathrm{nm}$. (b) Induced charge density for this case. Note that $k_x = k_y = 10^{-4}2\pi/a \approx 1.5 \times 10^{-6}/\,\mathrm{nm}$. (c) Transmittance at normal incidence comparing the common local response approximation (dashed) with the generalized nonlocal optical response (GNOR, solid). The film of thickness $t = 20\,\mathrm{nm}$ is comprised of a square array of circular air holes with radius $r = 100\,\mathrm{nm}$ and period $a = 400\,\mathrm{nm}$ as illustrated in the inset.

light has fascinated and inspired science and technology for two decades [58, 69, 190, 191, 198, 213–217]. The resonance of this phenomena is strongly influenced by the environment including the presence of molecules which makes label-free biosensing [218] an important application for hole arrays. The advantages lie in the straightforward optical detection at normal incidence, integration in microfluidic devices, [219] and miniaturization allowing a small sensor size and on-chip, multiplexing technology with high sensitivity and low detection limits [220]. Advancing the rich palette of applications and unravelling novel physics requires progress in the electromagnetic treatment of holey metal films. When the conduction band electrons in metals are strongly confined their quantum nature becomes important.

In this section, we investigate implications of nonlocal electron dynamics on the Extraordinary Optical Transmission (EOT) in holey gold films as illustrated in Fig. 3.3 based on the generalized hydrodynamic approach including electron diffusion. Beyond the familiar resonance blueshift with decreasing film thickness, the complex interference of longitudinal pressure waves in the holey structure generates an unexpected oscillatory response with geometrical parameters. An increase in the transmittance relative to the local result of up to 33% was observed, but it can also be suppressed when absorption dominates.

Fig. 3.3(a) shows an example for the distribution of the nonlocal field (inside the holey metal film, underneath the front surface) at the resonance wavelength of the nonlocal response using the standard hydrodynamic model ($D = 0, \lambda = 719\,\mathrm{nm}$). A strong dipolar mode is observed in the corresponding induced charge density $\rho^{\mathrm{ind}}$, see Fig. 3.3(b). Note that the finite number of modes included in this calculation (restricted to $N = 529$ plane waves) yields a real-space contribution to the Fourier transform even inside the metal. Note that the number of plane waves used ($N^2$) ranges from $N = 23$ ($N^2 = 529$) for the near-field plots at a specific wavelength to typically $N = 31$ ($N^2 = 961$) for the calculated spectra. The convergence was

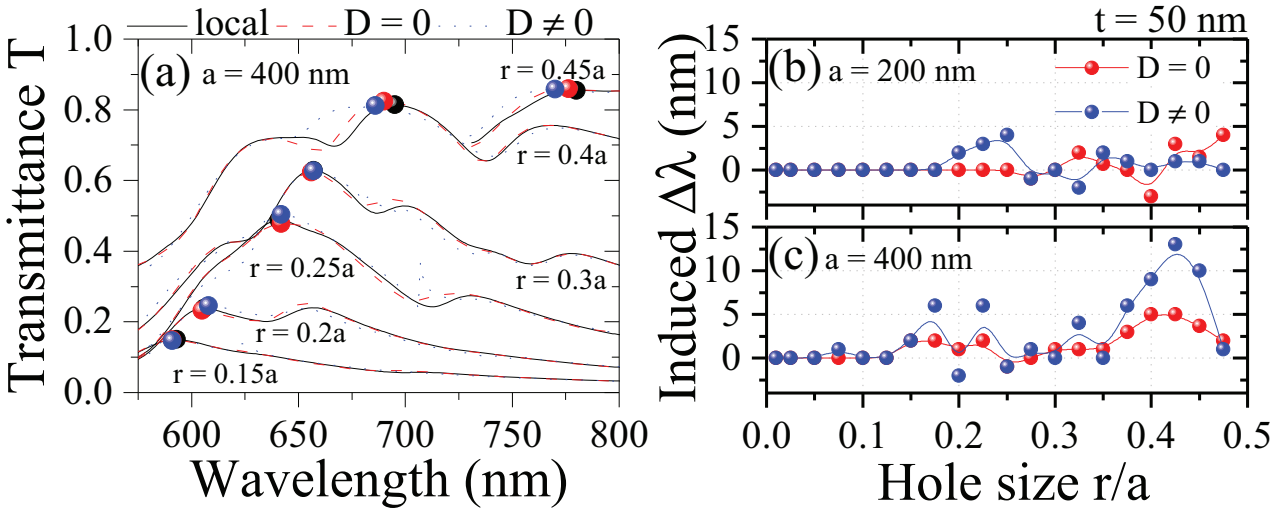


Fig. 3.4.: Comparing the transmittance spectra with varying hole radius $r/a$ for classical local calculations with the nonlocal optical response of the standard hydrodynamic model (diffusion constant $D = 0$) and GNOR ($D = v_F^2/\gamma_p$) for $t = 50$ nm and (a) $a = 400$ nm. The resonance position is marked with a dot for convenience. (b), (c) The resonance shift as a function of the hole size $r/a$ is shown for a lattice period of (b) $a = 200$ nm and (c) $a = 400$ nm. The datapoints are connected by a spline to stress the observed oscillatory behavior.

checked for several spectra using up to $N = 47$ ($N^2 = 2209$).

We plot the transmission spectra of the scattering parameters in Fig. 3.3(c) where we concentrate on the optical response beyond $\lambda/a > 1$ where transmission through the sub-wavelength air holes is enhanced. The intriguing result here is the increase in the observed EOT. At the resonance position $\lambda/a = 1.83$ (shifted by 16.5 nm) the transmittivity is increased by 3%. Comparing the transmittivity at $\lambda/a = 1.8$, we observe an increase of 33% due to strong broadening. In turn the absorbance of the system is also reduced. This means that the presence of the additional longitudinal waves provides an additional efficient coupling mechanism to add up to the extraordinary transmission instead of absorbing the incoming light. The emergence (or disappearance) of absorbance peaks, as well as the observation of Fano-type resonances further indicate that nonlocal optical response in holey metal films goes beyond the typically observed resonance shifts and plasmon broadening. Additional resonances in the optical response contrasting the predictions in the LRA might be a route to verify the presence of nonlocal modes in large-scale, two-dimensional systems.

We emphasize that increasing the lattice period (while scaling the radius as $r/a$) enhances the impact of nonlocal effects due to reducing the lowest order reciprocal vector $|\mathbf{G}_{10}| = {}^{2\pi}/_{a}$. Diffraction becomes more important where the wavelength $\lambda$ ($k = {}^{2\pi}/_{\lambda}$) is of the same magnitude as the structural parameter $a$.

In order to maintain a high impact of anomalous diffraction, the hole radius needs to be relatively large, which we study in Fig. 3.4. Again, a blueshift of the transmittance as well as a broadening is observed in the spectra in Fig. 3.4(a) when increasing the size of the air holes. A closer look at Figs. 3.4(b) and (c) reveals that, as could be expected, the GNOR approach

yields stronger blueshifts of the main transmittance peak and overall impacts the optical response of the metal holey film at structural parameters closer to the local limit. Interestingly, both nonlocal theories exhibit an oscillatory behavior on decreasing the hole size. This indicates, that the longitudinal, nonlocal mode excited in the crystal structure is subject to interference effects that allow canceling the observed phenomena arising from additional electron dynamics. We believe this can be understood with the formation of standing waves in metal bridges between air holes.

Next, we study how nonlocality influences the transmittance. We consider several values for the electron diffusion constant from the standard hydrodynamic model ($D = 0$) to the bulk model ($D = v_F^2/\gamma_p$) in Fig. 3.5(a) and compare the relative change in the transmittance calculated as $(1 - T_{\mathrm{loc}}/T_{\mathrm{nl}})$ in %. All cases of the nonlocal strength parameter behave similarly. However, it is surprising that both a reduction and an increase in the transmittance is observed, here as a function of the film thickness, with very steep transitions between these cases. This relative change in transmittance lies between $-4\%$ and $+6\%$ in the considered cases compared to the classical local result and increases e. g. when the lattice period is further increased. Figs. 3.5(b) and (c) show how the increase or decrease of the transmittance translates into an influence on both the reflectance and absorbance for two selected cases. In Fig. 3.5(b) the increase in transmittance–together with the appearance of an additional resonance–in the nonlocal case is accompanied by a reduction in both reflection on the front surface and absorbance, thus leading to an efficient transmittance through the $t = 10$ nm thick film. In addition, a pronounced absorption peak appears at a larger wavelength leading to the strong reduction in transmittance between the also classically observed resonances.

On the other hand, the transmittance is reduced in the $t = 20$ nm thick slab in Fig. 3.5(c) due to reflection at a resonant front surface mode which in turn reduces the share absorbed inside the film. It is such additional reflective or absorptive modes that might allow for experimental verification of the described effects. Increasing the parallel momentum of the incoming light enhances the impact of nonlocal phenomena [52]. However, varying the angle of incidence between $k_\parallel = 0$ $(0°)$ and $k_\parallel = \pm\pi/a$ $(90°)$, i. e. within the first Brillouin zone, does not dramatically increase the parallel momentum and does therefore not alter the observations significantly [176].

To summarize, we studied the impact of nonlocal, longitudinal electron waves on the optical properties on EOT phenomena. We discussed the electron diffusion added in the GNOR theory which leads to an effectively complex $\beta$-parameter. This results in stronger induced shifts (real part) and an increased broadening (imaginary part) of the considered resonances. We demonstrated up to $\pm 6\%$ relative change in transmittance compared to the local result at the resonance position and an increase of 33% under off-resonant conditions; other geometries might yield stronger modulations. This nonlocal increase in the linewidth of plasmon resonances limits the figure of merit (FOM) in nanoplasmonic sensors based on thin metal films patterned with hole arrays.

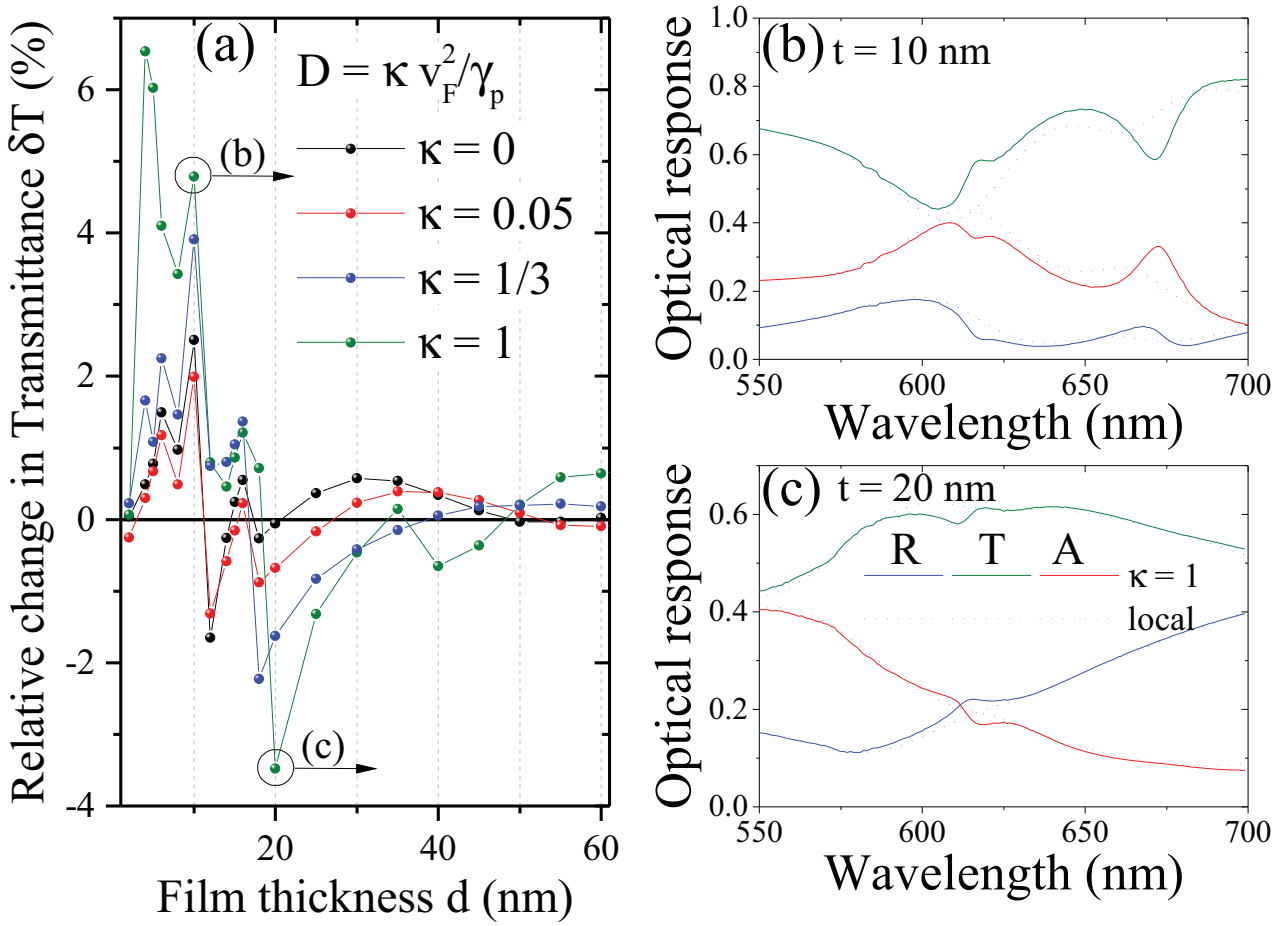


Fig. 3.5.: (a) Change in transmittance with film thickness for different diffusion constants $D = \kappa v_F^2/\gamma_p$, lattice period $a = 200\,\text{nm}$, hole size $r = 0.25a$. (b), (c) spectra corresponding to the geometries marked with a circle in (a) for (b) $t = 10\,\text{nm}$ and (c) $t = 20\,\text{nm}$.

# 4. Nonlocality in Nanoparticles

Nanoparticles–regularly patterned or randomly dispersed–are a key ingredient for emerging technologies in photonics. Of particular interest are scattering and field enhancement effects of metal nanoparticles and transition metal nitrides for energy harvesting and converting systems. An often neglected aspect in the modeling of nanoparticles are light interaction effects at the ultimate nanoscale that cannot be captured within classical electrodynamics. Those arise from microscopic electron dynamics in confined systems, the accelerated motion in the plasmon oscillation and the quantum nature of the free electron gas in metals, as discussed in the previous chapters. We give a detailed account on free electron phenomena in metal nanoparticles and discuss analytic expressions stemming from microscopic (RPA) and semiclassical (GNOR) theories. These can be incorporated into standard computational schemes to produce more reliable results on the optical properties of metal nanoparticles. We combine these solutions into a single framework and study their joint impact on isolated nanoparticles and dimer structures in section 4.2.1, and consider strong coupling of nanoparticle arrays with a semiconducting substrate in section 4.2.2. The spectral position of the plasmon resonance and its broadening as well as local field enhancement show an intriguing dependence on the particle size due to the relevance of additional damping channels. Moreover, including strong coupling effects with the substrate, we observe a mode splitting induced by nonlocal effects.

## 4.1 Spherical Geometries in the Hydrodynamic Model

We briefly present the derivation of nonlocal Mie scattering coefficients of individual spheres and nanoshells described with the hydrodynamic model [53] starting from Eq. (2.4) which describes the evolution of the electric field, together with Eq. (2.5) which is the wave equation for the induced charge. The resulting scattering matrices can be used to investigate interacting spheres with a multiple scattering method [60]. The hydrodynamic model has no free parameters which makes the resultant nonlocal response for the short distances involved in the interaction (Coulomb force, diffusion) between the charges of MNPs the sole source of these effects, in contrast to the quantum-confinement picture for plasmon broadening presented by Kreibig.

It is convenient to use an expansion of the electric field into scalar functions [221] as

$$\mathbf{E} = (1/k)\nabla\psi^L + \mathbf{L}\psi^M + \frac{\nabla\times\mathbf{L}}{ki}\psi^E, \tag{4.1}$$

where $\mathbf{L} = -i\mathbf{r}\times\nabla$ is the classical angular momentum operator, and the superscripts $E$, $M$, and $L$ indicate electric, magnetic, and longitudinal components, respectively. The additional

boundary condition, Eq. (2.9), becomes with $\hat{\mathbf{r}} \cdot \mathbf{j} = 0$

$$\beta^2_{\mathrm{GNOR}} \frac{\partial \rho^{\mathrm{ind}}}{\partial r} = \frac{\omega_p^2}{k} \left( \frac{\partial \psi^L}{\partial r} + \frac{1}{r} l(l+1) \psi^E \right) \tag{4.2}$$

in terms of the scalar functions and the angular momentum number $l$ using the identity $-\mathbf{r} \cdot (\nabla \times \mathbf{L}) = (-i\mathbf{r} \times \nabla) \cdot \mathbf{L} = L^2 = l(l+1)$. The boundary conditions for the electric and magnetic field components result in the continuity of $\psi^M$, $(1 + r\frac{\partial}{\partial r})\psi^M$, $\psi^L + (1 + r\frac{\partial}{\partial r})\psi^E$, and $\epsilon\psi^E$ for the scalar functions [53, 162, 221].

The magnetic and electric scalar functions $\psi^\nu$ ($\nu = \{E, M\}$) obey a Helmholtz equation of the form $(\nabla^2 + k^2\epsilon_\perp)\psi^\nu = 0$ and can therefore be expanded in terms of spherical Bessel functions $\psi^\nu = \sum_L \psi^\nu_L j_L(k_\perp r)$. Similarly, the electron density is expanded into $\rho^{\mathrm{ind}}(\mathbf{r}, \omega) = \sum_L \rho_L j_L(qr)$, with the longitudinal wave vector $q$ given by Eq. (2.6). The longitudinal scalar function satisfies a different wave equation, namely $\nabla^2\psi^L = {}^{k}/_{\varepsilon_b\epsilon_0}$, which we find from the Coulomb law $\nabla\epsilon_b\mathbf{E} = {}^{\rho^{\mathrm{ind}}}/_{\epsilon_0}$.

Note that the above analysis is needed for the metal region, where the electric ($\nu = E$) and magnetic ($\nu = M$) field are given by $A^\nu_l j_L$, with $j_L = j_{lm}(k_\perp r)$ and $k_\perp = k_0\sqrt{\varepsilon_\perp}$. Outside the particle, the longitudinal scalar function vanishes since there are no induced charges in the dielectric surrounding. Therefore, the electric scalar field in the outer region is given by $j_{lm}(k_0 r) + t^\nu_l h^+_{lm}(k_0 r)$, with the corresponding spherical Bessel and Hankel functions and the related vector field from Eq. (4.1). The unknown parameters $A^\nu_l$ and the particle scattering matrix $t^\nu_l$ are found exploiting the boundary conditions stated above. We then find a set of linear equations for the magnetic and electric scattering matrices. Interestingly, the magnetic scattering matrix is unchanged with respect to the local theory, indicating that magnetic modes are not sensitive to the induced longitudinal modes. This is in agreement with findings of the previous chapter for grating structures. The scattering matrix for the electric scalar function is more complicated than in the local approximation due to the appearance of $\psi^L$ in the metal region that contains information on the nonlocal response. The additional boundary condition yields a prescription to calculate $\rho_L$.

The local scattering matrix can then be extended by a single parameter describing nonlocal behavior of the electron motion in the conduction band

$$g_l = \frac{l(l+1) j_l(\theta_\perp) j_l(qR)}{qa j_l'(qR)} \left( \frac{\epsilon_\perp}{\epsilon_b} - 1 \right) \tag{4.3}$$

and becomes with $\theta_0 = kR\sqrt{\epsilon_0}$ and $\theta_\perp = kR\sqrt{\epsilon_\perp}$

$$t^E_l = \frac{-\epsilon_\perp j_l(\theta_\perp)[\theta_0 j_l(\theta_0)]' + \epsilon_0 j_l(\theta_0)([\theta_\perp j_l(\theta_\perp)]' + g_l)}{\epsilon_\perp j_l(\theta_\perp)[\theta_0 h^+_l(\theta_0)]' - \epsilon_0 h^+_l(\theta_0)([\theta_\perp j_l(\theta_\perp)]' + g_l)}, \tag{4.4}$$

where the primes indicate differentiation with respect to the $\theta$ variables. The scattering coefficients $t^\nu_l$ fully contain the optical response of the particle for an external observer.

Note that the nonlocal parameter $g$ vanishes under the assumption of local response

($\beta_{\mathrm{GNOR}} \to 0 \Rightarrow g_l \to 0$) fully recovering the original Mie coefficients [142, 222]. This allows us to study the electro-optical properties of NPs with only a small correction in available numerical procedures.

The magnetic response is also insensitive to the nonlocal properties of the material for a nonlocal metal nanoshell. The electric part, however, mixes with the longitudinal components from the two interfaces of the metal intermediate layer. For the electric scalar functions, we obtain a linear system of six equations and analytical solutions exist for the metal nanoshell [53, 223]. For more complex systems, such as dimers and particle clusters, we use a multiple elastic scattering approach [60].

The nonlocal theory introduces a novel type of electron motion, longitudinal pressure waves, in addition to the transversal modes stemming from the classical electromagnetic wave equation. This additional electronic excitation offers further damping channels due to the energy lost in dampened motion. Here, the Mie coefficients are derived from the coupled system of optical and electronic excitation yielding modified scattering matrices that can again be implemented in existing methods. The properties of the longitudinal wave are given by the analytic expressions derived above through their wave vector and their importance with respect to the common Mie solution is entirely captured in a single additional term.

To make predictions that can be compared to experiments, the expressions obtained are used to calculate, e. g., the extinction cross section of an individual sphere via

$$\sigma_{\mathrm{ext}} = \frac{2\pi}{k^2 \epsilon_0} \sum_l (2l+1) \mathrm{Im}(t_l^E + t_l^M). \tag{4.5}$$

Note that only the electric scattering matrix is sensitive to nonlocal contributions.

### 4.1.1 Damping from Random Phase Approximation (RPA) Calculations

We compare quantum correction models stemming from microscopic RPA derivations [162, 179] yielding the following, semi-classical damping expressions

$$\gamma = \gamma_p, \qquad (\mathrm{Mie}) \tag{4.6a}$$

$$\gamma = \gamma_p + \frac{C v_F}{R}, \qquad (\mathrm{Kreibig}) \tag{4.6b}$$

$$\gamma = \gamma_p + \frac{C v_F}{R} + \frac{\omega_1}{3} \left( \frac{\omega_1 R}{c} \right)^3, \qquad (\mathrm{perturbative}) \tag{4.6c}$$

$$\gamma = \mathrm{Im}(\Omega_2) = \frac{-1}{3l} + \frac{1+6lq}{2^{\frac{2}{3}} 3l\mathcal{A}} + \frac{\mathcal{A}}{2^{\frac{1}{3}} 6l}, \qquad (\mathrm{Lorentz}). \tag{4.6d}$$

The dynamics of the electron density can be described using a driven, damped oscillator, with the incident electromagnetic wave being the driving force and the damping arising from electron scattering (from bulk $\gamma_p$ and from the surface via Kreibig damping, Eq. (4.6b)) and from electromagnetic field irradiation, the so-called Lorentz friction.

Both of the presented semi-classical approaches towards microscopic corrections in the mesoscale electron dynamics in metal nanoparticles have the advantage of analytic ex-

pressions fully compatible with existing computational procedures. The modified damping terms above can be used to directly replace the damping in a Drude expression for the permittivity given in Eq. (2.1) and subsequently be used in standard Mie calculations and procedures to calculate optical properties of complex structures, e.g., with a multiple scattering approach [60] or within commercial software such as COMSOL (`http://www.comsol.com`) which is detailed in the next sections.

**Lorentz friction**

The accelerated movement of electrons in the plasmon oscillation leads to energy loss via irradiation of the electromagnetic field, see Figure 2.1(c). In case of nanoparticles much smaller than the incident wavelength, this effect can be expressed by the Lorentz friction, an effective field stemming from the plasmon induced dipole field $\mathbf{D}(t)$ as [224]

$$\mathbf{E}_L = \frac{2}{3c^3}\frac{\partial^3 \mathbf{D}(t)}{\partial t^3}. \tag{4.7}$$

An analytical form of the exact solution for the damping $\gamma$ and self-frequency $\omega_L$ (the exponents $\Omega_i$ of solutions $\sim e^{i\Omega_i t}$ for self-modes $i$) including Lorentz friction exists [54], which is discussed in more detail in the appendix C. They can be summarized as follows

$$\begin{aligned} \Omega_1 = &\ -\tfrac{i}{3l} - \tfrac{i2^{1/3}(1+6lq)}{3l\mathcal{A}} - \tfrac{i\mathcal{A}}{2^{1/3}3l} \in \mathrm{Im}, \\ \Omega_2 = &\ -\tfrac{i}{3l} + \tfrac{i(1+i\sqrt{3})(1+6lq)}{2^{2/3}3l\mathcal{A}} + \tfrac{i(1-i\sqrt{3})\mathcal{A}}{2^{1/3}6l} = \omega_L + i\gamma, \\ \Omega_3 = &\ -\omega_L + i\gamma = -\Omega_2^*, \end{aligned} \tag{4.8}$$

where $\mathcal{A} = \left(\mathcal{B} + \sqrt{4(-1-6lq)^3 + \mathcal{B}^2}\right)^{\frac{1}{3}}$, $\mathcal{B} = 2 + 27l^2 + 18lq$, $q = \frac{1}{\tau_0\omega_1}$, $l = \frac{2}{3\sqrt{\epsilon_0}}\left(\frac{R\omega_p}{c\sqrt{3}}\right)^3$ and $1/\tau_0 = \gamma_p$. The exact inclusion of the Lorentz friction indicates that the radiative losses and the self-frequencies are a complicated function of particle radius as given by Eq. (4.8).

It is important to note that although all electrons participate in plasmon oscillations, part of their irradiation is absorbed by other electrons in the system. This is in analogy with the skin-effect [225] in metals and introduces an effective radiation active electron layer of the depth $h \sim {}^1\!/_{\sigma\omega}$ with the conductivity $\sigma$ underneath the particle surface. Therefore, the effective energy transfer outside of the nanoparticle will be reduced by the factor $\frac{4\pi}{3}\left(R^3-(R-h)^3\right)/\frac{4\pi R^3}{3}$. According to this, we expect a decrease of radiative damping, especially for larger particles.

Direct comparison to experimental work for this framework is available within Refs. [54, 55, 72, 161] and good agreement has been found. Further experimental work focussed on the blueshift found for nanoparticles decreasing in size, as well as the influence of the electron-spill out [21, 76, 143–148, 174].

### 4.1.2 Combined RPA and GNOR Approach

The hydrodynamic model can be implemented into commercial software such as COMSOL Multiphysics 5.0 (`http://www.comsol.com`). This was also achieved in Ref. [174] for two-dimensional nanowires. In order to include the nonlocal effects arising from spatial dispersion

of the dielectric function, the main equation of the COMSOL model is modified

$$\nabla \times \left( \frac{1}{\mu_0} \nabla \times \mathbf{E} \right) - k_0^2 \left( \varepsilon - j \frac{\sigma}{\omega \epsilon_0} \right) \mathbf{E} = i\omega\mu_0 \mathbf{J}(\mathbf{r}, \omega). \tag{4.9}$$

In particular, we introduce the induced current density $\mathbf{J}(\mathbf{r}, \omega)$ on the right hand side, which is obtained via coupling with the (linearized) hydrodynamic equation in the form

$$\beta^2 \nabla[\nabla \cdot \mathbf{J}(\mathbf{r}, \omega)] + \omega(\omega + i\gamma)\mathbf{J}(\mathbf{r}, \omega) = i\omega\omega_p^2 \varepsilon_0 \mathbf{E}. \tag{4.10}$$

Note that in the limit $\beta \longrightarrow 0$ this equation simplifies to Ohm's law and describes the local case.

Comsol software allows introducing an additional partial differential equation in the weak formulation, by using the interface *Weak form PDE*. The function which we integrate weakly has three components and reads for the $x$ component:

$$0 = \int \left( \beta^2 \frac{\partial \widetilde{J}_x}{\partial x} \sum_{j \in \{x,y,z\}} \frac{\partial J_j}{\partial x} - \omega(\omega - i\gamma) J_x \widetilde{J}_x - i\omega\varepsilon_0 \omega_p E_x \widetilde{J}_x \right) dL, \tag{4.11}$$

where $\widetilde{J}_x$ is the weight function. We need to define an additional boundary condition on the particle boundary $\mathbf{J} \cdot \hat{\mathbf{r}} = 0$. In our case, this is a three-dimensional modification. The analytic damping expressions Eqs. (4.6a)–(4.6d) are directly introduced as damping terms in the permittivity of the different material permittivities, Eq. (2.1).

## 4.2 Applications

### 4.2.1 Quantum Corrections in Metal Nanoparticles

We compare and combine the different processes of mesoscale electron dynamics stemming from scattering, Figure 2.1(a), (b), irradiation (Lorentz friction), Figure 2.1(c), and nonlocal interaction, Figure 2.1(d), and study their impact on the optical response of isolated MNPs and dimers. An emphasis is put on the size regimes where these effects are dominant for different materials, see Figure 4.1.

Retardation is important when either the particle radius or the overall system size becomes large, i. e., for particle dimers, clusters and arrays. Although the presented microscopic effects are highly localized, coupling of nonlocal modes within particle arrays can have a strong impact on a larger system. It is noteworthy that the hydrodynamic theory and the damping terms stemming from microscopic analysis within the RPA allow fully retarded calculations; equally for planar geometries (nonlocal Fresnel coefficients) [75] and regular, two-dimensional particle arrays [52, 53, 176] and even charge carriers in ionic systems as discussed in the next chapter in the framework of *Nonlocal Soft Plasmonics* [141].

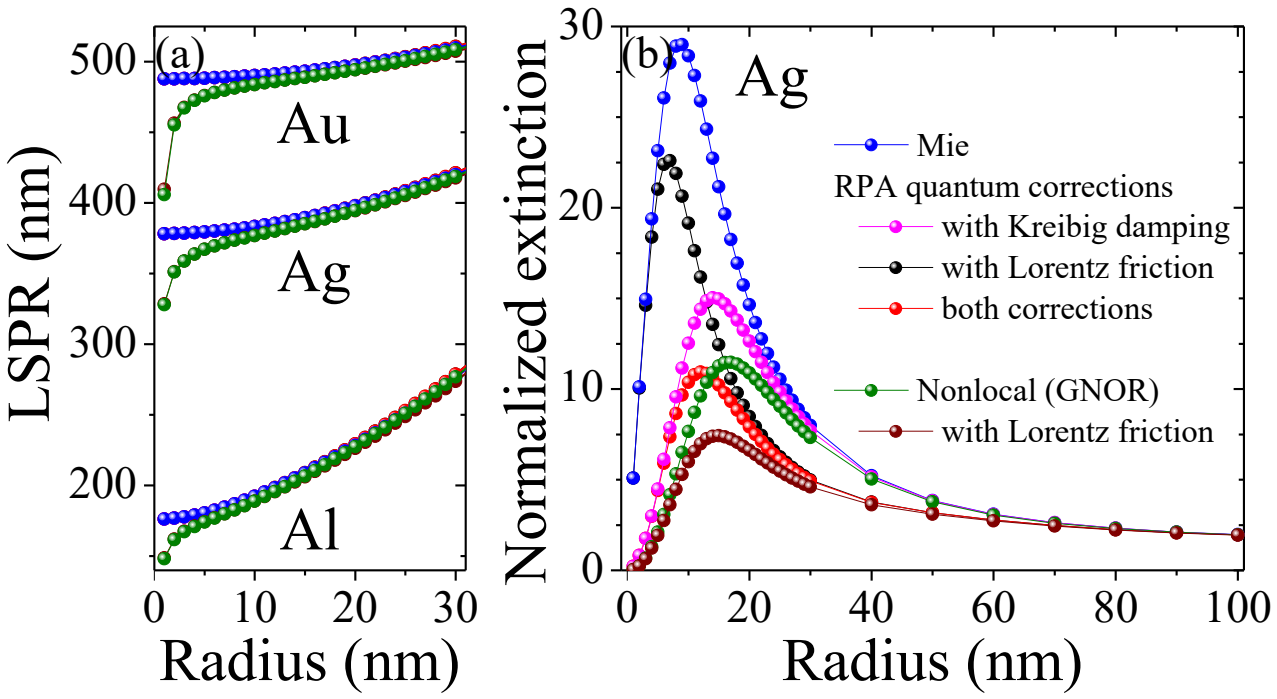


Fig. 4.1.: Impact of quantum corrections on single nanoparticles. (**a**) Spectral position of the localized surface plasmon resonance (LSPR) for gold, silver and aluminum; (**b**) Extinction cross section normalized to the surface of a hemisphere for silver evaluated at the respective LSPR wavelengths from (**a**).

#### Single Metal Nanoparticles

We compare the quantum correction models introduced in the previous sections, see Figure 2.1, as well as the combined effect of Kreibig damping Eq. (4.6b), Lorentz friction Eq. (4.6d) and spatial dispersion Eq. (4.4) to classical Mie calculations for silver in Figure 4.1. Hereby, we show the effect on the Localized Surface Plasmon Resonance (LSPR) for all materials in Figure 4.1(a), confirming that the modified damping rates do not alter the resonance position predicted by the classical calculations, whereas nonlocal response–and in combination with any damping model–does predict an increasing blueshift of the nanoparticle resonance with decreasing particle size. Looking at the extinction cross section as a function of particle radius in Figure 4.1(b) for silver, we find that all correction models result in a reduction of the optical response in dependence of the particle size. Different materials typically yield a different optimized particle size [162]. Hereby, Kreibig damping with a $\sim 1/a$ dependence drastically attenuates the optical response for the smaller size regime below the maxima (15 nm for Ag), while the complex size dependence of Lorentz friction results in a greater effect above this particle size. The diffusion coefficient in the hydrodynamic (GNOR) model (imaginary part of the nonlocal parameter $\beta_{\mathrm{GNOR}}$) is chosen thus that its damping effect captures the Kreibig result [70]. The hydrodynamic pressure (real part of the nonlocal parameter $\beta_{\mathrm{GNOR}}$) describes Coulomb interaction between electrons and results in the blueshift observed in Figure 4.1(a) at very small particle sizes below 5 nm. We can further incorporate the analytical expressions for Lorentz friction. This combined result shows the strongest attenuation since all different damping channels are included. At a larger particle

size (60 nm for Ag, 80 nm for Au, and 40 nm for Al) all material models converge with classical Mie theory where the mesoscale electron dynamics cease to have an impact.

The damping associated with the Lorentz friction can be approximated to the simpler perturbative expression Eq. (4.6c) in a narrow size window. Since the exact solution can be obtained with analytical expressions which can be incorporated into standard calculation schemes, we discuss exclusively exact Lorentz friction results. Lorentz friction is closest to the classical calculation for smaller sizes and deviates stronger at larger sizes, see Figure 4.1. The complexity of the Lorentz friction makes it necessary to restrict ourselves to the dipolar response of the plasmon oscillation. It is therefore important to consider the material, particle size and wavelength regime in order to assess whether the dipolar response model is adequate for the system under study. The dipolar approximation is valid up to ca. 100 nm in Au particle radius which in general covers the discussed microscopic effects well.

**Dimers**

For particle dimers, in addition to their size, the particle distance becomes important and retardation effects cannot be neglected for larger particles in close proximity. This can transfer the impact of localized microscopic electron dynamics onto a larger structure. Figure 4.2 shows the (maximum) field Field Enhancement Factor (EF) at the center of a gold dimer in water as a function of both particle size and distance for the different theories considered. The impact of nonlocal response, Figure 4.2(b), on the classical Mie theory, Figure 4.2(a), is visible as strong quenching of the local fields. In addition, the maximum field enhancement within the range of investigated particle and gap size is EF $\approx 9000$ for the Mie calculations and EF $\approx 3000$ for the nonlocal theory, showing that indeed there is a strong impact of the longitudinal waves. The damping observed within Kreibig theory, Figure 4.2(c), is dramatic for the dimer setup and the dominant contribution in the combined theory as seen in Figure 4.2(d). This is also evidenced by comparing the Lorentz friction with and without nonlocal damping, see Figure 4.2(e), (f), respectively. The Lorentz friction has a strong impact on the optical response for larger particle sizes, but also dampens the dimer setup for increasing gap size, which points towards retardation and the increasing structural size as the main source for this damping effect. This leads to slightly stronger damping when combined with the additional plasmon quenching within GNOR in Figure 4.2(f).

The strong field quenching poses limitations to many photonic applications, such as the photovoltaic effect in solar cells. However, considering different materials for MNPs and their environment, the size regimes where local field quenching is dominant can be avoided with the presented theory of combined sources of damping.

Pure damping models, such as the Kreibig damping and Lorentz friction, derived from microscopic RPA theory, show an intriguing dependence on the particle size, where the material influences relevant size regimes. On the other hand, semi-classical nonlocal theories allow evoking additional modes in the system by explicitly considering mesoscopic dynamics of free electrons. This results in a correction of the spectral position of resonant phenomena and introduces additional, implicit damping channels. The phenomenological Kreibig

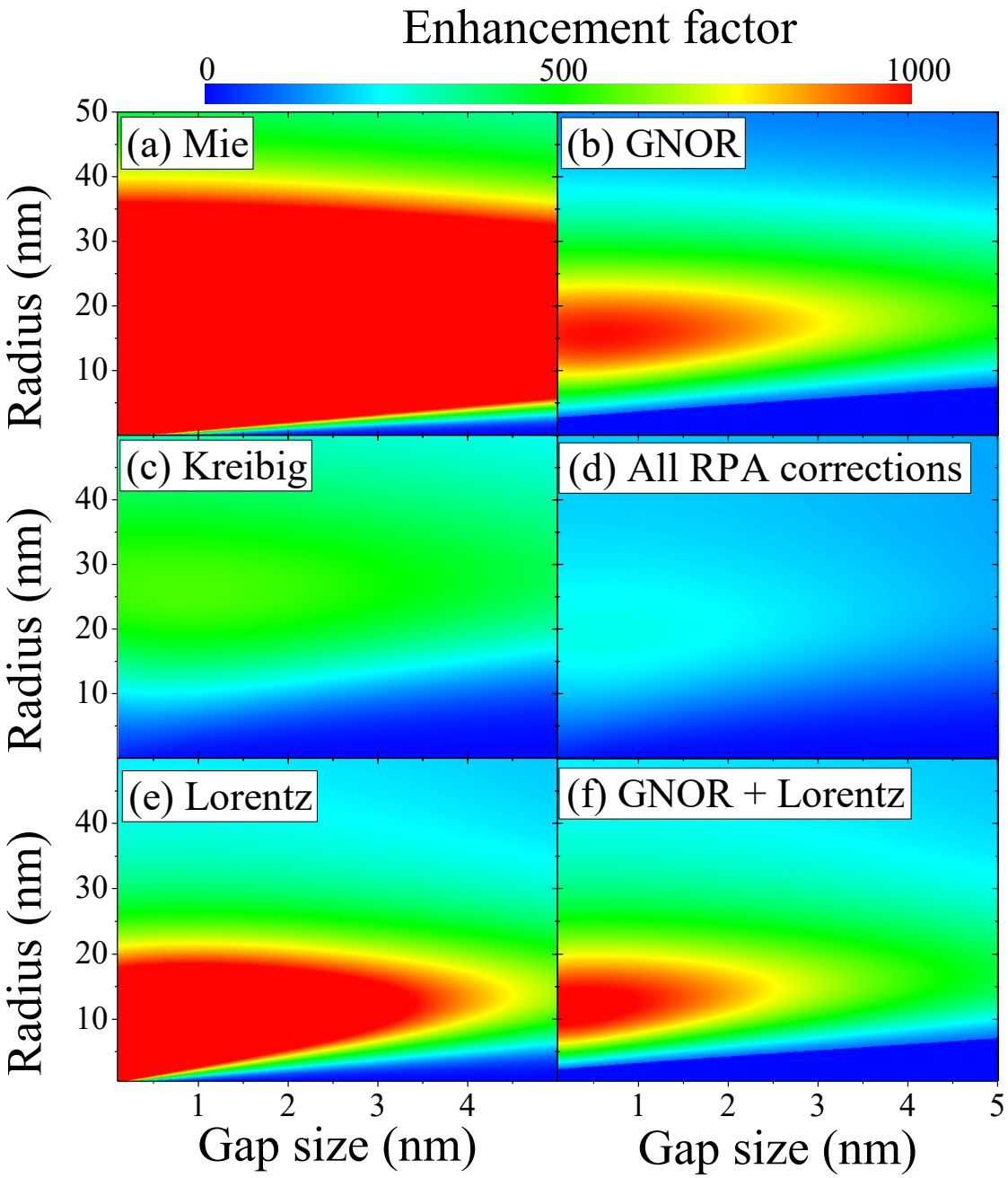


Fig. 4.2.: Impact of microscopic electron dynamics on gold dimers in water. Field enhancement at the gap center in dependence on particle radius ($a > 0.5$ nm) and separation (>0.1 nm) for (a) classical Mie calculations, (b) spatial dispersion with GNOR, (c) Kreibig damping, (d) all RPA corrections combined, (e) Lorentz friction and (f) GNOR with Lorentz friction. The incident field is polarized along the dimer axis and the maximum EF is evaluated at the respective resonance frequency calculated for each case.

damping does yield a plasmon broadening that agrees with experiments [157], however, it also introduces a redshift of the resonance with respect to the classical Mie result contrary to measurements on nanoparticles [76, 145, 146, 148]. This is addressed using the hydrodynamic Generalized Nonlocal Optical Response (GNOR) approach, i. e., by introducing a diffusion parameter, able to reproduce the Kreibig damping while fully capturing the observed

plasmon broadening. An important aspect is that the resulting analytical expressions can be implemented into existing computational procedures in a straightforward manner, as isolated theories or combined, allowing the comparison to experiments with little added numerical effort. The straightforward inclusion of electro-optical effects at the nanoscale into (metal) nanoparticle systems is of importance in nanostructures employed for photovoltaics and catalysis as well as in spectroscopy and sensing applications.

### 4.2.2 Strong Particle-Substrate Coupling and nonlocal Mode Splitting

We next consider strong optical coupling of metal nanoparticle arrays with dielectric substrates [226] applied to a simplified solar cell setup. One crucial parameter affecting the efficiency of solar cells is the absorption rate of the solar spectrum impinging on their surface. It was shown experimentally that the efficiency of the photo-effect increases due to the deposition of metal nanoparticles (MNPs) on the photoactive surface [95, 227, 228] for light emitters [180, 229–232], in catalytic [233–235] and photovoltaic devices [26, 34, 56, 82, 85, 90, 113, 236–243].

While the observed scattering effects can be described with classical linear electrodynamic theory for most applications, the coupling between plasmon oscillations and semiconductor states, and the energy transfer related to *hot* carriers are best captured within quantum mechanics. We use a model of plasmon-enhanced solar cells based on the microscopic description of the interaction between plasmon excitations inside MNPs and the semiconductor states using the Fermi Golden Rule [180]. A modified dielectric function of the semiconductor is derived by calculating the photon absorption probability in the presence of the dipole field arising from the plasmon oscillation. This enables us to compare with calculations accounting for scattering effects. In addition, we assume both local and nonlocal electron dynamics in the strong optical coupling model, i. e., the dipole near-field. In the local case, the dielectric function of the metal is assumed to be spatially constant, i. e., $\mathbf{D}(\mathbf{r},\omega) = \epsilon_0\varepsilon(\omega)\mathbf{E}(\mathbf{r},\omega)$, while in the more general, nonlocal case we account for spatial dispersion of it, i. e., $\varepsilon = \varepsilon(\mathbf{r},\mathbf{r}',\omega)$ and we have $\mathbf{D}(\mathbf{r},\omega) = \epsilon_0 \int \varepsilon(\mathbf{r},\mathbf{r}',\omega)\mathbf{E}(\mathbf{r}',\omega)d\mathbf{r}'$. Both strong coupling and nonlocality are inherently nonlinear effects [70, 177]. Appendix D shows how using the Fermi Golden Rule, the particle–substrate coupling can be derived in terms of the photon absorption probability assuming a local dipole field. Both, the expressions derived for the particle–substrate coupling and the additional hydrodynamic equation for electrons are integrated into COMSOL and the simulations presented here are conducted in two steps. In the first step, we calculate the electromagnetic field around the substrate without nanoparticles in response to the incident light wave defined on the top boundary of the mesh as a TM plane wave. Simultaneously, on the side boundaries of the computational cell, we apply Flouquet periodic boundary conditions. In the second step, we calculate the electromagnetic field distribution with Au NPs deposited on the top of a Si substrate within the scattered field formulation using the results from the first step as a background field.

The combined effect of the strong optical coupling between metal nanoparticles and the

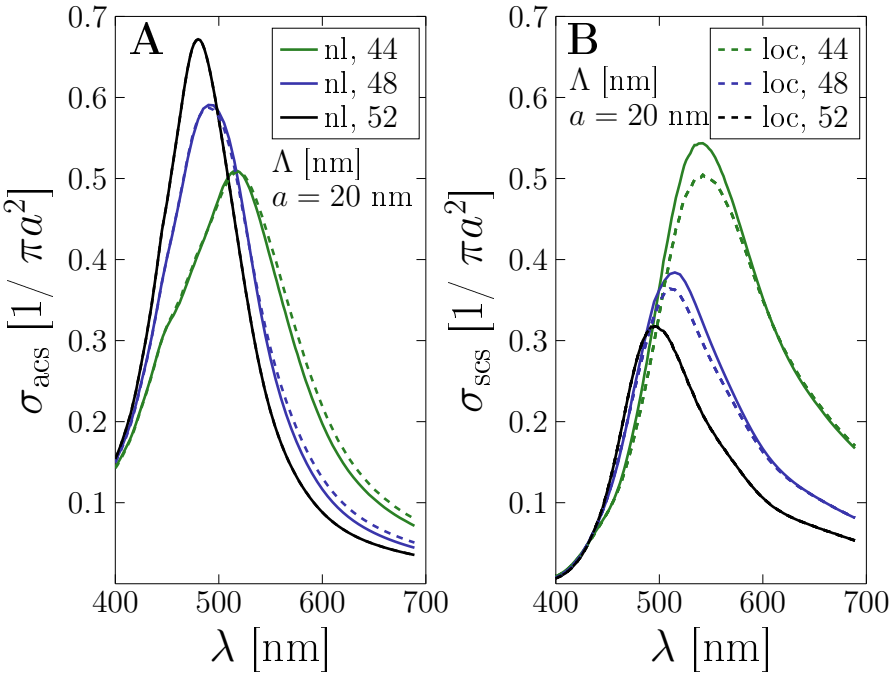


Fig. 4.3.: Impact of nonlocal effects on a gold nanoparticle array with $R = a = 20$ nm. Normalized (**A**) absorption ($\sigma_{acs}$) and (**B**) scattering cross section ($\sigma_{scs}$) are shown for several inter-particle distances $\Lambda$ comparing classical (*loc*, dashed) and nonlocal (*nl*, solid) electron dynamics.

dielectric substrate together with nonlocal electron dynamics is shown in Figure 4.3. The absorption and the scattering cross sections are shown for MNP arrays of $R = 20$ nm with several particle separations $\Lambda$. Hereby, the nonlocal electron–electron interactions in the metal nanoparticles become increasingly important for smaller particle separations, seen in a reduction and slight shift in the resonance of the photo-effect in the scattering efficiency and without significant effect in the absorption. Note that, next to the impact of particle size, the scattering cross section is larger for strong-coupling with additional electron dynamics, increasingly so as the particle size is reduced. This can be expected, as nonlocality becomes more important for structures with smaller features, where the surface-to-volume ratio is larger.

This is further investigated in terms of the photocurrent gain in the substrate region in our simplified solar cell setup in Figure 4.4. We study the influence of nanoparticle size (panels A and B) and the interparticle separation (panels C and D) in order to estimate the range of parameters for which the nonlocal effects significantly change the overall photocurrent gain. We have compared the strong coupling approach with the classical one. Without quantum corrections from the particle–substrate coupling, nonlocal electron dynamics enhances the photocurrent by up to 6%. On including the optical coupling via the Fermi Golden Rule, both theories yield significantly enhanced photocurrent and reduces the difference between classical and nonlocal theory to an enhancement of 1.5–2% due to the additional electron dynamics. Overall, the coupling theory allows quantifying the photocurrent gain to great agreement with recent experiments on solar cells [55].

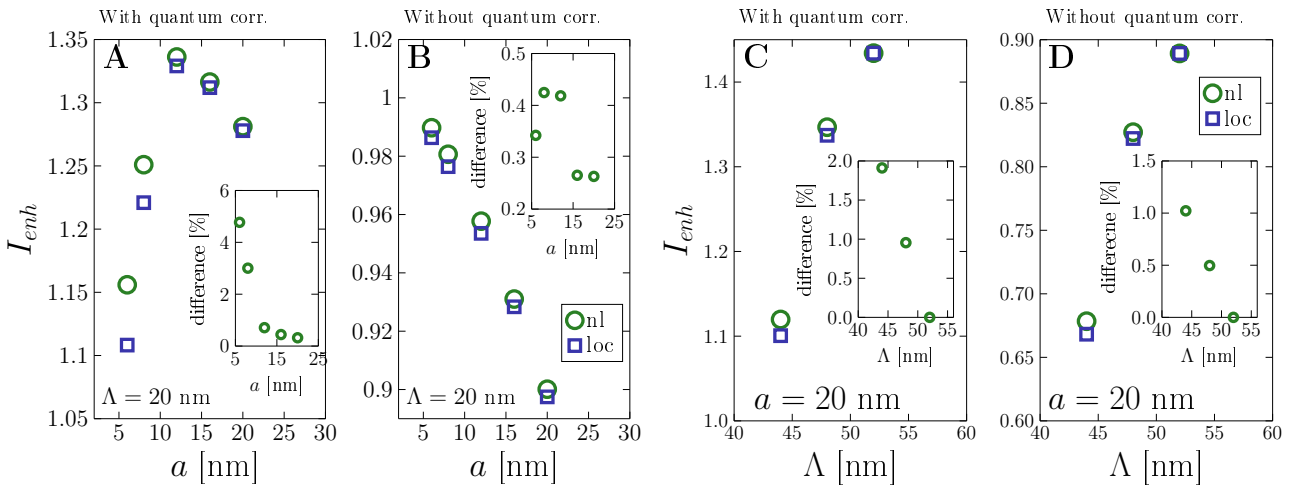


Fig. 4.4.: Impact of nonlocality on the photocurrent with and without particle–substrate coupling. The lattice period is $\Lambda = 20$ nm. The insets show the difference between classical and nonlocal theory results. (**A**) Strong coupling approach for various nanoparticle radii and constant interparticle separation $\Lambda = 20$ nm. (**B**) As in (**A**) for the standard classical theory. (**C**) Strong coupling approach for the radii $R = a = 20$ nm and various interparticle separations $\Lambda$. (**D**) As in (**C**) for the standard classical theory.

The impact of mesoscopic electron dynamics becomes significant for true nanoparticles. In Figure 4.5, we compare the absorption and scattering cross section for square nanoparticle arrays with an interparticle separation of 20 nm, reducing the NP radius from 20 nm to 12 nm in Figure 4.5A, B. While there is a sizeable impact of nonlocality, it becomes even more visible in Figure 4.5C, D, where we start to observe a splitting of the local resonance for particles of radius 6 nm and 8 nm strongly coupled to the semiconductor substrate. At the larger particle sizes, this is seen in the formation of a second peak at higher wavelengths, with only slightly shifting the main (local) resonance. The modes become evenly split spanning several tenths of nanometers, sharpened and largely enhanced with respect to the related local result.

We attribute the resonance mode splitting to the dynamical Stark effect, known as Autler–Townes splitting [244–246]. While strong coupling can by itself result in mode splitting, it is remarkable that we only observe this effect when the metal nanoparticle is described with mesoscopic electron dynamics. Nonlocal electron interaction in the hydrodynamic model is also a semi-classical approach and inherently nonlinear. It typically has an impact on particles with radii well below $20$ nm. In the classical picture, with local electron dynamics, the incident field can excite two known transversal modes with opposite directions within the metal nanoparticle (MNP). Nonlocal electron dynamics, however, allows for a third type of excitation, a longitudinal mode of a pressure-like electron density wave [53, 70, 75]. The strong optical coupling of the semiconductor states to this classically neglected excitation in small metal nanoparticles promotes the Autler–Townes splitting. We believe that these additional nonlocal modes are vital for this effect to be observed under solar irradiation. The shift observed in the presented simulations is around $\pm 14$ nm (ca. $\pm 80$–$87$ meV).

We study the mode splitting in more detail in Figure 4.6 showing the electromagnetic field

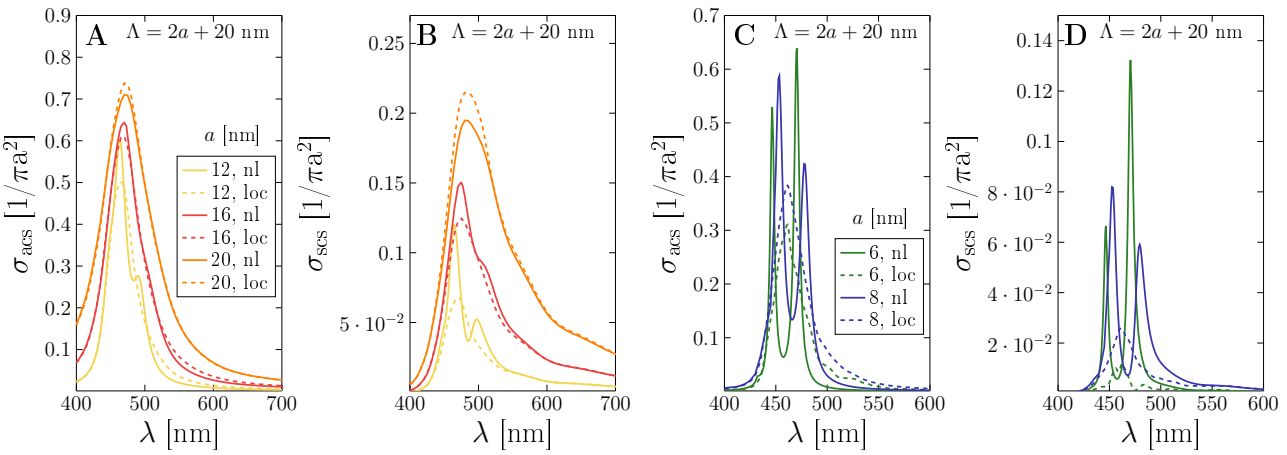


Fig. 4.5.: Impact of nonlocality on the strongly coupled system. A gold nanoparticle array with lattice period $\Lambda = 2a + 20$ nm is placed on a Si substrate. Normalized (**A**) absorption ($\sigma_{acs}$) and (**B**) scattering cross section ($\sigma_{scs}$) for particle sizes above 10 nm comparing classical and nonlocal theory. (**C**) Absorption and (**D**) scattering cross section for particle sizes below 10 nm comparing classical and nonlocal theory. In this regime, strong coupling leads to the Autler–Townes splitting of the local mode in the semi-classical picture.

in Figure 4.6A, B and charge distribution in Figure 4.6C, D at the two shifted resonances for the smallest particle size considered, $R = 6$ nm. It clearly shows a different mode pattern. Apart from the strongly localized charge and field at the particle–substrate interface, the modes spanning the nanoparticle can be characterised as a dipolar (at larger wavelengths) and quadrupolar (at lower wavelengths) distribution. Accounting for the additional nonlocal mode, the physical picture is thus: The incident electric field acts on the electrons and pushes them to different positions. If an electronic state has its electron displaced with the electric field direction, its energy is lowered, while its energy is raised if the electron is displaced against the field direction.

In our semi-classical treatment of the plasmon oscillation, we attribute this behaviour to the dynamical Stark effect, known as Autler–Townes splitting [244–246], which occurs due to nonlinear interactions between light and matter [247]. Electric fields affect the optical interband properties of semiconductors and, in particular, fields in the THz energy range can couple conduction or valence subbands [248, 249]. Typically, this quantum confined Stark effect is used in telecommunications, quantum-well modulators and switches [250].

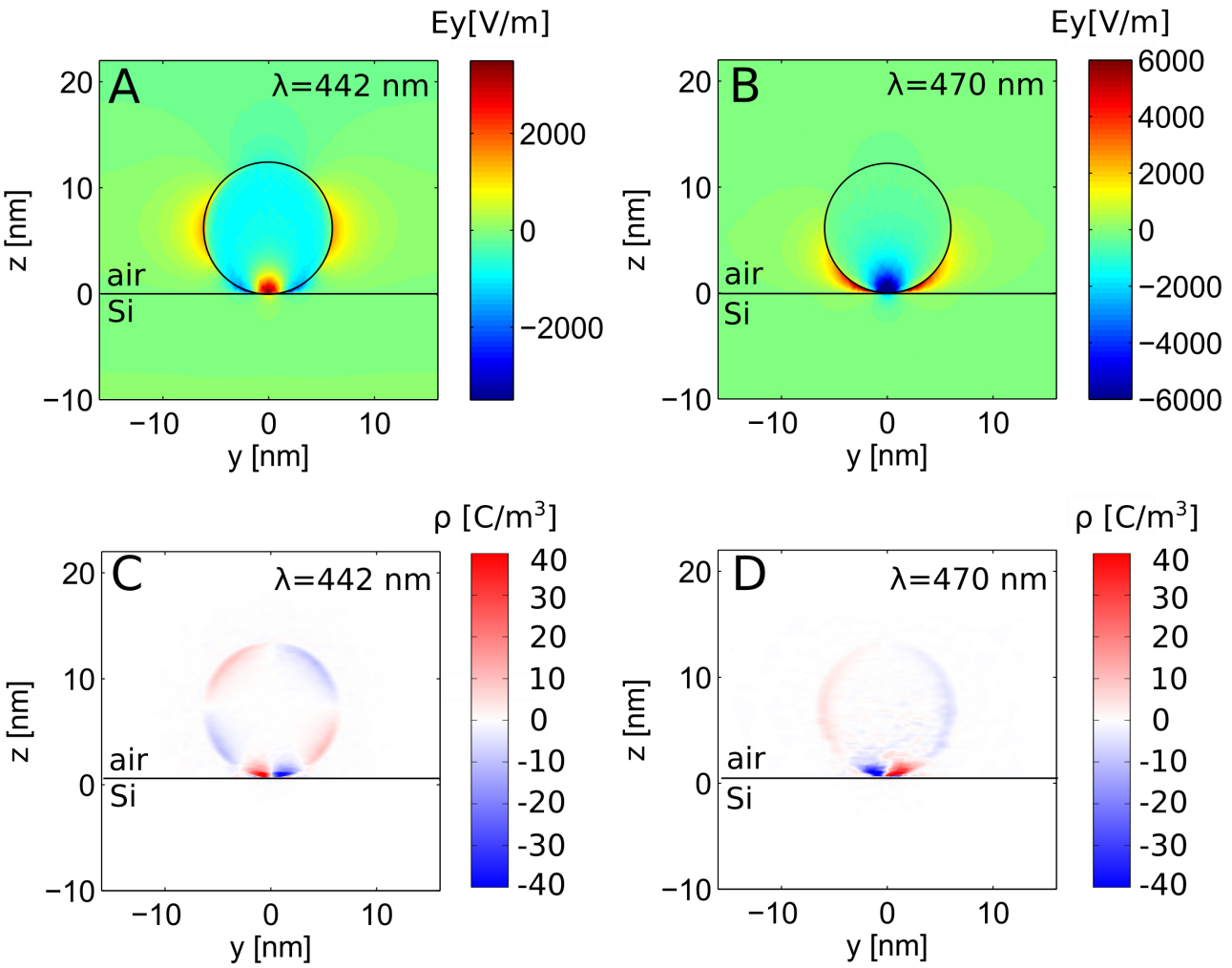


Fig. 4.6.: Nonlocal modes after Autler–Townes splitting due to strong coupling for $a = 6$ nm. Cut through the particle center at $x = 0$. (**A**,**B**) Field distribution and (**C**,**D**) induced charge distribution for the (**A**,**C**) mode shifted to higher energy and (**B**,**D**) Mode shifted to lower energy.

# 5. Nonlocal Soft Plasmonics

The field of plasmonics is widely understood as the investigation of collective oscillations of the electron plasma in metallic systems induced by an external electromagnetic field [39,164,183]. In a broader sense, such plasma oscillations can be found for any system where charged carriers are induced, such as stretchable [251] and amorphous materials [252] and charged plasmas in space [253, 254], e. g. the high energy nuclear plasma in the solar core, the ion gas in the ionosphere or intergalactic clouds. Coupled charge carriers relevant for photonic applications include electron-hole pairs in semiconductors [186, 187] and ionic systems [141,255,256] where both charge plasmas need to be considered. Their plasmonic properties can be derived from classical electrodynamics, introducing a two-fluid model for positive and negative ionic charges [141].

Plasmons of noble metals are studied with respect to applications in sensing and spectroscopy [218], optical filters [257], plasmonic colors [258], lasers [259], and quantum plasmonics [260] exploiting the extreme confinement and sensitivity of their electro-optical excitation. The plasmonic properties of ions in solution, on the other hand, are of interest in biological and chemical systems. Local energy transfer and communication are central in the signaling and conductivity of nerve cells (axons) [160] with great importance to the functionality of the biological system in question. The interaction of an electrolyte with its environment and, in particular, with functionalized surfaces is of central interest in catalytic processes.

The masses of ions are many orders of magnitude larger than the electron mass $m_e$ which results in a plasmon frequency in the far infrared (>3$\mu$m, GHz-regime). The ion concentration can be used to further tune the system similar to doping in semiconductors and, depending on the choice of material, the charge $Q$ itself can be different from the elementary charge $e$ allowing a wide range of resonance frequencies. Notably, due to these degrees of freedom, the ionic system is widely tunable via ion concentration, mass and charge, in contrast to solid metal nanoparticles. Using multiple scattering techniques [60,75], the plasmonic properties of both single ionic spheres and more complex structures, such as chains of ions, can be studied in comparison to solid metal nanoparticles. To achieve such geometries experimentally, lipid membranes can be used to confine ionic charge carriers in the desired way.

In addition, classical electrodynamics typically neglects interaction between strongly confined charges. The classical description of plasmons in metals starts to fail on the nanoscale as shown in the previous chapters. Spatial interaction effects between charge carriers in ionic systems play a sizable role beyond a classical Maxwellian description and are explored in this chapter. Soft plasmonics for spherical ions [255] and chains of axons [160] have been studied within the RPA method including Lorentz friction, i. e., electron radiation due to the acceleration of charges in the oscillations. We develop a nonlocal, two-fluid, hydrodynamic theory of charges and study ionic plasmon effects, i. e. collective charge oscillations in electrolytes. Analytic expressions can be found for nonlocal Mie coefficients for ionic spherical

particles. [53, 141] This has been generalized into a multi-fluid description by others [261]. Ionic spatial dispersion arises from both positive and negative charge dynamics with an impact in the (far-)infrared. Despite highly classical parameters, nonlocal quenching of up to 90% is demonstrated for particle sizes spanning orders of magnitude.

A nonlocal soft plasmonic theory for ions is relevant for biological and chemical systems bridging hard and soft matter theory and allowing the investigation of non-classical effects in electrolytes in full analogy to solid metal particles. The semi-classical approach presented here can be fully integrated into standard nano-optic simulation frameworks and is considered to be of great interest for plasmonic photo-catalysis [109] introducing nonlocal aspects into electrolyte-surface interactions possibly avoiding the hardship of DFT calculations. On the other hand, it provides a novel perspective on phenomena in biological systems, e. g. the signal transfer of nerve cells, can likewise profit from the plasmonic perspective on local field effects.

## 5.1 Two-fluid Model

Please note throughout this section the analogies to the hydrodynamic model for the electron plasma in metals, section 2.2. The optical response of an ionic system with free negative and positive charges in a fluid is based in the hydrodynamic model on separating the dynamics of both types of ions, assuming

$$\nabla \mathbf{D} = \epsilon_0 \varepsilon_b \nabla \mathbf{E} = \rho_- + \rho_+. \tag{5.1}$$

Hereby, $\varepsilon_b$ is the dielectric background permittivity of the solution and $\rho_\pm$ are the charge densities of the ions treated as additional charges in the system. Ion masses $m_\pm$ and charge $Q_\pm$ may differ for the ions in the system, however, the total charge is balanced, i. e. the charges are mutually compensated by setting

$$|n_+ Q_+| \equiv |n_- Q_-|. \tag{5.2}$$

This yields an equal density $n = n_+ = n_-$ of charges in most standard cases such as of hydronium ($H_3O^+$) and hydroxide ($OH^-$) in splitted water or dilluted salts in biological systems with equal but opposite charges of the constituent materials. The electromagnetic wave equation then reads

$$\nabla \times \nabla \times \mathbf{E} - k^2 \varepsilon_b \mathbf{E} = i\omega\mu_0 \left(\mathbf{j}_- + \mathbf{j}_+\right). \tag{5.3}$$

Hereby, $\mathbf{j}_\pm$ are the charge current densities of the ions in the electrolyte. Together with the

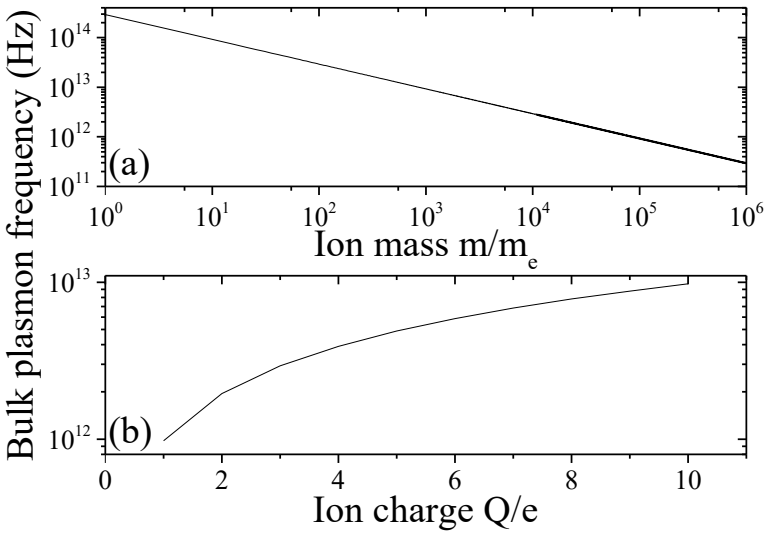


Fig. 5.1.: Ionic bulk plasmon frequency values $\omega_p^2 = {}^{nQ^2}/_{\epsilon_0 m}$ for (a) different choices of the mass and (b) different values of the charge. Fixed values are $Q = 3e, m = 10^4 m_e, \epsilon_b = 1.77, n = 10^{-2} N_0$, with the one-molar concentration $N_0$.

linearized hydrodynamic equations for each type of ion

$$\mathbf{j}_\pm = \frac{i\epsilon_0}{\omega + i\gamma_\pm}\left(\frac{Q_\pm^2 n_\pm}{\epsilon_0 m_\pm}\mathbf{E} - \nabla\beta^2_{\mathrm{GNOR}\pm}\rho_\pm\right) \tag{5.4}$$

this can be brought into the form [141] of

$$\nabla^2\mathbf{E} + k^2\epsilon_\perp^{\mathrm{ions}}\mathbf{E} = \nabla(\eta_-\rho_- + \eta_+\rho_+), \tag{5.5}$$

where the right hand side vanishes in the local limit, $\eta_\pm$ comprise of material dependent parameters

$$\eta_\pm = \frac{1}{\epsilon_0\epsilon_b} - \frac{k^2\beta^2_{\mathrm{GNOR}\pm}}{\omega(\omega + i\gamma_\pm)} \tag{5.6}$$

and we have defined the permittivity of the coupled ionic system as

$$\epsilon_\perp^{\mathrm{ions}} = \epsilon_b - \frac{\omega_{p-}^2}{\omega(\omega + i\gamma_-)} - \frac{\omega_{p+}^2}{\omega(\omega + i\gamma_+)}. \tag{5.7}$$

Note that we obtain the common expressions for the (ionic) bulk plasmon frequencies $\omega_{p\pm}^2 = {}^{Q_\pm^2 n_\pm}/_{\epsilon_0 m_\pm}$, shown in Fig. 5.1, without introducing an auxiliary jellium in which the ions are contained. The latter is a prerequisite for the RPA approach [255, 256].

For the nonlocal strength $\beta_{\mathrm{GNOR}\pm}$, we rely on the thermal velocity of the heavy ions $v_{\mathrm{th}} = \sqrt{{}^{3k_BT}/_m}$, which is much smaller than the Fermi velocities found for free charges in solid materials ($v_F = 1.4 \times 10^6$m/s for Au and Ag) due to the large masses involved ($v_{\mathrm{th}} \sim 10^3$m/s, see table 5.1 for some examples). Note that for positive charges $\beta_+ = -\beta_-$, due to integration over the valence band below the Fermi energy for positive charges, rather than over the conduction band above the Fermi energy for negative charges. The local limit is obtained for

| Ion | mass (Da) | mass ($m_e$) | $v_{\mathrm{th}}$ (m/s) | free mean path (nm) | $\gamma$ (meV) |
|---|---|---|---|---|---|
| $H^+$ | 1.007 | 1835 | 2727 | 0.33 | 17.22 |
| $OH^-$ | 17.008 | 31005 | 663 | 1.35 | 1.02 |
| $H_3O^+$ | 19.02 | 34670 | 627 | 1.42 | 0.91 |
| $Na^+$ | 22.990 | 41907 | 571 | 0.89 | 1.32 |
| $K^+$ | 39.098 | 64628 | 459 | 1.11 | 1.11 |
| $Cl^-$ | 35.453 | 71270 | 437 | 1.27 | 1.27 |

Table 5.1.: Electrolyte parameters for an aqueous solution in thermodynamic equilibrium. All charges are $Q_\pm = \pm 1e$.

$\beta_{\mathrm{GNOR}\pm} \to 0$ which suppresses the interaction of the charged particles in the fluid. However, part of the field induced current density remains and yields the ionic plasmon effects within classical electrodynamics.

To estimate the mean free path and damping of ions diluted in water as given in table 5.1, we use the density of water at a temperature $T = 25^{\circ}\mathrm{C}$, $\rho_{\mathrm{H20}} = 997^{\mathrm{kg}}/_{\mathrm{m}^3}$, and its dynamic viscosity $\mu_{\mathrm{H20}} = 8.9 \times 10^{-4\,\mathrm{kg}}/_{\mathrm{m\,s}} = 8.9 \times 10^{-4}\mathrm{Pa\ s}$, from which we deduce the kinematic viscosity

$$\nu = \mu/\rho. \tag{5.8}$$

For salts diluted in water [262–264], these values depend on parameters such as pressure and temperature and their concentrations. Crystalline sodium chloride has a density of $2160^{\mathrm{kg}}/_{\mathrm{m}^3}$ with an atomic mass of 58.443 Da and potassium chloride $1980^{\mathrm{kg}}/_{\mathrm{m}^3}$ with an atomic mass of 74.551 Da. In solution, these are reduced to values close to the above value for water and increase with concentration.

Furthermore, we can use the kinematic viscosity to calculate the mean free path

$$l = \nu/v_{\mathrm{th}} \tag{5.9}$$

and the damping of the ionic movement in the solution

$$\gamma = v_{\mathrm{th}}^2/(2\nu). \tag{5.10}$$

The range of the ionic bulk plasmon frequency is investigated in Fig. 5.1 with respect to the ion mass and charge which can be selected via the material. The ionic plasmon frequency is far smaller than that of common metals and lies in the infrared and beyond ($> 3\mu$m).

### 5.1.1 Coupled nonlocal Wave Equations

From the continuity equations $i\omega\rho_\pm = \nabla\mathbf{j}_\pm$, we find for each type of charge a separate wave equation yielding additional longitudinal modes. Introducing the Drude permittivity for the respective charges as $\varepsilon_{D\pm} = \varepsilon_b - \frac{\omega_{p\pm}^2}{\omega(\omega+i\gamma_\pm)}$ and using $\nabla E = {}^{(\rho_- + \rho_+)}/_{\epsilon_0\varepsilon_b}$, we obtain coupled

hydrodynamic equations typical for a two-fluid model

$$\rho_- = \frac{\varepsilon_b}{\omega_{p+}^2}\left(\nabla^2\beta_{\mathrm{GNOR}+}^2 + \frac{\omega(\omega+i\gamma_+)}{\epsilon_0\varepsilon_b}\varepsilon_{D+}\right)\rho_+ \tag{5.11}$$

and vice versa, exchanging the index sign for the result of the respective other charge. Inserting this into the above equation yields a wave equation of fourth order

$$0 = \beta_{\mathrm{GNOR}+}^2\beta_{\mathrm{GNOR}-}^2\left(\nabla^2+q_+^2\right)\left(\nabla^2+q_-^2\right)\rho_- - \frac{\omega_{p+}^2\omega_{p-}^2}{\varepsilon_b^2}\rho_-, \tag{5.12}$$

which can be solved analytically for different geometries. The analytic solutions confirm the simple fact that positive charges have the opposite oscillation direction from negative charges. Note that we introduced the nonlocal wave vectors $q_\pm$ from the single charged plasma result [53] $q_\pm^2 = \frac{1}{\beta_{\mathrm{GNOR}\pm}^2}\frac{\omega(\omega+i\gamma_\pm)}{\epsilon_0\varepsilon_b}\varepsilon_{D\pm}$.

## 5.2 Mie coefficients for nonlocal ionic spheres

In order to study specific geometries of the resulting plasmon oscillations, the electrolyte system has to be confined in the desired way. In this section, we apply boundary conditions to investigate finite spherical geometries. We concentrate on ionic carriers in a finite electrolyte system made of hydronium $H_3O^+$ (more abundant than $H^+$) and hydroxide $OH^-$ at room temperature. Together with their masses and charges, this yields the parameters collected in table 5.1. These can be created from confined ions within insulating membranes typically in the micrometer scale. In particular, the large ion mass and low concentration results in an energy and size regime very distinct from metal nanoparticles.

### 5.2.1 Finite Spherical Ionic Systems

The nonlocal two-fluid hydrodynamic approach has many parallels with the theory of a single electron plasma in metal nanoparticles with spatial dispersion for which we find Mie parameters extended by a single nonlocal term $g$, see Eq. (4.3) [53]. We derive the nonlocal Mie coefficients within the two-fluid model in analogy to the solid metal nanoparticle case presented in section 4.1 and report here the main differences in the derivation steps.

The additional boundary condition in spherical coordinates $\hat{\mathbf{e}}_r\mathbf{j} = 0$ yields

$$\beta_{\mathrm{GNOR}\pm}^2\frac{\partial}{\partial r}\rho_\pm = \frac{Q_\pm^2 n_\pm}{\epsilon_0 m_\pm k}\left(\frac{\partial\psi^L}{\partial r} + \frac{1}{r}l(l+1)\psi^E\right), \tag{5.13}$$

where the magnetic and electric scalar functions $\psi^\nu$ ($\nu = \{E, M\}$) obey a Helmholtz equation of the form $(\nabla^2 + k^2\epsilon^{\mathrm{ions}})\psi^\nu = 0$ and can therefore be expanded in terms of spherical Bessel functions $\psi^\nu = \sum_L \psi_L^\nu j_L(k^{\mathrm{ions}}r)$. Similarly, the electron density is expanded into $\rho^{\mathrm{ind}}(\mathbf{r},\omega) = \sum_L(\rho_{l+}j_L(q_+^{\mathrm{Mie}}r) + \rho_{l-}j_L(q_-^{\mathrm{Mie}}r))$.

The longitudinal wave vectors $q_\pm^{\mathrm{Mie}}$ given by $(q_\pm^{\mathrm{Mie}})^2 = -\frac{\tilde{p}}{2} \pm \sqrt{\left(\frac{\tilde{p}}{2}\right)^2 - \tilde{q}}$ are the solutions to

Eq. (5.12) with

$$\tilde{p} = -\left(q_+^2 + q_-^2\right), \qquad \tilde{q} = -\left(\frac{1}{\beta^2_{\text{GNOR-}}\beta^2_{\text{GNOR}+}}\frac{\omega^2_{p+}\omega^2_{p-}}{\epsilon_b^2} - q_-^2 q_+^2\right). \tag{5.14}$$

We demand $\text{Im}(q_\pm^{\text{Mie}}) > 0$, i. e. that nonlocal, longitudinal excitations remain absorptive, which reduces the four solutions to two physically relevant ones.

The boundary conditions above lead to the following set of equations for the electric scalar field

$$\varepsilon^{\text{ions}} A_l^E j_l(\Theta^{\text{ions}}) = \varepsilon_b \left(j_l(\Theta_0) + t_l^E h_l^+(\Theta_0)\right), \tag{5.15}$$

$$-\frac{k}{\varepsilon^{\text{ions}}}\left(\frac{\beta^2_{\text{GNOR}-}\rho_{l-} j'(q_-^{\text{Mie}}R)}{\epsilon_0\omega(\omega+i\gamma_-)} + \frac{\beta^2_{\text{GNOR}+}\rho_{l+} j'(q_+^{\text{Mie}}R)}{\epsilon_0\omega(\omega+i\gamma_+)}\right) + A_l^E\left[\Theta^{\text{ions}} j_l(\Theta^{\text{ions}})\right]' = \left[\Theta_0 j_l(\Theta_0)\right]' + t_l^E\left[\Theta_0 h_l^+(\Theta_0)\right]', \tag{5.16}$$

where $\Theta_\mu = k_\mu R\sqrt{\epsilon_\mu}$. We use the additional boundary conditions, Eq. (5.13), to find expressions allowing the substitution of $\rho_{l\pm}$ in the above equations.

$$\beta^2_{\text{GNOR-}}\rho_{l-} q_-^{\text{Mie}} j'(q_-^{\text{Mie}}R) = \frac{\omega^2_{p-} l(l+1)}{kR} A_l^E j_l(\Theta^{\text{ions}}) - \frac{\omega^2_{p-}}{\epsilon^{\text{ions}}}\left(\frac{\beta^2_{\text{GNOR-}} q_-^{\text{Mie}} j'(q_-^{\text{Mie}}R)}{\epsilon_0\omega(\omega+i\gamma_-)}\rho_{l-} + \frac{\beta^2_{\text{GNOR}+} q_+^{\text{Mie}} j'(q_+^{\text{Mie}}R)}{\epsilon_0\omega(\omega+i\gamma_+)}\rho_{l+}\right) \tag{5.17}$$

and vice versa. From this, we find for the charges

$$\rho_{l\pm} = A_l^E \frac{l(l+1)}{kR}\frac{j_l(\Theta^{\text{ions}})}{q_\pm^{\text{Mie}} j'(q_\pm^{\text{Mie}}R)}\frac{\epsilon^{\text{ions}}}{\epsilon_b}\frac{\omega^2_{p\pm}}{\beta^2_{\text{GNOR}\pm}}. \tag{5.18}$$

Next, we insert the charge densities into the equations obtained with the common boundary conditions (5.15) and (5.16) and rewrite after some algebra

$$A_l^E\left\{\left[\Theta^{\text{ions}} j_l(\Theta^{\text{ions}})\right]' + g_l^{\text{ions}}\right\} = \left[\Theta_0 j_l(\Theta_0)\right]' + t_l^E\left[\Theta_0 h_l^+(\Theta_0)\right]',$$

Exploiting the usual boundary conditions and additional boundary conditions stemming from the nonlocal wave equations for each type of ion, we obtain the scattering matrix for the two-fluid, spherical ionic system in full, formal analogy

$$t_l^E = \frac{-\epsilon_\perp j_l(\theta_\perp)[\theta_0 j_l(\theta_0)]' + \epsilon_b j_l(\theta_0)([\theta_\perp j_l(\theta_\perp)]' + g_l^{\text{ions}})}{\epsilon_\perp j_l(\theta_\perp)[\theta_0 h_l^+(\theta_0)]' - \epsilon_b h_l^+(\theta_0)([\theta_\perp j_l(\theta_\perp)]' + g_l^{\text{ions}})}, \tag{5.19}$$

with $g_l^{\text{ions}} = g_{l+} + g_{l-}$

$$g_{l\pm} = \frac{l(l+1) j_l(\Theta^{\text{ions}})}{R}\frac{j_l(q_\pm R)}{q_\pm^{\text{Mie}} j'(q_\pm^{\text{Mie}}R)}\left(\frac{\epsilon_{\perp\pm}}{\epsilon_b} - 1\right). \tag{5.20}$$

Note that the nonlocal parameter $g_l^{\text{ions}}$ vanishes under the assumption of local response fully

recovering the original Mie coefficients [142, 222] for a classical ionic system. This allows us to study the electro-optical properties of spherical membranes filled with a nonlocal electrolyte with only a small correction in available numerical procedures. This is very similar to the single plasma result, where we now sum nonlocal contributions from two charge carrier plasmas. The main differences lie in the nonlocal wavevectors $q_{\pm}^{\mathrm{Mie}}$ from Eq. (5.12) and the fact, that we have two contributions from different type of charge carriers $\pm$. Significantly different amplitudes can be expected when the masses and charges strongly differ.

### 5.2.2 Results for nonlocal Ionic Spheres

Fig. 5.2 exemplifies the similarities between the plasmons in a solid metal nanoparticle (gold in a simplified Drude model for clarity) and the electrolyte system at increased density in terms of both the extinction cross section and field enhancement.

Plasmons in metals are an excitation of the conduction band electrons via a polarizing electromagnetic field that displaces the freely moving electrons with respect to the positively charged atomic cores, see Fig. 5.2(a). In an electrolyte, we find even at thermal equilibrium a small density $n_{\pm}$ of ions of possibly different charge $Q_{\pm}$ and mass $m_{\pm}$, see Fig. 5.2(b). However, in the absence of a rigid crystal lattice, both types of ions can oscillate with typically different plasmon frequencies $\omega_{p\pm}^2 = {Q_{\pm}^2 n_{\pm}}/{\epsilon_0 m_{\pm}}$. The coupled system yields an effective localized surface plasmon resonance (LSPR) for spherical geometries at

$$\omega_{\mathrm{LSPR}} = \sqrt{{(\omega_{p+}^2+\omega_{p-}^2)}/{3\epsilon_b}}, \tag{5.21}$$

where $\epsilon_b$ is the background permittivity inside the confining membrane. Assuming self-ionization of water at the thermodynamic equilibrium, we arrive at a concentration $n_{ThermEq} = 6.022 \times 10^{16}\mathrm{m}^{-3}$ for each type of ion. The localized plasmon resonance for this low density limit for a hydroxide and hydronium system, see table 5.1 for further parameters, results in $\lambda_{\mathrm{LSPR}} = 6.38\mathrm{m}$ ($\omega_{\mathrm{LSPR}} = 4.7 \times 10^7\mathrm{Hz}$).

The plasmons of metals are of great interest due to their ability to capture electromagnetic fields, i. e. their optical cross section is far greater than their geometrical cross section, and the associated strong local field enhancement in the proximity of the particle surface as depicted in Figs. 5.2(c) and (e). Note that we used a Drude model for gold ($\omega_{p,Au} = 9\ \mathrm{eV}, \epsilon_{b,Au} = 9$, $\gamma_{p,Au} = 0.071\ \mathrm{eV}$) excluding intraband effects for clarity. This is put in comparison to the considered electrolyte system in Figs. 5.2(d) and (f). The aforementioned effective LSPR, Eq. (5.21) for the coupled system agrees with the extinction cross section maximum, see also Fig. 5.3 and given the small membrane size of $R = 10$ nm considered here the light trapping is several orders of magnitude higher than for the gold particle of the same size. However, the associated local field enhancement at resonance is much smaller than for the metal. This can be understood and potentially remedied as follows. We have considered (neutral) water as background everywhere, while in the metal system a strong refractive index contrast is found at the surface. Due to the commonly known boundary condition of continuous $\varepsilon\ \hat{\mathbf{n}} \cdot \mathbf{E}$ this yields an increase in the field on the outside of the spherical nanoparticle. In case of the

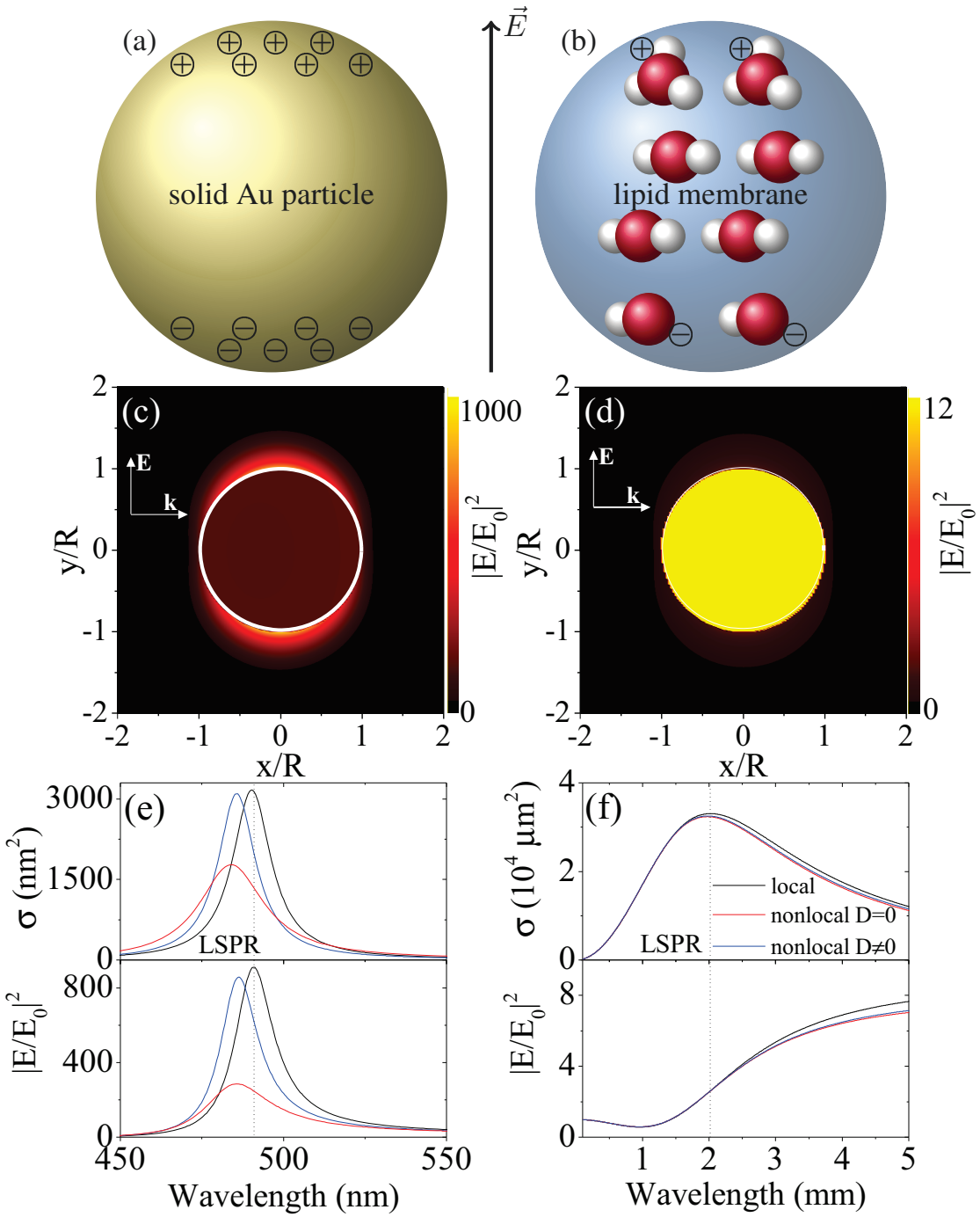


Fig. 5.2.: Concept of (localized surface) plasmon resonance (LSPR) in ionic systems compared to metals. Illustration of charge carrier displacement in (a) a metal solid and (b) an ionic fluid confined by e. g. a lipid cellular membrane. (c), (d) Field enhancement map of the plasmonic resonance in both systems. (e), (f) Impact of nonlocal charge dynamics (with and without electron diffusion $D$) on metals and ions in terms of the extinction cross section (upper panel) and the maximum field enhancement (lower panel). The particle size is $R = 10$ nm and a Drude model for gold was used for clarity. The charge density is $n = n_+ = n_- = 1^{\mathrm{mol}}/_{\mathrm{m}^3} N_A$.

ionic system, no such strong contrast is found, however, the lipid membrane used to confine the electrolyte could be filled with a different medium than water, e. g. a cytoplasm. It should also be noted that the field enhancement increases for even lower energies until it saturates.

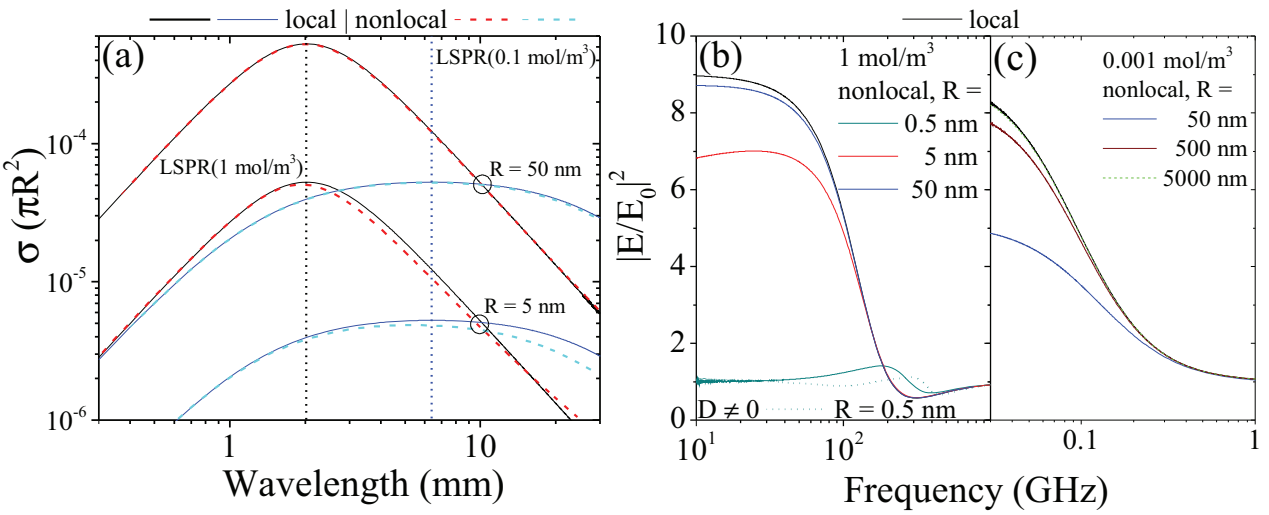


Fig. 5.3.: Extinction cross section and quenching of field enhancement at different ion concentration levels and for several orders of magnitude in particle size. (a) Extinction cross section normalized to geometrical cross section of the membrane. (b), (c) Comparing the maximum intensity at the particle surface for ionic systems with an ion concentration of (b) $n = 1^{\mathrm{mol}}/_{\mathrm{m}^3} N_A$ and (c) $n = 10^{-3\mathrm{mol}}/_{\mathrm{m}^3} N_A$ for varying membrane size.

This region is most strongly affected by non-classical charge carrier interactions.

Finally, we compare classical electrodynamic results (standard Mie coefficients) with our nonlocal model. For the metal system, as reported previously, a blueshift of the LSPR is observed and on inclusion of electron diffusion effects the resonance becomes more strongly broadened and attenuated, see Fig. 5.2(e). The coupled ionic system also shows an attenuation, see Fig. 5.2(f). The LSPR position is marked by a vertical line.

We observe the blueshift of the LSPR of the electrolyte with respect to the classical picture in Fig. 5.3(a). We consider two different ion concentrations that yield different resonance wavelengths and consider two membrane sizes, one that behaves classically ($R = 50$ nm) and one that shows nonlocal response ($R = 5$ nm). Zooming into the resonances (note the log-log axis), we indeed note a blueshift, though it is not as dramatic as for the metal system, since the resonances are much broader.

Next, we consider near-field quenching in dependence on the particle size for two different ion concentrations in Figs. 5.3(b) and (c). The ion concentration determines the LSPR and frequency range of interest for the system. With this, the impact of nonlocal quenching of the local field can be shifted to larger particle sizes. In general, a large enough membrane size yields the local limit where nonlocal charge carrier dynamics are no longer sizable. The minimum value for the diffusion constant to show an additional effect was found to be $D_\pm = 0.5 \times 10^{-5}\mathrm{m}^2/\mathrm{s}$ (with $\gamma_\pm \approx 10^{11}$ Hz, hence $D_\pm \gamma_\pm \approx 5 \times 10^5 \mathrm{m}^2/\mathrm{s}$), where in comparison $|\beta_\pm| \approx 1.5 \times 10^5 (\mathrm{m/s})^2$.

Fig. 5.4(a) and (b) show the penetration depth of the nonlocal excitation for the two types of ions as a function of ion mass and incident light frequency. Due to the difference in sign in the nonlocal parameters, the nonlocal contribution from the positive charges can be suppressed

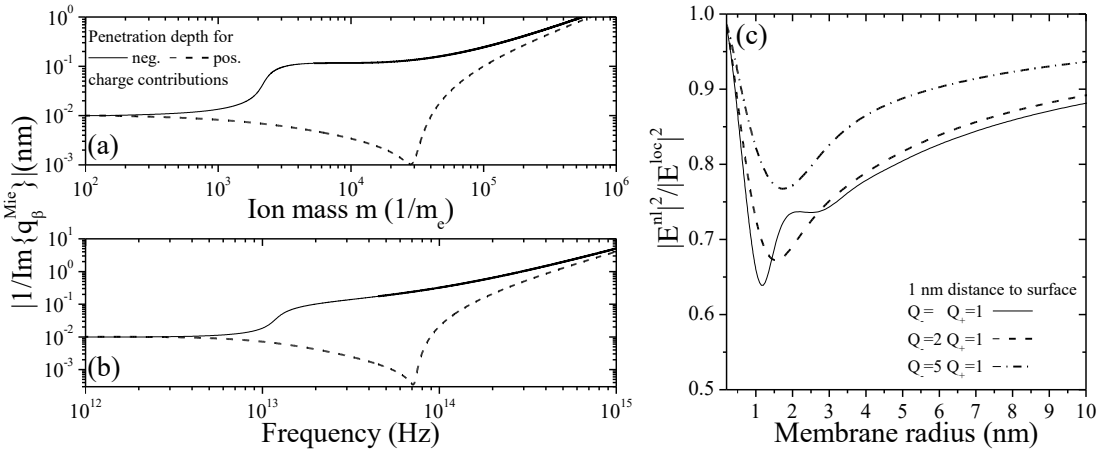


Fig. 5.4.: Properties of the coupled ionic system with spatial disperson. We compare exact solutions of the penetration depth of nonlocal pressure waves as a function of (a) photon energy and (b) ion mass. (c) Quenching of the field enhancement as a function of membrane size and charge imbalance.

under specific conditions, however, in general, the penetration depths is in the nanometer and subnanometer range and can be observed around the ionic spheres.

Fig. 5.4(c) shows that even at a distance of 1 nm away from the membrane surface, nonlocal field quenching of up to 30% can be expected depending to some extent on the imbalance of charges which yields an imbalance of ion concentration for the two types, balancing the total charge. Due to the different masses, it makes a difference which type of ions has the larger charge count. Evaluating this directly at the membrane surface for different ion concentrations results in more dramatic nonlocal field quenching, where the system with the largest charge imbalance shows the lowest quenching. This can be explained by noting that the LSPR of the systems is pushed further away from the excitation frequency.

A further imbalance of interest is the mass imbalance. We study the local field quenching due to spatial dispersion in Fig. 5.5. For heavy ions paired with light ions (lower part of the graph) stronger quenching can be expected for a larger range of membrane sizes.

The presented framework on nonlocal spherical ionic systems is bridging hard and soft matter theory by offering insights into non-classical effects in electrolytes in terms of plasmonic properties of oscillating charge carriers. We have relied on classical gas theory, where ionic charge carriers move much slower than free electrons in metals, and low diffusion parameters. In addition, in the absence of a solid crystal lattice as in metal nanoparticles, the probability of scattering events becomes strongly reduced, which is reflected in the small plasmon damping coefficients for the considered electrolyte system, see table 5.1. Despite these highly classical parameters resulting in a low nonlocal coupling strength $\beta$, we found that nonlocal charge interaction plays a sizable role in ionic systems mediated by the coupling of their dynamics and interaction with an external electromagnetic field. In contrast to spatial dispersion in solid metal particles, this is found even at large particle sizes and low plasmon frequencies. These nonlocal effects arise from both positive and negative charge dynamics and show an impact in the (far-) infrared depending on the composition of the ionic system being tunable via their

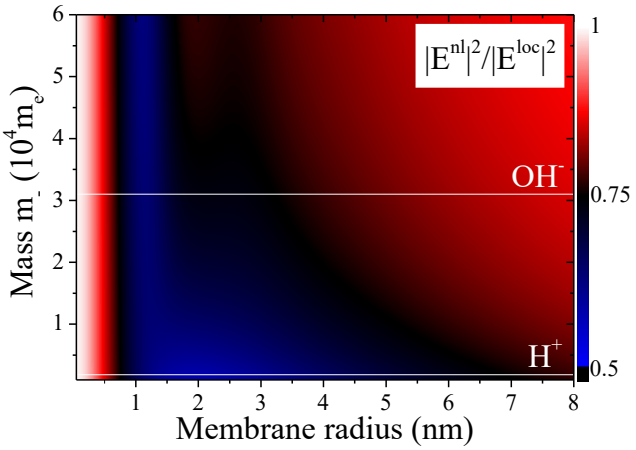


Fig. 5.5.: Quenching of field enhancement as a function of membrane size and mass imbalance. Comparing the ratio of the maximum intensity between local and nonlocal theories at a 1 nm distance from the membrane surface for ionic systems with an ion concentration of $n_- = 1^{\mathrm{mol}}/_{\mathrm{m}^3} N_A$ evaluated at $\omega = 10$ GHz as a function of membrane size and mass. The white lines mark the masses of $H^+$ and the parametrized $OH^-$. White areas show classical behavior, about 10% to 20% quenching is given in red areas. Black and blue areas are dominated by nonlocal charge dynamics.

charges and masses.

**Chains of Ionic Spheres**

We study ionic nanoparticle chains as an alternative plasmonic waveguide model for nerve cell (axon) communication [160]. Cell signaling is understood as electromagnetic energy transfer promoted by the alignement and geometrical parameters through (prolongated) microspheres filled with and surrounded by an ionic fluid.

Using multiple scattering techniques, we consider ionic particle chains in comparison to metallic ones in Fig. 5.6. Metallic nanoparticle chains in the upper row show clear dipolar, quadrupolar and octupolar modes with large scattering cross section values $\sim 10^3$ at their respective resonances as a function of particle size and particle separation. These observations can also be made for the ionic system, however, with less clearer modes as they are much broader and do not reach such high field enhancement values as discussed previously for single ionic spheres. Here, the maximum values normalized to the geometrical cross section and number of particles in the chain are around unity.

**Planar Ionic Interfaces**

With view to photocatalytic applications, overall planar, layered structures are of further interest to investigate plasmonic effects of charged ions. For electrolytes confined in a planar system, the local limit is additionally given for light at normal incidence. The vanishing parallel momentum of the incoming light suppresses coupling to longitudinal modes in the ionic system. Further studies for planar nonlocal ionic interfaces and nonlocal ionic Fresnel coefficents are carried out.

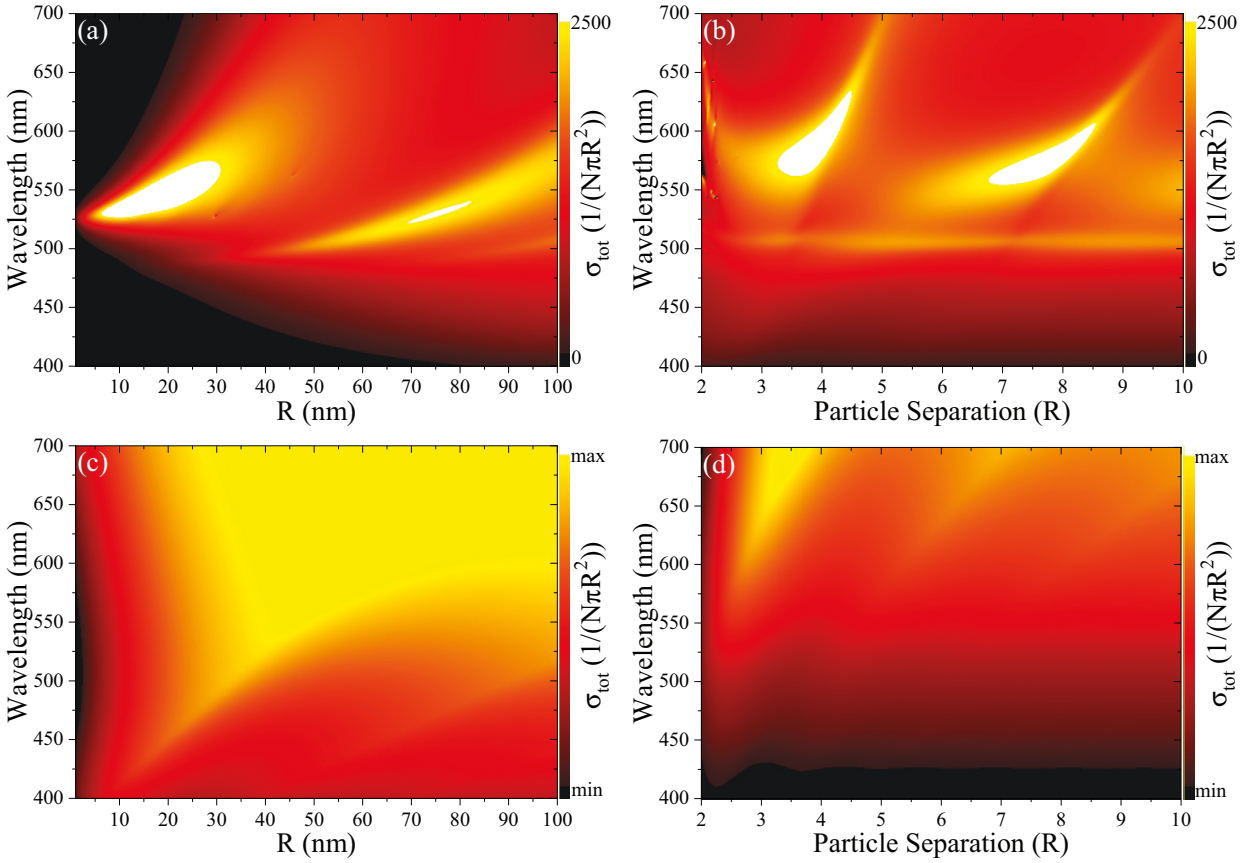


Fig. 5.6.: Comparison of (a), (b) metallic and (c), (d) ionic particle chains of 15 particles with the incident light polarized along the chain axis. The particle-to-particle distance is $d = 3R$. The ion concentration is $n = 10^{\mathrm{mol}}/_{\mathrm{m}^3} N_A$.

# III

# Nonlinear Optics

# 6. Modelling Nonlinear Optical Properties

Nonlinear materials enable ultrafast switching for a wealth of operations such as frequency conversion, pulse generation and signal processing [265, 266]. In addition, structuring can yield enhanced optical nonlinearities and metasurfaces not only allow efficient coupling of light into a nonlinear system boosting the weak multiple photon processes [267], but also controlling the nonlinear fields via beam steering, phase, polarization and amplitude modulation, as well as manipulating their spectral response. Both metal [268] and semiconductor [269] materials can provide strong nonlinearities. Nonlinear properties of several metals were investigated for thin films [270, 271], two-dimensional monocrystalline gold flakes [272] and metal metasurfaces made from both isotropic and anisotropic particles [273]. The enhancement of the optical nonlinearity of metals can reach several orders of magnitude but depends strongly on the employed structure and illumination conditions. This part of our work studies nonlinear optical properties from metal nanoparticles and metal nanostructures.

We take a classical perspective on nonlinear effects in nanostructures, namely, that we understand nonlinear properties of a material through the macroscopic nonlinear polarization $\mathbf{P}$ of a medium stemming from higher order response to a strong external electric field $\mathbf{E}$ [274]. Classical electrodynamics uses the refractive index $n$, the permittivity $\epsilon = n^2$ and the susceptibility $\chi = \epsilon - 1$ as fundamental material parameters. They connect the microscopic material response to an external electric field $\mathbf{E}$ through the macroscopic polarization $\mathbf{P}$ of the material. Depending on the strength of the incident light field, this can yield nonlinear contributions

$$\mathbf{D} = \epsilon_0 \mathbf{E} + \mathbf{P} = \epsilon_0 \epsilon^{\mathrm{lin}} \mathbf{E} + \mathbf{P}^{\mathrm{NLO}}, \tag{6.1}$$

with the linear response captured in the permittivity $\epsilon^{\mathrm{lin}}$. The nonlinear polarization $\mathbf{P}^{\mathrm{NLO}}$ is a function of the electric driving field to a higher order. For weak fields, this can be done in terms of an expansion $\mathbf{P} = \sum_n \mathbf{P}^{(n)}$, each order induced by corresponding multiple photon processes. We consider both (surface) second harmonic generation stemming from nanostructures and third order centrosymmetric nanoparticle systems, where the second order vanishes due to symmetry. Each order $\mathbf{P}^{(1)}$ (linear), $\mathbf{P}^{(2)}$ (quadratic nonlinearities), $\mathbf{P}^{(3)}$ (cubic nonlinearities) is determined through respective susceptibilities $\chi^{(1)}$, $\chi^{(2)}$, $\chi^{(3)}$ which become tensorial for higher orders. Both nonlinear models used in this work are explained in detail in the appendix, namely, the expressions used for the $\chi^{(2)}$ tensor are introduced in appendix E and the anharmonic oscillator model for the third order nonlinear polarization of free and quasi-free electrons in a metal is sketched in appendix F. Resonant nonlinear effects in nanostructures with third order nonlinearities are, thus, understood through a collective response of excited electrons via the standard anharmonic oscillator model yielding susceptibilities built upon Lorentz oscillators around resonances in the linear regime such

as the Mie resonances of the nanoparticles [275]. In this case, the nonlinear strength can be determined in different ways. For gold, we have used fitting of the susceptibility to experimental data in Ref. [271] and checked its overall shape, position and amplitudes with another nonlinear material model stemming from hot electron excitation [276]. However, a common estimation of the nonlinear optical response of materials away from their resonance is given by Miller's rule [274, 277] which can equally be used to obtain an estimate for the nonlinear amplitude strength and will be introduced in the related section.

At nanostructured surfaces, (surface) second harmonic generation is the most prominent type of nonlinear response where the symmetry of nonlinear contributions within the bulk is broken. We study surface second harmonic generation (SSHG) from gold nanogratings where the central goals are the efficient nonlinear optical response within higher diffraction orders and the resonant coupling of the macroscopic nonlinear polarization into the grating structure. The surface lattice resonance in the grating structure can be adjusted by tilting the angle of incidence and, thus, the second harmonic generation can be enhanced. For optimized geometries, both the fundamental and the second harmonic wavelength can be in resonance simultaneously further enhancing the nonlinear signal through doubly resonant lattice plasmon excitation [278].

Third order harmonics become important when due to symmetries in the structure the second order response can be neglected. This is the case for centrosymmetric systems such as spherical nanoparticles. For amorphous composites made from gold and iridium nanoparticles embedded in a transparent host material, we study the optical Kerr effect, i. e. assuming that the driving field and nonlinear polarization the coincide in frequency, and the influence of the mixture on the overall optical and nonlinear properties. For Cross-Phase Modulation (XPM), i. e. cases where the incident and polarization fields are at different frequencies, we study the impact of the metal loading on the dephasing time [279]. Different dephasing mechanisms, for instance, can lead to identical linear responses, however, nonlinear investigation techniques, such as nonlinear polarization holography [280, 281] with an increased parameter space in the XPM regime, enables insights into excitation dynamics and relaxation mechanisms such as dephasing times. This is done in collaboration with experimental partners where the fabrication of such amorphous composites is based on Atomic Layer Deposition (ALD) [282, 283]. Their work focuses on iridium composite structures used e. g. in x-ray mirrors. In the literature, the most comprehensive collection of experimentally obtained nonlinear data is available for gold [271] and we make use of this data to build and understand a model for iridium nanostructures. Here, we study thin films of gold and iridium nanocomposites with respect to saturated and reversed saturated absorption effects [284].

The ultimate goal of this line of research is the tailoring of nanostructured and nanocomposite metasurfaces with respect to not only their linear but also their nonlinear optical response.

# 7. Structure-induced Nonlinearities

## 7.1 Surface Second Harmonic Generation

We study gold nanostructures and their ability to produce and enhance a second harmonic signal stemming from symmetry breaking at the surface due to nanostructuring. Special attention is put to the question of efficient coupling of the nonlinear signal into specific diffraction orders maximizing their respective intensities. Conditions are investigated under which both the fundamental and the second harmonic wave are in resonance with the structure, thus, allowing a doubly resonant plasmonic lattice excitation in gold nanostructures [278].

Here, we present our results on one-dimensional Au gratings on a fused silica substrate in vacuum. The structure has a period of $a_x$ and the gold grating has a stripe width of $w_x$, along the $y$-axis the structure is assumed to be infinite with fully translational symmetry. The thickness of the gold diffraction grating is set to $d = 50$ nm.

### 7.1.1 Structure-induced diffraction anomalies

Evaluating the empty lattice condition for the lowest, non-vanishing diffraction order

$$|\mathbf{k}_{\parallel} - \mathbf{G}| = k_0\sqrt{\epsilon} \quad \Rightarrow \quad \frac{2\pi}{a_x} = \frac{2\pi}{\lambda}\sqrt{\epsilon} \tag{7.1}$$

at normal incidence ($\mathbf{k}_{\parallel} = 0$) yields the Rayleigh condition

$$\lambda_R = a_x\sqrt{\epsilon} \tag{7.2}$$

resulting in the expected wavelength with transmittance minima (reflection maxima) due to a low order lattice resonance with the environment. In non-dispersive, weakly interacting media, this is a good approximation and Rayleigh anomalies, including for higher angles, can be interpreted analytically for different environments and substrates $\epsilon$.

In metallic gratings, another type of anomaly can be observed when the folded SPP condition

$$|\mathbf{k}_{\parallel} - \mathbf{G}| = k_{\mathrm{SPP}} \tag{7.3}$$

if fulfilled, i. e. when the parallel momenta of the incident light matches the bound surface plasmon polariton (SPP) for the considered interface. At normal incidence and for the lowest, non-vanishing diffraction order similar to before

$$\frac{2\pi}{a_x} = \frac{2\pi}{\lambda}\sqrt{\frac{\epsilon\epsilon_{nn}}{\epsilon + \epsilon_{nn}}}. \tag{7.4}$$

Hereby, $\epsilon_{nn}$ represents the effective permittivity of the nanostructure. Its lowest order Fourier

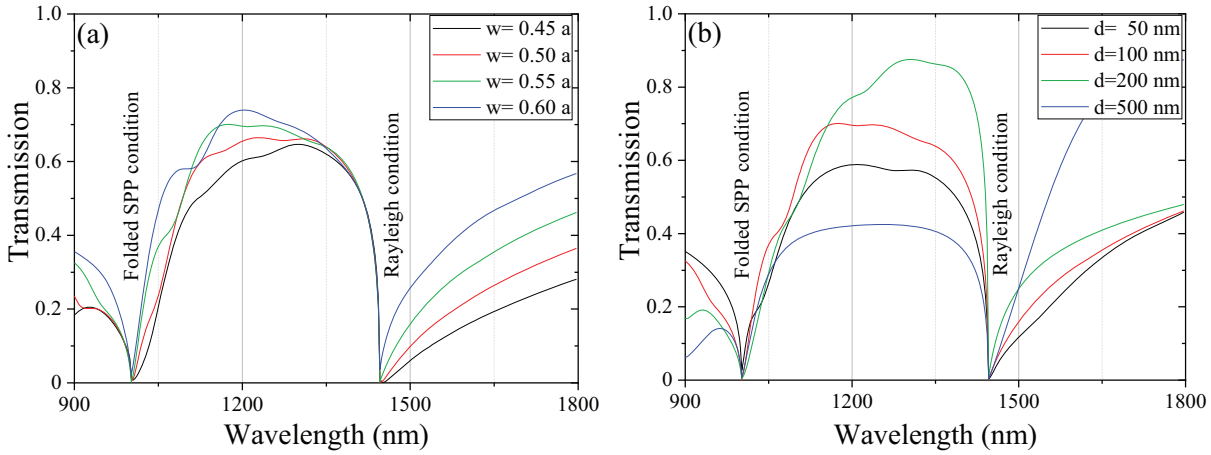


Fig. 7.1.: Transmission of one-dimensional gold gratings with grating period $a = 1000$ nm and (a) height of $d = 50$ nm and varying grating width and (b) varying grating height at constant width $w = 0.5a$.

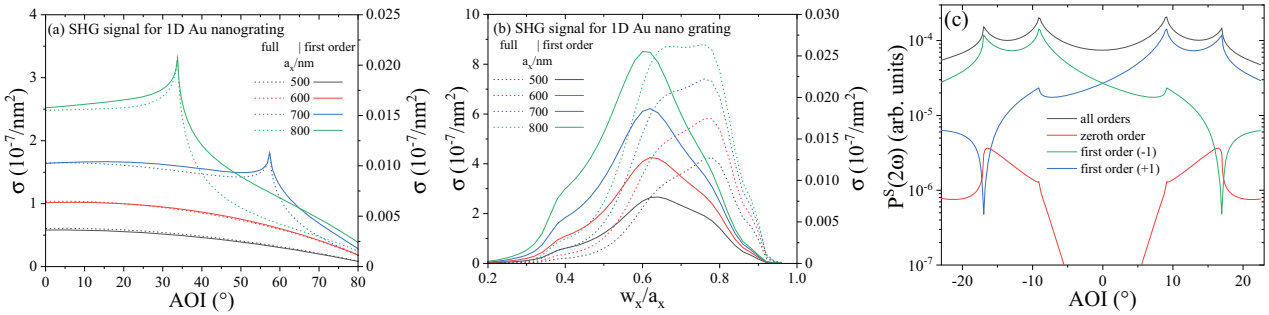


Fig. 7.2.: The nonlinear cross section, see eq. (7.6), is shown as a function of (a) the angle of incidence at $w_x/a_x = 0.5$ and (b) the fill factor of the gold grating in the unit cell at $\Theta = 0°$ for all orders of diffraction (dashed lines) and the first order of diffraction only (solid lines). The fundamental wavelength here is $1.5\mu$m. (c) Symmetries in the different diffraction orders of the second order macroscopic polarization with respect to the angle of incidence. The total polarization (black) and the zeroth diffraction order (red) are fully symmetric, while all higher numbers, here the positive first order (blue) and negative first order (green), are symmetric to each other and regain full symmetry upon summation.

coefficient is given by the diagonal element of the coefficient matrix derived in detail for different structures in appendix A. This allows for an improved estimation of the folded SPP condition in contrast to evaluating the $k_{\mathrm{SPP}}$ for flat interfaces between homogeneous structures.

We evaluate these photonic bandgap conditions for one-dimensional gold nanogratings shown in Fig. 7.1 varying stripe widths and heights. Despite these geometrical changes the numerically observed Rayleigh anomaly at $\lambda_R = a_x\sqrt{\epsilon} \approx 1446$nm for $a_x = 1000$ nm as well as the folded SPP position at $\lambda_{\mathrm{SPP}} \approx 1028$ nm are remarkably stable and confirm the analytic empty lattice picture. These analytics allow a first estimation of optimal parameters, here for the linear case. Considering the fundamental and second harmonic wavelength together, it enables us to find conditions under which both waves coexist and deepens the understanding of doubly resonant structures in the nonlinear case.

### 7.1.2 Second Order Macroscopic Polarization

We study the nonlinear properties of nanostructures in terms of the surface second order macroscopic polarization $\mathbf{P}^s_{2\omega} = \mathbf{P}^s_{2\omega\parallel} + \mathbf{P}^s_{2\omega\perp}$. The main ingredient are the near-fields calculated at the excitation wavelength along the surface. For the one-dimensional structure, this involves the four sides of the grating in the unit cell, as the $y$-direction contributes with a pure scaling factor. The expressions for the related susceptibilities relevant for the polarization field perpendicular and parallel to the nanostructure are given in appendix E.

The nonlinear polarization can further be used to calculate a nonlinear cross section from the Poynting vector $\mathrm{S}$ with electric $\mathbf{f}_E$ and magnetic $\mathbf{f}_H$ field amplitudes

$$\mathbf{f}_E = k^2\left(\mathbf{p} - \mathbf{r}(\mathbf{r}\cdot\mathbf{p})\right), \quad \mathbf{f}_H = k^2\left(\mathbf{r}\times\mathbf{p}\right), \quad \Rightarrow \quad \mathbf{f}_E \times \mathbf{f}_H \; = k^4\mathbf{p}(\mathbf{r}\times\mathbf{p}) = k^4\left(|\mathbf{p}|^2 - |\mathbf{p}\cdot\mathbf{r}|^2\right), \tag{7.5}$$

where $\mathbf{p}$ is the electric dipole moment. The number of scattered photons in terms of an energy rate or power is

$$\mathcal{P} = 2Re\int(\mathbf{S}\cdot\hat{\mathbf{r}})r^2 d\Theta = \frac{2c}{4\pi}k^4\int d\Theta\left(|\mathbf{p}|^2 - |\mathbf{p}\cdot\mathbf{r}|^2\right) = \frac{2\pi c}{2\pi}k^4\int_{-1}^{1} d\cos\theta|\mathbf{p}|^2(1-\cos^2\theta) = \frac{4}{3}\frac{ck^4}{\hbar\omega}|\mathbf{p}|^2.$$

This is set in relation with the incoming photons, i. e. the photon flux, normalized by the unit area, to obtain a nonlinear cross section $\sigma$

$$\mathcal{P}_0 = \frac{2c}{4\pi\hbar\omega}\frac{|\mathbf{E}_0|^2}{a^2} \qquad \sigma = \frac{\mathcal{P}}{\mathcal{P}_0} = \frac{8}{3}\pi k^4 a^2\frac{|\mathbf{P}^s_{2\omega}|^2}{|\mathbf{E}_0|^2}. \tag{7.6}$$

In Fig. 7.2(a), we study the second order cross section derived from the local near-fields at the fundamental wavelength for a number of changing setups as a function of the angle of incidence. Rayleigh anomalies are observed for only two of the setups while the other geometries do not show a resonance complying with the Rayleigh condition independently of the diffraction order. The careful tailoring of the geometry under given material parameters will allow to find illumination and geometrical conditions under which the incident light as well as the nonlinear polarization are resonant in the photonic crystal structure. Fig. 7.2(b) studies the second order nonlinear cross section for varying stripe width $w_x$. It substantiates that the SSHG truly stems from (i) the metal and (ii) the nanostructuring simultaneously since the nonlinear signal vanishes at low $w_x < 0.3a_x$ as much as towards high $w_x > 0.9a_x$ stripe widths. Noticeably, the optimum geometry in terms of maximizing the nonlinear signal at this fixed angle of incidence differs for the first order from the the full cross section summing up all contributions. The Fourier Modal Method (FMM) allows to study the surface second order macroscopic polarization in different diffraction orders. Fig. 7.2(c) shows the symmetries of the zeroth, first and total sum of the second order polarization varying the angle of incidence. Notably, the zeroth order vanishes for low angles so that the nonlinear polarization is concentrated in the first order, a behaviour in one-dimensional structures which

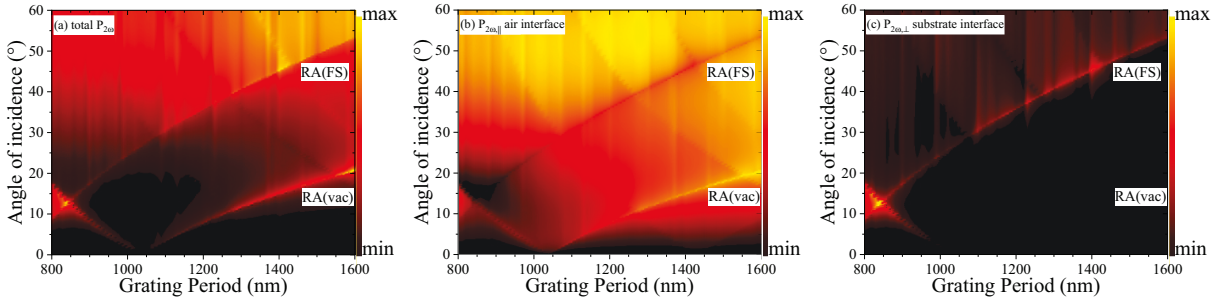


Fig. 7.3.: Second order macroscopic polarization stemming from surface near-fields around one-dimensional gold nanogratings of increasing grating period at varying angle of incidence. Showing (a) the total polarization including contributions from all faces, parallel and perpendicular fields; (b) the parallel contribution from the upper gold surface to the air/vacuum environment and (c) the perpendicular contribution from the lower gold interface to the fused silica substrate. The calculation uses a decomposition into 201 plane waves. Arbitrary units are used.

was experimentally observed in Ref. [285]. All orders show the aforementioned Rayleigh anomalies, here stemming from the near-fields at the fundamental wavelength at the upper and lower interface of the nanostructure.

In Fig. 7.3, we calculate the nonlinear polarization from different surfaces as well as for the parallel and perpendicular contributions. The contributions to the surface second order macroscopic polarization on each side of the nanograting reflect the Rayleigh anomalies (RA) in the system at the different surfaces. Note that the side contributions are minor compared to the upper and lower surface and cancel each other due to opposite signs when the ratio of the stripe width to the unit cell length is exactly $0.5 = {}^{w_x}/_{a_x}$. Next to the full result of all contributions in Fig. 7.3(a), it is instructive to consider them separately. From these results it can be seen that each setup exhibits two relevant resonant features at different angles of incidence related to the Rayleigh anomalies at the upper (RA air) and lower (RA substrate) surfaces. However, if we consider the upper interface contributions as in Fig. 7.3(b), the RA at the lower surface will be suppressed and vice versa in Fig. 7.3(c). We compare to experiments performed at one-dimensional gold nanostructures measuring the second harmonic signal in zeroth order for gratings with varying periodicity as a function of incident angle for both positive and negative angular range [278]. The angles of incidence showing Rayleigh anomalies are identified. In Fig. 7.4(a), we compare the measured signal at the RA of the upper surface as a function of the grating period with the calculated nonlinear polarization at the respective surface. While their units cannot be compared, the overall behaviour is in very good agreement. To allow quantitative comparisons, we evaluate for each grating period the relative amplitude of the Second Harmonic Generation (SHG) signals at the two Rayleigh anomalies at the upper and lower interfaces in Fig. 7.4(b). The experiment allows evaluating this for positive and negative angle of incidence with little differences between these two (shaded green area). Comparing the relative peak strength from the total nonlinear polarization to corresponding experimental results [278], we see that the agreement is very good up to the maximum value of the relative peak amplitudes. For larger grating periods, the theoretical approach does

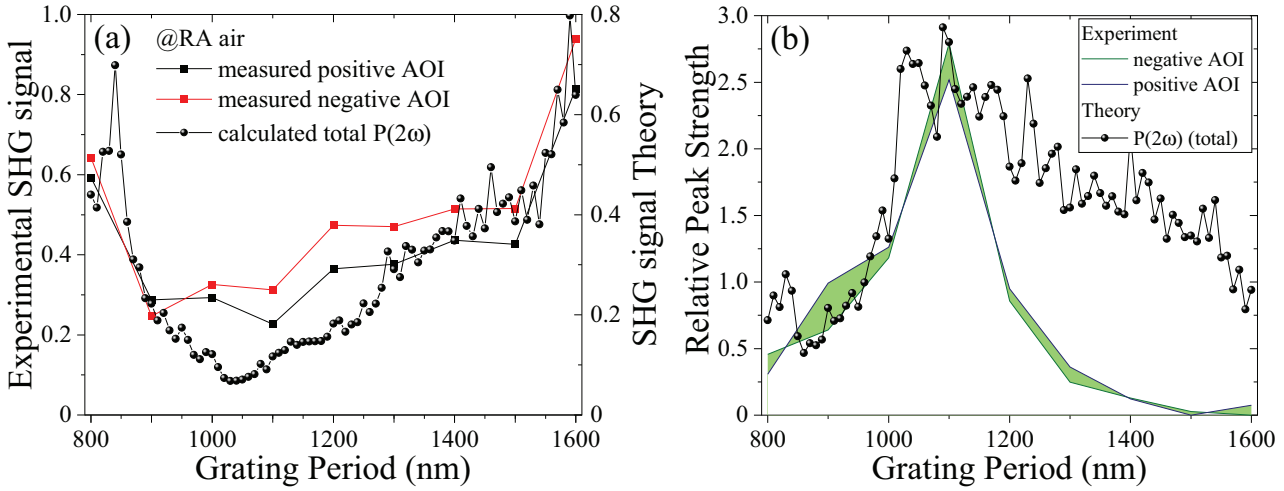


Fig. 7.4.: Comparison between experiment and theory for one-dimensional gold nanogratings. (a) Second harmonic signal measured (squares) and calculated (circles) at the upper interface towards air adjusting the angle of incidence to meet the Rayleigh condition. (b) Relative peak strength between the signal amplitudes at the two Rayleigh anomalies for the measured (green and blue curve) and the calculated (circles) SHG signal.

predict a reduction of the relative peak strength, but it does not drop as quickly as observed in the experiment. This can be better understood by considering the different contributions separately, as was shown in Fig. 7.3. One of the peaks associated to the Rayleigh condition matched at the upper or lower interface vanishes when considering the contribution from the opposite interface. Hence, the parallel and perpendicular contributions to the Rayleigh anomaly of the upper interface vanish at the lower interface and vice versa. In the relative peak strength, this leads to divergent contributions. Considering, therefore, the separate contributions, it can be seen that indeed, the ones not diverging agree with the measurements better, while still showing a broader peak structure than the experiment.

In both these results, the theoretical curves are oscillatory with the grating period. As they are calculated from the near-fields at the surfaces, this is directly connected to the oscillatory nature of the electric fields. The Bloch modes forming between the metallic stripes, which are calculated numerically from the FMM are highly sensitive to structural changes.

# 8. Properties of amorphous Composites

## 8.1 Kerr Nonlinearities of amorphous Nanostructures

Many applications exploit nanoparticles randomly distributed in a transparent layer. Amorphous composite materials can be obtained from techniques such as Atomic Layer Deposition (ALD) [282, 283] with high precision with respect to the final film thickness, composite density $f$ and surface morphology with very low root mean square (rms) randomness of the obtained surfaces. If using metal inclusions, such amorphous layers can be used for increasing local fields inside the host matrix allowing for intense near-field interactions with the host material, e. g. in polymer platforms for photovoltaic devices such as dye-sentisized and other organic solar cell technologies [34, 243]. Likewise, metal nanoparticles on surfaces enhance signals for spectroscopic measurements such as SERS or in microscopy such as Scanning Near-Field Optical Microscope (SNOM) and Atomic Force Microscopy (AFM). On the other hand, should the composite materials exhibit nonlinear optical properties, the total nonlinear output fields can likewise be enhanced due to the presence of nanoparticles. Ultimately, the design of nonlinear metasurfaces [265, 286–288] has the potential to add a new dimension to the control of light fields and enhancement phenomena at the nanometer scale.

Obtaining the optical response of such inhomogeneous materials from rigorous calculations is often tedious. Hence, amorphous composites are typically described with effective medium theories (EMTs) where the material parameters are homogenized to obtain a single, effective permittivity for the entire composite layer. To achieve this, however, a number of critical approximations are made such as dipolar and quasistatic approximations and an overall limitation to very low particle densities is needed to avoid particle-particle interactions and omit multiple scattering and coupling effects, which strongly restricts the applicability and quality of EMTs [289–291]. A more recent approach is a gradient model, where a film containing nanoparticles of different sizes is subdivided into layers for which an effective permittivity is calculated separately [292]. It does slightly improve upon the common EMTs, however, does not reach the material predictions of rigorous FDTD calculations.

Amorphous composites of low fill fraction $f$ both in solids and in liquids are typically studied within Maxwell-Garnett (MG) [293] and Bruggeman (Br) theory and to both of them nonlinear extensions exist [294–296] and are introduced in appendix G. In this section, we critically compare these two EMTs for thin gold films with third order nonlinear properties and give a detailed account on the conditions to observe saturated and induced absorption [284] as was discussed in experiments, see for instance Ref. [297] on nanoplanets. Our findings are important for understanding the mechanism of Kerr nonlinearity in amorphous composites and nonlinear enhancement in metallic composites with little losses at low densities. Moreover, our approach can be used to investigate stacks of amorphous composites building nonlinear hyperbolic materials [275].

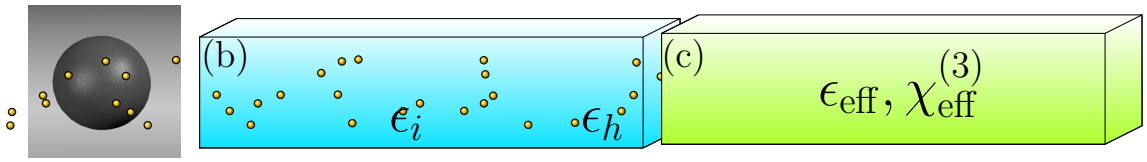


Fig. 8.1.: Illustration of effective medium theories: (a) Metal nanoparticle (b) with permittivity $\epsilon_i$ embedded in the nonlinear host material $Al_2O_3$ of permittivity $\epsilon_h$. (c) The system is treated within nonlinear Maxwell-Garnett and Bruggeman theory to arrive at a homogeneous layer with effective permittivity $\epsilon_{\text{eff}}$ and effective third order susceptibility $\chi^{(3)}_{\text{eff}}$.

We consider the two metals gold and iridium. While we can rely on their linear bulk properties being well described by tabulated data (gold [67], iridium [298, 299]) obtained from ellipsometry measurements, a lack of nonlinear optical data over a wide range of wavelength makes a simple, but consistent model of nonlinear parameters challenging. For a small number of incident wavelengths, pulse durations and measurement techniques, available datasets for gold were collected in Ref. [271]. In recent work, similar studies were performed on iridium nanoparticle layers [299]. As detailed in appendix F, we use a third order nonlinear susceptibility from the anharmonic oscillator model, ascribing the nonlinear optical response to the resonant excitation of the free electron gas. To obtain a nonlinear amplitude strength, we fit to experimental data available for gold [271] and to the common low frequency result from Miller's rule [274, 277] for a purely theoretical model for the low-frequency limit $\omega \to 0$. We find the latter to overestimate the susceptibilities in the resonant regime. The former is in good agreement with a material model based on temporal electron dynamics using thermo-modulation of the nonlinear response [276] for the bulk material.

In this section, we study nanoparticles embedded in a finite layer within linear and nonlinear Maxwell-Garnett (MG) and Bruggeman (Br) theory [293]. The former starts from spherical NP inclusions in a host matrix while the latter does not differentiate between the roles the materials in the composition take. For arbitrary mixtures, Br theory is often to be preferred. Nonlinear extensions to both MG and Br theory are available in the literature allowing to study either nonlinear host materials or inclusions or their combined nonlinear effects [294–296].

The lowest order electric Mie resonance of truly nano-sized particles in amorphous thin films determines the spectral position of their nonlinear response. It is therefore important to take the particle size distribution into account, in particular, for a large size spread [300]. Besides the dipole approximation, standard Maxwell-Garnett theory [293] uses the quasistatic approximation to the electric polarizability, a term that should be replaced by its corresponding dipolar Mie coefficient for larger particle sizes [300] to correctly include radiation losses.

For the thin films we study here, see Fig. 8.1, we restrict ourselves to metal nanoparticles of 5 nm size where the dipolar and quasistatic approximation are valid for both of the discussed materials, gold and iridium. The shift of their Localized Surface Plasmon Resonances (LSPR) with changing diameter can be neglected in this size range. Fig. 8.1(b) shows the amorphous structure in mind with metal nanoparticles dispersed in the nonlinear, transparent host material

and Fig. 8.1(c) illustrates the concept of effective medium theories. Here, an effective linear permittivity is calculated as well as an effective nonlinear third order susceptibility which together form the nonlinear effective permittivity. This latter quantity is dependent on the intensity the material system is exposed to and thus, ultimately, on the depth within such an amorphous layer as the intensity drops inside due to absorption.

### 8.1.1 Third order nonlinear susceptibilities

In general, the anharmonic oscillator model, see appendix F , yields for the $i$-th component ($i \in \{x, y, z\}$) of the third order macroscopic polarization $\mathbf{P}^{(3)}$

$$P_i^{(3)}(\omega_q) = \epsilon_0 \sum_{jkl} \sum_{mno} \frac{Nbe^4}{3\epsilon_0 m_e^3} \frac{(\delta_{ij}\delta_{kl} + \delta_{ik}\delta_{jl} + \delta_{il}\delta_{jk})\, E_j(\omega_m) E_k(\omega_n) E_l(\omega_o)}{D(\omega_m + \omega_n + \omega_o) D(\omega_m) D(\omega_n) D(\omega_o)} \delta(\omega_q - \omega_m - \omega_n - \omega_o). \tag{8.1}$$

Hereby, $e$ is the elementary charge of an electron, $m_e$ the electron mass, $\epsilon_0$ the free space permittivity and $N$ is the electron density, which can be summarized into the plasmon frequency $\omega_p$ of the considered material through $\omega_p^2 = {}^{Ne^2}/_{\epsilon_0 m_e}$. Furthermore $b$ characterizes the strength of the nonlinearity. The first sum runs over the components of the incident electric fields $E_i$ at different frequencies. The latter sum over frequencies demands that $\omega_q = \omega_m + \omega_n + \omega_o$. This is reflected in the denominators $D(\omega) = \omega_0^2 - \omega^2 - i\gamma\omega$, where $\omega_0$ is the material resonance stemming from the electron motion and $\gamma$ is the associated damping due to charge carrier collisions. These are given by the Mie resonances of the respective materials. As we are interested in studying amorphous materials, it is important to note that the size distribution should be taken into account if the size range covers multiple resonance frequencies. For the linear regime, this has been addressed by Ref. [300]. For particle sizes below 10 nm only small variations in the resonance position are expected within classical electrodynamics and, thus, we do not consider a shift in the resonance positions in our thin film calculations. Here, nonlinear properties are studied purely for the case of self-phase modulation, i. e. all fields are monochromatic at the same frequency $\pm\omega$, so that a major contribution to the macroscopic polarization stems from nonlinear response at the incident frequency. The anharmonic oscillator model yields the third order susceptibility at frequency $\omega$ as $\chi^{(3)}(-\omega|\omega,\omega,-\omega) = {}^{B}/_{(|D(\omega)|D(\omega))^2} \equiv \chi^{(3)}(\omega)$ for materials with an electronic response.

We consider planar thin films with p-polarized incident light. The total optical response including third order polarization effects stemming from Kerr nonlinearities at frequency $\omega$ and third harmonic generation (THG) at frequency $3\omega$ can be described through the electric displacement vector in frequency space

$$\begin{aligned}\mathbf{D}(\omega, \mathbf{r}) = \epsilon_0 \epsilon_{\mathrm{NLO}} \mathbf{E}(\omega, \mathbf{r}) = \epsilon_0 \mathbf{E}(\omega, \mathbf{r}) + \epsilon_0 \chi^{(1)}(\omega) \mathbf{E}(\omega, \mathbf{r}) \\ + \epsilon_0 \chi^{(3)}(-\omega|\omega,\omega,-\omega) |\mathbf{E}(\omega, \mathbf{r})|^2 \mathbf{E}(\omega, \mathbf{r}) + \epsilon_0 \chi^{(3)}(-3\omega|\omega,\omega,\omega) \mathbf{E}^3(\omega, \mathbf{r}).\end{aligned} \tag{8.2}$$

Note that we have already taken advantage of the fact, that spherical metal nanoparticles

exhibit vanishing second order nonlinear response. The contribution from the THG term is negligible for frequencies around the incident frequency $\omega$ and third order nonlinear effects can be considered separately. For thin film calculations around resonance, we determine an effective permittivity $\epsilon_{\mathrm{NLO}}$ from linear calculations [295] in a first step

$$\epsilon_{\mathrm{NLO}}(z,\omega) = \epsilon_{\mathrm{eff}}(\omega) + \chi^{(3)}_{\mathrm{eff}}(\omega)|\mathbf{E}(z,\omega)|^2. \tag{8.3}$$

and–as it is dependent on the incident, local field–iterate the input fields until we obtain a self-consistent result exploiting the scattering matrix scheme for several hundreds of subdivisions of the nonlinear amorphous layer.

Nonlinearities are sensitive to the duration of an incident laser pulse. A fully time- and space-dependent light beam of Gaussian shape can be described by

$$\mathcal{I}(x,y,t) = \mathcal{I}_0(\tau, w, f_{\mathrm{rep}})e^{-2(t/\tau)^2}e^{-\frac{x^2+y^2}{w^2}} \tag{8.4}$$

assuming the surface of the structure at $z = 0$. Hereby, $\tau$ is the pulse duration, $f_{\mathrm{rep}}$ is the repetition rate and $w$ is the beam width. The average power $P$ of the pulse is related to the pulse energy $\mathcal{E}$ via the repetition rate $P = \mathcal{E} f_{\mathrm{rep}}$. The peak intensity is then given by

$$\mathcal{I}_0 = \left(\frac{2}{\pi}\right)^{3/2} \frac{P}{\tau\ w^2 f_{\mathrm{rep}}}. \tag{8.5}$$

This allows us to deduce the equivalent electric field from

$$\mathcal{I}_0 = \frac{1}{2} c\epsilon_0 \sqrt{\epsilon} E^2_{\mathrm{eq}} \tag{8.6}$$

and connect experimental input parameters to our calculations. However, while this renders the local electric field input dependent on the pulse duration and beam width, it does not inform about intrinsic nonlinear material parameters. Next, we discuss different models for the third order nonlinear susceptibility $\chi^{(3)}_{\mathrm{eff}}(\omega)$.

### 8.1.2 Amplitude according to Miller's rule

Miller's empirical rule [274, 277] connects the nonlinear strength $b$ to material constants in the limit $\omega \to 0$. This allows an assessment of the nonlinear amplitude. Hereby, we rely on fundamental properties of the solid crystal structure such as the lattice constant $a_0$ which gives an estimate of the displacement an electron in the atomic crystal structure can experience. The shortest distance between atoms in an fcc atomic lattice is $a_0/\sqrt{2}$.

For the third order, it implies that $b = 2\omega_0^2/a_0^2$ yielding the low-frequency limit according to Miller's rule

$$\chi^{(3)}_{\mathrm{Miller}} = \chi^{(3)}(\omega \to 0) = \frac{2\omega_p^2 e^2}{m_e^2 \omega_0^6 a_0^2} = \mathrm{const.} \tag{8.7}$$

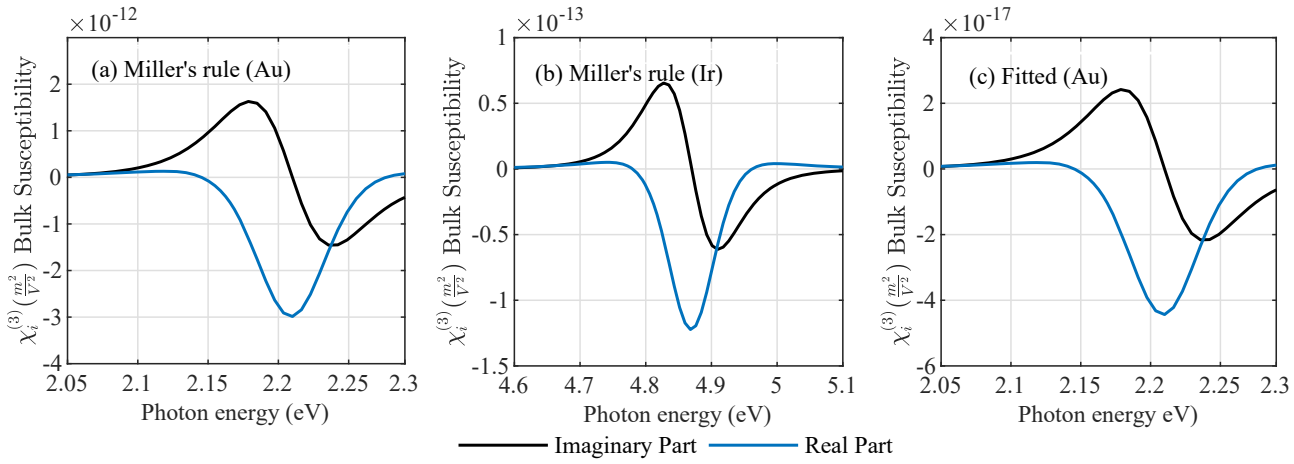


Fig. 8.2.: Third order bulk susceptibility $\chi_i^{(3)}$ as a function of photon energy $E = \hbar\omega$ for (a), (c) Au and (b) Ir using (a), (b) the analytic Miller's rule and (c) fitting the nonlinear strength amplitude to available experimental data [271].

In this limit, 5 nm gold nanoparticles ($a_0 = 4.078$Å, $\gamma = 0.13$ eV, $\omega_p = 8.9$ eV) close to their Mie resonance $\omega_0 = 2.23$ eV have an estimated third order nonlinear susceptibility of $\chi^{(3)}_{\text{Miller, Au}} = 2.0 \times 10^{-15}\text{m}^2/\text{V}^2$, while this yields $\chi^{(3)}_{\text{Miller, Ir}} = 2.51 \times 10^{-17}\text{m}^2/\text{V}^2$ for iridium ($a_0 = 3.839$Å, $\omega_0 = 4.87$ eV, $\gamma = 0.18$ eV, $\omega_p = 7.2$ eV) both in $Al_2O_3$. Note that the environment enters this estimation through the Mie resonances calculated for the nanoparticles in that specific host material.

The bulk susceptibilities of gold and iridium are compared in Fig. 8.2 for the two cases using Miller's rule for Au and Ir and experimental data for Au [271] to find a nonlinear amplitude. Miller's rule can support the understanding of the general behaviour of such systems, however, it shows a strong discrepancy compared to the bulk susceptibility fitted to available experimental values. In general, Miller's rule overestimates the nonlinearity of metal structures under resonant conditions [301]. A further factor that comes into play during experiments is the pulse duration of the incident light field which can shift the measured susceptibility by many orders of magnitude as was shown in Ref. [271]. The anharmonic oscillator model yields an instantaneous result which corresponds to $\tau \to 0$ and does not include the aspect of finite pulse duration. Density functional theory (DFT) could take into account the impact of a finite pulse [302–304] and will be discussed in future work. Finally, it should be noted that in the case of gold, measurements under both resonant and off-resonant conditions are available.

### 8.1.3 Ultra-Thin Films made from Nonlinear Composites

Within the composite thin films the incident light is absorbed by the present metal nanoparticles and we expect a typical absorption curve within the homogenized layers. The local intensity modifies the local permittivity depending on the nonlinear coefficients and the depth inside the thin film which is iterated until a stable output field at each position along the layer is found. In a first step, we present in Fig. 8.3 the modified nonlinear permittivity as a function of both frequency $\omega$ of the incident light wave and varying fill fraction $f$ independent

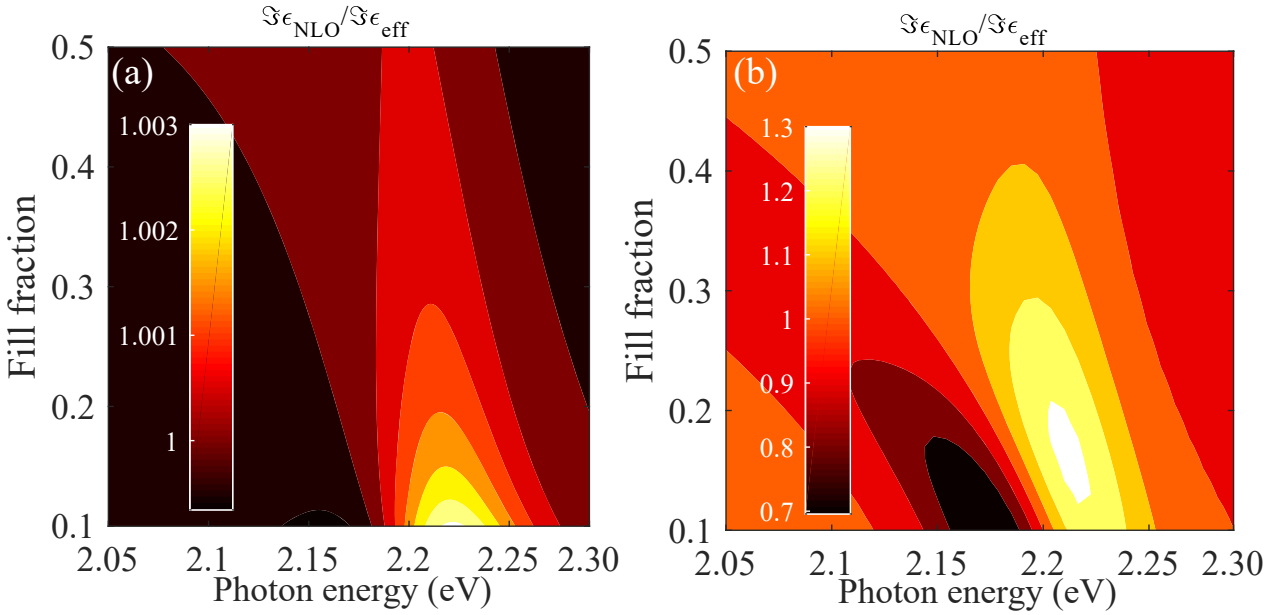


Fig. 8.3.: Imaginary part of the modified nonlinear permittivity, eq. (8.3), relative to the linear case for gold using the data fitted to available experimental data [271]. Results for (a) Bruggeman and (b) Maxwell-Garnett theory for varying fill fraction as a function of incident photon energy are compared. The incident field is $|\mathbf{E}|^2 = 7 \times 10^{14}\mathrm{V}^2/\mathrm{m}^2$. Note the strong difference in predicted changes in the local permittivity.

from the film thickness as different depths will be exposed to different light intensities. We concentrate on the case of gold with parameters fitted to experimentally available values [271] and show in Fig. 8.3(a) the results for Bruggeman and in Fig. 8.3(b) the corresponding results for Maxwell-Garnett theory of the nonlinear permittivity. Due to the nature of the effective susceptibility, we observe spectral regions with increased or decreased total permittivity depending on the sign of the effective susceptibility around the Mie resonance of the considered nanoparticle. Qualitatively, this is the same result for different metallic materials, where the main contribution to the suceptibility in the anharmonic oscillator model stems from the electronic excitation. Increasing the fill factor increases overall absorption with a critical value depending on the material as depicted in Fig. G.2(c) for gold and overall shifts the position of the maxima and minima observed. Here, again, the large local field factors in M-G theory are strongly overestimating the nonlinear response of the amorphous films leading to the prediction of strong changes in the modified permittivity several orders of magnitude larger than Bruggeman. This is in contradiction to observations made on nonlinear properties of thin films and we restrict our further considerations to Bruggeman theory.

Note that the sign of real and imaginary part are opposite in the respective spectral regions close to the resonance frequency. In total there are four possible sign combinations, as detailed in Fig. G.1 in the appendix: (i) Both real and imaginary part can be positive, typically close to but above the resonance frequency; (ii) the real part is negative shortly before reaching the resonance frequency while the imaginary part is still positive; (iii) far from resonance the real part is negative below and (iv) positive above the resonance, however, the sign of the imaginary part depends more subtly on the material model due to the local field

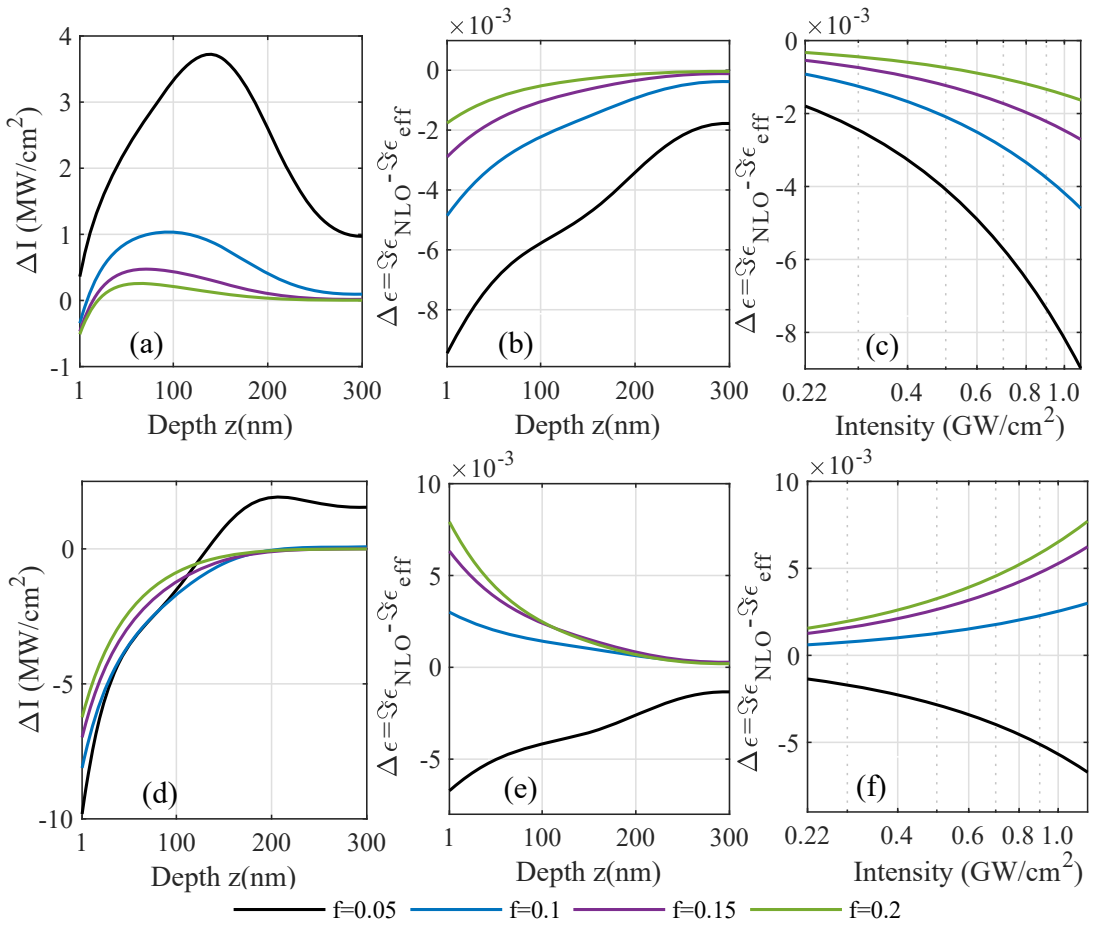


Fig. 8.4.: As a function of the position $z$ inside a 300 nm composite film for frequencies below the Mie resonance of gold nanoparticles the (a), (d) change in total intensity $\Delta I = I_{\mathrm{NLO}} - I_{\mathrm{lin}}$ (forward and backward scattering) and (b), (c), (e), (f) change in the imaginary part of the nonlinear permittivity $\Delta \mathrm{Im}\ \epsilon = \mathrm{Im}\ \epsilon_{\mathrm{NLO}} - \mathrm{Im}\ \epsilon_{\mathrm{eff}}$ are shown for gold with input values fitted to available experiments. [271] Cases with saturated and induced absorption are observed. The set frequencies are 2.15 eV in the upper panel and 2.20 eV in the lower panel. The incident power density is $1.6\ {}^{\mathrm{GW}}/_{\mathrm{cm}^2}$.

factors. These combinations can lead to different behaviours inside the film with increasing intensity. As the incident intensity modifies the local permittivity in eq. (8.3) it changes in turn the local intensity the particles experience.

We demonstrate in Fig. 8.4 cases for saturated and induced absorption in amorphous gold/$Al_2O_3$ films. A self-consistent, iterative scheme is used to recalulate the local, saturated intensity after reintroducing the modified nonlinear permittivity a number of times. This is done throughout the film to obtain the local permittivity self-consistently with the scattering matrix scheme for planar systems using a few hundred subdevisions of the film. The change in the imaginary part of the modified nonlinear permittivity $\Delta \mathrm{Im}\ \epsilon = \mathrm{Im}\ \epsilon_{\mathrm{NLO}} - \mathrm{Im}\ \epsilon_{\mathrm{eff}}$ is shown as a function of the depth in Figs. 8.4(b) and (e) and as a function of the incident power density in Fig. 8.4(c) and (f), respectively. For both dependencies, the change induced by the nonlinearity of the amorphous film is of the order of $10^{-3}$ refractive index units tending towards zero further inside the film where the local intensity drops towards the linear case. For

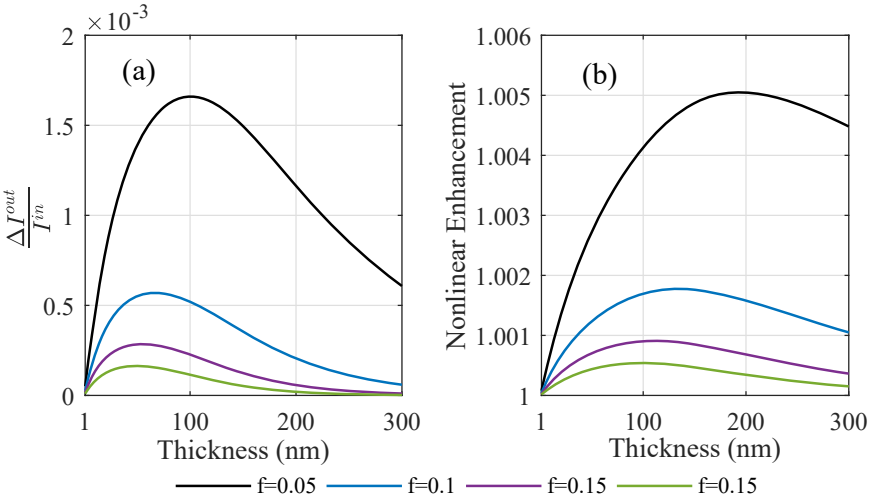


Fig. 8.5.: Varying the film thickness of amorphous composite films of different fill fractions $f$, (a) the normalized difference in transmitted intensity $\Delta I = I_{\mathrm{NLO}} - I_{\mathrm{lin}}$ and the (b) relative intensity enhancement due to nonlinear effects in ultra-thin metallic amorphous films are shown. The incident power density is $1.6\ {}^{\mathrm{GW}}/_{\mathrm{cm}^2}$.

frequencies well below the Mie resonance of the gold nanoparticles, the absorption related to the imaginary part of the nonlinear permittivity decreases for increasing laser intensity with increasing intensity. The changes induced by the nonlinearity are in the range of a few ${}^{\mathrm{MW}}/_{\mathrm{cm}^2}$. This effect is known as saturated absorption [284], i. e. the effective susceptibility is positive in its imaginary part.

In Bruggeman theory, the effective susceptibility decreases with the fill factor for gold which is why the strongest change in the imaginary part of the permittivity is seen for smaller fill fractions in contrast to Ir where the susceptibility does not change as notably with the fill fraction. In contrast, for frequencies much closer to the Mie resonance as depicted in Figs. 8.4(d), (e) and (f), this behaviour is reversed because the imaginary part of the effective susceptibility vanishes at resonance and reverses its sign. The lowest fill factor shows a weaker saturated absorption as before while the higher fill factors with a larger input from the small but negative nonlinear susceptibility enter the regime of induced absorption. This observation is independent of the considered material as it is directly related to the sign of the susceptibility given by the material-dependent Mie resonance and the overall position. It is shifted to lower frequencies for the amorphous structures with increasing fill factors as discussed in Fig. G.2 in the appendix.

We study the transmitted power flux of ultra-thin amorphous composite Au/$Al_2O_3$ layers in Fig. 8.5(a) as a function of film thickness using the experimentally available data [271]. The difference between linear and nonlinear case is notable in the relative enhancement factor extracted in Fig. 8.5(b). For large enough films, the intensity inside the composite layer drops due to absorption entering the linear regime before reaching the glass substrate. Nonlinear intensity enhancement effects take place within the first tenth to hundreds of nanometers in the homogenized film. The enhancement factors are susceptible to the fill fraction reaching a maximum for different film thicknesses. The detriment of metallic absorption to the nonlinear

enhancement is reflected in the fact that the larger fill factors show decreasing nonlinear enhancement as compared to smaller particle densities.

### 8.1.4 Concluding Remarks

In this section, we focused on self-phase modulated (SPM) nonlinear effects in amorphous composites made of gold and iridium nanoparticles embedded in an equally nonlinear host matrix employing nonlinear formulations of Maxwell-Garnett and Bruggeman theory. Effective medium theories allow homogenization of the linear and nonlinear material properties of amorphous composite layers [275]. The validity is bound to sufficiently low densities where interparticle effects are negligible both for the linear and the nonlinear regime. For the bulk susceptibility, we consider the anharmonic oscillator model and fit its nonlinear strength amplitude to both an analytic expression based on Miller's rule off-resonance and available experimental data for gold susceptibilities.

Note that such material parameters should ultimately be calculated from ab inito theories, e. g. Density Functional Theory (DFT) for bulk material as well as finite clusters of atoms. In addition to the instantaneous nature of the model used here ($\tau \to 0$), ab initio theories allow including the dependence of the susceptibility $\chi$ on the pulse duration $\tau$ of the system. A realistic material will not reach its full nonlinear optical response immediately, but build it up with some delay. Moreover, the longer the material is exposed to the incident electric fields, the stronger the nonlinear optical response can become until saturation sets in.

Such homogenized material properties can further be implemented in standard frameworks to evaluate light interaction with multi-layered systems such as the scattering matrix theory, reducing the light propagation problem to one dimension. This was used here in a self-consistent approach, i. e. the thin films were subdivided into hundreds of layers and in each the modified, depth-dependent nonlinear permittivity was calculated. Moreover, as it is also intensity-dependent, this was done several times recalculating the local intensity each layer is exposed to when nonlinear enhancement is included. This approach is applicable to nonlinear hyperbolic materials from stacks of amorphous composites and nonlinear enhancement in metallic composites with little losses at low densities. We evaluate thin films of amorphous composites with a focus on achievable nonlinear enhancement, saturated and induced absorption based on the compositional configuration. Reasonable values are found with Bruggeman theory using a nonlinear material model fitted to available experimental data for gold. In contrast, both Miller's rule and Maxwell-Garnett theory tend to strongly overestimate the nonlinear susceptibility.

The limits of effective medium theories, in particular for large nanoparticle densities and distances that make interaction effects sizable can be addressed using rigorous methods such as multiple scattering from nanoparticles using nonlinear Mie theory [305–307], and comparison with random nanoparticle distributions at increasing fill factors [26]. A further difficulty with homogenization could be waveguiding effects arising in the host material that are suppressed in EMTs. Another interesting aspect is the influence of finite-size effects in

ultrasmall metal nanoparticles, such as nonlocal optical response which can be addressed with semi-classical theories [53,162,179] and ab initio methods [308,309]. This typically yields shifts of the LSPR position directly impacting the nonlinear susceptibility and, in addition, is accompanied by nonlocal quenching of the local fields overall reducing local intensites found in the classical picture.

## 8.2 Cross-Phase Modulation (XPM)

So far, we have concentrated on the case of a single monochromatic input field and self-phase modulation involving a single frequency. The more general case of Cross-Phase Modulation (XPM) considers several input fields at different frequencies as is the case in pump-probe and wave-mixing experiments. In this section, we expand the case of amorphous composite materials to Cross-Phase Modulation, i. e. allow the third order nonlinear susceptibility to result from several incident frequencies. For the bulk susceptibility, according to eq. (F.18) derived in appendix F

$$\chi_i^{(3)}(-\omega_q|\omega_n,\omega_m,\omega_o) = \frac{\tilde{f}}{D(\omega_q)D(\omega_n)D(\omega_m)D(\omega_o)}. \tag{8.8}$$

The effective third order susceptibility for such nonlinear nanoparticle inclusions $\chi_i^{(3)}(\omega)$ becomes within nonlinear Maxwell-Garnett theory [293]

$$\chi_{\text{eff}}^{(3)}(-\omega_q|\omega_n,\omega_m,\omega_o) = f\mu(\omega_q)\mu(\omega_n)\mu(\omega_m)\mu(\omega_o)\chi_i^{(3)}(-\omega_q|\omega_n,\omega_m,\omega_o), \tag{8.9}$$

while the corresponding expression for nonlinear Bruggeman mixtures becomes

$$\begin{aligned}\chi_{\text{eff}}^{(3)}(-\omega_q|\omega_n,\omega_m,\omega_o) = {} & \frac{1}{f}\left(\frac{\partial\epsilon_{\text{eff}}}{\partial\epsilon_i}\right)_{\omega_q}^{\frac{1}{2}}\left(\frac{\partial\epsilon_{\text{eff}}}{\partial\epsilon_i}\right)_{\omega_n}^{\frac{1}{2}}\left(\frac{\partial\epsilon_{\text{eff}}}{\partial\epsilon_i}\right)_{\omega_m}^{\frac{1}{2}}\left(\frac{\partial\epsilon_{\text{eff}}}{\partial\epsilon_i}\right)_{\omega_o}^{\frac{1}{2}}\chi_i^{(3)}(-\omega_q|\omega_n,\omega_m,\omega_o) \\ & + \frac{1}{1-f}\left(\frac{\partial\epsilon_{\text{eff}}}{\partial\epsilon_h}\right)_{\omega_q}^{\frac{1}{2}}\left(\frac{\partial\epsilon_{\text{eff}}}{\partial\epsilon_h}\right)_{\omega_n}^{\frac{1}{2}}\left(\frac{\partial\epsilon_{\text{eff}}}{\partial\epsilon_h}\right)_{\omega_m}^{\frac{1}{2}}\left(\frac{\partial\epsilon_{\text{eff}}}{\partial\epsilon_h}\right)_{\omega_o}^{\frac{1}{2}}\chi_h^{(3)}.\end{aligned} \tag{8.10}$$

For the derivation of this, it is important to realize that the total energy of each electric field is conserved within the volume leading to the homogenized effective permittivity at the given frequencies [289, 310]

$$\epsilon_{\text{eff}}(\omega_\alpha)E_{\text{eff}}^2(\omega_\alpha) = \frac{1}{V}\int_V \epsilon(\mathbf{r},\omega_\alpha)E^2(\mathbf{r},\omega_\alpha)\mathrm{d}^3r. \tag{8.11}$$

Here, $E_{\text{eff}}$ is the corresponding homogeneous incident field. Taking the spatial average of the electric field leads to the expression

$$\epsilon_{\text{eff}} = f\epsilon_i\frac{\langle E^2(\mathbf{r},\omega_\alpha)\rangle}{E_{\text{eff}}^2(\omega_\alpha)} \tag{8.12}$$

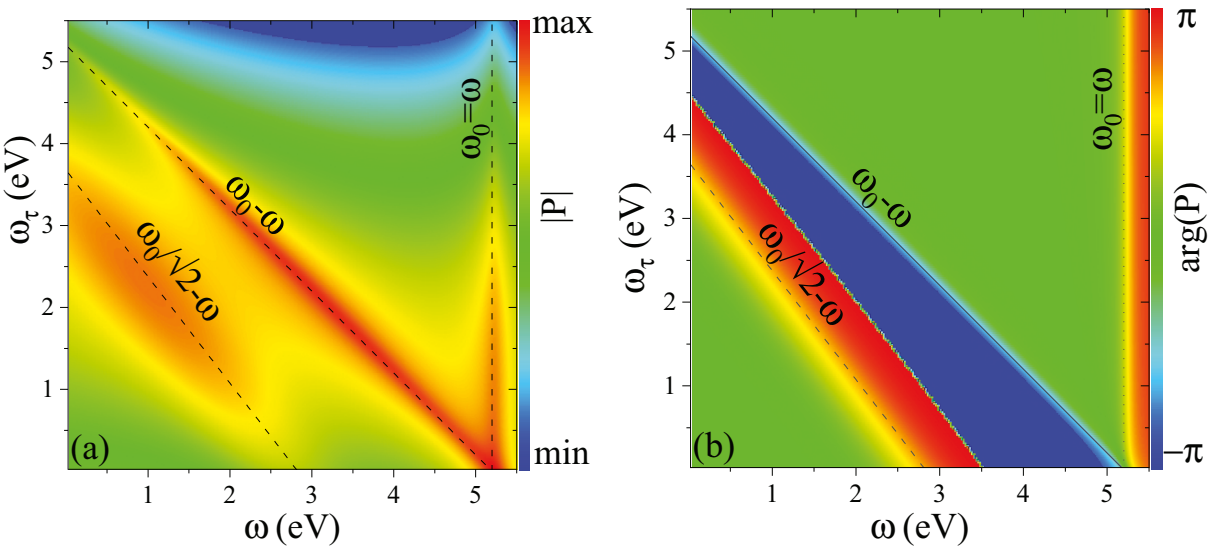


Fig. 8.6.: The (a) amplitude and (b) phase of the nonlinear polarization from XPM, eq. (8.13) for the metallic bulk susceptibility and electric fields stemming from two Gaussian pulses at frequencies $\omega$ and $\omega_\tau$. Observed resonances can be tied to the material resonance $\omega_0$ obtained from Mie calculations for Ir nanoparticles in a specific environment (fused silica).

and the above effective third order susceptibility in the case of different incident frequencies during a Cross-Phase Modulation (XPM) process follows by differentiation and evaluation at the different incident frequencies $\alpha \in \{q, m, n, o\}$.

### 8.2.1 Nonlinear Polarization Holography

The dynamics of energy transfer in dielectric holographic films can be revealed experimentally by attosecond nonlinear polarization spectroscopy [280]. In contrast to standard spatial holography, a spatial off-axis hologram is produced. An object emits a wave from a nonlinear process together with the probe pulse. A reference wave is overlapped on a spectrometer and their combined interference pattern is, thus, investigated in time and frequency space. The pump pulse and the reference wave have a determined time delay $\tau$, however, the nonlinear polarization only emits a sizable signal where $\tau$ is close to zero and the pulses overlap temporally. We consider the case of an amorphous metal composite holographic film of low metal density in which data was stored using the Cross-Phase Modulation (XPM) technique [281]. Its nonlinear polarization induced by a sufficiently intense laser is subsequently obtained as described and analysed in Fourier space. In this scenario [279], we consider the cross-phase modulated effective susceptibility for amorphous composites of varying fill fraction and study the dependence of the nonlinear polarization on the properties of the mixture. In particular, we study integrals of the form

$$P_\tau^{\mathrm{NL}}(\omega) \sim \int_\infty^\infty \mathrm{d}\omega' R(\omega') R(\omega_\tau - \omega') \chi^{(3)}(-(2\omega + \omega_\tau - \omega')|\omega, \omega_\tau + \omega, \omega'), \tag{8.13}$$

with normalized and dimensionless Gaussian beam profiles $R(\omega)$ of 25 fs pulses, representing

the pump and the delayed probe pulse. Note that a third electric input field is missing here as the information on this is not experimentally accessible and we aim to reproduce data obtained in a two-dimensional parameter space. In this expression, we use the third order, cross-phase modulated susceptibility $\chi^{(3)}$ for bulk iridium in Fig. 8.6 and the effective susceptibility for Ir nanoparticles in fused silica in Fig. 8.7 for both effective medium theories discussed.

Fig. 8.6(a) shows the amplitude of the nonlinear polarization from XPM calculations and Fig. 8.6(b) the related phase. The observed resonances can be traced back to material dependent properties in relation to the Mie resonance $\omega_0$ of the Ir nanoparticles due to the dependence on $D(\omega) = \omega_0^2 - \omega^2 - i\gamma\omega$. Observed phase changes are strongly correlated to the main resonance feature where $\omega = \omega_0 - \omega_\tau$ corresponding to the delayed probe pulse term $R(\omega_\tau - \omega')$. Another resonant response is found for the pump pulse term $R(\omega')$ itself where $\omega = \omega_0$. A third resonant feature can be observed following $\omega = {}^{\omega_0}/_{\sqrt{2}} - \omega_\tau$. The resonance conditions in the bulk susceptibility stem from the denominators $D(\omega_\alpha)$ for fields at different incident frequencies $\omega_\alpha$. Hence, $\omega_0^2 \cong \omega_\alpha^2$ for negligible imaginary part. As we integrated over $\omega'$ two of the $D(\omega_\alpha)$ terms change and can become equal to others. The third resonance is connected to the higher order term $D^2(\omega + \omega_t au)$ developped into a Taylor series to second order

$$D(\omega + \omega_\tau)^2 = \omega_0^4 - 2\omega_0^2(\omega + \omega_\tau)^2 + \mathcal{O}((\omega + \omega_\tau)^4) \quad \Rightarrow \quad \omega_\tau = \pm\frac{\omega_0}{\sqrt{2}} - \omega. \tag{8.14}$$

It is weaker and broader than the other resonances observed for the bulk case as this approximated condition is met for different $\omega'$ during the integration process.

Fig. 8.7 shows this two-dimensional parameter space of the nonlinear polarization using the effective susceptibility of the amorphous composites for both Maxwell-Garnett (upper panel) and Bruggeman (lower panel) theory increasing the fill fraction from left to right. While both effective medium theories employed are quantitatively and qualitatively rather different, they overall predict equal material specific resonances with respect to the pump-probe setup with pump at frequency $\omega$ and the probe pulse delayed by $\tau$ with frequency $\omega_\tau$. Further higher order terms appear when integrating over $\omega'$. Connected to the second order through the total sum of all incident fields is

$$D(2\omega + \omega_\tau)^2 = \omega_0^4 - 2\omega_0^2(2\omega + \omega_\tau)^2 + \mathcal{O}((2\omega + \omega_\tau)^4) \quad \Rightarrow \quad \omega_\tau = \pm\frac{\omega_0}{\sqrt{2}} - 2\omega, \tag{8.15}$$

which is a very weak resonance at low fill fractions but gains prominance on increasing the metal load. The other two lines observed that were not seen in the bulk case arise from the third order and the total sum of the incident fields, i. e.

$$D(2\omega)^3 = \omega_0^6 - 3\omega_0^4(2\omega)^2 + \mathcal{O}((2\omega)^4) \quad \Rightarrow \quad \omega = \pm\frac{\omega_0}{2\sqrt{3}}, \tag{8.16}$$

$$D(2\omega + \omega_\tau)^3 = \omega_0^6 - 3\omega_0^4(2\omega + \omega_\tau)^2 + \mathcal{O}((2\omega + \omega_\tau)^4) \quad \Rightarrow \quad \omega_\tau = \pm\frac{\omega_0}{2\sqrt{3}} - \omega. \tag{8.17}$$

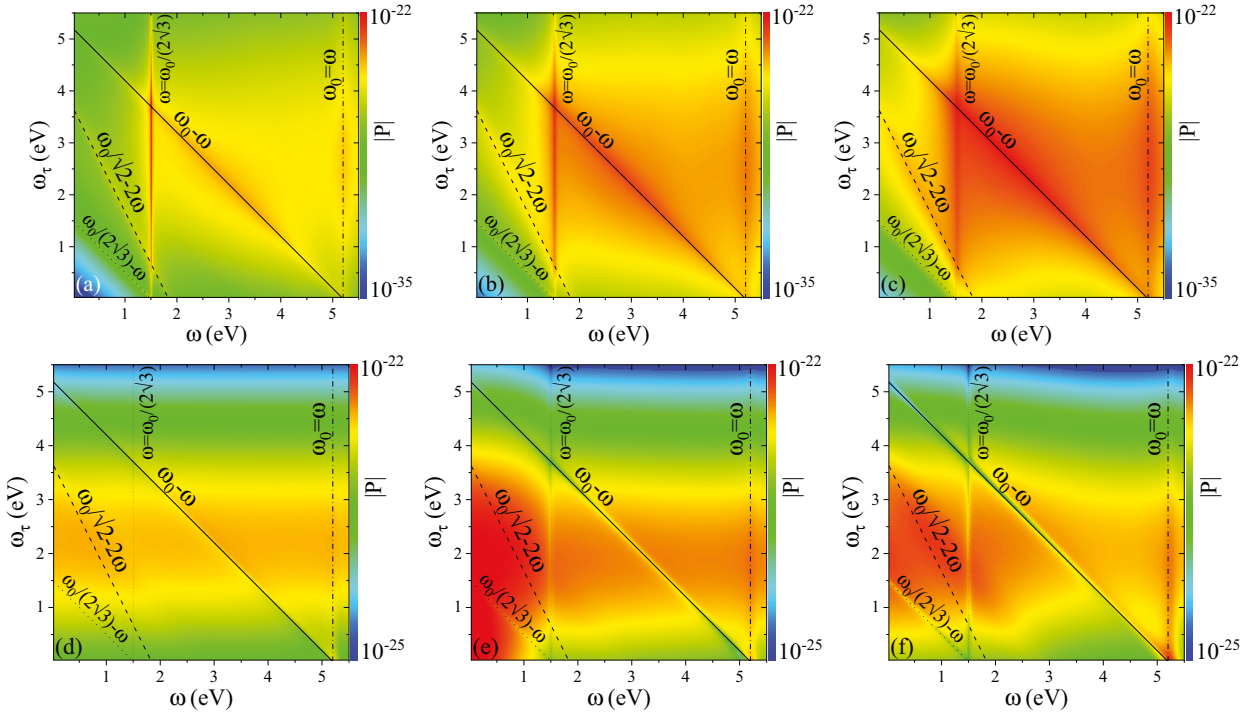


Fig. 8.7.: The amplitude of the nonlinear polarization from XPM using the effective susceptibility from (a)-(c) Maxwell-Garnett and (d)-(f) Bruggeman theory. Incident electric fields stem from two Gaussian pulses at frequencies $\omega$ and $\omega_\tau$. Observed resonances can be tied to the material resonance $\omega_0$ obtained from Mie calculations for Ir nanoparticles in fused silica. The nonlinear polarization is given in units of $1/E^2_{\text{Hartree}}$. Fill factors are (a), (d) $f = 0.1$, (b), (e) $f = 0.4$ and (c), (f) $f = 0.7$.

The first case occurs when $\omega'$ cancels $\omega_\tau$ from the frequency sum and the second case occurs when $\omega'$ vanishes. With this, all observed resonances can be traced back to the Lorentzian form of the bulk susceptibility. Additionally, increasing the metal load in the mixture, the line broadening clearly increases for both effective medium theories. The final form is determined by the further prefactors in the EMTs.

The future goal of this study is to further study the line width as a function of the material density in the amorphous mixture and to relate this to experimentally observed dephasing times of the optical excitation [279].

# 9. Overall conclusions and Outlook

Nanostructured materials interact with light in various ways. Localized resonances are in interplay with lattice resonances over a large scale. Diffuse scattering from rough surfaces can excite optical modes–classical and non-classical–that are not predicted under ideal circumstances. Apart from the structure at hand, the properties of light such as its polarization state, incident angle and, most prominently, its wavelength determine the optical response of a material. Computational nanophotonics is a powerful tool to decipher the structure-performance relationship, to design and optimize nanostructured devices towards targeted tasks. We discussed various numerical methods in the first chapter of which several were applied in our research.

With a focus on the Fourier Modal Method (FMM), suitable to optically characterize one- and two-dimensional nanostructures as part of a multilayered device based on scattering matrix theory, we discussed in this body of work a number of applications under assumption of purely classical and linear optics from photovoltaics and spectroscopy and we studied how to expand this standard approach to include mesoscopic charge dynamics and nonlinear properties. Mesoscopic electron dynamics plays a central role in nanostructures with metal components, where at least one dimension–particle separation, particle width or height and nanofilm thickness–reaches below 10 nm while, however, other dimensions can be notably larger than this finite-size limit. Here, anomalous diffraction in the structured films induced by the additional mesoscopic electron dynamics plays a major role. We detailed the necessary steps to expand the standard FMM to include the hydrodynamic model of electron dynamics for hard-wall boundary conditions and studied their impact on holey metal films which show extraordinary optical transmission. In addition, we discussed the extension of Mie coefficients applied for spherical geometries towards inclusion of both the single-fluid hydrodynamic model for the electron gas in metal nanoparticles and the two-fluid hydrodynamic model for spherical ionic particles, where both positive and negative charge carriers are interacting through coupled electromagnetic wave and hydrodynamic equations. For such nonclassical electrolyte systems we continue studying planar and large-scale nanostructured systems. One futue goal is to study hyperbolic ionic systems and demonstrate soft plasmonic sensing platforms. The quantum corrections for spherical nanoparticles are used to study strong particle-substrate or metal-dielectric coupling which yields a mode splitting induced by non-classical effects and compare their influence on dimers and particle chains.

In the second part of this work, we study nonlinear optical properties from nanostructures, namely, structure-induced surface second harmonic generation in one-dimansional gold nanogratings and third order nonlinearities stemming from amorphous nanocomposites. The former uses the computational abilities of the FMM in the linear regime to calculate the second order polarization from local fields at the fundamental harmonic. Symmetry and resonance conditions were studied. A direct comparison with measurements yields very

good agreement. This approach can widely be adapted to further geometries and material compositions and will be explored in future collaborations to study the efficient enhancement of higher harmonics with resonant nanostructures. In contrast, the latter is based on and compares effective medium theories that allow homogenization of the composite material parameters. Third order nonlinearities are investigated for both Kerr or self-phase modulated nonlinearities where all incident and outgoing frequencies are assumed to be equal and cross-phase modulated (XPM) nonlinearities where all incident frequencies are different and a number of outgoing frequency combinations can be achieved. In case of SPM, heterogeneous stacks of materials will be studied in the future. In the linear regime, Ir-based amorphous multilayers are typically used for conventional X-ray mirrors while we seek to study their nonlinear optical properties as a nonlinear source for the UV region. These structures were further used to simulate a setup from nonlinear polarization holography where pump and probe pulse are temporally shifted via a time delay $\tau$ yielding a two-dimensional map of the nonlinear polarization. We clearly observe line broadening of the resonances for amorphous films of varying composition tied to both the material resonances and sum frequencies as obtained from a simple Taylor series. We will further study the details of this line broadening to deduce the lifetime of excitations and gain an insight into dephasing mechanisms through the multiparameter-space offered by the nonlinear polarization holography technique.

It is our goal to provide a deeper comprehension of mesoscopic charge dynamics and nonlinear optical properties in large-scale nanostructured devices with continued efforts towards active metasurfaces where optical properties can be understood from localized spatial features under the influence of nano-scale effects in strongly nonlocal and strongly nonlinear materials. Ultimately, highly tunable, robust and actively switchable structures will need to account for such localized effects as they are in the interplay with retardation and lattice modes across the larger scale.

# IV

# Appendix

# A. Analytic Fourier Transforms

The Fourier Modal Method (FMM) is a plane-wave expansion (PWE) approach in frequency space in which the Fourier Transform (FT) of a unit cell — representing a periodic one- or two-dimensional nanostructured grating or particle array, respectively — is central to solving the related electromagnetic eigenvalue problem. The decomposition into plane waves in reciprocal space reads

$$\epsilon(\omega, \mathbf{r}) = \sum_{\mathbf{G}} \epsilon(\mathbf{G}) e^{i\mathbf{G}\mathbf{R}}, \tag{A.1}$$

where $\mathbf{R}$ and $\mathbf{G}$ are the in-plane (two-dimensional) real space and reciprocal lattice vector, respectively. This yields a permittivity matrix $\epsilon_{\mathbf{G}\mathbf{G}'}$ with the Fourier coefficients derived from

$$\epsilon_{\mathbf{G}\mathbf{G}'} = \epsilon(\omega, \mathbf{G} - \mathbf{G}') = \frac{1}{\mathcal{A}} \int_{\mathcal{A}} \epsilon(\omega, \mathbf{r}) e^{-i(\mathbf{G}-\mathbf{G}')\mathbf{R}} d\mathcal{A}, \tag{A.2}$$

where $\mathcal{A}$ represents the unit cell length or area or volume, respectively, depending on the dimension of the considered nanostructure. Note that the expressions derived in this chapter are independent of the choosen material model and their frequency dependence.

It is important to notice that the periodicity of $\epsilon(\omega, \mathbf{r})$ is passed on to its inverse

$$\frac{1}{\epsilon(\omega, \mathbf{r})} = \sum_{\mathbf{G}} \kappa(\mathbf{G}) e^{i\mathbf{G}\mathbf{R}} \tag{A.3}$$

with Fourier coefficients

$$\kappa_{\mathbf{G}\mathbf{G}'} = \kappa(\mathbf{G} - \mathbf{G}') = \frac{1}{\mathcal{A}} \int_{\mathcal{A}} \frac{e^{-i(\mathbf{G}-\mathbf{G}')\mathbf{R}}}{\epsilon(\omega, \mathbf{r})} d\mathcal{A}. \tag{A.4}$$

For abrupt boundaries, the spatial dependence is entirely governed by unit step (Heaviside) functions and the substitution $\epsilon(\omega, \mathbf{r}) \rightarrow \frac{1}{\epsilon(\omega, \mathbf{r})}$ in the real-space material functions is valid. However, only if all Fourier components are taken into account, the expressions actually coincide in Fourier space.

Simple nanostructures feature analytic Fourier Transforms. However, more complex structures can be won through direct numerical transformation, best optimized with adaptive meshes and Fast Fourier Transform (FFT) [65, 78–81].

## A.1 One-dimensional laminar grating structures

We consider a one-dimensional grating of alternating materials with periodicity $a_x$ and width $w_x$ of the nanostructure along the $x$-direction, see Figure A.1. We denote the surrounding material with $\epsilon_0$ and the nanostructure material with $\epsilon_m$. The permittivity of the unit cell can

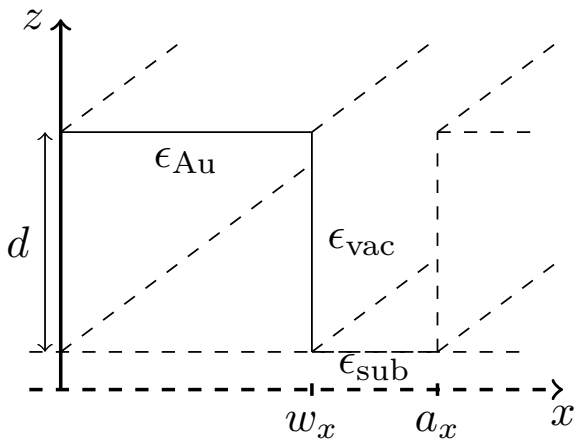


Fig. A.1.: Illustration of the structure. The one-dimensional unit cell of a grating structure consisting of material stripes of width $w_x$ and height $d$, the lattice period is $a_x$. The grating is extended indefinitely in the $y$-direction.

then be described as

$$\epsilon(\omega, \mathbf{r}) = (\epsilon_m - \epsilon_0)\Theta(w_x - x) + \epsilon_0 \qquad (\text{for } 0 < x < a_x). \tag{A.5}$$

The reciprocal wave vectors are themselves one-dimensional $\mathbf{G}_n = n^{2\pi}/_{a_x}\,\hat{\mathbf{x}}$ with $n \in \mathbb{Z}_0$. Note that the FT yields two terms. One for the case of $n \equiv n'$ (diagonal term) and $n \neq n'$ (off-diagonal contributions). We find

$$\begin{aligned}
\epsilon_{GG'} &= \frac{1}{a_x}\int_0^{a_x} \epsilon(\omega, \mathbf{r}) e^{-i\frac{2\pi}{a_x}(n-n')x}\,\mathrm{d}\,x \\
&= \frac{1}{a_x}\int_0^{w_x} \epsilon_m e^{-i\frac{2\pi}{a_x}(n-n')x}\,\mathrm{d}\,x + \frac{1}{a_x}\int_{w_x}^{a_x} \epsilon_0 e^{-i\frac{2\pi}{a_x}(n-n')x}\,\mathrm{d}\,x \\
&= \delta_{nn'}\left[\frac{w_x}{a_x}(\epsilon_m - \epsilon_0) + \epsilon_0\right] + \frac{\epsilon_m - \epsilon_0}{\pi(n-n')} e^{-i\pi\frac{w_x}{a_x}(n-n')} \sin\left(\pi(n-n')\frac{w_x}{a_x}\right).
\end{aligned} \tag{A.6}$$

We exploited the fact that $e^{\pm 2\pi i(n-n')} \equiv 1$ for all values of $n \neq n'$.

## A.2 Two-dimensional structures

We consider various two-dimensional nanostructures in a rectangular unit cell. The reciprocal wave vectors are $\mathbf{G} = n^{2\pi}/_{a_x}\,\hat{\mathbf{x}} + m^{2\pi}/_{a_y}\,\hat{\mathbf{y}}$ with $n, m \in \mathbb{Z}_0$, with the lattice vectors with $a_x$ and $a_y$ along the $x$- and $y$-direction, respectively.

### A.2.1 Rectangular nanoantenna structures

Rectangular nanostructures, i. e. nanoantennas or nanobars, have a width $w_x$ along $x$-direction and $w_y$ along $y$-direction. The permittivity of the unit cell is defined through

$$\epsilon(\omega, \mathbf{r}) = (\epsilon_m - \epsilon_0)\Theta(w_x - x)\Theta(w_y - y) + \epsilon_0. \tag{A.7}$$

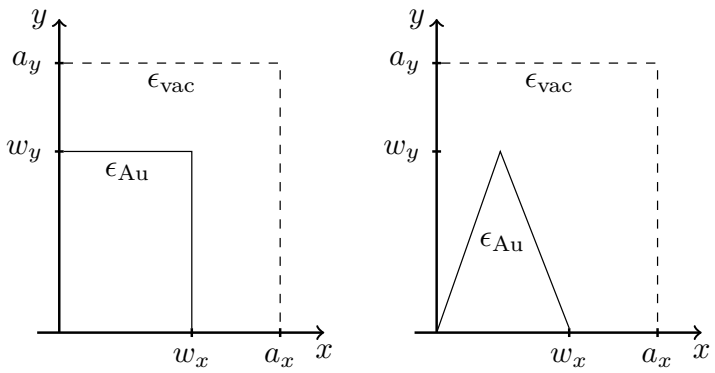


Fig. A.2.: Illustration of the unit cell of two-dimensional nanostructures. The unit cell is made of lattice vectors $a_x, a_y$ and height $d$. In the case of (Left) nanobars, the nanostructure has widths $w_x, w_y$. For the (Right) triangular structure, we consider a symmetric triangle with base side length $w_x$ and height $w_y$ at $x = {}^{w_x}/_2$.

In similar steps as for the one-dimensional case, we find the result

$$\begin{aligned}\epsilon_{GG'} =&\delta_{nn'}\delta_{mm'}\left[\frac{w_x w_y}{a_x a_y}\left(\epsilon_m-\epsilon_0\right)+\epsilon_0\right]\\ &+\delta_{nn'}\frac{w_x}{a_x}\frac{\epsilon_m-\epsilon_0}{\pi(m-m')}e^{-i\pi\frac{w_y}{a_y}(m-m')}\sin\left(\pi(m-m')\frac{w_y}{a_y}\right)\\ &+\delta_{mm'}\frac{w_y}{a_y}\frac{\epsilon_m-\epsilon_0}{\pi(n-n')}e^{-i\pi\frac{w_x}{a_x}(n-n')}\sin\left(\pi(n-n')\frac{w_x}{a_x}\right)\\ &+\left(\epsilon_m-\epsilon_0\right)\frac{e^{-i\pi\frac{w_x}{a_x}(n-n')}e^{-i\pi\frac{w_y}{a_y}(m-m')}}{\pi(n-n')\pi(m-m')}\sin\left(\pi(n-n')\frac{w_x}{a_x}\right)\sin\left(\pi(m-m')\frac{w_y}{a_y}\right).\end{aligned} \tag{A.8}$$

Fig. A.3 shows the quality of the reconstructed permittivity for an increasing number of Fourier coefficients taken into account in the reconstruction based on eq. (A.1) once the FT has been performed. A low number of Fourier coefficients reveals the underlying $\sin$-functions present in the reconstruction. For a sufficiently high number of Fourier coefficients, there is no difference to the original material functions.

### A.2.2 Spherical nanostructures

We consider circular dielectric holes of radius $R$ at position $\mathbf{r}_0 = (x_0, y_0)$, e. g. in the center of the unit cell, defined through the material function

$$\epsilon(\omega, \mathbf{r}') = (\epsilon_0 - \epsilon_m)\Theta(R - |\mathbf{r}' - \mathbf{r}_0|) + \epsilon_m. \tag{A.9}$$

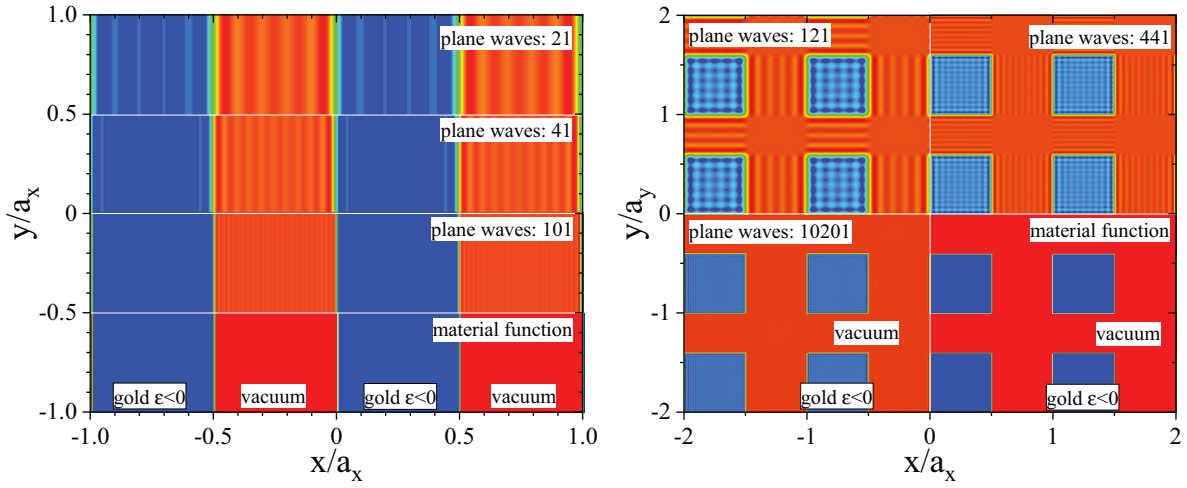


Fig. A.3.: Reconstructed real parts of the real-space material functions (permittivities) of the (Left) one-dimensional and (Right) two-dimensional rectangular structure from analytic Fourier coefficients for different numbers of coefficients taken into account. Blue areas are a metal with negative real permittivity, red areas are vacuum with positive real permittivity.

The linear shift of the center of the structure to $\mathbf{r}_0$ leads to a constant factor and we use the prescription $\mathbf{r} = \mathbf{r}' - \mathbf{r}_0,\ dr = dr'$ and finally $dxdy = rdrd\phi$. We find

$$\begin{aligned}
\epsilon_{\mathbf{G}\mathbf{G}'} &= \frac{1}{a_x}\frac{1}{a_y}\int_0^{a_x} \mathrm{d}\, x \int_0^{a_y} \mathrm{d}\, y \epsilon(\omega, \mathbf{r}) e^{-i(\mathbf{G}-\mathbf{G}')(\mathbf{r}'-\mathbf{r}_0)} \\
&= \delta(\mathbf{G}-\mathbf{G}')\left[\frac{\pi R^2}{a_x a_y}(\epsilon_0 - \epsilon_m) + \epsilon_m\right] \\
&\quad + \frac{1}{a_x}\frac{1}{a_y} e^{i(\mathbf{G}-\mathbf{G}')r_0} \int_0^{a_x} \mathrm{d}\, x \int_0^{a_y} \mathrm{d}\, y \epsilon_m e^{-i2\pi((n-n')x/a_x + (m-m')y/a_y)} \\
&\quad + \frac{2\pi}{a_x a_y} e^{i(\mathbf{G}-\mathbf{G}')r_0} \int_0^{R} \mathrm{d}\, r r(\epsilon_0 - \epsilon_m) J_0(|\mathbf{G}-\mathbf{G}'|r) \qquad \text{(A.10)} \\
&= \delta(\mathbf{G}-\mathbf{G}')\left[\frac{\pi R^2}{a_x a_y}(\epsilon_0 - \epsilon_m) + \epsilon_m\right] + \frac{2\pi R^2}{a_x a_y}(\epsilon_0 - \epsilon_m) e^{i(\mathbf{G}-\mathbf{G}')r_0} \frac{J_1(|\mathbf{G}-\mathbf{G}'|R)}{|\mathbf{G}-\mathbf{G}'|R},
\end{aligned}$$

with the Bessel functions $J_n(x)$ of $n$'th order and $\int \mathrm{d}\, \phi e^{-i|\mathbf{G}-\mathbf{G}'|r\cos\phi} = 2\pi J_0(|\mathbf{G}-\mathbf{G}'|r)$. The Fourier transform is analytical for spherical shapes and via coordinate transformations [311] also for elliptical particles.

#### Hollow nanotubes and multilayered disks

The Fourier Transform of a spherical nanostructure allows the straightforward extension towards multilayered, such as core-shell structures like arrays of thin-walled nanotubes [66, 101]. We study generalized unit cells of multilayered spherical disks with a material function of the form

$$\epsilon(\omega, \mathbf{r}) = \epsilon_0 + \sum_{n=1}^{N} (\epsilon_n - \epsilon_{n-1}) \Theta(R_n - |\mathbf{r} - \mathbf{r}_0|). \qquad \text{(A.11)}$$

All disks have the same center $\mathbf{r}_0$ and different radii $R_n$. This can be solved in complete analogy to the simple case above, such that

$$\epsilon_{\mathbf{GG}'} = \delta(\mathbf{G}-\mathbf{G}')\left[\epsilon_0 + \sum_{n=1}^{N} \frac{\pi R_n^2}{a_x a_y}(\epsilon_n - \epsilon_{n-1})\right] + \sum_{n=1}^{N} \frac{2\pi R_n^2}{a_x a_y}(\epsilon_n - \epsilon_{n-1}) e^{i(\mathbf{G}-\mathbf{G}')r_0} \frac{J_1(|\mathbf{G}-\mathbf{G}'|R_n)}{|\mathbf{G}-\mathbf{G}'|R_n}. \tag{A.12}$$

These results remain analytical and the computational effort is increased by a summation. Such a straightforward summation can be performed with any of the other structures discussed previously as well.

#### Multi-type particle arrays

We consider inhomogeneous nanodisk arrays made of particles of different sizes, shapes and even materials randomly distributed in the unit cell [56]. The material function in real space is

$$\epsilon(\omega, \mathbf{r}') = \sum_n \left((\epsilon_0 - \epsilon_n)\Theta(R_n - |\mathbf{r}' - \mathbf{r}_{0n}|) + \epsilon_n\right) \tag{A.13}$$

for nanodisks of different radii $R_n$ and positions $\mathbf{r}_{0n}$. We obtain

$$\epsilon_{\mathbf{GG}'} = \delta(\mathbf{G}-\mathbf{G}')\sum_n \left[\frac{\pi R_n^2}{a_x a_y}(\epsilon_0 - \epsilon_n) + \epsilon_n\right] + \sum_n \frac{2\pi R_n^2}{a_x a_y}(\epsilon_0 - \epsilon_n) e^{i(\mathbf{G}-\mathbf{G}')\mathbf{r}_{0n}} \frac{J_1(|\mathbf{G}-\mathbf{G}'|R_n)}{|\mathbf{G}-\mathbf{G}'|R_n} \tag{A.14}$$

in Fourier space.

## A.3 Nonlocal Material Models in the Fourier Modal Method

Metallic components with spatial dispersion are described by additional parameters, in particular the nonlocal strength $\beta$, that vanishes in the dielectric material, such that for the unit cell in one-dimensional systems we can write

$$\beta^2(x) = \beta^2\Theta(w_x - x) \qquad \text{and, e. g.,} \qquad \beta^2(\mathbf{r}) = \beta^2\Theta(R - |\mathbf{r}' - \mathbf{r}_0|) \tag{A.15}$$

in circular two-dimensional structures. The FT results are the same as before, substituting the corresponding $\epsilon_m \to \beta^2$ and $\epsilon_0 \to 0$. Similar results are obtained where $\omega_p$ or $\gamma_p$ are needed explicitly in the nonlocal wave equation as for the Generalized Nonlocal Optical Response (GNOR) theory further including diffusion effects.

# B. Pressure of an Electron Plasma

In Thomas-Fermi theory the free electron gas is associated with a characteristic pressure term $p$. The internal energy $U = \sum_{\mathbf{k}} \epsilon_{\mathbf{k}} n_{\mathbf{k}}^F$ is locally defined as a sum over all occupied energy states $\epsilon_{\mathbf{k}}$ [312–314]. The total number $N$ of states of the fermionic system in volume $V$ results in the density $n = \frac{N}{V}$ and is described by a sphere in momentum space with radius $\frac{2\pi}{k_F}$, where $k_F$ is the corresponding Fermi wave vector. With the $T \to 0$ Fermi distribution function this results in

$$n = \frac{g}{V} \sum_{\mathbf{k}} n_{\mathbf{k}}^F = g \frac{4\pi}{3} \left( \frac{k_F}{2\pi} \right)^3 \quad \Rightarrow \quad k_F = \left( \frac{N}{V} \frac{6\pi^2}{g} \right)^{\frac{1}{3}} \tag{B.1}$$

where we account for the degeneration of states with $g = 2s + 1$. With the energy at the Fermi level $\epsilon_F = \frac{\hbar^2 k_F^2}{2m_e}$ and the spin of electrons $s = \frac{1}{2}$ we find

$$\epsilon_F = \frac{\hbar^2}{2m_e} \left(3\pi^2\right)^{\frac{2}{3}} n^{\frac{2}{3}}. \tag{B.2}$$

With that, the kinetic internal energy $U$ results in

$$U = \sum_{\mathbf{k}} \epsilon_{\mathbf{k}} n_{\mathbf{k}}^F = \frac{V}{(2\pi)^3} \frac{\hbar^2}{2m_e} \int d^3k k^2 n_{\mathbf{k}}^F = \frac{3}{5} \epsilon_F \frac{4\pi}{3} \frac{k_F^3}{(2\pi)^3} = \frac{3}{5} \epsilon_F N, \tag{B.3}$$

leading to a mean energy per fermionic particle of $U/N = \frac{3}{5}\epsilon_F$. The pressure $p$ of the electron plasma is given by the variation of the kinetic energy with respect to volume $-p = \frac{\partial U}{\partial V}$

$$p = \frac{1}{5} \frac{\hbar^2}{m_e} (3\pi)^{2/3} n^{5/3}. \tag{B.4}$$

Assuming small changes $\delta n$ in the electron density $n = n_0 + \delta n$ with respect to the equilibrium state of an unperturbed electron density profile $n_0$, we find

$$p = \frac{1}{5} \frac{\hbar^2}{m_e} (3\pi)^{2/3} n_0^{5/3} + \frac{1}{3} \frac{\hbar^2}{m_e} (3\pi)^{2/3} n_0^{2/3} \delta n + \mathcal{O}(\delta n^2) \equiv p_0 + \beta_{\mathrm{cl}}^2 \delta n + \mathcal{O}(\delta n^2). \tag{B.5}$$

This defines the nonlocal interaction strength from classical gas theory

$$\beta_{\mathrm{cl}}^2 = \frac{1}{3} \frac{\hbar^2}{m_e^2} (3\pi)^{2/3} n_0^{2/3} = \frac{1}{3} v_F^2 \approx (p - p_0)/(m_e \delta n) \tag{B.6}$$

from the statistics of a free non-interacting Fermi gas. Fully taking the quantum nature of electrons into account, the prefactor is corrected to $\frac{3}{5}$, as found by Refs. [183, 315] . This quantum mechanical result is in agreement with the low momentum limit of the Lindhard dielectric function.

# C. Electron Dynamics in the RPA

We describe electron dynamics inside metal nanoparticles (MNPs) [18, 54, 72] with an extension to the Random Phase Approximation (RPA) theory developed by Pines and Bohm [17] for bulk metals. A finite, rigid jellium defines the shape of the MNP. Plasmon oscillations are described as local electron density fluctuations $\hat{\rho}(\mathbf{r},t)$ obtained from the Heisenberg equation

$$\frac{d^2\hat{\rho}(\mathbf{r},t)}{dt^2} = \frac{1}{(i\hbar)^2}\left[\left[\hat{\rho}(\mathbf{r},t),\hat{H}_e\right]\hat{H}_e\right] \tag{C.1}$$

with a corresponding Hamiltonian $\hat{H}_e$ for electrons inside the MNP in the jellium model

$$\hat{H}_e = \sum_{j=1}^{N}\left[-\frac{\hbar^2\nabla_j^2}{2m} - e^2\int\frac{n_e(\mathbf{r})d^3r}{|\mathbf{r_j}-\mathbf{r}|}\right] + \frac{1}{2}\sum_{j\neq j'}\frac{e^2}{|\mathbf{r_j}-\mathbf{r_{j'}}|}. \tag{C.2}$$

The first term gives the kinetic energy of electrons, the second the interaction between electrons and positive background charges (approximating the ion lattice potential) and the last the electron-electron Coulomb interaction. The operator of the local electron density is

$$\rho(\mathbf{r},t) = \langle\Psi_e(t)|\sum_j \delta(\mathbf{r}-\mathbf{r_j})|\Psi_e\rangle \tag{C.3}$$

where $\Psi_e$ is the electron wave function, $N$ is the number of collective electrons, $\mathbf{r_j}$ and $m$ are their positions and mass. The ion field is approximated as background charge density and described as $n_e(\mathbf{r})|e| = n_e\Theta(R-r)|e|$, where $R$ is the radius of the MNP and $n_e = {}^{N}/_{V}$.

Taking into account the sharp form of the positive charge density $n_e(\mathbf{r})$, one can decompose Eq. (C.1) into contributions from the inside and outside of the NP, which leads to two separate solutions describing the surface and bulk plasmons. This description is valid for NPs larger than ca. 5 nm for which the surface is well defined and the spill-out effect is negligible.

$$\delta\tilde{\rho}(\mathbf{r},t) = \begin{cases} \delta\tilde{\rho}_1(\mathbf{r},t), \text{ for } r < R, \\ \delta\tilde{\rho}_2(\mathbf{r},t), \text{ for } r \geq R, \ (r \to R+) \end{cases}. \tag{C.4}$$

The electron density fluctuations are then described with the formulas

$$\frac{\partial^2\delta\tilde{\rho}_1(\mathbf{r},t)}{\partial t^2} = \frac{2}{3}\frac{\epsilon_F}{m}\nabla^2\delta\tilde{\rho}_1(\mathbf{r},t) - \omega_p^2\delta\tilde{\rho}_1(\mathbf{r},t) \tag{C.5}$$

and

$$\frac{\partial^2\delta\tilde{\rho}_2(\mathbf{r},t)}{\partial t^2} = -\Bigg[\frac{2}{3}\frac{\epsilon_F}{m}\frac{\mathbf{r}}{r}\nabla\delta\tilde{\rho}_2(\mathbf{r},t) +$$

$$\frac{\omega_p^2}{4\pi}\frac{\mathbf{r}}{r}\nabla\int d^3r_1\frac{1}{|\,\mathbf{r}-\mathbf{r_1}\,|}(\delta\tilde{\rho}_1(\mathbf{r_1},t)\Theta(R-r_1) + \delta\tilde{\rho}_2(\mathbf{r_1},t)\Theta(r_1-R))\Bigg]\delta(R+\varepsilon-r)$$

$$-\frac{2}{3m}\nabla\left\{\left[\frac{3}{5}\epsilon_F n_e+\epsilon_F\delta\tilde{\rho}_2(\mathbf{r},t)\right]\frac{\mathbf{r}}{r}\delta(R+\varepsilon-r)\right\}. \tag{C.6}$$

The structure of the above equations is of an harmonic oscillator, which allows including a damping term in a phenomenological manner by adding to the right hand side $-{}^{2}\!/_{\tau_0}{}^{\partial\tilde{\rho}_{1(2)}(\mathbf{r},t)}\!/_{\partial t}$. The damping ${}^{2}\!/_{\tau_0}=\gamma_p+\gamma_K$ includes collision effects and Kreibig damping due to the particle boundary [157].

Assuming homogeneity of the external electric field $\mathbf{E}(t)$ inside the NP (dipole approximation), the solution for surface modes reduces to a single dipole mode

$$\delta\tilde{\rho}(\mathbf{r},t)=\sum_{m=-1}^{1}Q_{1m}Y_{1m}(\Omega),\quad \text{for } r\geq R,(r\to R+) \tag{C.7}$$

and for bulk modes $\delta\tilde{\rho}(\mathbf{r},t)=0$ where $r<R$.

The function $Q_{1m}(t)$ $(m=-1,0,1)$ represents dipole modes and $Y_{lm}(\Omega)$ is the spherical Legendre function. The former can be related to the vector $\mathbf{q}(t)$ via $Q_{11}=\sqrt{{}^{8\pi}\!/_{3}}\,q_x(t)$, $Q_{10}=\sqrt{{}^{4\pi}\!/_{3}}\,q_x(t)$, $Q_{1-1}=\sqrt{{}^{8\pi}\!/_{3}}\,q_y(t)$ satisfying the equation

$$\left[\frac{\partial^2}{\partial t^2}+\frac{2}{\tau_0}\frac{\partial}{\partial t}+\omega_1^2\right]\mathbf{q}(t)=\frac{en_e}{m}\mathbf{E}(t). \tag{C.8}$$

Then the plasmon dipole can be defined as

$$\mathbf{D}(t)=e\int d^3r\mathbf{r}\delta\rho(\mathbf{r},t)=\frac{4\pi}{3}e\mathbf{q}(t)R^3. \tag{C.9}$$

**Lorentz friction**

Knowing this, the damping caused by the electric field irradiation can be added to the right hand side of Eq. (C.8) as additional field $\mathbf{E}_L={}^{2}\!/_{3c^3}{}^{\partial^3\mathbf{D(t)}}\!/_{\partial t^3}$ hampering charge oscillations and can be rewritten in the form

$$\left[\frac{\partial^2}{\partial t^2}+\omega_1^2\right]\mathbf{D}(t)=\frac{\partial}{\partial t}\left[-\frac{2}{\tau_0}\mathbf{D}(t)+\frac{2}{3\omega_1\sqrt{\epsilon_0}}\left(\frac{\omega_p R}{c\sqrt{3}}\right)^3\frac{\partial^2}{\partial t^2}\mathbf{D}(t)\right]. \tag{C.10}$$

The above equation is a third order linear differential equation and the exponents $\sim e^{i\Omega_i t}$ of its solutions are given in Eq. (4.8). A perturbation approach can be applied to Eq. (C.10) for small particles using ${}^{\partial^2\mathbf{D}(t)}\!/_{\partial t^2}=-\omega_1^2\mathbf{D}(t)$. Then the resulting damping term takes the form $\gamma={}^{2}\!/_{\tau_0}+\left({}^{\omega_1}\!/_{3\sqrt{\epsilon_0}}\right)\left({}^{\omega_p R}\!/_{c\sqrt{3}}\right)^3$.

For larger radii, the discrepancy between both solutions grows rapidly since the irradiation losses within the perturbation approach scale as $R^3$. Therefore, the radiative losses dominate plasmon damping for large nanospheres. On the other hand, scattering is more important for smaller nanospheres scaling as $\frac{1}{R}$.

# D. Particle-Substrate Coupling

Our derivation of the semi-classical coupling between a plasmonic particle on an Si substrate is based on the following assumptions. The presence of the semiconductor in the vicinity of MNPs provides an additional damping channel of the plasmon energy via coupling to the semiconductor band states. We consider a simple parabolic band semiconductor model. The plasmon coupling to the semiconductor can be described as a driven and damped oscillator, where the driving force is the electromagnetic field of the incident plane wave, and the damping force is the near-field energy transfer to the semiconductor. For this, we consider that the field generated by the plasmon oscillation stems from dipole radiation, i. e., we restrict ourselves to a regime where the near-field coupling is the most important, while medium- and far-field contributions are neglected. This is justified as long as the particle size is much smaller than the incident wavelength $R \ll \lambda$. Furthermore, we apply this to particle arrays on Si substrates, which is justified as long as the particle size is also much smaller than the interparticle separation $R \ll \Lambda$, see Fig. D.1A for an illustration of the geometrical parameters.

With this, we calculate the photon absorption probability $\delta w$ with the Fermi Golden Rule approach for a dipole near-field via

$$\delta w(\mathbf{k}_1, \mathbf{k}_2) = \frac{2\pi}{\hbar} \left|\langle \mathbf{k}_1 | W | \mathbf{k}_2 \rangle\right|^2 \delta(E_p(\mathbf{k}_1) - E_n(\mathbf{k}_2) + \hbar\omega). \tag{D.1}$$

Hereby, $\mathbf{k}_1(\mathbf{k}_2)$ is the momentum of the holes (electrons) and $W$ defines the coupling between the subbands. With this, we obtain the absorption coefficient

$$\alpha(\omega) = \frac{\hbar\omega\delta w}{E_e}, \tag{D.2}$$

where $E_e = \langle|\mathbf{S}|\rangle \cos\theta$ is the irradiance and $\theta$ is the angle between the Poynting vector $\mathbf{S}$ and the vector normal to the semiconductor surface. The coupling matrix $W$ depends on the environment. Without nanoparticles, it is governed solely through the incident planar electromagnetic wave with vector potential $\mathbf{A}_0$

$$W = i\hbar \frac{e}{m_n} e^{i(\omega t - \mathbf{kr})} \mathbf{A}_0 \cdot \nabla \tag{D.3}$$

and the properties of the semiconductor via the effective electron mass $m_n$. This changes in the presence of the dipole field of a NP with radius $R$ and bulk plasma frequency $\omega_p$ to

$$W = \frac{e}{4\pi\epsilon_0 d^2} \hat{\mathbf{n}} \cdot \mathbf{D}_0 \sin(\omega t + \phi) = W^+ e^{i\omega t} + W^- e^{-i\omega t},$$

where terms $W^+$ and $W^-$ corresponds to the absorption and emission of photons, respectively

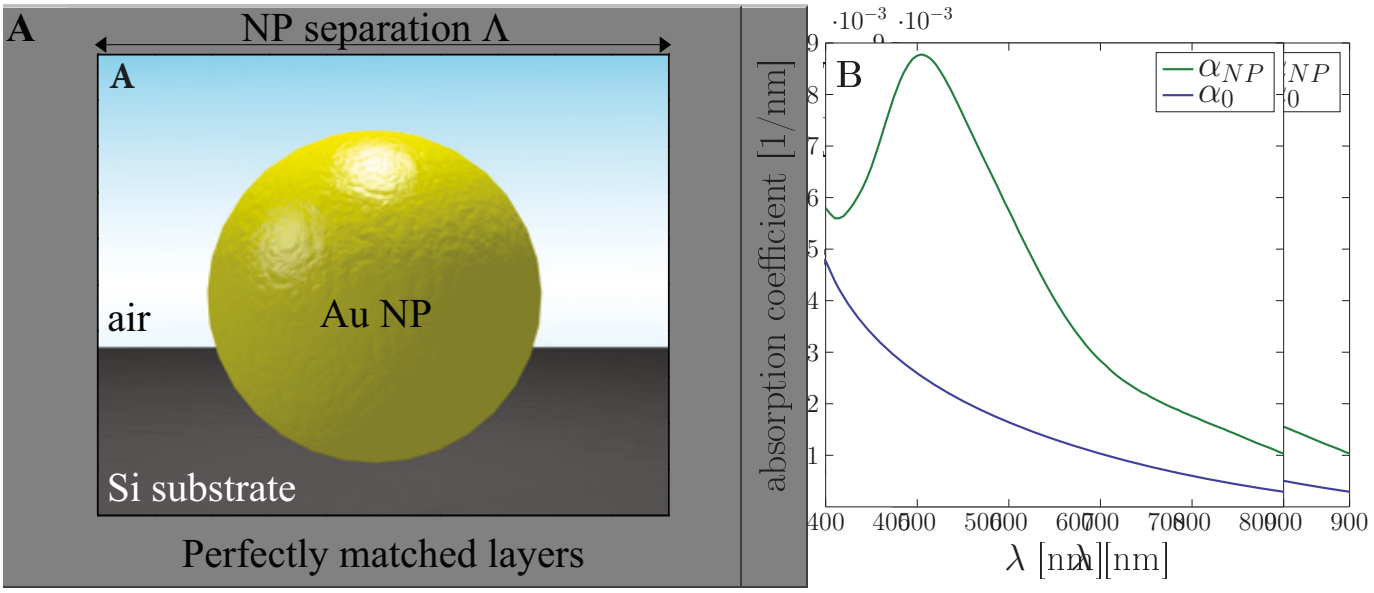


Fig. D.1.: Illustration of the photo-effect. (**A**) The computational square unit cell of width $\Lambda$ consists of a gold nanoparticle in its center on a Si substrate. (**B**) The probability of photon absorption for a single gold nanoparticle of $R = 50$ nm in the Si substrate increases significantly in the optically coupled system compared to the bare substrate.

and have the form

$$W^+ = (W^-)^* = \frac{e}{4\pi d^2 \epsilon_0} \frac{e^{i\phi}}{2i} \hat{\mathbf{n}} \cdot \mathbf{D}_0,$$

where $\phi$ is a phase factor, $d$ is the distance from the dipole axis and $\hat{\mathbf{n}}$ the surface normal of the substrate. The dipole moment $\mathbf{D}_0$ is analytic for a spherical nanoparticle and local electron dynamics, namely $\mathbf{D}_0 = \frac{\omega_p^2}{\omega_1^2} \mathbf{E} \frac{R^3}{2}$, where $\omega_1 = \omega_p/\sqrt{3}$ is the related Mie frequency of the dipole and $\mathbf{E} = i\omega \mathbf{A}_0 e^{i(\omega t - \mathbf{kr})}$ is the incident field at frequency $\omega$ as before.

We calculate the plasmonic dipole amplitude $D_0$ from the formula for the total power of the dipole radiation, which allows us to account for either local or nonlocal electron dynamics

$$D_0^2 = \frac{4\pi\varepsilon_0 \lambda^4}{(2\pi)^4 c} \int_\Sigma \mathbf{S} \cdot d\sigma, \tag{D.4}$$

by integrating the Poynting vector $\mathbf{S}$ over the electromagnetic field at the NP surface $\Sigma$ for either case. For the ordinary photo-effect without nanoparticles, eq. (D.3), the above approach yields

$$\delta w_0 = \frac{\sqrt{2}}{3\pi} \frac{e^2 \mu^{5/2}}{\omega \varepsilon_0 m_p^2 \hbar^3} (\hbar\omega - E_g)^{\frac{3}{2}}. \tag{D.5}$$

The probability of photon absorption by the semiconductor substrate in the vicinity of the

MNP results in [180]:

$$\delta w = \frac{4}{3}\frac{\mu^{3/2}\sqrt{2}\sqrt{\hbar\omega - E_g}e^2 D_0^2}{R\hbar^4\varepsilon^2}. \tag{D.6}$$

Both expressions reflect the semiconductor band gap $E_g$ and the effective masses of the electrons $m_n$ and holes $m_p$, respectively, via their reduced mass $\mu = \frac{m_p m_n}{m_p + m_n}$. From this, we calculate the absorption coefficient. Figure D.1B shows the increase of the photo-effect effect in the semiconductor substrate due to the presence of a single gold nanoparticle.

The ratio of the probabilities with and without MNPs deposited on the surface of the semiconductor defines the photocurrent gain

$$\frac{I'}{I} = 1 + \frac{\beta N_m \delta w}{\delta w_0}, \tag{D.7}$$

where $N_m$ is the number of MNPs and $\beta$ is a factor accounting for any additional effects, such as separation and surface properties reducing the coupling strength [180]. Likewise, the absorption enhancement is defined as

$$\mathcal{A}(\omega) = \frac{Q_{NP}}{Q_0} = \frac{\frac{\omega}{4\pi}\int_V n\varepsilon_m^{''}(\omega)\mathbf{E}^2_{\text{with NP}}dV}{\frac{\omega}{4\pi}\int_V n\varepsilon_0^{''}(\omega)\mathbf{E}^2_{\text{without NP}}dV}, \tag{D.8}$$

where

$$\varepsilon_{m(0)}^{''} = \frac{nc\hbar\delta w}{E_{irradiance}} \tag{D.9}$$

is imaginary part of the modified dielectric function of Si with ($\varepsilon_m^{''}$) and without ($\varepsilon_0^{''}$) MNPs on the top. The numerical evaluation with COMSOL uses for the photocurrent gain

$$I_{enh} = \frac{\int Q_{NP}\mathrm{AM}_{1.5G}(\lambda)d\lambda}{\int Q_0\mathrm{AM}_{1.5G}(\lambda)d\lambda}, \tag{D.10}$$

integrating over the solar spectrum $\mathrm{AM}_{1.5G}(\lambda)$. In the balanced state, we consider the stationary solution of a driven and damped oscillator, which yields for the second term

$$\frac{\beta N_m \delta w}{\delta w_0} = \frac{8\pi R^2 \beta C_0 m_p^2 e^4 n_e^2 \omega^2 f^2(\omega)}{3\mu m_n^2(\hbar\omega - E_g)\hbar^2\varepsilon^2}, \tag{D.11}$$

where $C_0 = n_s 4\pi R^3/(3H)$, $n_s$ is the MNP density, $H$ is the depth of Si layer. Since we consider the near-field close to the Si surface, $H = 200$ nm is sufficient to calculate the localized quantities. The damping force $f(\omega) = \frac{1}{\sqrt{(\omega_1^2 - \omega^2)^2 + 4\omega^2/\tau^2}}$ is calculated by comparison of the average power of the oscillator with the total power transfer to the semiconductor via the photon absorption: $\langle P\rangle = \hbar\omega\beta\delta w$ and is of the form of $\frac{1}{\tau} = \frac{\omega_p^2 R^3}{3\omega^2}\beta\hbar\omega\frac{\delta w}{D_0^2}$.

The modified local dipole field of a MNP is calculated in the nonlocal theory and inserted in eq. (D.4) in order to switch from classical local to mesoscopic electron dynamics.

# E. Second Order Susceptibility

## E.1 Macroscopic second harmonic surface polarization

The macroscopic second harmonic surface polarization $\mathbf{P}^s_{2\omega} = \mathbf{P}^s_{2\omega\parallel} + \mathbf{P}^s_{2\omega\perp}$ is determined from the near-fields at the excitation wavelength along the a considered surface. Its contributions stem from polarization fields perpendicular $\mathbf{P}^s_{2\omega\perp}$ and parallel $\mathbf{P}^s_{2\omega\parallel}$ to the nanostructure surface. These are in turn based on respective susceptibilities $\chi^s_\perp(\omega)$ and $\chi^s_\parallel(\omega)$.

The SSHG signal is calculated following the procedure by Mendoza et al. [316]. The bulk dielectric function is used as $\epsilon^B \equiv 1 + \omega_\mathrm{p}^2 \alpha(\omega)$. Note that bound and free electron contributions could be separated explicitely [317]. The electron density $n_0$ is connected to the plasma frequency via $\omega_\mathrm{p}^2 = \frac{n_0 e^2}{\epsilon_0 m_e}$. The polarizability $\alpha(\omega)$ is given as a Lorentzian in their approach leading to a typical Drude model for metals. Spatial variations of the driving field lead to nonlinear response in terms of sizable surface nonlinear polarization which has a dipolar character and can be written in terms of the macroscopic fields. We use, however, tabulated material data $\epsilon^B(\omega)$ by calculating $\alpha(\omega)$ from the above expression. This way, both inter- and intraband transitions are included in the material data.

The macroscopic second harmonic surface polarization $\mathbf{P}^s_{2\omega}$ depends on the geometrical parameters that define the grating, such as the height of the structure and the distance between grating stripes (lattice period or pitch) through the near-fields which are Bloch modes following the overall photonic crystal structure. Here,

$$P^s_{2\omega\perp} = \chi^s_\perp(\omega) D^2_\perp, \tag{E.1}$$

$$P^s_{2\omega\parallel} = \chi^s_\parallel(\omega) E_\parallel D_\perp, \tag{E.2}$$

where $\chi^s_\perp(\omega)$ and $\chi^s_\parallel(\omega)$ are the corresponding susceptabilities taken from Ref. [316] as

$$\chi^s_\perp(\omega) = \frac{\alpha^2(\omega)}{8\pi e} \frac{\alpha(2\omega)\ln(\epsilon^B(\omega)/(\epsilon^B(2\omega)))}{[\alpha(\omega)-\alpha(2\omega)]^2} + \frac{\alpha(\omega)}{8\pi e}\frac{\epsilon^B(\omega)-1}{\epsilon^B(\omega)}\left(\frac{1}{\epsilon^B(\omega)} + \frac{\alpha(2\omega)}{\alpha(2\omega)-\alpha(\omega)}\right), \tag{E.3}$$

$$\chi^s_\parallel(\omega) = \frac{1}{2e}\frac{n_0\alpha^2(\omega)}{\epsilon^B(\omega)}. \tag{E.4}$$

The local near-field at the surface of a metal object is obtained with FMM/RCWA calculations. For our grating system of rectangular symmetry being infinite along $y$-direction, we describe the macroscopic second harmonic surface polarization vectors as

$$\mathbf{P}^s_{2\omega} = P^s_{\perp,2\omega}\hat{\mathbf{n}} + P^s_{\parallel,2\omega}\hat{\mathbf{t}}. \tag{E.5}$$

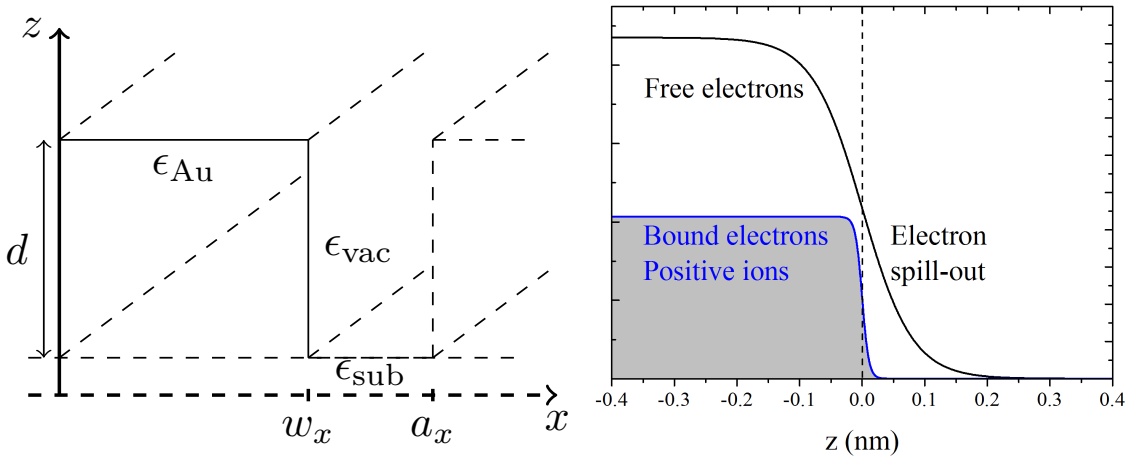


Fig. E.1.: (Left) Illustration of the structure. The one-dimensional unit cell of a grating structure consists of gold stripes of width $w_x$ and thickness $d$, the lattice period is $a_x$. The grating is in vacuum on a $SiO_2$ substrate. We calculate the local fields close to the surface of the Au stripes (green lines) to obtain the surface generated SHG signal. (Right) Transition of the electron density distribution from a metal region to a dielectric.

with contributions from fields parallel and perpendicular to the surface with orthonormal vectors $\hat{\mathbf{n}} = \pm\hat{\mathbf{z}}, \hat{\mathbf{t}} = \pm\hat{\mathbf{x}}$. The sign determines whether we consider opposite normal vectors on front or back, and left and right of the structure, resp. We obtain the following field vectors

$$E_{\parallel} = \mathbf{E}\cdot\hat{\mathbf{t}} = E_x \qquad D_{\perp} = \epsilon^B(\omega)\mathbf{E}\cdot\hat{\mathbf{n}} = \epsilon^B(\omega)E_z \tag{E.6}$$

Here, $E_{\parallel} = E_x$ for the parallel components. At normal incidence $E_y \equiv 0$ for this geometry, though the above conditions suppress the $y$-contribution in any case for a one-dimensional structure.

Thus, the macroscopic second harmonic surface polarization $\mathbf{P}^s_{2\omega}$ can be evaluated in reciprocal space within the FMM formulation and real space information can be obtained from inverse Fourier transform. This is in particular interesting to obtain the nonlinear electric field

$$\mathbf{E}^{\mathrm{nlo}}(2\omega) = \int_{\mathcal{S}} \mathbf{P}^s_{2\omega}\cdot\mathbf{E}^{\mathrm{lin}}(2\omega) \tag{E.7}$$

which is the integral of the scalar product of the local fields at the second harmonic frequency with the macroscopic polarization along the surface $\mathcal{S}$ of the structure as depicted in Fig. E.1.

## E.2 Detailed derivation

### E.2.1 First order (linear) polarization

To arrive at the second order susceptibilities, we start from the equation of motion for an electric charge $e$ of mass $m_e$ at a position $\mathbf{x}(t)$ away from its equilibrium $\mathbf{x}_0$.

$$m_e\ddot{\mathbf{x}} = -e\mathbf{E} - m_e\omega_0^2\mathbf{x} - m_e\gamma\dot{\mathbf{x}} - \frac{e}{c}\dot{\mathbf{x}}\times\mathbf{B}. \tag{E.8}$$

We use linear response theory for monochromatic driving fields

$$\mathbf{E}(\mathbf{x}_0+\mathbf{x},t)\approx\mathbf{E}(\mathbf{x}_0,t)+\mathbf{x}\nabla\mathbf{E}(\mathbf{x}_0,t),\qquad \mathbf{B}(\mathbf{x}_0+\mathbf{x},t)\approx\mathbf{B}(\mathbf{x}_0,t)+\mathbf{x}\nabla\mathbf{B}(\mathbf{x}_0,t) \tag{E.9}$$

leading to the parametric forced oscillator equation

$$m_e\ddot{\mathbf{x}}=-e\mathbf{E}(\mathbf{x}_0,t)-e\mathbf{x}\nabla\mathbf{E}(\mathbf{x}_0,t)-m_e\omega_0^2\mathbf{x}-m_e\gamma\dot{\mathbf{x}}+e\dot{\mathbf{x}}\times\int_0^t\mathrm{d}\,t'\nabla\times\mathbf{E}(\mathbf{x}_0,t'). \tag{E.10}$$

The nonlinearity stems from spatial variations of the driving field, in particular, across an interface. We consider the perturbation approach $\mathbf{x}(t)=\mathbf{x}^{(1)}+\mathbf{x}^{(2)}$ with the stationary solution $\mathbf{x}^{(1)}=\mathrm{Re}(\mathbf{x}_\omega e^{-i\omega t})$. The first order polarization is solved as $\mathbf{p}_\omega=-e\mathbf{x}_\omega=\alpha(\omega)\mathbf{E}_\omega$ with the linear polarizability

$$\alpha(\omega)=\frac{{}^{e^2}\!/_{m_e}}{\omega_0^2-\omega^2-i\gamma\omega}\mathbf{E}_\omega=\frac{{}^{e^2}\!/_{m_e}}{D(\omega)}\mathbf{E}_\omega=\epsilon_0\frac{\omega_p^2}{D(\omega)}\mathbf{E}_\omega. \tag{E.11}$$

### E.2.2 Second order (nonlinear) polarization

After evaluating the first order polarization, the remaining terms which are quadratic in $\mathbf{E}$ are, accounting for the fact that $\mathbf{x}^{(1)}$ is linear in $\mathbf{E}$,

$$m_e\ddot{\mathbf{x}}^{(2)}=-e\mathbf{x}^{(1)}\nabla\mathbf{E}(\mathbf{x}_0,t)-m_e\omega_0^2\mathbf{x}^{(2)}-m_e\gamma\dot{\mathbf{x}}^{(2)}+e\mathbf{x}^{(1)}\times\left(\nabla\times\mathbf{E}(\mathbf{x}_0,t)\right), \tag{E.12}$$

which can be solved to

$$-m_e(2\omega)^2\mathbf{x}_{2\omega}=\frac{{}^{e^2}\!/_{m_e}}{D(\omega)}\mathbf{E}_\omega\nabla\mathbf{E}_\omega-m_e\omega_0^2\mathbf{x}_{2\omega}+im_e\gamma 2\omega\mathbf{x}_{2\omega}-\frac{{}^{e^2}\!/_{m_e}}{D(\omega)}\mathbf{E}_\omega\times\left(\nabla\times\mathbf{E}_\omega\right). \tag{E.13}$$

The dipole contribution to the second order nonlinear polarization becomes

$$\mathbf{p}_{2\omega}=-e\mathbf{x}_{2\omega}={}^{-1}\!/_{e}\;\alpha(\omega)\alpha(2\omega)\left(\mathbf{E}_\omega\nabla\mathbf{E}_\omega-\mathbf{E}_\omega\times\left(\nabla\times\mathbf{E}_\omega\right)\right). \tag{E.14}$$

Using the vector identity $\frac{1}{2}\nabla\mathbf{E}^2=\mathbf{E}\nabla\mathbf{E}+\mathbf{E}\times(\nabla\times\mathbf{E})$ yields

$$\mathbf{p}_{2\omega}={}^{-1}\!/_{2e}\;\alpha(\omega)\alpha(2\omega)\left(\nabla\mathbf{E}_\omega^2-4\mathbf{E}_\omega\times\left(\nabla\times\mathbf{E}_\omega\right)\right). \tag{E.15}$$

The relevant quadrupole contribution can be added via

$$q_{2\omega}=-e\mathbf{x}_\omega\mathbf{x}_\omega={}^{-1}\!/_{e}\;\alpha(\omega)^2\mathbf{E}_\omega\mathbf{E}_\omega. \tag{E.16}$$

#### Electron density distribution

The next step is to consider the change in the electron density across the interface. First, assuiming a system size $a\ll\lambda$, we can neglect the contribution of the magnetic field $\sim(\nabla\times\mathbf{E}_\omega)$ and overall retardation effects, i. e., we are entering a quasistatic picture from here

on. Let the surface be situated at $z = 0$ with the limits $n(z \to -\infty) = 0$ and $n(z \to \infty) = n^B$, defining the dielectric and metal region through the bulk density $n^B$. The transition shall be smooth but arbitrary on a sub-nanometer length scale, see Fig. E.1(Right). The surface second harmonic generation (SSHG) contributions stem from the spatial variation of only the electric fields across the surface region, i. e. the discrete positions of atoms is not considered and, thus, modifications induced by the local shape of the surface in $x$ and $y$ direction are not considered.

The second order polarization derived so far reads

$$\mathbf{P}_{2\omega} = n\mathbf{p}_{2\omega} - \frac{1}{2}\nabla\left(nq_{2\omega}\right) = n\alpha(2\omega)\mathbf{E}_{2\omega} - \frac{1}{2e}\left(\alpha(\omega)\alpha(2\omega)n\nabla\mathbf{E}_{\omega}^2 - \alpha(\omega)^2\nabla\left(n\mathbf{E}_{\omega}\mathbf{E}_{\omega}\right)\right). \quad \text{(E.17)}$$

It is assumed that the external field is only contributing at the fundamental harmonic. With no external field at the second harmonic, we can assume the nonlinear field to be entirely governed by the polarization itself $\epsilon_0\mathbf{E}_{2\omega} = -\mathbf{P}_{2\omega}$. The shape of the surface enters via $\epsilon(\omega, z) = 1 + n(z)^{\alpha(\omega)}/\epsilon_0$. These two aspects yield

$$\mathbf{P}_{2\omega}(z) = -\frac{1}{2e}\frac{1}{\epsilon(2\omega, z)}\left(\alpha(\omega)\alpha(2\omega)n(z)\nabla\mathbf{E}_{\omega}^2 - \alpha(\omega)^2\nabla\left(n(z)\mathbf{E}_{\omega}\mathbf{E}_{\omega}\right)\right). \quad \text{(E.18)}$$

Finally, the macroscopic second order polarization stemming from the surface is obtained from integration over the surface region

$$\mathbf{P}_{2\omega}^s = \int_{-\infty}^{\infty} \mathrm{dz}\, \mathbf{P}^{2\omega}(z). \quad \text{(E.19)}$$

Note that this integration is analytical by substituting $\mathrm{dz} = \frac{\mathrm{dn}}{\mathrm{dn/dz}}$ and independent of the given profile $n(z)$ as long as it is smooth.

Performing the integration with respect to the electron density distribution $n$ for the parallel $\mathbf{P}_{2\omega,\parallel}^s$ and perpendicular $\mathbf{P}_{2\omega,\perp}^s$ polarization fields, we can derive the corresponding susceptibilities $\chi_{\parallel z\parallel}^s = \chi_{\parallel\parallel z}^s$ and $\chi_{zzz}^s$.

#### Perpendicular contributions of the bulk material

The polarization perpendicular to the surface from the above equations results in

$$P_{2\omega,z}(z) = -\frac{1}{2e}\frac{1}{\epsilon(2\omega, z)}\left(\alpha(\omega)\alpha(2\omega)n(z)\frac{\partial}{\partial_z}\mathbf{E}_{\omega}^2 - \alpha^2(\omega)\frac{\partial}{\partial_z}n(z)\mathbf{E}_{\omega}\mathbf{E}_{\omega}\right) \quad \text{(E.20)}$$

with $\mathbf{D}_{\omega} = \epsilon_0\epsilon(\omega, z)\mathbf{E}_{\omega}$ and $P_{2\omega,z}^s = \chi_{zzz}^s D_z^2$, we rearrange to the form

$$P_z^{2\omega}(z) = -\frac{1}{2e}\frac{1}{\epsilon(2\omega, z)}\left(\frac{\alpha(\omega)\alpha(2\omega)}{\epsilon_0^2}n(z)\frac{\partial}{\partial_z}\frac{1}{\epsilon^2(\omega, z)} - \frac{\alpha^2(\omega)}{\epsilon_0^2}\frac{\partial}{\partial_z}\frac{n(z)}{\epsilon^2(\omega, z)}\right)D_z^2. \quad \text{(E.21)}$$

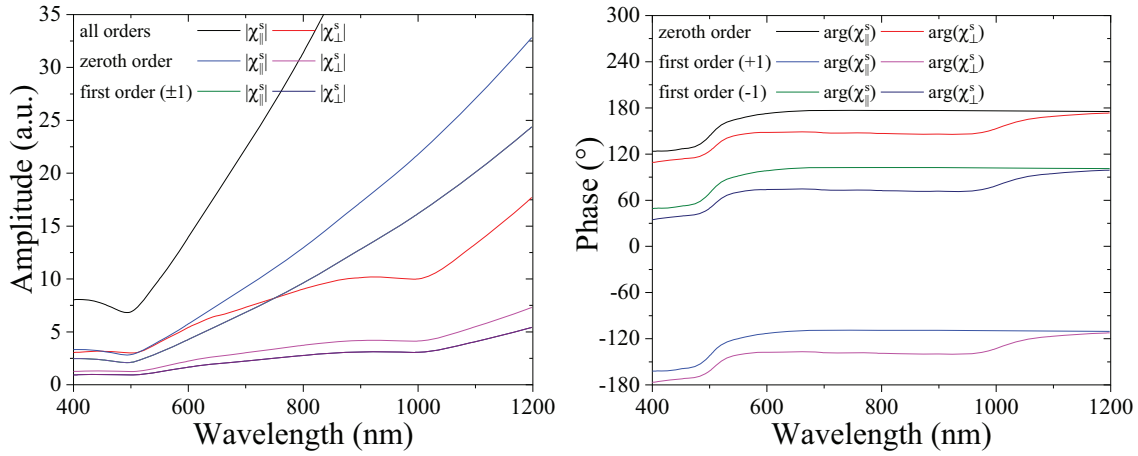


Fig. E.2.: Surface second order nonlinear susceptibilities. (Left) Amplitude and (Right) argument of surface susceptibilites in different orders of diffraction.

After integration along the interface, this allows to deduce the corresponding second order surface susceptibility

$$\chi^s_{zzz} = \frac{\alpha(\omega)}{2e}\left(\frac{\alpha(\omega)\alpha(2\omega)\ln {}^{\epsilon^B(\omega)}/_{\epsilon^B(2\omega)}}{(\alpha(\omega)-\alpha(2\omega))^2} + \frac{\epsilon^B(\omega)-1}{\epsilon^B(\omega)}\left(\frac{1}{\epsilon^B(\omega)} + \frac{\alpha(2\omega)}{\alpha(2\omega)-\alpha(\omega)}\right)\right). \tag{E.22}$$

**Parallel contributions of the bulk material**

In similar steps as for the perpendicular contribution, we arrive at

$$\mathbf{P}_{2\omega,\parallel}(z) = \frac{1}{2e}\alpha^2(\omega)\frac{\partial}{\partial_z}\, n(z)\mathbf{E}_{\omega,\parallel}E_{\omega,z}(z) \tag{E.23}$$

for the parallel polarization field and compare the expression after integration to $\mathbf{P}^s_{2\omega,\parallel} = \chi^s_{\parallel\parallel z}\mathbf{E}_{\omega,\parallel}D_z$. Due to symmetry

$$\chi^s_{\parallel z\parallel} = \chi^s_{\parallel\parallel z} = \frac{1}{2e}\frac{n^B\alpha^2(\omega)}{\epsilon^B(\omega)}. \tag{E.24}$$

**Susceptibilities at nanostructured surfaces**

As a final note, given a simple enough nanostructure, the effective susceptibility of a textured surface can be deduced from the lowest order Fourier coefficients used in the FMM procedure. In a one-dimensional grating, this yields $\chi^s(0,0) = \chi^s\frac{w_x}{a_x}$ for the zeroth diffraction order and $\chi^s(0,\pm1) = \pm\chi^s\frac{1}{\pi}e^{\mp i\pi w_x/a_x}\sin(\pm\pi w_x/a_x)$ for the first diffration orders. In Fig. E.2, the amplitude and argument of the parallel and perpendicular susceptibilities are shown for the two lowest orders as obtained from a one-dimensional structure with grating period $a_x = 800$ nm and gold stripe width of $w_x = 300$ nm. In comparison with results from Ref. [317] where the susceptibility is calculated based on Fresnel coefficients the overall shape and range of values is in good agreement.

# F. Anharmonic Oscillator Model

In this section, we briefly discuss the anharmonic oscillator model used to describe third order nonlinearities. It should be noted that for the third order to be the dominant nonlinear contribution the second order needs to vanish. This is usually the case in centrosymmetric systems to which spherical nanoparticles belong.

## F.1 Harmonic Oscillator model for linear response $\chi^{(1)}$

In first order as linear response to an electric field the polarization can be understood from the physical displacement $\mathbf{x}$ of electrons beyond their equilibrium position $\mathbf{x} = 0$

$$\mathbf{P} = -en\mathbf{x} = \epsilon_0 \chi^{(1)} \mathbf{E}. \tag{F.1}$$

Hereby, $n$ is the density of oscillating electrons. For the linear susceptibility and permittivity $\epsilon = \epsilon_b + \chi^{(1)}$ follows $\chi^{(1)} = {|\mathbf{P}|}/{\epsilon_0 |\mathbf{E}|}$. The equation of motion for electrons under the influence of an external electric field in the harmonic oscillator model is

$$\ddot{\mathbf{x}} + \gamma \dot{\mathbf{x}} + \omega_0^2 \mathbf{x} = \frac{F}{m_e} = -\frac{e}{m_e} \mathbf{E}_0 e^{-i\omega t}. \tag{F.2}$$

The characteristic equation of the related homogeneous differential equation yields the resonance condition $D(\omega) = \omega_0^2 - \omega^2 - i\omega\gamma \equiv 0$ as in the previous case. We obtain

$$\chi^{(1)}(t) = \frac{-en|\mathbf{x}(t)|}{\epsilon_0 |\mathbf{E}(t)|} = \frac{\omega_p^2}{D(\omega)} \tag{F.3}$$

for the linear susceptibility with the plasmon frequency $\omega_p$.

## F.2 Higher order response $\chi^{(n)}$

To study susceptibilities for higher order nonlinear effects, the above harmonic oscillator is extended by an anharmonic term with nonlinear strength amplitude $f$

$$\ddot{\mathbf{x}} + \gamma \dot{\mathbf{x}} + \omega_0^2 \mathbf{x} + f x^2 = -\frac{e}{m_e} \mathbf{E}_0 e^{-i\omega t}. \tag{F.4}$$

We assume that the nonlinear response is weak compared to the dominant linear response and make use of a perturbative approach introducing a small parameter $\lambda$

$$\mathbf{x}(t) = \sum_n \lambda^n \mathbf{x}^{(n)}, \qquad \mathbf{E} \to \lambda \mathbf{E}. \tag{F.5}$$

For each order of $n$ we obtain a separate equation with analytic solutions. The lowest order is the linear result of the harmonic oscillator briefly introduced in the previous section. The first and second order in $n$ yield

$$\ddot{\mathbf{x}}^{(2)} + \gamma\dot{\mathbf{x}}^{(2)} + \omega_0^2\mathbf{x}^{(2)} + f(x^{(1)})^2 = 0, \quad \text{and} \quad \ddot{\mathbf{x}}^{(3)} + \gamma\dot{\mathbf{x}}^{(3)} + \omega_0^2\mathbf{x}^{(3)} + 2fx^{(1)}x^{(2)} = 0, \tag{F.6}$$

so that the second order nonlinearity becomes

$$\ddot{\mathbf{x}}^{(2)} + \gamma\dot{\mathbf{x}}^{(2)} + \omega_0^2\mathbf{x}^{(2)} = -f\left(\frac{e\mathbf{E}_0}{\epsilon_0 m_e D(\omega)}\right)^2 e^{-i2\omega t}. \tag{F.7}$$

The displacement $\mathbf{x}^{(2)}$ is driven by light at the second harmonic wavelength if all incident fields are monochromatic at this wavelength. Analoguous to the previous case, we introdcue higher order susceptibilities as

$$\chi^{(n)} = \frac{|\mathbf{P}|}{\epsilon_0|\mathbf{E}|^n}. \tag{F.8}$$

This leads to the second order (Second Harmonic Generation (SHG)), here, generalized to any incident frequencies $\omega_n, \omega_m$

$$\chi^{(2)}(-\omega_q \mid \omega_n, \omega_m) = \frac{ef}{m_e}\frac{\omega_p^2}{D(\omega_q)D(\omega_n)D(\omega_m)}\delta(\omega_q - \omega_n - \omega_m) \tag{F.9}$$

with a small nonlinear field strength $f$. Note that $D(\omega_q)$ is the resonance term stemming from the second order differential equation and the condition $\omega_q = \omega_n + \omega_m$ must hold for any frequency combination. Many experimental situtations, such as pump-probe experiments or four-wave-mixing make use of cross-phase modulation with fields incident at different frequencies. Higher orders of the nonlinear susceptibility are, therefore, in general of tensorial character. Each component of the second order polarization takes the form

$$P_i^{(2)}(\omega_q) = \epsilon_0 \sum_{nm}\sum_{kj} \chi_{ikj}^{(2)}(-\omega_q \mid \omega_n, \omega_m)E_k(\omega_n)E_j(\omega_m)\delta(\omega_q - \omega_n - \omega_m) \tag{F.10}$$

where the indices $i, k, j$ run over $x, y, z$ components. The second order polarization strongly depends on the polarization of the incoming fields.

Due to symmetry, the second order polarization may vanish in centrosymmetric systems where all contributions interfere destructively. However, surface second harmonic generation (SSHG) is an important aspect in nonlinear nanostructures where the symmetry is broken at nanostructured surfaces.

**Third order nonlinear susceptibility**

In the case of third order nonlinearities at a frequency $\omega_q = \omega_n + \omega_m + \omega_p$ this becomes

$$P_i^{(3)}(\omega_q) = \epsilon_0 \sum_{nmp} \sum_{jkl} \chi_{ijkl}^{(3)}(-\omega_q \mid \omega_n, \omega_m, \omega_o) E_k(\omega_n) E_j(\omega_m) E_l(\omega_o). \tag{F.11}$$

Possible contributions of exclusively third order are

$$\begin{aligned}\frac{1}{\epsilon_0} P_i^{(3)} = \sum_{jkl} [\ & \chi_{ijkl}^{(3)}(-3\omega|\omega,\omega,\omega) E_k(\omega) E_j(\omega) E_l(\omega) + \chi_{ijkl}^{(3)}(3\omega|-\omega,-\omega,-\omega) E_k(-\omega) E_j(-\omega) E_l(-\omega) \\ & + \chi_{ijkl}^{(3)}(\omega|-\omega,\omega,-\omega) \{E_k(-\omega) E_j(-\omega) E_l(\omega) + E_k(\omega) E_j(-\omega) E_l(-\omega) + E_k(-\omega) E_j(\omega) E_l(-\omega)\} \\ & + \chi_{ijkl}^{(3)}(-\omega|-\omega,\omega,\omega) \{E_k(-\omega) E_j(\omega) E_l(\omega) + E_k(\omega) E_j(-\omega) E_l(\omega) + E_k(\omega) E_j(\omega) E_l(-\omega)\}\ ].\end{aligned} \tag{F.12}$$

Identifying possible permutations and symmetries, we can make the transition

$$\sum_{jkl} \to \frac{1}{3} \sum_{jkl} \left(\delta_{jk}\delta_{il} + \delta_{jl}\delta_{ik} + \delta_{ji}\delta_{kl}\right). \tag{F.13}$$

Introducing Kleinmann symmetry $\chi^{(3)} \equiv \chi_{iikk}^{(3)} = \chi_{ikik}^{(3)} = \chi_{ikki}^{(3)}$ to summarize the above expression and simplifying the notation for the susceptibility overall, we obtain

$$\begin{aligned}\frac{1}{\epsilon_0} P_i^{(3)} = \frac{1}{3} \sum_k [\ & 3\chi^{(3)}(3\omega) E_k^2(\omega) E_i(\omega) + 3\chi^{(3)}(-3\omega) E_k^2(-\omega) E_i(-\omega) \\ & + 3\chi^{(3)}(-\omega) \left\{E_k^2(-\omega) E_i(\omega) + 2E_k(-\omega) E_k(\omega) E_i(-\omega)\right\} \\ & + 3\chi^{(3)}(\omega) \left\{E_k^2(\omega) E_i(-\omega) + 2E_k(\omega) E_k(-\omega) E_i(\omega)\right\}\ ].\end{aligned} \tag{F.14}$$

Finally, as vectors

$$\begin{aligned}\frac{1}{\epsilon_0} \mathbf{P}^{(3)} = & \chi^{(3)}(3\omega) \mathbf{E}^2(\omega) \mathbf{E}(\omega) + \chi^{(3)}(-3\omega) \mathbf{E}^2(-\omega) \mathbf{E}(-\omega) \\ & + \chi^{(3)}(-\omega) \left\{\mathbf{E}^2(-\omega) \mathbf{E}(\omega) + 2|\mathbf{E}(\omega)|^2 \mathbf{E}(-\omega)\right\} + \chi^{(3)}(\omega) \left\{\mathbf{E}^2(\omega) \mathbf{E}(-\omega) + 2|\mathbf{E}(\omega)|^2 \mathbf{E}(\omega)\right\}.\end{aligned} \tag{F.15}$$

The different contributions to the third order nonlinear polarizability result in Third Harmonic Generation (THG) at triple the incident frequency

$$\mathbf{P}^{(\mathrm{THG})}(3\omega) = \epsilon_0 \chi^{(3)}(3\omega) \mathbf{E}^2(\omega) \mathbf{E}(\omega) \tag{F.16}$$

and Kerr nonlinearities at the fundamental harmonic

$$\mathbf{P}^{(\mathrm{Kerr})}(\omega) = \epsilon_0 \chi^{(3)}(\omega) \left(\mathbf{E}^2(\omega) \mathbf{E}^*(\omega) + 2|\mathbf{E}(\omega)|^2 \mathbf{E}(\omega)\right). \tag{F.17}$$

In case of the anharmonic oscillator model, the susceptibility can be deduced as

$$\chi^{(3)}(-\omega_q|\omega_n,\omega_m,\omega_o) = \frac{\tilde{f}}{D(\omega_q)D(\omega_n)D(\omega_m)D(\omega_o)} \tag{F.18}$$

and for self-modulated Kerr nonlinearities, where all frequencies are at the fundamental wavelength, i. e. $\omega_\alpha = \pm\omega$, the third order susceptibility reduces to the simplified notation

$$\chi^{(3)}(\omega) = \frac{\tilde{f}}{|\omega_0^2 - \omega^2 - i\Gamma\omega|^2(\omega_0^2 - \omega^2 - i\Gamma\omega)^2}. \tag{F.19}$$

The main contribution of electrons in nanoparticles is given at Mie resonances $\omega_0$.

This case is often given in terms of a higher order refractive index $n_2$

$$n_2 = \frac{3}{2}\frac{1}{n_0^2\epsilon_0 c}\chi^{(3)}, \qquad \bar{n} = n_0 + n_2 I. \tag{F.20}$$

The related nonlinear absorption coefficient $\beta$ is defined as

$$\beta = 2k_0\mathrm{Im}(n_2), \qquad \bar{\alpha} = \alpha_0 + \beta I. \tag{F.21}$$

# G. Effective Nonlinear Media

We compare results for nonlinear gold and iridium nanoparticles in alumina for different fill fractions $f$ describing the relative volume density of particles in the host. Within effective medium theory (EMT), amorphous composites are described as a homogeneous film with an effective (linear) permittivity and in its nonlinear extension an effective third order susceptibility as the nanoparticles are assumed to be centrosymmetric and, thus, do not exhibit a second order nonlinear response.

## G.1 Nonlinear Maxwell-Garnett-Theory

Maxwell-Garnett (MG) theory [293] assumes spherical inclusions of a material $i$ with permittivity $\epsilon_i$ arbitrarily distributed in a host material $h$ with permittivity $\epsilon_h$. The volume fraction $f = {}^{V_i}/_{V_h} = {}^{N4\pi R_{av}^3}/_{3V_h}$ for $N$ inclusions of average size $R_{av}$ has to be small, so that we can exclude interactions between them with distances larger than the wavelength. Moreover, assuming sufficiently small spherical inclusions allows us to work in the dipolar regime and electrostatic approximation [222] where the polarization of a single nanoparticle becomes $\mathbf{p} = \alpha_1^E \mathbf{E}$ with the (electric) polarizability given by

$$\alpha_1^E = R^3 \frac{\epsilon_i(\omega) - \epsilon_h(\omega)}{\epsilon_i(\omega) + 2\epsilon_h(\omega)} \equiv R^3\, \eta(\omega). \tag{G.1}$$

In this approximation, the effective permittivity is

$$\epsilon_{\text{eff}} = \epsilon_h(\omega) \frac{1 + 2\eta(\omega) f}{1 - \eta(\omega) f}. \tag{G.2}$$

For larger particle sizes or a large particle size variance, the quasistatic polarizability should be replaced by the lowest order Mie coefficient [300] to account for radiation losses and other size effects such as a size-dependent shift in the resonance position as given by eq. (4.4) in section 4.1.

The effective third order susceptibility for nonlinear nanoparticle inclusions $\chi_i^{(3)}(\omega)$ reads [294–296]

$$\chi_{\text{eff}}^{(3)} = f \mu^2 \left|\mu\right|^2 \chi_i^{(3)}, \tag{G.3}$$

with an enhancement factor from the linear response of a nanoparticle mixture

$$\mu = \frac{\epsilon_{\text{eff}}(\omega) + 2\epsilon_h(\omega)}{\epsilon_i(\omega) + 2\epsilon_h(\omega)} \tag{G.4}$$

and the effect of a nonlinear host material $\chi_h^{(3)}(\omega)$ can be included as well, though its impact

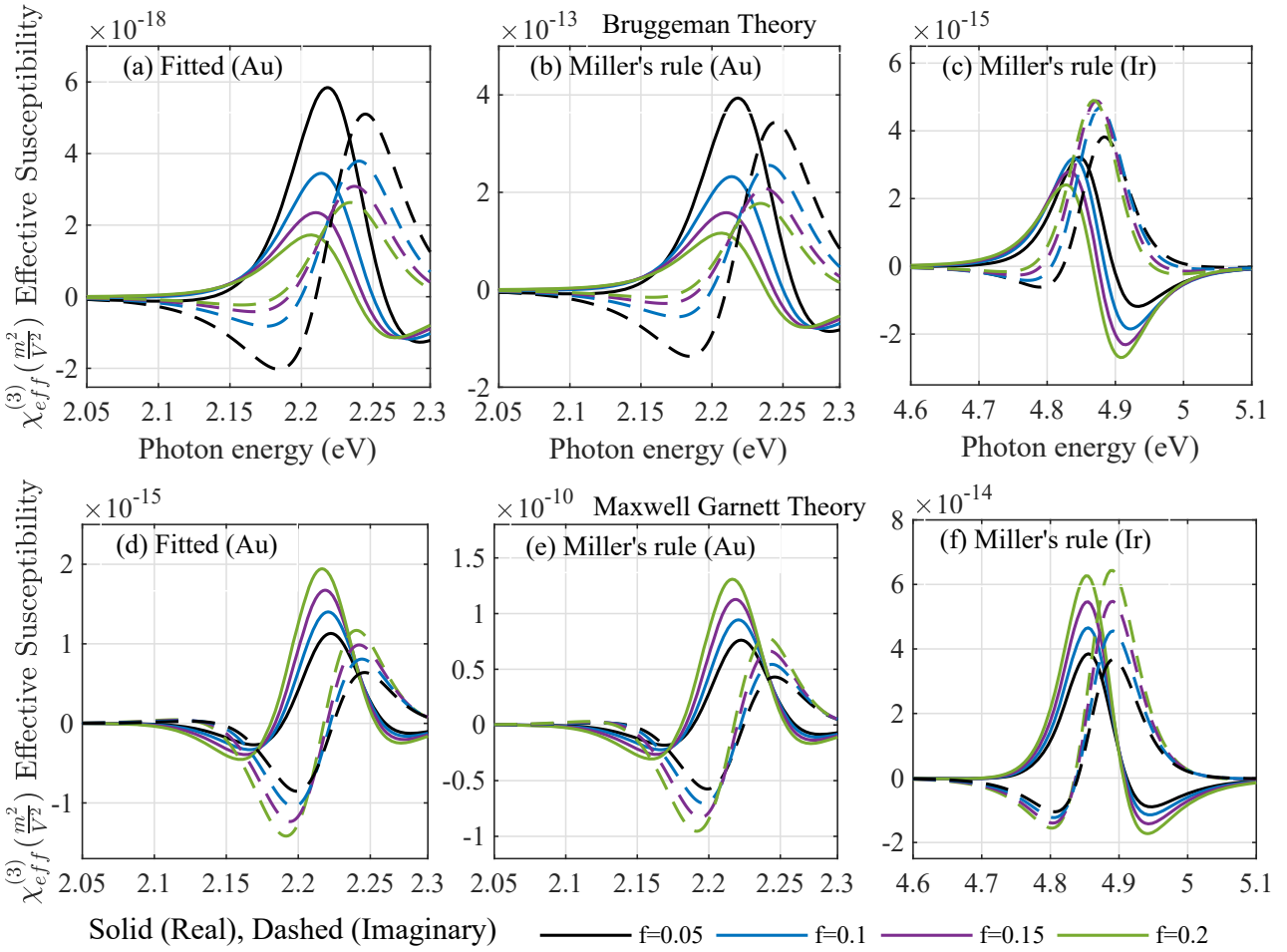


Fig. G.1.: Real (solid) and imaginary (dashed) parts of the third order effective susceptibility $\chi^{(3)}_{\text{eff}}$ for nonlinear (upper panel) Br theory and (lower panel) MG theory as a function of photon energy $E = \hbar\omega$ for (a), (b), (d), (e) Au and (c), (f) Ir using (a), (d) fitting the nonlinear strength amplitude to available experiments [271] and (b), (c), (e), (f) the analytic Miller's rule.

is rather small with metallic inclusions.

## G.2 Nonlinear Bruggeman Theory

For high concentrations, i. e. larger volume fractions $f$, and more homogeneous mixtures, the Bruggeman (Br) model for the effective permittivities is to be preferred [294]. The general equation describing the mixture of two materials is given by

$$f\frac{\epsilon_i - \epsilon_{\text{eff}}}{\epsilon_{\text{eff}} + g(\epsilon_i - \epsilon_{\text{eff}})} + (1-f)\frac{\epsilon_h - \epsilon_{\text{eff}}}{\epsilon_{\text{eff}} + g(\epsilon_h - \epsilon_{\text{eff}})} = 0. \tag{G.5}$$

There is no difference made between host and inclusion material and, thus, no restrictions to the shape of the composite. Both constituents are treated on equal footing and the resulting differences to Maxwell-Garnett theory can be striking [290, 318]. The geometrical factor $g$ is typically set to $\frac{1}{3}$ (as here) for three-dimensional and $\frac{1}{2}$ for two-dimensional inclusions. This

equation results in two explicit solutions from a quadratic equation of which one is physical

$$\epsilon_{\text{eff}} = \frac{-c \pm \sqrt{c^2 + 4(1-g)g\epsilon_h\epsilon_i}}{2(1-g)} \quad \text{with} \quad c = (g-(1-f))\epsilon_h + (g-f)\epsilon_i. \tag{G.6}$$

To determine the physical branch, the condition $\mathrm{Im}(\epsilon_{\text{eff}}(\omega)) > 0$ needs to be fulfilled. The effective degenerate third-order susceptibility in case of weakly nonlinear composites [310] is

$$\chi^{(3)}_{\text{eff}} = \frac{1}{1-f}\left|\frac{\partial\epsilon_{\text{eff}}}{\partial\epsilon_h}\right|\left(\frac{\partial\epsilon_{\text{eff}}}{\partial\epsilon_h}\right)\chi^{(3)}_h + \frac{1}{f}\left|\frac{\partial\epsilon_{\text{eff}}}{\partial\epsilon_i}\right|\left(\frac{\partial\epsilon_{\text{eff}}}{\partial\epsilon_i}\right)\chi^{(3)}_i,$$

where in the case of two constituent materials the derivatives can be determined analytically to

$$\frac{\partial\epsilon_{\text{eff}}}{\partial\epsilon_h} = \frac{g+f-1}{2(g-1)} - \frac{(1-f-g)A(\omega) - 2(g-1)g\epsilon_i}{2(g-1)\sqrt{A(\omega)^2 - 4(g-1)g\epsilon_h\epsilon_i}}, \tag{G.7}$$

$$\frac{\partial\epsilon_{\text{eff}}}{\partial\epsilon_i} = \frac{g-f}{2(g-1)} - \frac{(f-g)A(\omega) - 2(g-1)g\epsilon_i}{2(g-1)\sqrt{A(\omega)^2 - 4(g-1)g\epsilon_h\epsilon_i}}, \tag{G.8}$$

with $A(\omega) = \epsilon_i(f-g) + \epsilon_h(1-f-g)$.

The real and imaginary part of the effective third order susceptibilities of the amorphous mixture in the two considered EMTs are shown in Fig. G.1 varying the fill fraction. Bruggeman in the upper and Maxwell-Garnett theory in the lower panel agree on the resonance position at low fill factors, but differ by two to three orders of magnitude in the predicted amplitudes of the amorphous composite. For MG theory in the lower panel, a typical redshift of resonances is observed with increasing fill factor for gold but is not yet seen for iridium at low fill factors. Both the linear and nonlinear local field factors yield a strong increase in the effective susceptibilities with respect to their bulk counterparts for gold, but have little impact on iridium, as they are close to unity. This means that amorphous films are expected to show stronger nonlinear response than bulk materials which is reflected in the collected experimental data in Ref. [271]. The large susceptibilities observed around resonance for MG theory are strongly overestimating the nonlinear response of weakly metallic films as it would allow strong alterations in the material properties at moderate incident intensities. We will, therefore, concentrate on evaluating further the impact of the effective nonlinear material parameters predicted by Bruggeman theory.

The susceptibilities in both EMTs clearly have two separable contributions from the host and from the inclusion material and are easily reduced to the case of only one component being nonlinear. We assume the host to be nonlinear with constant [274] $\chi^{(3)}_h = 3.1 \times 10^{-22}\text{m}^2/\text{V}^2$ which has little effect on the overall properties of the films even at low fill factors. We denote the absolute values of the prefactors $f\mu^2\left|\mu\right|^2$ to $\chi^{(3)}_i$ in the Maxwell-Garnett EMT and $\frac{1}{f}\left|\frac{\partial\epsilon_{\text{eff}}}{\partial\epsilon_i}\right|\left(\frac{\partial\epsilon_{\text{eff}}}{\partial\epsilon_i}\right)$ in the Bruggeman EMT the corresponding nonlinear local field factors. We consider the nonlinear local field factor from MG theory in Fig. G.2(a) for gold and (b) for iridium and with it the expected nonlinear enhancement of the third order susceptibility

$\max\left|\chi_{\text{eff}}^{(3)}(\omega)\right| / \max\left|\chi_i^{(3)}(\omega)\right|$ of different amorphous composites in Figs. G.2(c) with gold and (d) with iridium nanoparticle inclusions compared to the bulk case. Fig. G.2(a) underlines that for gold strong enhancement factors are expected both for the linear and the nonlinear material parameters while it can be seen in Fig. G.2(b) that iridium yields enhancement factors of around unity. Considering the maximum of the total effective susceptibility for increasing metal load of the transparent, nonlinear host material in Figs. G.2(c) and (d), we find an optimum nanoparticle density with maximum enhancement factor with respect to the bulk case before absorption processes start to dominate the material response. Furthermore, the increase in the nonlinear response from Ir remains moderate which could be expected already from comparing the Ir results in Fig. 8.2 showing minor changes. These findings are, however, contrary to the observations with Bruggeman theory where the values are well below unity (and thus not shown in Figs. G.2(a) and (b)). Here, in Fig. G.2(c), the largest relative nonlinear coefficent for amorphous gold/$Al_2O_3$ composites is found for smallest fill fractions. With increasing metal load and absorption it drops from the beginning. On the other hand, the predictions for Ir follow a similar path.

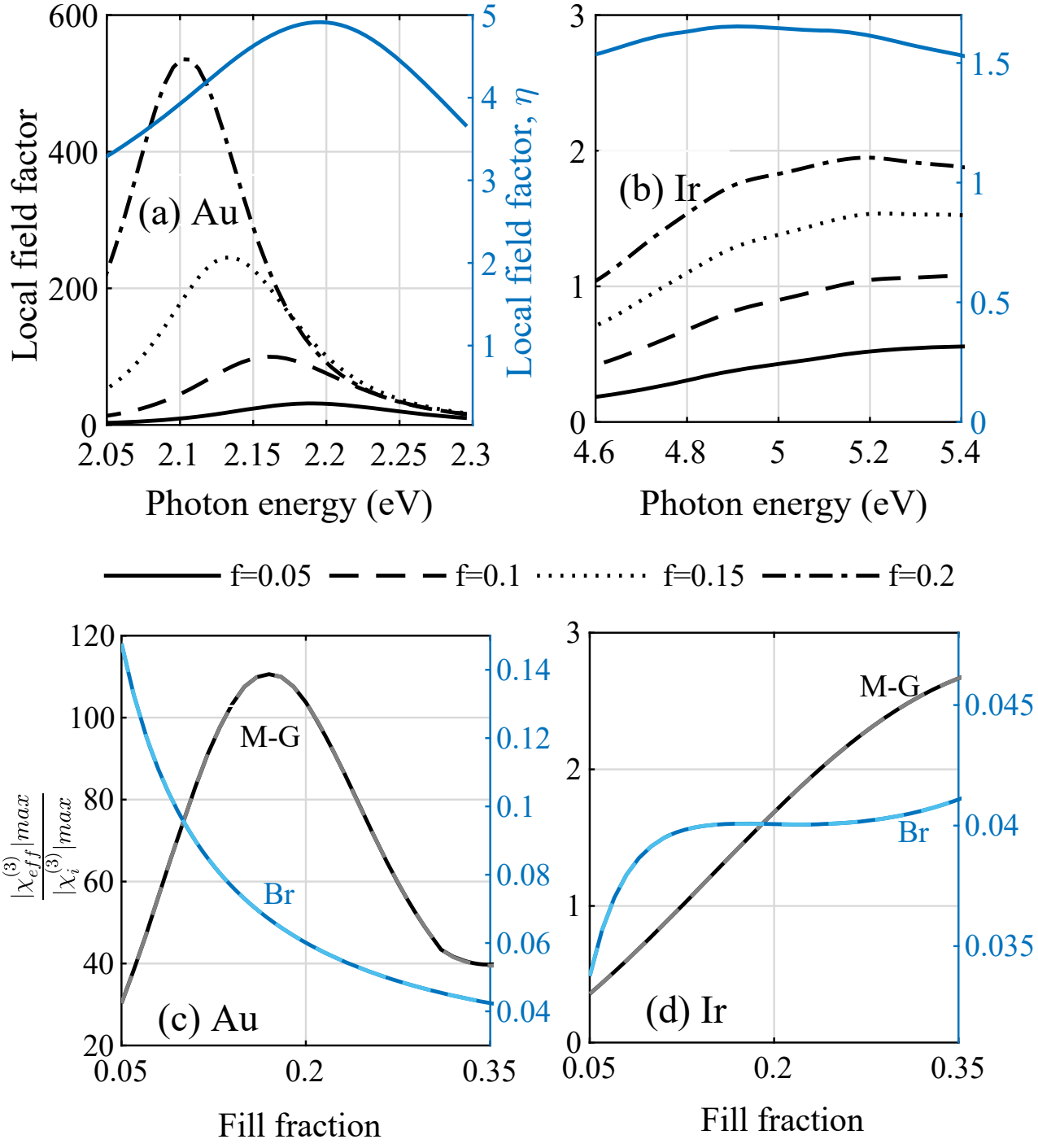


Fig. G.2.: Absolute values of the (a), (b) local field enhancement factors for (a) gold and (b) iridium in the Maxwell-Garnett theory for the nonlinear coefficients compared to the single particle enhancement factor $|\eta|$ in the linear case. (c), (d) Enhancement of the nonlinear coefficient comparing the amorphous structures relative to the bulk case for increasing fill factors $f$ for both of the two effective medium theories used (MG grey, Br blue) comparing the prediction from Miller's rule (light color) with the one fitted to experimental values (dark color).

# Acknowledgements

I started studying physics in 2004 because it seemed one of the most challenging subjects I could do. Soon the challenge turned into utter fascination. It is said that if you love what you do it does not feel like work. While there is indeed a lot of work in research there is also great reward and joy in the successes, in the collaborations and in the friendships formed.

Equally in 2004, I met the man who shares this passion and together we carry it through the world. Thank you Robert for everything past, present and future. You complete my square.

I would like to thank my co-workers and supporting funding agencies from my previous postdoctoral stages in no particular, somewhat chronological order.

I am grateful to the Deutsche Forschungsgemeinschaft (DFG), the German Research Foundation, for financial support. My time at DTU Fotonik at Danmarks Tekniske Universitet (DTU) was made possibly through a DFG research fellowship (GEPRIS Grant No. 268910011) and the support of the Center for Nanostructured Graphene which is sponsored by the Danish National Research Foundation, Project DNRF103. Here, I would like to acknowledge Sanshui Xiao, Andrei V. Lavrinenko, Martijn Wubs, and my host N. Asger Mortensen for fruitful scientific discussions and for creating an inclusive and open-minded research environment.

Denmark and its culture will always have a special place in my heart thanks to you.

I highly appreciate Andreas Knorr at Technische Universität Berlin (TUB) for keeping a door open to alumnis for years and years after their graduation. Your support and advice during my undergraduate studies as well as much later when searching for postdoc opportunities is invaluable.

Likewise, Inez M. Weidinger, who leads her own group at Technische Universität Dresden today and her current and former group members at TUB, in particular, Khoa Hoang Ly, have been wonderful to work with during the years and I am deeply indebted for their continued trust and collaborations.

Part of the presented research was funded by the European Cooperation in Science and Technology (COST), Action MP1406 MultiscaleSolar. Here, I would like to wholeheartedly thank James Connolly, Jelena Radovanovic, Søren Peder Madsen, Matthias Auf der Maur, Spiros Kassavetis and Lejo J. Koduvelikulathu and many more from our joint network on solar cell research for stimulating discussions and joyful meetings around Europe.

In particular, I would like to thank Katarzyna Kluczyk-Korch, Lucjan and Witold Aleksander Jacak from Wrocław University of Science and Technology for their hospitality. Our collaboration during this time was highly fruitful and I am looking forward to further joint work.

Madrid, Spain, is my second home, after not only obtaining my PhD degree there, but also spending some time as a postdoc at IMDEA Nanociencia. My research there was funded initially by the Marie-Curie Action AMAROUT-II and later on by the Comunidad de Madrid, Spain, grant number 2017-T2/IND-6092, as well as the Spanish Ministry of Economy, Industry and Competition (MINECO) via funding of the Centers of Excellence Severo Ochoa, grant

number SEV-2016-0686. I am equally grateful to the Center of Scientific Computations of the Autónoma University of Madrid (CCC-UAM), Spain, for access to their computational resources.

IMDEA Nanociencia has become a family thanks to the warm welcome, the kind, appreciative work environment with constant support in all scientific endeavours and the continued contact even after moving on in my career integrating me through presentations and committee work. Here, I would like to mention David Écija, Alberto Martín Jiménez, Koen Lauwaet, Roberto Otero and Rodolfo Miranda. A special shout-out to my fellow female postdoctoral researchers Amalia Rapakousiou, Ana Espinosa and Manuela Garnica. You are an inspiration to me and others who will follow us.

My tenure at IMDEA was but short due to the calling of new challenges at Friedrich-Schiller-University Jena. Thanks to scientific and financial support within the CRC 1375 NOA *Nonlinear optics down to atomic scales*, I have returned to Germany as a junior group leader involved in several collaborative projects by now. Special thanks are due to the Thüringer Universitäts- und Landesbibliothek Jena (ThULB) for financial support with Open Access publications, an important pillar of scientific research and progress.

I am grateful to Ulf Peschel and Stefanie Gräfe for inviting me to this opportunity and allowing me to add my own take on nonlinear optics research to the CRC, as well as to Carsten Rockstuhl for suggesting me for this position despite not knowing me at all. I would like to thank Oleg Egorov for making my day-to-day in the office fun and being supportive in many aspects of a first time PI's life. I would also like to thank the students who are going on this adventure with me, oftentimes not fully aware that I still learn as much as they do from their projects.

# Bibliography


[1] J. Watchi, S. Cooper, B. Ding, C. M. Mow-Lowry, and C. Collette, "Contributed review: A review of compact interferometers," *Review of Scientific Instruments*, vol. 89, no. 12, p. 121501, 2018.

[2] A. A. Michelson and E. W. Morley, "On the relative motion of the earth and the luminiferous ether," *American Journal of Science*, vol. s3-34, no. 203, p. 333, 1887.

[3] T. A. Hamed, N. Adamovic, U. Aeberhard, D. Alonso-Alvarez, Z. Amin-Akhlaghi, M. A. der Maur, N. Beattie, N. Bednar, K. Berland, S. Birner, M. Califano, I. Capan, B. Cerne, I. Chilibon, J. P. Connolly, F. C. Juan, J. Coutinho, **Christin David**, K. Deppert, V. Donchev, M. Drev, B. Ehlen, N. Ekins-Daukes, J. Even, L. Fara, D. F. Marron, A. Gagliardi, B. Garrido, V. Gianneta, M. Gomes, J.-F. Guillemoles, M. Guina, J. Halme, M. Hocevar, L. Jacak, W. Jacak, Z. Jaksic, L. k. Joseph, S. Kassavetis, V. Kazukauskas, J.-P. Kleider, K. Kluczyk, R. Kopecek, U. O. Krasovec, J.-L. Lazzari, E. Lifshitz, M. Loncaric, S. P. Madsen, A. M. Vega, D. Mencaraglia, M. E. Messing, F. M. Armando, A. G. Nassiopoulou, A. Neijm, A. Nemcsics, V. Neto, L. Pedesseau, C. Persson, K. Petridis, L. Popescu, G. Pucker, J. Radovanović, J. C. Rimada, M. Ristova, I. Savic, H. Savin, M. Sendova-Vassileva, A. Sengul, J. Silva, U. Steiner, J. Storch, E. Stratakis, S. Tao, P. Tomanek, S. Tomić, A. Tukiainen, R. Turan, J. M. Ulloa, S. Wang, F. Yuksel, J. Zadny, and J. Zarbakhsh, "Multiscale in modelling and validation for solar photovoltaics," *EPJ Photovoltaics*, vol. 9, p. 10, 2018.

[4] A. Liebsch, "Surface-plasmon dispersion and size dependence of Mie resonance: Silver versus simple metals," *Phys. Rev. B*, vol. 48, no. 15, pp. 11317–11328, 1993.

[5] I. A. Larkin and M. I. Stockman, "Imperfect perfect lens," *Nano Lett.*, vol. 5, p. 339, 2005.

[6] J. Zuloaga, E. Prodan, and P. Nordlander, "Quantum description of the plasmon resonances of a nanoparticle dimer," *Nano Lett.*, vol. 9, pp. 887–891, 2009.

[7] J. Lermé, B. Palpant, B. Prével, E. Cottancin, M. Pellarin, M. Treilleux, J. L. Vialle, A. Perez, and M. Broyer, "Optical properties of gold metal clusters: A time-dependent local-density-approximation investigation," *Eur. Phys. J. D*, vol. 4, pp. 95–108, 1998.

[8] K. J. Savage, M. M. Hawkeye, R. Esteban, A. G. Borisov, J. Aizpurua, and J. J. Baumberg, "Revealing the quantum regime in tunnelling plasmonics," *Nature*, vol. 491, no. 7425, pp. 574–577, 2012.

[9] R. Esteban, A. G. Borisov, P. Nordlander, and J. Aizpurua, "Bridging quantum and classical plasmonics with a quantum-corrected model," *Nat. Commun.*, vol. 3, p. 825, 2012.

[10] F. Latorre, S. Kupfer, T. Bocklitz, D. Kinzel, S. Trautmann, S. Gräfe, and V. Deckert, "Spatial resolution of tip-enhanced raman spectroscopy – DFT assessment of the chemical effect," *Nanoscale*, vol. 8, no. 19, pp. 10229–10239, 2016.

[11] S. Dapprich, I. Komáromi, K. Byun, K. Morokuma, and M. J. Frisch, "A new ONIOM implementation in gaussian98. part i. the calculation of energies, gradients, vibrational frequencies and electric field derivatives," *Journal of Molecular Structure: THEOCHEM*, vol. 461-462, pp. 1–21, 1999.

[12] T. Vreven, K. S. Byun, I. Komáromi, S. Dapprich, J. A. Montgomery, K. Morokuma, and M. J. Frisch, "Combining quantum mechanics methods with molecular mechanics methods in ONIOM," *Journal of Chemical Theory and Computation*, vol. 2, no. 3, pp. 815–826, 2006.

[13] S. Kupfer, L. Zedler, J. Guthmuller, S. Bode, M. D. Hager, U. S. Schubert, J. Popp,

S. Gräfe, and B. Dietzek, “Self-healing mechanism of metallopolymers investigated by QM/MM simulations and raman spectroscopy,” *Physical Chemistry Chemical Physics*, vol. 16, no. 24, p. 12422, 2014.

[14] M. Pourfath, *The Non-Equilibrium Green’s Function Method for Nanoscale Device Simulation*, vol. 3. Springer, 2014.

[15] A. Doronin and I. Meglinski, “Peer-to-peer monte carlo simulation of photon migration in topical applications of biomedical optics,” *Journal of Biomedical Optics*, vol. 17, no. 9, p. 0905041, 2012.

[16] N. T. Thomopoulos, *Essentials of Monte Carlo simulation: Statistical methods for building simulation models*. Springer Science & Business Media, 2012.

[17] D. Bohm and D. Pines, “A collective description of electron interactions: III. coulomb interactions in a degenerate electron gas,” *Physical Review*, vol. 92, no. 3, p. 609, 1953.

[18] J. Jacak, J. Krasnyj, W. Jacak, R. Gonczarek, A. Chepok, and L. Jacak, “Surface and volume plasmons in metallic nanospheres in semiclassical RPA-type approach; near-field coupling of surface plasmons with semiconductor substrate,” *Physical Review B*, vol. 82, p. 035418, 2010.

[19] X. Ren, P. Rinke, C. Joas, and M. Scheffler, “Random-phase approximation and its applications in computational chemistry and materials science,” *Journal of Materials Science*, vol. 47, no. 21, pp. 7447–7471, 2012.

[20] P. Lalanne and G. M. Morris, “Antireflection behavior of silicon subwavelength periodic structures for visible light,” *Nanotechnology*, vol. 8, pp. 53–56, 1997.

[21] P. S. Kumar, I. Pastoriza-Santos, B. Rodríguez-González, F. J. G. de Abajo, and L. M. Liz-Marzán, “High-yield synthesis and optical response of gold nanostars,” *Nanotechnology*, vol. 19, no. 1, p. 015606, 2007.

[22] V. Myroshnychenko, J. Rodríguez-Fernández, I. Pastoriza-Santos, A. M. Funston, C. Novo, P. Mulvaney, L. M. Liz-Marzán, and F. J. G. de Abajo, “Modelling the optical response of gold nanoparticles,” *Chem. Soc. Rev.*, vol. 37, pp. 1792–1805, 2008.

[23] R. Alvarez-Puebla, L. M. Liz-Marzán, and F. J. García de Abajo, “Light concentration at the nanometer scale,” *The Journal of Physical Chemistry Letters*, vol. 1, p. 2428, 2010.

[24] Y. Liu, T. Lai, H. Li, Y. Wang, Z. Mei, H. Liang, Z. Li, F. Zhang, W. Wang, A. Y. Kuznetsov, and X. Du, “Nanostructure formation and passivation of large-area black silicon for solar cell applications,” *Small*, vol. 8, no. 9, pp. 1392–1397, 2012.

[25] T. Sakai, N. Nedyalkov, and M. Obara, “Positive and negative nanohole-fabrication on glass surface by femtosecond laser with template of polystyrene particle array,” *Journal of Physics D: Applied Physics*, vol. 40, no. 7, p. 2102, 2007.

[26] **Christin David**, J. P. Connolly, C. Chaverri Ramos, F. J. García de Abajo, and G. Sánchez Plaza, “Theory of random nanoparticle layers in photovoltaic devices applied to self-aggregated metal samples,” *Solar Energy Materials and Solar Cells*, vol. 109, pp. 294–299, 2013.

[27] K. Wu, T. Rindzevicius, M. S. Schmidt, K. B. Mogensen, S. Xiao, and A. Boisen, “Plasmon resonances of ag capped si nanopillars fabricated using mask-less lithography,” *Opt. Express*, vol. 23, no. 10, pp. 12965–12978, 2015.

[28] F. Cortés-Juan, C. C. Ramos, J. P. Connolly, **Christin David**, F. J. G. de Abajo, J. Hurtado, V. D. Mihailetchi, S. Ponce-Alcántara, and G. Sánchez, “Effect of ag nanoparticles integrated within antireflection coatings for solar cells,” *Journal of Renewable and Sustainable Energy*, vol. 5, p. 033116, 2013.

[29] N. Kalfagiannis, A. Siozios, D. V. Bellas, D. Toliopoulos, L. Bowen, N. Pliatsikas, W. M. Cranton, C. Kosmidis, D. C. Koutsogeorgis, E. Lidorikis, and P. Patsalas, “Selective modification of nanoparticle arrays by laser-induced self assembly (MONA-LISA):

putting control into bottom-up plasmonic nanostructuring," *Nanoscale*, vol. 8, no. 15, pp. 8236–8244, 2016.

[30] O. Watanabe, T. Ikawa, M. Hasegawa, M. Tsuchimori, and Y. Kawata, "Nanofabrication induced by near-field exposure from a nanosecond laser pulse," *Applied Physics Letters*, vol. 79, no. 9, pp. 1366–1368, 2001.

[31] A. Sundaramurthy, P. J. Schuck, N. R. Conley, D. P. Fromm, G. S. Kino, and W. E. Moerner, "Toward nanometer-scale optical photolithography: Utilizing the near-field of bowtie optical nanoantennas," *Nano Lett.*, vol. 6, no. 3, pp. 355–360, 2006.

[32] P. Spinelli, V. E. Ferry, J. van de Groep, M. van Lare, M. A. Verschuuren, R. E. I. Schropp, H. A. Atwater, and A. Polman, "Plasmonic light trapping in thin-film Si solar cells," *Journal of Optics*, vol. 14, no. 2, p. 024002, 2012.

[33] **Christin David**, P. Kühler, F. J. G. de Abajo, and J. Siegel, "Near-field nanoimprinting using colloidal monolayers," *Opt. Express*, vol. 22, pp. 8226–8233, 2014.

[34] Y. H. Jang, Y. J. Jang, S. Kim, L. N. Quan, K. Chung, and D. H. Kim, "Plasmonic solar cells: From rational design to mechanism overview," *Chem. Rev.*, vol. 116, no. 24, pp. 14982–15034, 2016.

[35] T. Phan, D. Sell, E. W. Wang, S. Doshay, K. Edee, J. Yang, and J. A. Fan, "High-efficiency, large-area, topology-optimized metasurfaces," *Light: Science & Applications*, vol. 8, no. 1, 2019.

[36] Z. A. Kudyshev, A. V. Kildishev, V. M. Shalaev, and A. Boltasseva, "Machine-learning-assisted metasurface design for high-efficiency thermal emitter optimization," *Applied Physics Reviews*, vol. 7, no. 2, p. 021407, 2020.

[37] J. Zhu, H. Zhou, C. Wang, L. Zhou, S. Yuan, and W. Zhang, "A review of topology optimization for additive manufacturing: Status and challenges," *Chinese Journal of Aeronautics*, vol. 34, no. 1, pp. 91–110, 2021.

[38] S. Koppen, M. van der Kolk, F. C. M. van Kempen, J. de Vreugd, and M. Langelaar, "Topology optimization of multicomponent optomechanical systems for improved optical performance," *Structural and Multidisciplinary Optimization*, vol. 58, no. 3, p. 885, 2018.

[39] S. A. Maier and H. A. Atwater, "Plasmonics: Localization and guiding of electromagnetic energy in metal/dielectric structures," *Journal of Applied Physics*, vol. 98, no. 1, p. 011101, 2005.

[40] E. Klampaftis and B. S. Richards, "Improvement in multi-crystalline silicon solar cell efficiency via addition of luminescent material to EVA encapsulation layer," *Progress in Photovoltaics: Research and Applications*, vol. 19, no. 3, pp. 345–351, 2010.

[41] Z. Yuan, G. Pucker, A. Marconi, F. Sgrignuoli, A. Anopchenko, Y. Jestin, L. Ferrario, P. Bellutti, and L. Pavesi, "Silicon nanocrystals as a photoluminescence down shifter for solar cells," *Solar Energy Materials and Solar Cells*, vol. 95, no. 4, p. 1224, 2011.

[42] D. Alonso-Álvarez, D. Ross, E. Klampaftis, K. R. McIntosh, S. Jia, P. Storiz, T. Stolz, and B. S. Richards, "Luminescent down-shifting experiment and modelling with multiple photovoltaic technologies," *Progress in Photovoltaics: Research and Applications*, vol. 23, no. 4, pp. 479–497, 2014.

[43] S. Gardelis and A. G. Nassiopoulou, "Evidence of significant down-conversion in a si-based solar cell using CuInS2/ZnS core shell quantum dots," *Applied Physics Letters*, vol. 104, no. 18, p. 183902, 2014.

[44] S. R. Johannsen, S. P. Madsen, B. R. Jeppesen, J. V. Nygaard, B. Julsgaard, P. Balling, and A. N. Larsen, "Up-conversion enhancement in $Er3^{+}$ doped TiO2 through plasmonic coupling: Experiments and finite-element modeling," *Applied Physics Letters*, vol. 106, no. 5, p. 053101, 2015.

[45] D. Fuertes Marrón, E. Barrigón, M. Ochoa, and I. Artacho, "Quantitative determina-

tion of luminescent coupling in multijunction solar cells from spectral photovoltage measurements," *Physical Review Applied*, vol. 6, no. 1, p. 014001, 2016.

[46] S. Gardelis, V. Gianneta, and A. Nassiopoulou, "Twenty-fold plasmon-induced enhancement of radiative emission rate in silicon nanocrystals embedded in silicon dioxide," *Journal of Luminescence*, vol. 170, pp. 282–287, 2016.

[47] J.-M. Nam, C. S. Thaxton, and C. A. Mirkin, "Nanoparticle-based bio-bar codes for the ultrasensitive detection of proteins," *Science*, vol. 301, no. 5641, p. 1884, 2003.

[48] B. M. Reinhard, M. Siu, H. Agarwal, A. P. Alivisatos, and J. Liphardt, "Calibration of dynamic molecular rulers based on plasmon coupling between gold nanoparticles," *Nano Lett.*, vol. 5, no. 11, pp. 2246–2252, 2005.

[49] M. E. Anderson, M. Mihok, H. Tanaka, L.-P. Tan, M. W. Horn, G. S. McCarty, and P. S. Weiss, "Hybrid approaches to nanolithography: Photolithographic structures with precise, controllable nanometer-scale spacings created by molecular rulers," *Adv. Mater.*, vol. 18, pp. 1020–1022, Apr. 2006.

[50] Y. Wu, W. Yang, Y. Fan, Q. Song, and S. Xiao, "TiO2 metasurfaces: From visible planar photonics to photochemistry," *Science Advances*, vol. 5, no. 11, p. eaax0939, 2019.

[51] J. Yan, X. Liu, C. Ma, Y. Huang, and G. Yang, "All-dielectric materials and related nanophotonic applications," *Materials Science and Engineering: R: Reports*, vol. 141, p. 100563, 2020.

[52] **Christin David**, J. Christensen, and N. A. Mortensen, "Spatial dispersion in two-dimensional plasmonic crystals: Large blueshifts promoted by diffraction anomalies," *Phys. Rev. B*, vol. 94, no. 16, p. 165410, 2016.

[53] **Christin David** and F. J. G. de Abajo, "Spatial nonlocality in the optical response of metal nanoparticles," *J. Phys. Chem. C*, vol. 115, pp. 19470–19475, 2011.

[54] W. Jacak, "Lorentz friction for surface plasmons in metallic nanospheres," *The Journal of Physical Chemistry C*, vol. 119, no. 12, pp. 6749–6759, 2015.

[55] W. Jacak, E. Popko, A. Henrykowski, E. Zielony, K. Gwozdz, G. Luka, R. Pietruszka, B. Witkowski, L. Wachnicki, M. Godlewski, L.-B. Chang, and M.-J. Jeng, "On the size dependence and spatial range for the plasmon effect in photovoltaic efficiency enhancement," *Solar Energy Materials and Solar Cells*, vol. 147, pp. 1–16, 2016.

[56] **Christin David**, "Multi-type particle layer improved light trapping for photovoltaic applications," *Appl. Opt.*, vol. 55, no. 28, pp. 7980–7986, 2016.

[57] U. Hohenester, "Nano and quantum optics," in *Graduate Texts in Physics*, Springer International Publishing, 2019.

[58] F. J. García de Abajo, "Colloquium: Light scattering by particle and hole arrays," *Rev. Mod. Phys.*, vol. 79, pp. 1267–1290, 2007.

[59] J. D. Joannopoulos, S. G. Johnson, J. N. Winn, and R. D. Meade, *Photonic Crystals: Molding the Flow of Light (Second Edition)*. Princeton University Press, 2 ed., 2008.

[60] F. J. G. de Abajo, "Multiple scattering of radiation in clusters of dielectrics," *Phys. Rev. B*, vol. 60, pp. 6086–6102, 1999.

[61] F. J. García de Abajo and A. Howie, "Relativistic electron energy loss and electron-induced photon emission in inhomogeneous dielectrics," *Physical Review Letters*, vol. 80, no. 23, pp. 5180–5183, 1998.

[62] F. J. García de Abajo and A. Howie, "Retarded field calculation of electron energy loss in inhomogeneous dielectrics," *Phys. Rev. B*, vol. 65, p. 115418, 2002.

[63] P. Lalanne and G. M. Morris, "Highly improved convergence of the coupled-wave method for tm polarization," *Journal of the Optical Society of America A-optics Image Science and Vision*, vol. 13, pp. 779–784, 1996.

[64] D. M. Whittaker and I. S. Culshaw, "Scattering-matrix treatment of patterned multilayer photonic structures," *Phys. Rev. B*, vol. 60, pp. 2610–2618, 1999.

[65] V. Liu and S. Fan, “S4 : A free electromagnetic solver for layered periodic structures,” *Computer Physics Communications*, vol. 183, pp. 2233–2244, 2012.

[66] **Christin David**, “TiO2 self-assembled, thin-walled nanotube arrays for photonic applications,” *Materials*, vol. 12, p. 1332, apr 2019.

[67] P. B. Johnson and R. W. Christy, “Optical constants of noble metals,” *Phys. Rev. B*, vol. 6, no. 12, pp. 4370–4379, 1972.

[68] D. E. Aspnes and A. A. Studna, “Dielectric functions and optical parameters of Si, Ge, GaP, GaAs, GaSb, InP, InAs, and InSb from 1.5 to 6.0 eV,” *Phys. Rev. B*, vol. 27, pp. 985–1009, 1983.

[69] S. G. Rodrigo, F. J. García-Vidal, and L. Martín-Moreno, “Influence of material properties on extraordinary optical transmission through hole arrays,” *Physical Review B*, vol. 77, no. 7, p. 075401, 2008.

[70] S. Raza, S. I. Bozhevolnyi, M. Wubs, and N. A. Mortensen, “Nonlocal optical response in metallic nanostructures,” *J. Phys. Cond. Matter.*, vol. 27, no. 18, p. 183204, 2015.

[71] P. T. Leung, “Decay of molecules at spherical surfaces: Nonlocal effects,” *Phys. Rev. B*, vol. 42, no. 12, pp. 7622–7625, 1990.

[72] K. Kluczyk and W. Jacak, “Damping-induced size effect in surface plasmon resonance in metallic nano-particles: Comparison of rpa microscopic model with numerical finite element simulation (comsol) and mie approach,” *Journal of Quantitative Spectroscopy and Radiative Transfer*, vol. 168, pp. 78–88, 2016.

[73] **Christin David** and F. J. García de Abajo, “Surface plasmon dependence on the electron density profile at metal surfaces,” *ACS Nano*, vol. 8, pp. 9558–9566, 2014.

[74] N. A. Mortensen, S. Raza, M. Wubs, T. Søndergaard, and S. I. Bozhevolnyi, “A generalized non-local optical response theory for plasmonic nanostructures,” *Nat. Commun.*, vol. 5, p. 3809, 2014.

[75] **Christin David**, N. A. Mortensen, and J. Christensen, “Perfect imaging, epsilon-near zero phenomena and waveguiding in the scope of nonlocal effects,” *Scientific Reports*, vol. 3, p. 2526, 2013.

[76] C. Ciracì, R. T. Hill, J. J. Mock, Y. Urzhumov, A. I. Fernández-Domínguez, S. A. Maier, J. B. Pendry, A. Chilkoti, and D. R. Smith, “Probing the ultimate limits of plasmonic enhancement,” *Science*, vol. 337, pp. 1072–1074, 2012.

[77] C. Ciracì, “Current-dependent potential for nonlocal absorption in quantum hydrodynamic theory,” *Physical Review B*, vol. 95, no. 24, p. 245434, 2017.

[78] S. Essig and K. Busch, “Generation of adaptive coordinates and their use in the fourier modal method,” *Optics Express*, vol. 18, no. 22, p. 23258, 2010.

[79] J. Küchenmeister, T. Zebrowski, and K. Busch, “A construction guide to analytically generated meshes for the fourier modal method,” *Optics Express*, vol. 20, no. 16, p. 17319, 2012.

[80] J. Küchenmeister, “Three-dimensional adaptive coordinate transformations for the fourier modal method,” *Optics Express*, vol. 22, no. 2, p. 1342, 2014.

[81] J. Küchenmeister, “Generalization and modularization of two-dimensional adaptive coordinate transformations for the fourier modal method,” *Optics Express*, vol. 22, no. 8, p. 9404, 2014.

[82] K. R. Catchpole and A. Polman, “Design principles for particle plasmon enhanced solar cells,” *Appl. Phys. Lett.*, vol. 93, p. 191113, 2008.

[83] Y. A. Akimov, W. S. Koh, S. Y. Sian, and S. Ren, “Nanoparticle-enhanced thin film solar cells: Metallic or dielectric nanoparticles?,” *Appl. Phys. Lett.*, vol. 96, pp. 073111–3, 2010.

[84] H. A. Atwater and A. Polman, “Plasmonics for improved photovoltaic devices,” *Nature Materials*, vol. 9, pp. 205–213, 2010.

[85] M. A. Green and S. Pillai, “Harnessing plasmonics for solar cells,” *Nat Photon*, vol. 6, no. 3, pp. 130–132, 2012.

[86] P. Spinelli, M. A. Verschuuren, and A. Polman, “Broadband omnidirectional antireflection coating based on subwavelength surface Mie resonators,” *Nature Communications*, vol. 3, p. 692, 2012.

[87] W. Yan, N. Stokes, B. Jia, and M. Gu, “Enhanced light trapping in the silicon substrate with plasmonic ag nanocones,” *Opt. Lett.*, vol. 38, no. 4, pp. 395–397, 2013.

[88] C. Barugkin, Y. Wan, D. Macdonald, and K. R. Catchpole, “Evaluating plasmonic light trapping with photoluminescence,” *IEEE Journal of Photovoltaics*, vol. 3, no. 4, pp. 1292–1297, 2013.

[89] X. Chen, B. Jia, Y. Zhang, and M. Gu, “Exceeding the limit of plasmonic light trapping in textured screen-printed solar cells using al nanoparticles and wrinkle-like graphene sheets,” *Light Sci Appl*, vol. 2, p. e92, 2013.

[90] H. Cui, S. Pillai, P. Campbell, and M. Green, “A novel silver nanoparticle assisted texture as broadband antireflection coating for solar cell applications,” *Solar Energy Materials and Solar Cells*, vol. 109, pp. 233–239, 2013.

[91] C. Barugkin, T. Allen, T. K. Chong, T. P. White, K. J. Weber, and K. R. Catchpole, “Light trapping efficiency comparison of si solar cell textures using spectral photoluminescence,” *Opt. Express*, vol. 23, no. 7, pp. A391–A400, 2015.

[92] H. M. Branz, V. E. Yost, S. Ward, K. M. Jones, B. To, and P. Stradins, “Nanostructured black silicon and the optical reflectance of graded-density surfaces,” *Applied Physics Letters*, vol. 94, p. 231121, 2009.

[93] S. Fischer, J. C. Goldschmidt, P. Löper, G. H. Bauer, R. Brüggemann, K. Krämer, D. Biner, M. Hermle, and S. W. Glunz, “Enhancement of silicon solar cell efficiency by upconversion: Optical and electrical characterization,” *Journal of Applied Physics*, vol. 108, no. 4, p. 044912, 2010.

[94] X. Huang, S. Han, W. Huang, and X. Liu, “Enhancing solar cell efficiency: the search for luminescent materials as spectral converters,” *Chem. Soc. Rev.*, vol. 42, no. 1, pp. 173–201, 2013.

[95] V. E. Ferry, L. A. Sweatlock, D. Pacifici, and H. A. Atwater, “Plasmonic nanostructure design for efficient light coupling into solar cells,” *Nano Lett.*, vol. 8, p. 4391, 2008.

[96] A. Basch, F. J. Beck, T. Söderström, S. Varlamov, and K. R. Catchpole, “Combined plasmonic and dielectric rear reflectors for enhanced photocurrent in solar cells,” *Appl. Phys. Lett.*, vol. 100, pp. 243903–5, 2012.

[97] A. Basch, F. Beck, T. Söderström, S. Varlamov, and K. R. Catchpole, “Enhanced light trapping in solar cells using snow globe coating,” *Prog. Photovolt: Res. Appl.*, vol. 20, pp. 837–842, 2012.

[98] M. L. Brongersma, Y. Cui, and S. Fan, “Light management for photovoltaics using high-index nanostructures,” *Nat Mater*, vol. 13, pp. 451–460, 2014.

[99] C. Yang, G. Zhang, H. M. Li, and W. J. Yoo, “Localized surface plasmon resonances caused by Ag nanoparticles on SiN for solar cell applications,” *Journal of the Korean Physical Society*, vol. 56, pp. 1488–1491, 2010.

[100] M. Green, E. Dunlop, J. Hohl-Ebinger, M. Yoshita, N. Kopidakis, and X. Hao, “Solar cell efficiency tables (version 57),” *Progress in Photovoltaics: Research and Applications*, vol. 29, no. 1, pp. 3–15, 2020.

[101] I. H. Öner, C. J. Querebillo, **Christin David**, U. Gernert, C. Walter, M. Driess, S. Leimkühler, K. H. Ly, and I. M. Weidinger, “High electromagnetic field enhancement of TiO2 nanotube electrodes,” *Angewandte Chemie International Edition*, vol. 57, no. 24, pp. 7225–7229, 2018.

[102] J. Bai and B. Zhou, "Titanium dioxide nanomaterials for sensor applications," *Chem. Rev.*, vol. 114, no. 19, p. 10131, 2014.

[103] T. Rajh, N. M. Dimitrijevic, M. Bissonnette, T. Koritarov, and V. Konda, "Titanium dioxide in the service of the biomedical revolution," *Chem. Rev.*, vol. 114, no. 19, pp. 10177–10216, 2014.

[104] Y. Sintov, D. Malka, and Z. Zalevsky, "Prospects for diode-pumped alkali-atom-based hollow-core photonic-crystal fiber lasers," *Optics Letters*, vol. 39, no. 16, p. 4655, 2014.

[105] R. Dadabayev, N. Shabairou, Z. Zalevsky, and D. Malka, "A visible light RGB wavelength demultiplexer based on silicon-nitride multicore PCF," *Optics & Laser Technology*, vol. 111, pp. 411–416, 2019.

[106] D. Malka and G. Katz, "An eight-channel c-band demux based on multicore photonic crystal fiber," *Nanomaterials*, vol. 8, no. 10, p. 845, 2018.

[107] X. X. Han, C. Köhler, J. Kozuch, U. Kuhlmann, L. Paasche, A. Sivanesan, I. M. Weidinger, and P. Hildebrandt, "Potential-dependent surface-enhanced resonance raman spectroscopy at nanostructured TiO2: A case study on cytochrome b5," *Small*, vol. 9, no. 24, pp. 4175–4181, 2013.

[108] K. Awazu, M. Fujimaki, C. Rockstuhl, J. Tominaga, H. Murakami, Y. Ohki, N. Yoshida, and T. Watanabe, "A plasmonic photocatalyst consisting of silver nanoparticles embedded in titanium dioxide," *J. Am. Chem. Soc.*, vol. 130, no. 5, pp. 1676–1680, 2008.

[109] A. V. Akimov, A. J. Neukirch, and O. V. Prezhdo, "Theoretical insights into photoinduced charge transfer and catalysis at oxide interfaces," *Chem. Rev.*, vol. 113, no. 6, pp. 4496–4565, 2013.

[110] J. Schneider, M. Matsuoka, M. Takeuchi, J. Zhang, Y. Horiuchi, M. Anpo, and D. W. Bahnemann, "Understanding tio2 photocatalysis: Mechanisms and materials," *Chem. Rev.*, vol. 114, no. 19, pp. 9919–9986, 2014.

[111] C. Mo, H. Wei, and T. Wang, "Fabrication of a self-doped TiO sub2/sub nanotube array electrode for electrochemical degradation of methyl orange," *Journal of the Chinese Chemical Society*, vol. 66, no. 7, pp. 740–747, 2019.

[112] E. Wang, T. P. White, and K. R. Catchpole, "Resonant enhancement of dielectric and metal nanoparticle arrays for light trapping in solar cells," *Opt. Express*, vol. 20, no. 12, pp. 13226–13237, 2012.

[113] S. Mubeen, J. Lee, W.-r. Lee, N. Singh, G. D. Stucky, and M. Moskovits, "On the plasmonic photovoltaic," *ACS Nano*, vol. 8, no. 6, pp. 6066–6073, 2014.

[114] Y. Bai, I. Mora-Seró, F. De Angelis, J. Bisquert, and P. Wang, "Titanium dioxide nanomaterials for photovoltaic applications," *Chem. Rev.*, vol. 114, no. 19, p. 10095, 2014.

[115] M. Kapilashrami, Y. Zhang, Y.-S. Liu, A. Hagfeldt, and J. Guo, "Probing the optical property and electronic structure of tio2 nanomaterials for renewable energy applications," *Chem. Rev.*, vol. 114, no. 19, pp. 9662–9707, 2014.

[116] H. Lakhotiya, A. Nazir, S. P. Madsen, J. Christiansen, E. Eriksen, J. Vester-Petersen, S. R. Johannsen, B. R. Jeppesen, P. Balling, A. N. Larsen, and B. Julsgaard, "Plasmonically enhanced upconversion of 1500 nm light via trivalent Er in a TiO2 matrix," *Applied Physics Letters*, vol. 109, no. 26, p. 263102, 2016.

[117] P. Roy, S. Berger, and P. Schmuki, "TiO2 nanotubes: Synthesis and applications," *Angewandte Chemie International Edition*, vol. 50, no. 13, pp. 2904–2939, 2011.

[118] H. P. Paudel and M. N. Leuenberger, "Light-controlled plasmon switching using hybrid metal-semiconductor nanostructures," *Nano Lett.*, 2012.

[119] X. Liu, T. Tyler, T. Starr, A. F. Starr, N. M. Jokerst, and W. J. Padilla, "Taming the blackbody with infrared metamaterials as selective thermal emitters," *Phys. Rev. Lett.*, vol. 107, no. 4, p. 045901, 2011.

[120] B. Zhang, Y. Zhao, Q. Hao, B. Kiraly, I.-C. Khoo, S. Chen, and T. J. Huang, "Polarization-

independent dual-band infrared perfect absorber based on a metal-dielectric-metal elliptical nanodisk array," *Opt. Express*, vol. 19, no. 16, pp. 15221–15228, 2011.

[121] S. Thongrattanasiri, F. H. L. Koppens, and F. J. García de Abajo, "Complete optical absorption in periodically patterned graphene," *Phys. Rev. Lett.*, vol. 108, no. 4, p. 047401, 2012.

[122] M. B. Dúhring, N. Asger Mortensen, and O. Sigmund, "Plasmonic versus dielectric enhancement in thin-film solar cells," *Applied Physics Letters*, vol. 100, p. 211914, 2012.

[123] H. V. Bui, A. Kovalgin, and R. Wolters, "On the difference between optically and electrically determined resistivity of ultra-thin titanium nitride films," *Applied Surface Science*, vol. 269, pp. 45–49, 2013.

[124] P. Patsalas, N. Kalfagiannis, S. Kassavetis, G. Abadias, D. Bellas, C. Lekka, and E. Lidorikis, "Conductive nitrides: Growth principles, optical and electronic properties, and their perspectives in photonics and plasmonics," *Materials Science and Engineering: R: Reports*, vol. 123, pp. 1–55, 2018.

[125] C. Metaxa, S. Kassavetis, J. Pierson, D. Gall, and P. Patsalas, "Infrared plasmonics with conductive ternary nitrides," *ACS Applied Materials & Interfaces*, vol. 9, no. 12, pp. 10825–10834, 2017.

[126] P. Patsalas, N. Kalfagiannis, and S. Kassavetis, "Optical properties and plasmonic performance of titanium nitride," *Materials*, vol. 8, no. 12, pp. 3128–3154, 2015.

[127] M. Milanova, V. Donchev, K. L. Kostov, D. Alonso-Álvarez, P. Terziyska, G. Avdeev, E. Valcheva, K. Kirilov, and S. Georgiev, "Study of GaAsSb:n bulk layers grown by liquid phase epitaxy for solar cells applications," *Materials Research Express*, vol. 6, no. 7, p. 075521, 2019.

[128] **Christin David**, L. J. Koduvelikulathu, and R. Kopecek, "Comparative simulations of conductive nitrides as alternative plasmonic nanostructures for solar cells," *Energies*, vol. 14, no. 14, p. 4236, 2021.

[129] S. C. Baker-Finch, K. R. McIntosh, D. Yan, K. C. Fong, and T. C. Kho, "Near-infrared free carrier absorption in heavily doped silicon," *Journal of Applied Physics*, vol. 116, no. 6, 2014.

[130] K. Lee, A. Mazare, and P. Schmuki, "One-dimensional titanium dioxide nanomaterials: Nanotubes," *Chem. Rev.*, vol. 114, no. 19, pp. 9385–9454, 2014.

[131] T. Siefke, S. Kroker, K. Pfeiffer, O. Puffky, K. Dietrich, D. Franta, I. Ohlídal, A. Szeghalmi, E.-B. Kley, and A. Tünnermann, "Materials pushing the application limits of wire grid polarizers further into the deep ultraviolet spectral range," *Advanced Optical Materials*, vol. 4, no. 11, pp. 1780–1786, 2016.

[132] P. Balling, J. Christiansen, R. E. Christiansen, E. Eriksen, H. Lakhotiya, M. Mirsafaei, S. H. Møller, A. Nazir, J. Vester-Petersen, B. R. Jeppesen, P. B. Jensen, J. L. Hansen, S. K. Ram, O. Sigmund, M. Madsen, S. P. Madsen, and B. Julsgaard, "Improving the efficiency of solar cells by upconverting sunlight using field enhancement from optimized nano structures," *Optical Materials*, vol. 83, pp. 279–289, 2018.

[133] J. Springer, A. Poruba, L. Müllerova, M. Vanecek, O. Kluth, and B. Rech, "Absorption loss at nanorough silver back reflector of thin-film silicon solar cells," *Journal of Applied Physics*, vol. 95, no. 3, pp. 1427–1429, 2004.

[134] D. Dominé, F.-J. Haug, C. Battaglia, and C. Ballif, "Modeling of light scattering from micro- and nanotextured surfaces," *Journal of Applied Physics*, vol. 107, no. 4, p. 044504, 2010.

[135] K. Jäger, M. Fischer, R. A. C. M. M. van Swaaij, and M. Zeman, "A scattering model for nano-textured interfaces and its application in opto-electrical simulations of thin-film silicon solar cells," *Journal of Applied Physics*, vol. 111, no. 8, p. 083108, 2012.

[136] M. Dehghani and **Christin David**, "Light scattering from rough silver surfaces: Modeling of absorption loss measurements," *Nanomaterials*, vol. 11, no. 1, p. 113, 2021.

[137] I. H. Öner, **Christin David**, C. J. Querebillo, I. M. Weidinger, and K. H. Ly, "Electromagnetic field enhancement of nanostructured TiN electrodes probed with surface-enhanced raman spectroscopy," *Sensors*, vol. 22, no. 2, p. 487, 2022.

[138] S. K. Cushing, J. Li, F. Meng, T. R. Senty, S. Suri, M. Zhi, M. Li, A. D. Bristow, and N. Wu, "Photocatalytic activity enhanced by plasmonic resonant energy transfer from metal to semiconductor," *J. Am. Chem. Soc.*, vol. 134, no. 36, pp. 15033–15041, 2012.

[139] X. Zhang, Y. L. Chen, R.-S. Liu, and D. P. Tsai, "Plasmonic photocatalysis," *Rep. Prog. Phys.*, vol. 76, p. 046401, 2013.

[140] X.-C. Ma, Y. Dai, L. Yu, and B.-B. Huang, "Energy transfer in plasmonic photocatalytic composites," *Light Sci Appl*, vol. 5, p. e16017, 2016.

[141] **Christin David**, "Two-fluid, hydrodynamic model for spherical electrolyte systems," *Scientific Reports*, vol. 8, no. 1, p. 7544, 2018.

[142] G. Mie, "Beiträge zur Optik trüber Medien, speziell kolloidaler Metallösungen," *Ann. Phys.*, vol. 330, no. 3, pp. 377–445, 1908.

[143] E. Prodan, P. Nordlander, and N. J. Halas, "Electronic structure and optical properties of gold nanoshells," *Nano Lett.*, vol. 3, pp. 1411–1415, 2003.

[144] M. Danckwerts and L. Novotny, "Optical frequency mixing at coupled gold nanoparticles," *Phys. Rev. Lett.*, vol. 98, p. 026104, 2007.

[145] J. A. Scholl, A. L. Koh, and J. A. Dionne, "Quantum plasmon resonances of individual metallic nanoparticles," *Nature*, vol. 483, no. 7390, pp. 421–427, 2012.

[146] S. Raza, N. Stenger, S. Kadkhodazadeh, S. V. Fischer, N. Kostesha, A.-P. Jauho, A. Burrows, M. Wubs, and N. A. Mortensen, "Blueshift of the surface plasmon resonance in silver nanoparticles studied with EELS," *Nanophotonics*, vol. 2, p. 131, 2013.

[147] H. Haberland, "Looking from both sides," *Nature*, vol. 494, pp. E1–E2, 2013.

[148] S. Raza, S. Kadkhodazadeh, T. Christensen, M. Di Vece, M. Wubs, N. A. Mortensen, and N. Stenger, "Multipole plasmons and their disappearance in few-nanometer silver nanoparticles," *Nat. Commun.*, vol. 6, p. 8788, 2015.

[149] R. Fuchs and K. L. Kliewer, "Surface plasmon in a semi-infinite free-electron gas," *Physical Review B*, vol. 3, no. 7, pp. 2270–2278, 1971.

[150] R. Ruppin, "Optical properties of a plasma sphere," *Physical Review Letters*, vol. 31, no. 24, pp. 1434–1437, 1973.

[151] R. Ruppin, "Optical properties of spatially dispersive dielectric spheres," *J. Opt. Soc. Am.*, vol. 71, no. 6, pp. 755–758, 1981.

[152] B. B. Dasgupta and R. Fuchs, "Polarizability of a small sphere including nonlocal effects," *Phys. Rev. B*, vol. 24, pp. 554–561, 1981.

[153] R. Fuchs and F. Claro, "Multipolar response of small metallic spheres: Nonlocal theory," *Phys. Rev. B*, vol. 35, no. 8, pp. 3722–3727, 1987.

[154] R. Rojas, F. Claro, and R. Fuchs, "Nonlocal response of a small coated sphere," *Phys. Rev. B*, vol. 37, pp. 6799–6808, 1988.

[155] R. Ruppin, "Optical absorption by excitons in microcrystals," *Journal of Physics and Chemistry of Solids*, vol. 50, no. 9, pp. 877–882, 1989.

[156] R. Ruppin, "Optical absorption by a small sphere above a substrate with inclusion of nonlocal effects," *Phys. Rev. B*, vol. 45, no. 19, pp. 11209–11215, 1992.

[157] U. Kreibig and M. Vollmer, *Optical Properties of Metal Clusters*. Springer-Verlag, Berlin, 1995.

[158] R. Ruppin, "Extinction properties of thin metallic nanowires," *Optics Communications*, vol. 190, pp. 205–209, 2001.

[159] F. J. García de Abajo, "Nonlocal effects in the plasmons of strongly interacting nanoparticles, dimers, and waveguides," *J. Phys. Chem. C*, vol. 112, pp. 17983–17987, 2008.
[160] W. A. Jacak, "Propagation of collective surface plasmons in linear periodic ionic structures: Plasmon polariton mechanism of saltatory conduction in axons," *The Journal of Physical Chemistry C*, vol. 119, no. 18, pp. 10015–10030, 2015.
[161] K. Kluczyk, **Christin David**, and W. A. Jacak, "On quantum approach to modeling of plasmon photovoltaic effect," *J. Opt. Soc. Am. B*, vol. 34, no. 10, pp. 2115–2127, 2017.
[162] K. Kluczyk, L. Jacak, W. Jacak, and **Christin David**, "Microscopic electron dynamics in metal nanoparticles for photovoltaic systems," *Materials*, vol. 11, no. 7, p. 1077, 2018.
[163] F. Bloch, "Zur Bremsung rasch bewegter Teilchen beim Durchgang durch Materie," *Z. Phys.*, vol. 81, pp. 363–376, 1933.
[164] A. Eguiluz, S. C. Ying, and J. J. Quinn, "Influence of the electron density profile on surface plasmons in a hydrodynamic model," *Phys. Rev. B*, vol. 11, p. 2118, 1975.
[165] J. E. Sipe, V. C. Y. So, M. Fukui, and G. I. Stegeman, "Analysis of second-harmonic generation at metal surfaces," *Phys. Rev. B*, vol. 21, pp. 4389–4402, 1980.
[166] J. Aizpurua and A. Rivacoba, "Nonlocal effects in the plasmons of nanowires and nanocavities excited by fast electron beams," *Phys. Rev. B*, vol. 78, p. 035404, 2008.
[167] J. M. McMahon, S. K. Gray, and G. C. Schatz, "Optical properties of nanowire dimers with a spatially nonlocal dielectric function," *Nano Lett.*, vol. 10, no. 9, p. 3473, 2010.
[168] S. Raza, G. Toscano, A.-P. Jauho, M. Wubs, and N. A. Mortensen, "Unusual resonances in nanoplasmonic structures due to nonlocal response," *Phys. Rev. B*, vol. 84, no. 12, p. 121412(R), 2011.
[169] A. Wiener, A. I. Fernández-Domínguez, A. P. Horsfield, J. B. Pendry, and S. A. Maier, "Nonlocal effects in the nanofocusing performance of plasmonic tips," *Nano Lett.*, vol. 12, pp. 3308–3314, 2012.
[170] D. de Ceglia, S. Campione, M. A. Vincenti, F. Capolino, and M. Scalora, "Low-damping epsilon-near-zero slabs: Nonlinear and nonlocal optical properties," *Phys. Rev. B*, vol. 87, p. 155140, 2013.
[171] T. V. Teperik, P. Nordlander, J. Aizpurua, and A. G. Borisov, "Robust subnanometric plasmon ruler by rescaling of the nonlocal optical response," *Phys. Rev. Lett.*, vol. 110, p. 263901, 2013.
[172] Y. Luo, A. I. Fernandez-Dominguez, A. Wiener, S. A. Maier, and J. B. Pendry, "Surface plasmons and nonlocality: A simple model," *Phys. Rev. Lett.*, vol. 111, no. 9, p. 093901, 2013.
[173] T. Christensen, W. Yan, S. Raza, A.-P. Jauho, N. A. Mortensen, and M. Wubs, "Nonlocal response of metallic nanospheres probed by light, electrons, and atoms," *ACS Nano*, vol. 8, pp. 1745–1758, 2014.
[174] G. Toscano, J. Straubel, A. Kwiatkowski, C. Rockstuhl, F. Evers, H. Xu, N. A. Mortensen, and M. Wubs, "Resonance shifts and spill-out effects in self-consistent hydrodynamic nanoplasmonics," *Nat. Commun.*, vol. 6, p. 7132, 2015.
[175] W. Yan, M. Wubs, and N. A. Mortensen, "Projected dipole model for quantum plasmonics," *Physical Review Letters*, vol. 115, no. 13, p. 137403, 2015.
[176] **Christin David** and J. Christensen, "Extraordinary optical transmission through nonlocal holey metal films," *Applied Physics Letters*, vol. 110, no. 26, p. 261110, 2017.
[177] V. Krasavin Alexey, G. Pavel, and V. Zayats Anatoly, "Free-electron optical nonlinearities in plasmonic nanostructures: A review of the hydrodynamic description," *Laser & Photonics Reviews*, vol. 12, no. 1, p. 1700082, 2018.
[178] N. A. Mortensen, "Mesoscopic electrodynamics at metal surfaces," *Nanophotonics*, vol. 10, no. 10, pp. 2563–2616, 2021.
[179] K. Kluczyk-Korch, L. Jacak, W. A. Jacak, and **Christin David**, "Mode splitting induced

by mesoscopic electron dynamics in strongly coupled metal nanoparticles on dielectric substrates," *Nanomaterials*, vol. 9, no. 9, p. 1206, 2019.

[180] K. Kluczyk, **C. David**, J. Jacak, and W. Jacak, "On modeling of plasmon-induced enhancement of the efficiency of solar cells modified by metallic nano-particles," *Nanomaterials*, vol. 9, no. 1, p. 3, 2019.

[181] U. Kreibig and C. v. Fragstein, "The limitation of electron mean free path in small silver particles," *Z. Physik*, vol. 224, pp. 307–323, 1969.

[182] E. A. Coronado and G. C. Schatz, "Surface plasmon broadening for arbitrary shape nanoparticles: A geometrical probability approach," *The Journal of Chemical Physics*, vol. 119, pp. 3926–3934, 2003.

[183] D. Pines and D. Bohm, "A collective description of electron interactions: II. collective vs individual particle aspects of the interactions," *Phys. Rev.*, vol. 85, pp. 338–353, 1952.

[184] S. Raza, M. Wubs, S. I. Bozhevolnyi, and N. A. Mortensen, "Nonlocal study of ultimate plasmon hybridization," *Opt. Lett.*, vol. 40, no. 5, pp. 839–842, 2015.

[185] N. D. Lang and W. Kohn, "Theory of metal surfaces: Charge density and surface energy," *Phys. Rev. B*, vol. 1, pp. 4555–4568, 1970.

[186] J. R. Maack, N. A. Mortensen, and M. Wubs, "Size-dependent nonlocal effects in plasmonic semiconductor particles," *EPL (Europhysics Letters)*, vol. 119, no. 1, p. 17003, 2017.

[187] J. R. Maack, N. A. Mortensen, and M. Wubs, "Two-fluid hydrodynamic model for semiconductors," *Physical Review B*, vol. 97, no. 11, 2018.

[188] J. A. Porto, F. J. García-Vidal, and J. B. Pendry, "Transmission resonances on metallic gratings with very narrow slits," *Physical Review Letters*, vol. 83, no. 14, pp. 2845–2848, 1999.

[189] T. A. Kelf, Y. Sugawara, J. J. Baumberg, M. Abdelsalam, and P. N. Bartlett, "Plasmonic band gaps and trapped plasmons on nanostructured metal surfaces," *Phys. Rev. Lett.*, vol. 95, no. 11, p. 116802, 2005.

[190] T. W. Ebbesen, H. J. Lezec, H. F. Ghaemi, T. Thio, and P. A. Wolff, "Extraordinary optical transmission through sub-wavelength hole arrays," *Nature*, vol. 391, pp. 667–669, 1998.

[191] E. Popov, M. Neviere, S. Enoch, and R. Reinisch, "Theory of light transmission through subwavelength periodic hole arrays," *Physical Review B*, vol. 62, no. 23, pp. 16100–16108, 2000.

[192] W. L. Barnes, A. Dereux, and T. Ebbesen, "Surface plasmon subwavelength optics," *Nature*, vol. 424, pp. 824–830, 2003.

[193] G. Vecchi, V. Giannini, and J. Gómez Rivas, "Surface modes in plasmonic crystals induced by diffractive coupling of nanoantennas," *Phys. Rev. B*, vol. 80, no. 20, p. 201401, 2009.

[194] X. Yang, A. Ishikawa, X. Yin, and X. Zhang, "Hybrid photonic-plasmonic crystal nanocavities," *ACS Nano*, vol. 5, no. 4, pp. 2831–2838, 2011.

[195] K. J. Russell, T.-L. Liu, S. Cui, and E. L. Hu, "Large spontaneous emission enhancement in plasmonic nanocavities," *Nat. Photon.*, vol. 6, no. 7, pp. 459–462, 2012.

[196] T. V. Teperik, F. J. García de Abajo, A. G. Borisov, M. Abdelsalam, P. N. Bartlett, Y. Sugawara, and J. J. Baumberg, "Omnidirectional absorption in nanostructured metal surfaces," *Nat. Photon.*, vol. 2, pp. 299–301, 2008.

[197] F. Przybilla, A. Degiron, J.-Y. Laluet, C. Genet, and T. W. Ebbesen, "Optical transmission in perforated noble and transition metal films," *J. Opt. A: Pure Appl. Opt.*, vol. 8, no. 5, p. 458, 2006.

[198] L. Martín-Moreno, F. J. García-Vidal, H. J. Lezec, K. M. Pellerin, T. Thio, J. B. Pendry, and T. W. Ebbesen, "Theory of extraordinary optical transmission through subwavelength hole arrays," *Phys. Rev. Lett.*, vol. 86, pp. 1114–1117, 2001.

[199] S. Feng and Y. Wang, “Unidirectional reciprocal wavelength filters based on the square-lattice photonic crystal structures with the rectangular defects,” *Opt. Express*, vol. 21, pp. 220–228, 2013.

[200] A. Boardman and R. Ruppin, “The boundary conditions between spatially dispersive media,” *Surf. Sci.*, vol. 112, pp. 153–167, 1981.

[201] W. Yan, M. Wubs, and N. A. Mortensen, “Hyperbolic metamaterials: Nonlocal response regularizes broadband supersingularity,” *Phys. Rev. B*, vol. 86, no. 20, p. 205429, 2012.

[202] D. Jin, Q. Hu, D. Neuhauser, F. von Cube, Y. Yang, R. Sachan, T. S. Luk, D. C. Bell, and N. X. Fang, “Quantum-spillover-enhanced surface-plasmonic absorption at the interface of silver and high-index dielectrics,” *Phys. Rev. Lett.*, vol. 115, p. 193901, 2015.

[203] S. Raza, T. Christensen, M. Wubs, S. I. Bozhevolnyi, and N. A. Mortensen, “Nonlocal response in thin-film waveguides: Loss versus nonlocality and breaking of complementarity,” *Phys. Rev. B*, vol. 88, no. 11, p. 115401, 2013.

[204] H. F. Ghaemi, T. Thio, D. E. Grupp, T. W. Ebbesen, and H. J. Lezec, “Surface plasmons enhance optical transmission through subwavelength holes,” *Phys. Rev. B*, vol. 58, no. 11, pp. 6779–6782, 1998.

[205] J. Zhang and C. Noguez, “Plasmonic optical properties and applications of metal nanostructures,” *Plasmonics*, vol. 3, no. 4, pp. 127–150, 2008.

[206] L. Rodríguez-Lorenzo, R. A. Álvarez-Puebla, I. Pastoriza-Santos, S. Mazzucco, O. Stéphan, M. Kociak, L. M. Liz-Marzán, and F. J. García de Abajo, “Zeptomol detection through controlled ultrasensitive surface-enhanced raman scattering,” *Journal of the American Chemical Society*, vol. 131, no. 13, pp. 4616–4618, 2009.

[207] J.-J. Feng, U. Gernert, M. Sezer, U. Kuhlmann, D. H. Murgida, **Christin**. **David**, M. Richter, A. Knorr, P. Hildebrandt, and I. M. Weidinger, “Novel Ag-Au Hybrid Device for Electrochemical SE(R)R Spectroscopy in a Wide Potential and Spectral Range,” *Nano Lett.*, vol. 9, pp. 298–303, 2009.

[208] G. Toscano, S. Raza, S. Xiao, M. Wubs, A.-P. Jauho, S. I. Bozhevolnyi, and N. A. Mortensen, “Surface-enhanced raman spectroscopy: nonlocal limitations,” *Opt. Lett.*, vol. 37, no. 13, pp. 2538–2540, 2012.

[209] A. Yanai, N. A. Mortensen, and U. Levy, “Absorption and eigenmode calculation for one-dimensional periodic metallic structures using the hydrodynamic approximation,” *Phys. Rev. B*, vol. 88, p. 205120, 2013.

[210] A. Moreau, C. Ciracì, and D. R. Smith, “Impact of nonlocal response on metallodielectric multilayers and optical patch antennas,” *Phys. Rev. B*, vol. 87, p. 045401, 2013.

[211] M. Dechaux, P.-H. Tichit, C. Ciracì, J. Benedicto, R. Pollès, E. Centeno, D. R. Smith, and A. Moreau, “Influence of spatial dispersion in metals on the optical response of deeply subwavelength slit arrays,” *Phys. Rev. B*, vol. 93, p. 045413, 2016.

[212] V. Yannopapas, “Non-local optical response of two-dimensional arrays of metallic nanoparticles,” *J. Phys. Cond. Matter.*, vol. 20, no. 32, p. 325211, 2008.

[213] Q. Cao and P. Lalanne, “Negative role of surface plasmons in the transmission of metallic gratings with very narrow slits,” *Physical Review Letters*, vol. 88, p. 057403, 2002.

[214] M. Beruete, M. Sorolla, I. Campillo, J. S. Dolado, L. Martin-Moreno, J. Bravo-Abad, and F. J. Garcia-Vidal, “Enhanced millimeter-wave transmission through subwavelength hole arrays,” *Optics Letters*, vol. 29, pp. 2500–2502, 2004.

[215] M. Beruete, M. Sorolla, and I. Campillo, “Left-handed extraordinary optical transmission through a photonic crystal of subwavelength hole arrays,” *Optics Express*, vol. 14, pp. 5445–5455, 2006.

[216] H. T. Liu and P. Lalanne, “Microscopic theory of the extraordinary optical transmission,” *Nature*, vol. 452, pp. 728–731, 2008.

[217] F. J. Garcia-Vidal, L. Martin-Moreno, T. W. Ebbesen, and L. Kuipers, “Light passing through subwavelength apertures,” *Reviews of Modern Physics*, vol. 82, pp. 729–787, 2010.

[218] R. Gordon, D. Sinton, K. L. Kavanagh, and A. G. Brolo, “A new generation of sensors based on extraordinary optical transmission,” *Acc. Chem. Res.*, vol. 41, no. 8, pp. 1049–1057, 2008.

[219] J. W. Menezes, J. Ferreira, M. J. L. Santos, L. Cescato, and A. G. Brolo, “Large-area fabrication of periodic arrays of nanoholes in metal films and their application in biosensing and plasmonic-enhanced photovoltaics,” *Advanced Functional Materials*, vol. 20, no. 22, pp. 3918–3924, 2010.

[220] T. Sannomiya, O. Scholder, K. Jefimovs, C. Hafner, and A. B. Dahlin, “Investigation of plasmon resonances in metal films with nanohole arrays for biosensing applications,” *Small*, vol. 7, no. 12, pp. 1653–1663, 2011.

[221] F. E. Low, *Classical Field Theory - Electromagnetism and Gravitation*. Wiley-VCH Verlag, 1997.

[222] J. D. Jackson, *Classical Electrodynamics*. John Wiley & Sons, Inc., 1976.

[223] C. Tserkezis, N. Stefanou, M. Wubs, and N. A. Mortensen, “Molecular fluorescence enhancement in plasmonic environments: exploring the role of nonlocal effects,” *Nanoscale*, vol. 8, no. 40, pp. 17532–17541, 2016.

[224] L. D. Landau and E. M. Lifshits, *Field theory*. Nauka, Moscow, 1973.

[225] A. A. Abrikosov, *Fundamentals of the theory of metals*. Amsterdam etc.: North-Holland, 1988.

[226] K. Kluczyk-Korch, **Christin David**, W. Jacak, and J. Jacak, “Application of core–shell metallic nanoparticles in hybridized perovskite solar cell—various channels of plasmon photovoltaic effect,” *Materials*, vol. 12, no. 19, p. 3192, 2019.

[227] D. M. Schaadt, B. Feng, and E. T. Yu, “Enhanced semiconductor optical absorption via surface plasmon excitation in metal nanoparticles,” *Applied Physics Letters*, vol. 86, no. 6, p. 063106, 2005.

[228] F. J. Beck, S. Mokkapati, and K. R. Catchpole, “Light trapping with plasmonic particles: beyond the dipole model,” *Opt. Express*, vol. 19, pp. 25230–25241, 2011.

[229] K. Okamoto, I. Niki, A. Shvartser, Y. Narukawa, T. Mukai, and A. Scherer, “Surface-plasmon-enhanced light emitters based on InGaN quantum wells,” *Nat. Mater.*, vol. 3, no. 9, pp. 601–605, 2004.

[230] S. Pillai, K. R. Catchpole, T. Trupke, G. Zhang, J. Zhao, and M. A. Green, “Enhanced emission from si-based light-emitting diodes using surface plasmons,” *Applied Physics Letters*, vol. 88, no. 16, p. 161102, 2006.

[231] S. P. Sundararajan, N. K. Grady, N. Mirin, and N. J. Halas, “Nanoparticle-induced enhancement and suppression of photocurrent in a silicon photodiode,” *Nano Lett.*, vol. 8, no. 2, pp. 624–630, 2008.

[232] K. Y. Yang, K. C. Choi, and C. W. Ahn, “Surface plasmon-enhanced spontaneous emission rate in an organic light-emitting device structure: Cathode structure for plasmonic application,” *Applied Physics Letters*, vol. 94, no. 17, p. 173301, 2009.

[233] S. C. Warren and E. Thimson, “Plasmonic solar water splitting,” *Energy & Environmental Science*, vol. 5, p. 5133, 2012.

[234] P. Wang, B. Huang, Y. Dai, and M.-H. Whangbo, “Plasmonic photocatalysts: harvesting visible light with noble metal nanoparticles,” *Phys. Chem. Chem. Phys.*, vol. 14, no. 28, pp. 9813–9825, 2012.

[235] A. Naldoni, F. Riboni, U. Guler, A. Boltasseva, V. M. Shalaev, and A. V. Kildishev,

"Solar-powered plasmon-enhanced heterogeneous catalysis," *Nanophotonics*, vol. 5, no. 1, p. 1, 2016.

[236] S. Pillai, K. R. Catchpole, T. Trupke, and M. A. Green, "Surface plasmon enhanced silicon solar cells," *J. Appl. Phys.*, vol. 101, no. 9, p. 093105, 2007.

[237] S.-S. Kim, S.-I. Na, J. Jo, D.-Y. Kim, and Y.-C. Nah, "Plasmon enhanced performance of organic solar cells using electrodeposited Ag nanoparticles," *Appl. Phys. Lett.*, vol. 93, no. 7, pp. 073307–3, 2008.

[238] K. R. Catchpole and A. Polman, "Plasmonic solar cells," *Opt. Express*, vol. 16, pp. 21793–21800, 2008.

[239] R. A. Pala, J. White, E. Barnard, J. Liu, and M. L. Brongersma, "Design of plasmonic thin-film solar cells with broadband absorption enhancements," *Adv. Mater.*, vol. 21, no. 34, pp. 3504–3509, 2009.

[240] A. J. Nozik, "Nanoscience and nanostructures for photovoltaics and solar fuels," *Nano Letters*, vol. 10, no. 8, pp. 2735–2741, 2010.

[241] S. Xiao, E. Stassen, and N. A. Mortensen, "Ultrathin silicon solar cells with enhanced photocurrents assisted by plasmonic nanostructures," *Journal of Nanophotonics*, vol. 6, no. 1, pp. 061503–1–061503–7, 2012.

[242] A. Polman and H. A. Atwater, "Photonic design principles for ultrahigh-efficiency photovoltaics," *Nat. Mater.*, vol. 11, no. 3, pp. 174–177, 2012.

[243] J. Villanueva-Cab, J. L. Montaño-Priede, and U. Pal, "Effects of plasmonic nanoparticle incorporation on electrodynamics and photovoltaic performance of dye sensitized solar cells," *J. Phys. Chem. C*, vol. 120, no. 19, pp. 10129–10136, 2016.

[244] S. H. Autler and C. H. Townes, "Stark effect in rapidly varying fields," *Physical Review*, vol. 100, no. 2, pp. 703–722, 1955.

[245] J. Qi, G. Lazarov, X. Wang, L. Li, L. M. Narducci, A. M. Lyyra, and F. C. Spano, "Autler-townes splitting in molecular lithium: Prospects for all-optical alignment of nonpolar molecules," *Physical Review Letters*, vol. 83, no. 2, pp. 288–291, 1999.

[246] D. McGloin, "Coherent effects in a driven Vee scheme," *Journal of Physics B: Atomic, Molecular and Optical Physics*, vol. 36, no. 13, pp. 2861–2871, 2003.

[247] I. Haque and M. R. Singh, "A study of the ac Stark effect in doped photonic crystals," *Journal of Physics: Condensed Matter*, vol. 19, no. 15, p. 156229, 2007.

[248] S. A. Empedocles and M. G. Bawendi, "Quantum-confined stark effect in single CdSe nanocrystallite quantum dots," *Science*, vol. 278, no. 5346, pp. 2114–2117, 1997.

[249] V. Ciulin, S. G. Carter, M. S. Sherwin, A. Huntington, and L. A. Coldren, "Terahertz optical mixing in biased GaAs single quantum wells," *Physical Review B*, vol. 70, no. 11, 2004.

[250] Y.-H. Kuo, Y. K. Lee, Y. Ge, S. Ren, J. E. Roth, T. I. Kamins, D. A. B. Miller, and J. S. Harris, "Strong quantum-confined stark effect in germanium quantum-well structures on silicon," *Nature*, vol. 437, no. 7063, pp. 1334–1336, 2005.

[251] X. Zhang, J. Zhang, H. Liu, X. Su, and L. Wang, "Soft plasmons with stretchable spectroscopic response based on thermally patterned gold nanoparticles," *Scientific Reports*, vol. 4, no. 1, 2014.

[252] R. Caputo, L. De Sio, U. Cataldi, and C. Umeton, "Active plasmonics in self-organized soft materials," in *Amorphous Nanophotonics*, pp. 307–326, Springer, 2013.

[253] A. L. Peratt, *Physics of the plasma universe*. Springer, 1992.

[254] A. R. Choudhuri, *The physics of fluids and plasmas: an introduction for astrophysicists*. Cambridge University Press, 1998.

[255] W. A. Jacak, "Plasmons in finite spherical electrolyte systems: RPA effective jellium model for ionic plasma excitations," *Plasmonics*, vol. 11, no. 2, pp. 637–651, 2016.

[256] J. Jacak and W. Jacak, "Plasmons and plasmon–polaritons in finite ionic systems:

Toward soft-plasmonics of confined electrolyte structures," *Applied Sciences*, vol. 9, no. 6, p. 1159, 2019.

[257] C. Genet and T. W. Ebbesen, "Light in tiny holes," *Nature*, vol. 445, pp. 39–46, 2007.

[258] A. Kristensen, J. K. W. Yang, S. I. Bozhevolnyi, S. Link, P. Nordlander, N. J. Halas, and N. A. Mortensen, "Plasmonic colour generation," *Nature Reviews Materials*, vol. 2, no. 1, p. 16088, 2016.

[259] N. Yu, J. Fan, Q. J. Wang, C. Pflugl, L. Diehl, T. Edamura, M. Yamanishi, H. Kan, and F. Capasso, "Small-divergence semiconductor lasers by plasmonic collimation," *Nat Photon*, vol. 2, no. 9, pp. 564–570, 2008.

[260] S. I. Bozhevolnyi and N. A. Mortensen, "Plasmonics for emerging quantum technologies," *Nanophotonics*, vol. 6, no. 5, pp. 1185–1188, 2017.

[261] T. Dong, K. Yin, X. Gao, and X. Ma, "Multi-fluid generalization," *J. Phys. D: Appl. Phys.*, vol. 5, p. 022, 2020.

[262] A. V. Grosse, "Viscosities of liquid sodium and potassium, from their melting points to their critical points," *Science*, vol. 147, no. 3664, pp. 1438–1441, 1965.

[263] H. Ozbek, J. A. Fair, and S. L. Phillips, "Viscosity of aqueous sodium chloride solutions from 0-150deg C," *C. Lawrence Berkeley National Laboratory. LBNL Report #: LBL-5931*, 1977.

[264] A. A. Aleksandrov, E. V. Dzhuraeva, and V. F. Utenkov, "Viscosity of aqueous solutions of sodium chloride," *High Temperature*, vol. 50, no. 3, pp. 354–358, 2012.

[265] S. Keren-Zur, L. Michaeli, H. Suchowski, and T. Ellenbogen, "Shaping light with nonlinear metasurfaces," *Advances in Optics and Photonics*, vol. 10, no. 1, p. 309, 2018.

[266] A. M. Shaltout, V. M. Shalaev, and M. L. Brongersma, "Spatiotemporal light control with active metasurfaces," *Science*, vol. 364, no. 6441, 2019.

[267] B. Metzger, M. Hentschel, and H. Giessen, "Ultrafast nonlinear plasmonic spectroscopy: From dipole nanoantennas to complex hybrid plasmonic structures," *ACS Photonics*, vol. 3, no. 8, pp. 1336–1350, 2016.

[268] M. Kauranen and A. V. Zayats, "Nonlinear plasmonics," *Nature Photonics*, vol. 6, no. 11, pp. 737–748, 2012.

[269] Y. Kivshar, "All-dielectric meta-optics and non-linear nanophotonics," *National Science Review*, vol. 5, no. 2, pp. 144–158, 2018.

[270] D. Krause, C. W. Teplin, and C. T. Rogers, "Optical surface second harmonic measurements of isotropic thin-film metals: Gold, silver, copper, aluminum, and tantalum," *Journal of Applied Physics*, vol. 96, no. 7, pp. 3626–3634, 2004.

[271] R. W. Boyd, Z. Shi, and I. De Leon, "The third-order nonlinear optical susceptibility of gold," *Optics Communications*, vol. 326, pp. 74–79, 2014.

[272] S. Boroviks, T. Yezekyan, Á. R. Echarri, F. J. García de Abajo, J. D. Cox, S. I. Bozhevolnyi, N. A. Mortensen, and C. Wolff, "Anisotropic second-harmonic generation from monocrystalline gold flakes," *Optics Letters*, vol. 46, no. 4, p. 833, 2021.

[273] M. Ren, B. Jia, J.-Y. Ou, E. Plum, J. Zhang, K. F. MacDonald, A. E. Nikolaenko, J. Xu, M. Gu, and N. I. Zheludev, "Nanostructured plasmonic medium for terahertz bandwidth all-optical switching," *Advanced Materials*, vol. 23, no. 46, pp. 5540–5544, 2011.

[274] R. W. Boyd, *Nonlinear optics*. Elsevier, 2003.

[275] N. Daryakar and **Christin David**, "Thin films of nonlinear metallic amorphous composites," *Nanomaterials*, vol. 12, no. 19, p. 3359, 2022.

[276] A. Marini, M. Conforti, G. D. Valle, H. W. Lee, T. X. Tran, W. Chang, M. A. Schmidt, S. Longhi, P. S. J. Russell, and F. Biancalana, "Ultrafast nonlinear dynamics of surface plasmon polaritons in gold nanowires due to the intrinsic nonlinearity of metals," *New Journal of Physics*, vol. 15, no. 1, p. 013033, 2013.

[277] R. C. Miller, “Optical second harmonic generation in piezoelectric crystals,” *Applied Physics Letters*, vol. 5, no. 1, pp. 17–19, 1964.

[278] S. Beer, J. Gour, A. Alberucci, **Christin David**, S. Nolte, and U. Zeitner, “Second harmonic generation under doubly resonant lattice plasmon excitation,” *Optics Express*, 10.1364/OE.470578, 2022.

[279] M. Hazra, P. Paul, D. Kim, **Christin David**, S. Gräfe, U. Peschel, M. Kübel, A. Szeghalmi, and A. Pfeiffer, “Nonlinear polarization holography of nanoscale iridium films,” *New Journal of Physics (under review)*, 2022.

[280] A. Sommer, E. M. Bothschafter, S. A. Sato, C. Jakubeit, T. Latka, O. Razskazovskaya, H. Fattahi, M. Jobst, W. Schweinberger, V. Shirvanyan, V. S. Yakovlev, R. Kienberger, K. Yabana, N. Karpowicz, M. Schultze, and F. Krausz, “Attosecond nonlinear polarization and light–matter energy transfer in solids,” *Nature*, vol. 534, no. 7605, pp. 86–90, 2016.

[281] J. Reislöhner, C. Leithold, and A. N. Pfeiffer, “Characterization of weak deep ultraviolet pulses using cross-phase modulation scans,” *Optics Letters*, vol. 44, no. 7, p. 1809, 2019.

[282] A. Szeghalmi, S. Senz, M. Bretschneider, U. Gösele, and M. Knez, “All dielectric hard x-ray mirror by atomic layer deposition,” *Applied Physics Letters*, vol. 94, no. 13, p. 133111, 2009.

[283] T. Weber, T. Käsebier, A. Szeghalmi, M. Knez, E.-B. Kley, and A. Tünnermann, “Iridium wire grid polarizer fabricated using atomic layer deposition,” *Nanoscale Research Letters*, vol. 6, no. 1, pp. 1–4, 2011.

[284] K.-H. Kim, A. Husakou, and J. Herrmann, “Saturable absorption in composites doped with metal nanoparticles,” *Optics Express*, vol. 18, no. 21, p. 21918, 2010.

[285] J. L. Coutaz, M. Neviere, E. Pic, and R. Reinisch, “Experimental study of surface-enhanced second-harmonic generation on silver gratings,” *Physical Review B*, vol. 32, no. 4, p. 2227, 1985.

[286] M. J. Huttunen, O. Reshef, T. Stolt, K. Dolgaleva, R. W. Boyd, and M. Kauranen, “Efficient nonlinear metasurfaces by using multiresonant high-q plasmonic arrays,” *Journal of the Optical Society of America B*, vol. 36, no. 7, p. E30, 2019.

[287] T. Stolt, A. Vesala, H. Rekola, P. Karvinen, T. K. Hakala, and M. J. Huttunen, “Multiply-resonant second-harmonic generation using surface lattice resonances in aluminum metasurfaces,” *Optics Express*, vol. 30, no. 3, p. 3620, 2022.

[288] O. Reshef, M. Saad-Bin-Alam, M. J. Huttunen, G. Carlow, B. T. Sullivan, J.-M. Ménard, K. Dolgaleva, and R. W. Boyd, “Multiresonant high-iq/i plasmonic metasurfaces,” *Nano Letters*, vol. 19, no. 9, pp. 6429–6434, 2019.

[289] D. J. Bergman, “The dielectric constant of a composite material—a problem in classical physics,” *Physics Reports*, vol. 43, no. 9, pp. 377–407, 1978.

[290] A. Sihvola and H. Wallén, “Homogenization of amorphous media,” in *Amorphous Nanophotonics*, pp. 67–87, Springer Berlin Heidelberg, 2013.

[291] D. Werdehausen, X. G. Santiago, S. Burger, I. Staude, T. Pertsch, C. Rockstuhl, and M. Decker, “Modeling optical materials at the single scatterer level: The transition from homogeneous to heterogeneous materials,” *Advanced Theory and Simulations*, vol. 3, no. 11, p. 2000192, 2020.

[292] K. M. Czajkowski, D. Świtlik, C. Langhammer, and T. J. Antosiewicz, “Effective optical properties of inhomogeneously distributed nanoobjects in strong field gradients of nanoplasmonic sensors,” *Plasmonics*, vol. 13, no. 6, pp. 2423–2434, 2018.

[293] V. A. Markel, “Introduction to the maxwell garnett approximation: tutorial,” *Journal of the Optical Society of America A*, vol. 33, no. 7, p. 1244, 2016.

[294] J. J. Saarinen, E. M. Vartiainen, and K.-E. Peiponen, “On tailoring of nonlinear spectral

properties of nanocomposites having Maxwell Garnett or Bruggeman structure," *Optical Review*, vol. 10, no. 2, pp. 111–115, 2003.

[295] K.-E. Peiponen, O. A. Martti, J. J. Saarinen, and T. Asakura, "Dispersion theory of liquids containing optically linear and nonlinear maxwell garnett nanoparticles," *Optical Review*, vol. 8, no. 1, pp. 9–17, 2001.

[296] J. E. Sipe and R. W. Boyd, "Nonlinear susceptibility of composite optical materials in the maxwell garnett model," *Physical Review A*, vol. 46, no. 3, pp. 1614–1629, 1992.

[297] T. Cesca, P. Calvelli, G. Battaglin, P. Mazzoldi, and G. Mattei, "Local-field enhancement effect on the nonlinear optical response of gold-silver nanoplanets," *Optics Express*, vol. 20, no. 4, p. 4537, 2012.

[298] E. D. Palik, ed., *Handbook of optical constants of solids*. Academic Press, 1985.

[299] P. Schmitt, V. Beladiya, N. Felde, P. Paul, F. Otto, T. Fritz, A. Tünnermann, and A. V. Szeghalmi, "Influence of substrate materials on nucleation and properties of iridium thin films grown by ALD," *Coatings*, vol. 11, no. 2, p. 173, 2021.

[300] Y. Battie, A. Resano-Garcia, N. Chaoui, Y. Zhang, and A. E. Naciri, "Extended Maxwell-Garnett-Mie formulation applied to size dispersion of metallic nanoparticles embedded in host liquid matrix," *The Journal of Chemical Physics*, vol. 140, no. 4, p. 044705, 2014.

[301] K. O'Brien, H. Suchowski, J. Rho, A. Salandrino, B. Kante, X. Yin, and X. Zhang, "Predicting nonlinear properties of metamaterials from the linear response," *Nature Materials*, vol. 14, no. 4, pp. 379–383, 2015.

[302] G. F. Bertsch, J.-I. Iwata, A. Rubio, and K. Yabana, "Real-space, real-time method for the dielectric function," *Physical Review B*, vol. 62, no. 12, pp. 7998–8002, 2000.

[303] R. del Coso and J. Solis, "Relation between nonlinear refractive index and third-order susceptibility in absorbing media," *Journal of the Optical Society of America B*, vol. 21, no. 3, p. 640, 2004.

[304] K. Yabana, T. Nakatsukasa, J.-I. Iwata, and G. F. Bertsch, "Real-time, real-space implementation of the linear response time-dependent density-functional theory," *physica status solidi (b)*, vol. 243, no. 5, pp. 1121–1138, 2006.

[305] S. Wunderlich, B. Schürer, C. Sauerbeck, W. Peukert, and U. Peschel, "Molecular Mie model for second harmonic generation and sum frequency generation," *Physical Review B*, vol. 84, no. 23, p. 235403, 2011.

[306] A. G. F. de Beer and S. Roke, "Nonlinear Mie theory for second-harmonic and sum-frequency scattering," *Physical Review B*, vol. 79, no. 15, 2009.

[307] Y. Pavlyukh and W. Hübner, "Nonlinear Mie scattering from spherical particles," *Physical Review B*, vol. 70, no. 24, 2004.

[308] D. C. Marinica, A. K. Kazansky, P. Nordlander, J. Aizpurua, and A. G. Borisov, "Quantum plasmonics: Nonlinear effects in the field enhancement of a plasmonic nanoparticle dimer," *Nano Lett.*, vol. 12, no. 3, pp. 1333–1339, 2012.

[309] M. Farshad, D. C. Perera, and J. C. Rasaiah, "Theoretical study of the stability, structure, and optical spectra of small silver clusters and their formation using density functional theory," *Physical Chemistry Chemical Physics*, vol. 23, no. 45, pp. 25507–25517, 2021.

[310] X. C. Zeng, D. J. Bergman, P. M. Hui, and D. Stroud, "Effective-medium theory for weakly nonlinear composites," *Physical Review B*, vol. 38, no. 15, p. 10970, 1988.

[311] R. Guo, L. You, Y. Zhou, Z. Shiuh Lim, X. Zou, L. Chen, R. Ramesh, and J. Wang, "Non-volatile memory based on the ferroelectric photovoltaic effect," *Nat Commun*, vol. 4, 2013.

[312] K. Huang, *Statistical Mechanics*. Wiley, New York, 1963.

[313] I. Nagy, "Short-range correlation in a two-dimensional electron gas," *Phys. Rev. B*, vol. 52, no. 3, pp. 1497–1499, 1995.

[314] M. Rusek, H. Lagadec, and T. Blenski, "Cluster explosion in an intense laser pulse: Thomas-fermi model," *Phys. Rev. A*, vol. 63, no. 1, p. 013203, 2000.
[315] R. H. Ritchie, "Plasma losses by fast electrons in thin films," *Phys. Rev.*, vol. 106, no. 5, p. 874, 1957.
[316] B. S. Mendoza and W. L. Mochán, "Exactly solvable model of surface second-harmonic generation," *Phys. Rev. B*, vol. 53, no. 8, pp. 4999–5006, 1996.
[317] B. Busson and L. Dalstein, "Nonlinear optical response of a gold surface in the visible range: A study by two-color sum-frequency generation spectroscopy. II. model for metal nonlinear susceptibility," *The Journal of Chemical Physics*, vol. 149, no. 3, p. 034701, 2018.
[318] H. Wallén, H. Kettunen, and A. Sihvola, "Mixing formulas and plasmonic composites," in *Metamaterials and Plasmonics: Fundamentals, Modelling, Applications*, pp. 91–102, Springer Netherlands, 2009.

# Abbreviations

**ABC** Additional Boundary Condition
**AFM** Atomic Force Microscopy
**ALD** Atomic Layer Deposition
**BEM** Boundary Element Method
**Br** Bruggeman
**CDM** Coupled Dipole Method
**DDA** Discrete Dipole Approximation
**DFT** Density Functional Theory
**EF** Field Enhancement Factor
**EMTs** effective medium theories
**EOT** Extraordinary Optical Transmission
**FDTD** Finite Difference Time Domain
**FEM** Finite Element Method
**FFT** Fast Fourier Transform
**FH** Fundamental Harmonic
**FMM** Fourier Modal Method
**FT** Fourier Transform
**GNOR** Generalized Nonlocal Optical Response
**HDM** hydrodynamic model
**IR** infrared
**LIGO** Laser Interferometer Gravitational-Wave Observatory
**LRA** local response approxmiation
**LSPR** localized surface plasmon resonance
**NEGF** Non-Equilibrium Green's Functions
**NP** nanoparticle
**NPs** nanoparticles
**NT** nanotube
**NTs** nanotubes
**MD** Molecular-Dynamic
**MESME** Multiple Elastic Scattering of the Multipole Expansion
**MG** Maxwell-Garnett
**MMGM** modified Maxwell-Garnett-Mie
**MNP** metal nanoparticle
**MNPs** metal nanoparticles
**PV** photovoltaic
**PWE** plane-wave expansion
**RCWA** Rigorous Coupled Wave Analysis
**RI** refractive index
**RPA** Random Phase Approximation
**SEM** scanning electron microscopy
**SERS** surface enhanced Raman scattering
**SH** Second Harmonic
**SHG** Second Harmonic Generation
**SNOM** Scanning Near-Field Optical Microscope
**SPP** surface plasmon polariton
**SSHG** surface second harmonic generation
**(TD)LDA** (time dependent) local density approximation
**THG** Third Harmonic Generation
**UV** ultraviolet
**VIS** visible
**XPM** Cross-Phase Modulation

# Index

# Ehrenwörtliche Erklärung

Ich erkläre hiermit, dass mir die Habilitationsordnung der Friedrich-Schiller-Universität Jena vom 7. Januar 1997 (Lesefassung, letzte Änderung 19. Dezember 2017) bekannt ist.

Ferner erkläre ich ehrenwörtlich, dass ich die vorliegende Arbeit selbständig, ohne unzulässige Hilfe Dritter und ohne Benutzung anderer als der angegebenen Hilfsmittel und Literatur angefertigt habe. Die aus anderen Quellen direkt oder indirekt übernommenen Daten und Konzepte sind unter Angabe der Quelle gekennzeichnet.

Bei der Auswahl und Auswertung folgenden Materials haben mir die nachstehend aufgeführten Personen in der jeweils beschriebenen Weise unentgeltlich geholfen:

1. Von mir betreute Studierende, insbesondere Herr Navid Daryakar [275], Doktorand im SFB NOA 1375 zu nichtlinearen Eigenschaften amorpher Nanostrukturen; Herr Matin Dehghani [136], Bachelorand der Kashan University, Iran, nunmehr Masterand an der FSU Jena zu diffuser Streuung von rauen Oberflächen; sowie Dr. Katarzyna Kluczyk-Korch [3, 161, 162, 179, 180, 226], ehemalige Doktorandin an der WUST, Polen, zur plasmonverstärkten Photovoltaik unter Beachtung nichtklassischer Effekte.
2. Für zur Analyse und Weiterverarbeitung bereitgestellte Messwerte gilt mein Dank folgenden Partnern außerhalb Jenas Prof. Dr. Inez Weidinger, Technische Universität Dresden [101, 137, 207] zur Ramanspektroskopie, dem International Solar Energy Research Center Konstanz (ISC Konstanz) vertreten durch Herr Lejo Joseph Koduvelikulathu [3, 128] zur Photovoltaik und dem Forschungszentrum Jülich vertreten durch Prof. Dr. Bernd Rech [133, 136] zu diffuser Streuung rauer Oberflächen.
3. Für die Zusammenarbeit in Jena gilt mein Dank den Experimentatoren Prof. Dr. Stefan Nolte des Instituts für Angewandte Physik der FSU Jena, sowie Prof. Dr. Uwe Zeitner Fraunhofer-Instituts für Angewandte Optik und Feinmechanik (IOF) [278] zur Oberflächennichtlinearität von nanoskalen Gittern und Dr. Adriana Szeghalmi des IOFs zur ALD und Nichtlinearitäten amorpher Strukturen, sowie Dr. Adrian Pfeiffer des Instituts für Optik und Quantenelektronik zur nichtlinearen Polarisationsholographie.

Weitere Personen waren an der inhaltlich-materiellen Erstellung der vorliegenden Arbeit nicht beteiligt. Insbesondere habe ich hierfür nicht die entgeltliche Hilfe von Vermittlungs- bzw. Beratungsdiensten in Anspruch genommen. Niemand hat von mir unmittelbar oder mittelbar geldwerte Leistungen für Arbeiten erhalten, die im Zusammenhang mit dem Inhalt der vorgelegten Habilitationsschrift stehen.

Die Arbeit wurde bisher weder im In- noch im Ausland in gleicher oder ähnlicher Form einer anderen Prüfungsbehörde vorgelegt.

Ich versichere, dass ich nach bestem Wissen die reine Wahrheit gesagt und nichts verschwiegen habe.

Ort, Datum

Unterschrift der Verfasserin

# Lebenslauf

*Christin David*

## Ausbildung

| | |
|---|---|
| 03.10.2014 | **Doktorgrad der Physik**, Universidad Autónoma de Madrid (UAM), Spanien, sehr gut mit den Auszeichnungen *cum laude* und *Europäischer Doktor* |
| 02.07.2009 | **Diplom-Physikerin**, Technische Universität Berlin (TUB), sehr gut mit Auszeichnung |
| Schwerpunkte | Theoretische Nanophotonik und -plasmonik: Nanostrukturen wie photonische Kristalle, raue Oberflächen, Nanopartikel; nichtlokale und kollektive Effekte; Photovoltaik, Katalyse |
| 1997–2004 | **Abitur**, Humboldt-Gymnasium Eichwalde |
| 1991–1997 | Grundschule Schönefeld |

## Aktuelle Tätigkeit

| | |
|---|---|
| seit 1. Juli 2019 | **Nachwuchsgruppenleiterin** an der Friedrich-Schiller-Universität Jena (FSU) und dem Abbe Center of Photonics (ACP) zu optischen Eigenschaften hybrider Nanostrukturen |

## Bisherige Tätigkeiten

| | |
|---|---|
| 09.17 – 06.19 | **Postdoktorandin**, EU-FP7 (Marie Curie), IMDEA Nanoscience, Madrid, Spanien |
| 04.17 – 09.17 | **Postdoktorandin**, DFG Returnee, Institut für Theoretische Physik, TUB |
| 04.15 – 03.17 | **Postdoktorandin**, DFG Projekt, Technische Universität Dänemarks, DTU Fotonik |
| 01.10 – 03.15 | **Doktorandin**, Consejo Superior de Investigaciones Cientifícas (CSIC), Madrid; Instituto de Ciencias Fotónicas - ICFO, Barcelona, Spanien, Leitung Prof. F. J. García de Abajo |
| 02.13 – 05.13 | **Gastwissenschaftlerin**, DTU Fotonik, Center for Nanostructured Graphene (CNG) |
| Doktorarbeit | *Nonlocal and Collective Phenomena in the Plasmons of Metallic Nanostructures* |
| 10.09 – 12.09 | **Wissenschaftliche Mitarbeiterin**, SFB 429, Institut für Theoretische Physik, TUB |
| 10.04 – 07.09 | **Diplomstudentin**, Technische Universität Berlin, Leitung Prof. A. Knorr, Institut für Theoretische Physik, und Prof. P. Hildebrandt, Institut für Chemie |
| Diplomarbeit | *Theory of Plasmonic Optical Enhancement in Hybrid Metal-Molecule Structures* |
| 10.07 – 09.09 | **Tutorin**, *Institut für Theoretische Physik, TUB*, Betreuung Bachelorkurse |
| 10.07 – 06.08 | **Tutorin**, *EU gefördertes Projekt LabGirls, Institut für Festkörperphysik, TUB* |
| 07.06 – 09.06 | **Werkstudentin**, *Automatisierungstechnik für PITZ/XFEL, DESY, Zeuthen/Hamburg* |

✉ *christin.david@uni-jena.de*

## Auszeichnungen und Stipendien

07.20 – 12.22 **ProChance-career** Programm der FSU Jena zur Förderung von Nachwuchswissenschaftlerinnen auf ihrem Weg zur Professur (2.11.3-A1/2020-02)

07.20 – 06.22 **Mentoring-Programm** des Unibunds Halle-Leipzig-Jena für Postdoktorandinnen

02.18 – 06.19 **Attraktion von Talent** Postdoktorandenstipendium (2017-T2/IND-6092) des Rats für Bildung, Jugend und Sport der Gemeinde Madrid, Spanien

09.17 – 01.18 **AMAROUT-II Forschungsstipendium** eine Marie Curie Action (EU-FP7-People-2011-Cofund, n° 291803) des IMDEA Nanoscience, Madrid, Spanien

04.17 – 09.17 **DFG Rückkehrerstipendium** der Deutschen Forschungsgemeinschaft

04.15 – 03.17 **DFG Forschungsstipendium** (Gepris 268910011) der Deutschen Forschungsgemeinschaft zur Durchführung eines Forschungsprojekts an der DTU Fotonik, Dänemark

Dez. 2015 **Premio Extraordinario** de Doctorado de la Universidad Autónoma de Madrid, Spanien

12.11 – 03.15 **FPU Promotionsstipendium** des Spanischen Bildungsministeriums (AP2010-0750)

Juli 2010 **Physik-Studienpreis** der Wilhelm und Else Heraeus Stiftung für die Diplomarbeit

Juni 2004 Beginn **Mitgliedschaft in der Deutschen Physikalischen Gesellschaft (DPG)**; Abitur mit Humboldt-Preis und Humboldt-Ehrung zur Anerkennung der in der Oberstufe erbrachten Leistungen und sozialem Engagement am Humboldt-Gymnasium Eichwalde

## Projektmanagement

10.22 – 09.23 **pintXsum:** *Photo-INduced Thermal eXpansion of rough SUrface Morphologies*, Strategische Projekte 2022/23 der Profillinie Light, Friedrich-Schiller-Universität Jena

01.22 – 06.26 **IRTG/GRK 2675 META-ACTIVE** *Tailored metasurfaces - generating, programming and detecting light*, Deutsche Forschungsgemeinschaft DFG, Projektleiterin im Projekt C4 *Semiconductor metasurfaces for energy applications*

10.20 – 09.20 **Doktorandenstipendium** aus dem Graduate School Scholarship Programme (GSSP) der DAAD zur Leitung einer Promotion an der Abbe School of Photonics (ASP)

07.19 – 06.23 **CRC/SFB 1375 NOA** *Nonlinear Optics down to Atomic scales*, Deutsche Forschungsgemeinschaft DFG, Projektleiterin im Projekt A5 *Nonlinear and nonlocal optical response in complex nanostructured multilayers*

09.19 – 08.22 **QuPoLET**: Quantum Properties of the Light Emitted from a Tunnel Junction; spanisches Staatsbüro für wissenschaftliche Forschung. Leiter: Roberto Otero Martín.

05.15 – 04.19 **MPNS COST Action MP1406 MultiscaleSolar** (*Multiscale in modelling and validation for solar photovoltaics*), stellvertretende Vorsitzende, Leitung der Arbeitsgruppen: *Plasmonik und Spektrale Konverter* und *Optik auf der Mesoskala*

Aug. 2015 **Nanophotonics Workshop**, DTU Fotonik, Dänemark, Organisation und Moderation geladener Vorträge durch lokale Wissenschaftler

Nov. 2012 **Nanophotonics for photovoltaics, a step forward**, Workshop in Valencia, Spanien, Organisation und Moderation der Session:

*Enhanced light management by exploiting (plasmonic) nanostructures*

01.10 – 12.12 **LIMA** (*Improve Photovoltaic efficiency by applying novel effects at the limits of light-matter interaction*) (FP7-ICT-248909)

## Arbeiten als Gasteditor und Beiträge zum Peer-Review

WOS verifizierte Gutachter- und Editorakte auf WOS (Researcher ID `G-8831-2015`)

2022, MDPI *Advances in Photovoltaic Technologies from Atomic to Device Scale*, Photonics

2017, Hindawi *Multiscale Modeling of Photovoltaic Devices*, International Journal of Photoenergy

seit 2010 >150 Gutachten in ca. 35 wissenschaftlichen Zeitschriften; Auswahl von Konferenzbeiträgen

✉ *christin.david@uni-jena.de*

## Gutachtertätigkeit für Forschungsprojektanträge

ANR Gutachten für die französische Agence Nationale de la Recherche

NCN Gutachten für das polnische Narodowe Centrum Nauki (Nationales Wissenschaftszentrum)

## Engagement in Gremien und Auswahlkomitees

RdGA Vertreterin der wissenschaftlichen Mitarbeiter:innen im Rat der Graduierten-Akademie an der Friedrich-Schiller-Universität Jena, seit Oktober 2022

MSCA-IF Postdoktorand:innen-Programm IDEAL des IMDEA Nanociencia, Spanien

Berufungen Vertreterin der wissenschaftlichen Mitarbeiter:innen bei der Auswahl eines Kandidaten für den Lehrstuhl *Theorie der Quanteninformation* an der FSU Jena

## Publikationen

ORCID verifiziertes Publikationsverzeichnis 0000-0002-5492-9398

ResearcherID verifiziertes Publikationsverzeichnis via Web of Science G-8831-2015

H-Index 12 (WOS), 12 (Scopus), beitragende Artikel sind mit * gekennzeichnet

**eingereicht** **Nonlinear polarization holography of nanoscale iridium films**, *M. Hazra, P. Paul, D. Kim, C. David, S. Gräfe, U. Peschel, A. Szeghalmi and A. N. Pfeiffer*, eingereicht bei New Journal of Physics (2023), arXiv:2211.03436

**2023** **Linear and nonlinear optical properties of iridium nanoparticles by atomic layer deposition**, *P. Schmidt, P. Paul, W. Li, Z. Wang, C. David, N. Daryakar, K. Hanemann, N. Felde, A.-S. Munser, M. F. Kling, S. Schröder, A. Tünnermann, A. Szeghalmi*, Coatings 13(4), 787 (2023)

**2022** **Cathodoluminescence investigation of complex Au architectures and their applications in plasmon-mediated photocatalysis**, *Z. Fusco, A. Riaz, C. David, F. Beck*, Adv. Mater. Interfaces 2202236 (2022)

**Advances in Photovoltaic Technologies from Atomic to Device Scale**, *C. David, R. Hussein, Opinion*, Photonics 9(11), 837 (2022)

**Second harmonic generation under doubly resonant lattice plasmon excitation**, *S. Beer, J. Gour, A. Alberucci, C. David, S. Nolte, U. Zeitner*, Optics Express 30(22), 40884–40896 (2022)

**Thin Films of Nonlinear Metallic Amorphous Composite Materials**, *N. Daryakar, C. David*, Nanomaterials 12(19), 3359 (2022)

**Electromagnetic Field Enhancement of Nanostructured TiN Electrodes Probed with Surface-Enhanced Raman Spectroscopy**, *I. H. Öner, C. David, C. J. Querebillo, I. M. Weidinger, K. H. Ly*, Sensors 22 (2), 487 (2022)

**2021** **Comparative Simulations of Conductive Nitrides as Alternative Plasmonic Nanostructures for Solar Cells**, *C. David, L. J. Koduvelikulathu, R. Kopecek*, Energies 14 (14), 4236 (2021)

**Light Scattering from Rough Silver Surfaces: Modeling of Absorption Loss Measurements**, *M. Dehghani, C. David*, Nanomaterials 11 (1), 113 (2021)

**2019** **Application of Core-Shell Metallic Nanoparticles in Hybridized Perovskite Solar Cell-Various Channels of Plasmon Photovoltaic Effect**, *K. Kluczyk-Korch, C. David, W. Jacak, J. Jacak*, Materials 12, 3192 (2019)

**Mode Splitting Induced by Mesoscopic Electron Dynamics in Strongly Coupled Metal Nanoparticles on Dielectric Substrates**, *K. Kluczyk-Korch, J. Jacak, W. Jacak, C. David*, Nanomaterials 9(9), 1206 (2019)

**$TiO_2$ Self-Assembled, Thin-Walled Nanotube Arrays for Photonic Applications**, *C. David*, Materials 12(8), 1332 (2019)

✉ *christin.david@uni-jena.de*

**On Modeling of Plasmon-Induced Enhancement of the Efficiency of Solar Cells Modified by Metallic Nano-Particles**, *K. Kluczyk, C. David, J. Jacak, W. Jacak*, Nanomaterials 9(1), 3 (2019)

**2018** **Two-fluid, hydrodynamic model for spherical electrolyte systems**, *C. David*, Scientific Reports, 8, 7544 (2018)

**Microscopic Electron Dynamics in Metal Nanoparticles for Photovoltaic Systems**, *K. Kluczyk, L. Jacak, W. Jacak, C. David*, Materials, SI: Advanced Nanostructures for Photonics and Photovoltaics, Materials 11(7), 1077 (2018)

**Multiscale Modeling of Photovoltaic Devices (Special Issue; Editorial)**, *Matthias Auf der Maur, Urs Aeberhard, Christin David, and Alessio Gagliardi*, Int. Journal of Photoenergy, 3065252, 1 (2018)

***High electromagnetic field enhancement of TiO2 nanotubes electrodes**, *I. H. Öner, C. J. Querebillo, C. David, U. Gernert, C. Walter, M. Driess, S. Leimkühler, K. H. Ly, I. M. Weidinger*, Angewandte Chemie IE, 57, 7225 (2018)

**Multiscale in modelling and validation for solar photovoltaics**, *T. Abu Hamed, N. Adamovic, U. Aeberhard, D. Alonso-Alvarez, Z. Amin-Akhlaghi, M. Auf der Maur, N. Beattie, N. Bednar, K. Berland, S. Birner, M. Califano, I. Capan, B. Cerne, I. Chilibon, J. P. Connolly, F. Cortes Juan, J. Coutinho, C. David et al.*, EPJ Photovolt., 9, 10 (2018)

**2017** ***On quantum approach to modeling of plasmon photovoltaic effect**, *K. Kluczyk, C. David, und W. Jacak*, J. Opt. Soc. Am. B, 34(19), 2115–2127 (2017) [*Editor's Pick*]

***Extraordinary optical transmission through nonlocal holey metal films**, *C. David und J. Christensen*, Appl. Phys. Lett., 110, 261110 (2017) [*Editor's Pick*]

**2016** ***Spatial dispersion in 2D plasmonic crystals: Large blueshifts promoted by diffraction anomalies**, *C. David, J. Christensen, und N. A. Mortensen*, Phys. Rev. B 94, 165410 (2016)

**Multi-type particle layer enhanced light trapping for photovoltaic applications**, *C. David*, Applied Optics, 55(28), 7980–7986 (2016)

**2014** ***Surface plasmon dependence on the electron density profile at metal surfaces**, *C. David, F. J. García de Abajo*, ACS Nano 8 (9), 9558 (2014)

***Near-field nanoimprinting using colloidal monolayers**, *C. David, P. Kühler, F. J. García de Abajo, J. Siegel*, OE 22(7), 8226 (2014)

**2013** ***Perfect imaging, ENZ phenomena und waveguiding in the scope of nonlocal effects**, *C. David, N. A. Mortensen, J. Christensen*, Sci. Rep. 3, 2526 (2013)

***Effect of Ag nanoparticles integrated within anti reflection coatings for solar cells**, *F. Cortés-Juan, C. Chaverri Ramos, J. P. Connolly, C. David, F. J. García de Abajo, J. Hurtado, V. D. Mihailetchi, S. Ponce-Alcántara, G. Sánchez*, J. Renewable Sustainable Energy 5 (3) 033116 (2013)

***Theory of random nanoparticle layers in photovoltaic devices applied to self-aggregated metal samples**, *C. David, J. P. Connolly, C. Chaverri Ramos, F. J. García de Abajo, G. Sánchez*, Solar Energy Materials und Solar Cells 109, 294-299 (2013)

**2011** ***Spatial Nonlocality in the Optical Response of Metal Nanoparticles**, *C. David, F. J. García de Abajo*, J. Phys. Chem. C 115, 19470–19475 (2011)

**2010** ***Image Dipoles Approach to the Local Field Enhancement in Nanostructured Ag–Au Hybrid Devices**, *C. David, M. Richter, A. Knorr, P. Hildebrandt, I. M. Weidinger*, J. Chem. Phys. 132, 024712 (2010)

**2009** ***Novel Au-Ag Hybrid Device for Electrochemical SE(R)R Spectroscopy in a Wide Potential und Spectral Range**, *J.-J. Feng, U. Gernert, M. Sezer, U. Kuhlmann, D. H. Murgida, C. David, M. Richter, A. Knorr, P. Hildebrandt, I. M. Weidinger*, Nano Letters 9(1), 298–303 (2009)

### Artikel in begutachteten Konferenzproceedings

**2022** **Nonlocal Soft Plasmonics: Investigating the ionic plasmon effects of planar electrolyte systems**, *P. R. Narayan and C. David*, Conference on Lasers and Electro-Optics, Technical Digest Series (Optica Publishing Group, JTu3B.31 (2022)

**Light Scattering from Rough Silver Surfaces in Multilayered systems**, *M. Dehghani and C. David*, Conference on Lasers and Electro-Optics, Technical Digest Series (Optica Publishing Group, JTu3B.8 (2022)

**2020** **Quantum corrections to the efficiency of solar cells with conductive nanostructured layers**, *C. David*, 2020 International Conference on Numerical Simulation of Optoelectronic Devices (NUSOD), IEEE (2020)

**Soft Plasmonics: A novel perspective on electrolyte-metal interactions**, *C. David*, Photonics North (PN), IEEE 1-1 (2020)

**2019** **Plasmonic Properties of Electrolytes Beyond Classical Nanophotonics – A Two-fluid, Hydrodynamic Approach to Nonlocal Soft Plasmonics**, *C. David*, IEEE Xplore: 2018 Progress in Electromagnetics Research Symposium (PIERS-Toyama), 1-4 August 2018, 490–495 (2019)

**2018** **Metal Films with Subwavelength Holes: Optical Properties in the Scope of Nonlocal Charge Carrier Dynamics**, *C. David, J. Christensen, N. A. Mortensen*, Progress in electrom. research symposium, 40th PIERS, Session 3A4 SC3, 960 (2018)

**Alternative Plasmonic Materials in Photovoltaics: Photocurrent Gain with Conductive Nitride Nanopillars**, *C. David*, Progress in electromagnetics research symposium, 40th PIERS, Session 3P14a, 1352 (2018)

**2013** **Perfect imaging und ENZ phenomena for Metallic Slabs in the scope of Nonlocal Effects**, *C. David, N. A. Mortensen, J. Christensen*, Progress in electromagnetics research symposium, 34th PIERS, Session 4P4 SC2, 1569 (2013)

**Inclusion of nonlocal effects in the hydrodynamic description of metal surfaces with smooth density profiles**, *C. David und F. J. García de Abajo*, 34th PIERS, Session 4P4 SC2, 1563 (2013)

**Plasmonic Nanoparticle Integration with Si Back Contact Solar Cells**, *F. Cortés-Juan, C. Chaverri Ramos, J. P. Connolly, C. David, V. D. Mihailetchi, S. Ponce-Alcántara, G. Sánchez* , 28th EPVSEC, 375–379 (2013)

**2011** **Towards Efficient Integration of metallic Nanoparticle Layers in Photovoltaic Devices**, *C. David, J. P. Connolly, G. Sánchez, F. J. García de Abajo*, Int. Conference on Electrodynamics of Complex Materials for Advanced Technologies (PLASMETA'11)

**2010** **Spatial nonlocality in the optical response of metal nanoparticles**, *C. David und F. J. García de Abajo*, Metamaterials'2010 Karlsruhe Proceedings (2010)

**Analysis of Plasmonic Nanoparticle Fabrication Techniques for Efficient Integration in Photovoltaic Devices**, *J. P. Connolly, C. David, P. Rodriguez, A. Griol, P. Welti, L. Bellières, J. Ayucar, J. Hurtado, R. López, G. Sánchez, F. J. García de Abajo*, 25th EPVSEC, 773–776 (2010)

**Nonlocal Effects in the Optical Response of Metal Nanoparticles**, *C. David und F. J. García de Abajo*, AIP Conference Proceedings, 1291, 43-45 (2010)

## Eingeladene Vorträge, Gastvorträge, Kolloquien

Juli 2023 **Meta2023**, *Paris, Frankreich*, Nanostructures for Photocatalysis - From regular to dendritic Architectures

Juli 2023 **Piers2023**, *Prag, Tschechien*, Selectively Enhancing Second Harmonic Generation from Diffraction at Gold Nanogratings

Juni 2023 **AES2023 - Antennas and Electromagnetic Systems**, *Torremolinos, Spanien*, Nonlinear Metasurfaces: Third order Nonlinearities of amorphous Composites and structure-induced Second order Surface Nonlinearities

Mai 2023 **Habilitationsvorteidigung**, *Friedrich-Schiller-Univeristät Jena*, Hybrid Nanostructured Systems beyond classical Electrodynamics: Mesoscale Electron Dynamics and Nonlinear Effects (*Kolloquium*)

Nov. 2022 **Leibniz Universität Hannover**, Structure-induced optical phenomena: Their potential and their limits (*Kolloquium*)

Okt. 2022 **3D-ICOMAS 2022 – International Conference on Materials Science**, *Verona, Italien*, eingeladener Vortrag, Selectively enhancing second harmonic generation from diffraction at gold nanogratings

Mai 2022 **Habilitationsvorstellung**, *Friedrich-Schiller-Univeristät Jena*, Hybrid Nanostructured Systems beyond classical Electrodynamics: Mesoscale Electron Dynamics and Nonlinear Effects (*Kolloquium*)

April 2021 **Gastvortrag Seminar**, *Universität von Twente, Niederlande (online)*, Willem Vos, Plasmonic Properties of Electrolytes Beyond Classical Nanophotonics – Nonlocal Soft Plasmonics

Sept. 2020 **NUSOD 2020 – International Conference on Numerical Simulation of Optoelectronic Devices**, *Turin, Italien (online)*, eingeladener Vortrag (aufgenommen)
Quantum corrections to the efficiency of solar cells with conductive nanostructured layers

Sept. 2020 **KIT Summer School in Computational Photonics**, *Karlsruhe*, *Vorlesungen*, Fourier Modal Method *und* Nonlocality in Nanophotonics *sowie Übungen*

Mai 2020 **Photonics North2020**, *Niagara Falls, Kanada (online)*, eingeladener Vortrag
Soft Plasmonics: A novel perspective on electrolyte-metal interactions

Juli 2019 **Meta2019**, *Lissabon, Portugal*, Holey metal films for sensing applications - Impact of nonlocality on extraordinary optical transmission

Okt. 2018 **Leibniz Universität Hannover**, Application of the Rigorous Coupled Wave Approach (RCWA) for optical technologies in spectroscopy and photovoltaics (*Kolloquium*)

Aug. 2018 **Friedrich-Schiller-Univeristät**, *Jena*, Enhancing electro-optical effects with nanostructures – Spectroscopy, Optical Data Storage, Photovoltaics (*Lecture*)

Aug. 2017 **Plasmonica2017**, *Belgrade, Serbien*, Enhancing Solar Cells with Nanostructures (*Lecture*)

Sept. 2016 **METANANO-2016**, *Anapa, Russland*, Spatial dispersion in plasmonic crystals

seit 2009 des Weiteren 19 eigene Vorträge und 16 eigene Posterbeiträge auf Konferenzen

seit 2018 7 Vorträge und 12 Posterbeiträge auf Konferenzen von Mitgliedern meiner Arbeitsgruppe

## Berufungsverfahren

Nov. 2022 A-Liste für die W2 Professur "Optische Materialien: Rechnergestützte Methoden" an der Leibniz Universität Hannover

Okt. 2018 A-Liste für die Nachwuchspaktprofessur "Optisches Design und Multiphysics Simulation" an der Leibniz Universität Hannover

## Ehrenamt

Wahlvorstände Wahlhelferin zur Ortsteilbürgermeisterwahl in Jena-Süd und Closewitz am 26.06.2022

Wahlhelferin zur Bundestagswahl in der Stadt Jena am 26.09.2021

Bürgergremium Mitglied des *Observatorio de la Ciudad* der Stadt Madrid, 2019/2020

C. David 19. Juni 2023

✉ *christin.david@uni-jena.de*